Advanced physical modeling of PEM fuel cells to enhance their performances

Raphaël Gass

Aix Marseille Université

THÈSE DE DOCTORAT

Soutenue à AMU — Aix-Marseille Université
dans le cadre d'un co-encadrement avec FEMTO-ST
le 17 décembre 2024 par

Raphaël GASS

Advanced physical modeling of PEM fuel cells to enhance their performances

Modélisation physique avancée des piles à combustible PEM pour améliorer leurs performances

Discipline
Automatique

École doctorale
ED 184 Mathématiques et Informatique

Laboratoire/Partenaires de recherche
Laboratoire d'Informatique et des Systèmes (LIS), Marseille FRANCE

Institut de Franche-Comté Electronique Mécanique Thermique et Optique – Sciences et Technologies (FEMTO-ST), Besançon FRANCE

Composition du jury

Sophie DIDIERJEAN PU (LEMTA/UL)	Rapporteure
Liangfei XU PA (TSINGHUA)	Rapporteur
Serge SIMOENS DR (LMFA/CNRS)	Président du jury
Mohamed BOUTAYEB PU (CRAN/UL)	Examinateur
Rachid OUTBIB PU (LIS/AMU)	Directeur de thèse
Zhongliang LI PCS (FEMTO-ST/UFC)	Co-directeur de thèse
Samir JEMEI PU (FEMTO-ST/UFC)	Co-encadrant de thèse
Daniel HISSEL PU (FEMTO-ST/UFC)	Co-encadrant de thèse

femto-st SCIENCES & TECHNOLOGIES

LIS LABORATOIRE D'INFORMATIQUE & SYSTÈMES

Affidavit

I, undersigned, Raphaël Gass, hereby declare that the work presented in this manuscript is my own work, carried out under the scientific supervision of Zhongliang Li, Rachid Outbib, Samir Jemei and Daniel Hissel, in accordance with the principles of honesty, integrity and responsibility inherent to the research mission. The research work and the writing of this manuscript have been carried out in compliance with both the french national charter for Research Integrity and AMU charter on the fight against plagiarism.

This work has not been submitted previously either in this country or in another country in the same or in a similar version to any other examination body.

Marseille, July 10, 2024

List of publications and conference participation

List of publications produced within the framework of the thesis project :

1. R. Gass, Z. Li, R. Outbib, S. Jemei, D. Hissel, « A Critical Review of Proton Exchange Membrane Fuel Cells Matter Transports and Voltage Polarisation for Modelling » in the *Journal of The Electrochemical Society* (2024). DOI : 10.1149/1945-7111/ad305a.
2. R. Gass, Z. Li, R. Outbib, S. Jemei, D. Hissel, « An advanced 1D physics-based model for PEM hydrogen fuel cells with enhanced overvoltage prediction » in the *International Journal of Hydrogen Energy* (2025). DOI : 10.1016/j.ijhydene.2024.11.374.
3. R. Gass, Z. Li, R. Outbib, S. Jemei, D. Hissel, « AlphaPEM : an open-source dynamic 1D physics-based PEM fuel cell model for embedded applications » in the *SoftwareX* journal (2025). DOI : 10.1016/j.softx.2024.102002.
4. R. Gass, Z. Li, R. Outbib, S. Jemei, D. Hissel, « Modélisation spatiale de la pile à combustible PEM » in the *Techniques de l'Ingénieur* journal (2024). DOI : 10.51257/a-v1-re193.

Participation in conferences during the thesis period :

1. R. Gass, Z. Li, R. Outbib, S. Jemei, D. Hissel, « Modélisation dynamique à 9 nœuds d'une pile à combustible PEMFC » in the *Conférence des Jeunes Chercheurs en Génie Électrique* (JCGE), oral presentation, June 2022, Le Croisic, France.
2. R. Gass, Z. Li, R. Outbib, S. Jemei, D. Hissel, « Un modèle physique 1D+1D dynamique de la pile à hydrogène PEMFC pour des systèmes embarqués » in the *3ème Réunion Plénières de la Fédération Hydrogène du CNRS* (FRH2), oral presentation, May 2023, Île de la Réunion, France.
3. R. Gass, Z. Li, R. Outbib, S. Jemei, D. Hissel, « Advancing fuel cell control : a dynamic 1D physics-based model for PEM fuel cells » in the *9th International Conference on Fundamentals & Development of Fuel Cell* (FDFC), oral presentation, September 2023, Ulm, Germany.

4. R. Gass, Z. Li, « A 1-D 2-phase control-oriented mass transfer model of PEM fuel cells » in the *7th CAA International Conference on Vehicular Control and Intelligence* (CVCI), oral presentation, October 2023, Changsha, China. DOI : 10.1109/CVCI59596.2023.10397331.
5. R. Gass, Z. Li, R. Outbib, S. Jemei, D. Hissel, « AlphaPEM : un modèle de pile à combustible PEM 1D dynamique et open-source pour des applications embarquées » in the *4ème Réunion Plénières de la Fédération Hydrogène du CNRS* (FRH2), oral presentation, October 2024, La Grande Motte, France.

Résumé et mots clés

Les technologies de l'hydrogène offrent des perspectives prometteuses pour répondre aux futures demandes énergétiques dans un monde plus durable. Compte tenu de leur potentiel, leur développement technologique est au cœur de nombreuses politiques. Ainsi, la modélisation précise des piles à combustible est essentielle pour optimiser leur contrôle et améliorer leur performance.

Cette thèse commence par une analyse approfondie des avancées récentes concernant les principes régissant le transport de la matière et le calcul de la tension des piles à combustible à membrane échangeuse de protons (PEMFC). Elle fournit une compréhension détaillée de ces principes en présentant les équations associées, leur applicabilité et les hypothèses sous-jacentes, ce qui constitue une base solide pour le développement de futurs modèles.

En s'appuyant sur ces travaux, un modèle unidimensionnel, dynamique, à deux phases et isotherme pour les PEMFC, utilisant une approche par différences finies, a été développé. Ce modèle constitue un compromis entre la simplicité des modèles à blocs fonctionnels et la précision des modèles de mécanique des fluides numériques (en anglais : computational fluid dynamics models), offrant ainsi une description précise des états internes tout en ayant une faible demande de calcul. En outre, un nouveau paramètre physique, le coefficient de saturation limite en eau liquide (s_{lim}), ainsi que les formules correspondantes, sont introduits dans le calcul de la surtension. Ce nouveau paramètre relie la chute de tension à des densités de courant élevées à la quantité d'eau liquide présente dans les couches catalytiques et aux conditions de fonctionnement de la pile à combustible. Ce lien nouvellement établi entre les états internes de la pile à combustible et ses conditions de fonctionnement est prometteur pour l'optimisation de son contrôle et, par conséquent, pour l'amélioration de ses performances.

Un logiciel open-source, AlphaPEM, basé sur ce modèle et implémenté en Python, a ensuite été développé et publié. Il présente une architecture modulaire qui facilite l'intégration de nouvelles fonctionnalités et comprend une interface graphique conviviale. AlphaPEM intègre également une méthode de calibration automatique, permettant une calibration précise du modèle à la pile à combustible spécifique étudiée. En utilisant ce logiciel, des informations détaillées sur les états internes en réponse à toutes densités de courant peuvent être calculées efficacement. Les performances statique et dynamique, caractérisées par les courbes de polarisation et d'EIS, peuvent aussi être simulées sous différentes conditions opératoires.

En outre, AlphaPEM ouvre la voie à l'usage de simulations avancées de piles à combustible dans les systèmes embarqués, car il permet des réponses précises et rapides sous des conditions opératoires dynamiques. Une version simplifiée du modèle a

été formulée sous forme de représentation d'état, pour le rendre compatible avec un cadre de commande prédictive. Cela faciliterait l'optimisation des conditions opératoires de la pile à combustible à partir du modèle. En tant qu'application pratique, une stratégie de contrôle de l'humidité entrante dérivée du modèle est proposée, permettant théoriquement à la pile à combustible d'atteindre des puissances de sortie plus élevées tout en réduisant le risque de noyage.

Mots clés : Pile à combustible à membrane échangeuse de protons (PEMFC), Contrôle-commande, Modèle 1D, Gestion de l'eau, Transport d'hydrogène et d'oxygène, Tension de polarisation.

Abstract and keywords

Hydrogen-based technologies hold great promise for meeting future energy demands in a more sustainable world. Given their potential, their technological development is central to many policies. Thus, accurately modeling fuel cells is essential for optimizing their control to enhance performance.

This thesis first presents an in-depth analysis of recent advancements in the governing principles of matter transport and voltage polarization specific to proton exchange membrane fuel cells (PEMFCs). It provides a thorough understanding of these principles, including the associated governing equations, their applicability, and underlying assumptions, serving as a foundation for future model development.

Building on this foundation, a one-dimensional, dynamic, two-phase, isothermal model for PEMFCs using a finite-difference approach has been developed. This model balances the simplicity of lumped-parameter models with the detailed accuracy of computational fluid dynamics models, offering precise internal state descriptions with low computational demand. In addition, a novel physical parameter, the limit liquid water saturation coefficient (s_{lim}) and corresponding formulas, are introduced in the overvoltage calculation. This new parameter links the voltage drop at high current densities to the amount of liquid water present in the catalyst layers and the operating conditions of the fuel cell. This newly established link between the internal states of the fuel cell and its operating conditions is promising for optimizing its control and thereby improving its performance.

An open-source software package, AlphaPEM, based on this model and implemented in Python, was then developed and released. It features a modular architecture that eases the integration of new functionalities and includes a user-friendly graphical interface. AlphaPEM also incorporates an automatic calibration method, enabling precise calibration of the model to the specific fuel cell under study. Using this software, detailed internal state information in response to varying current densities can be calculated efficiently. The static and dynamic performance, characterized by polarization and EIS curves, can also be simulated under various operating conditions.

Further, AlphaPEM paves the way for the use of advanced fuel cell simulations in embedded systems, as it enables precise and rapid responses under dynamic operating conditions. A simplified version of the model has been formulated in state-space form to make it compatible with a predictive control framework. This would facilitate the optimization of fuel cell operating conditions based on the model. As a practical application, an inlet humidity control strategy derived from the model is proposed, which theoretically allows the fuel cell to achieve higher power outputs while mitigating the risk of flooding.

Keywords: Proton exchange membrane fuel cell (PEMFC), Control-oriented, 1D model, Water management, Hydrogen and oxygen transport, Voltage polarisation.

Acknowledgments

This research work was funded by the French National Research Agency (ANR) through the DEAL project and conducted within the LIS laboratory at Aix-Marseille University, in co-supervision with the FEMTO-ST laboratory at the University of Franche-Comté. I would like to thank these institutions for allowing me to carry out my work.

I would also like to thank the members of my thesis jury who accepted my invitation: Sophie Didierjean, Liangfei Xu, Serge Simoens, and Mohamed Boutayeb.

I would like to extend my warmest thanks to my thesis supervisors: Zhongliang Li, Rachid Outbib, Samir Jemei, and Daniel Hissel, for the trust they placed in me, their involvement, and their expertise in the fields of hydrogen and control engineering. Despite the distance between the two institutions where I worked, I was able to maintain excellent online contact with all of my supervisors, and I continuously learned from them. I would like to especially thank Zhongliang, who is the leader of this project, and with whom I had an excellent relationship. His availability, regular follow-up, expertise, passion, and daily kindness truly supported me throughout these three years and allowed me to experience my doctoral journey with peace of mind. I feel fortunate and intend to continue my research career while maintaining excellent connections with this entire team.

Thank you also to the PhD students and interns I met during these three years. You are so many that I cannot name you all, but you will recognize yourselves. I have warm memories of the weekends spent camping, the many afterworks and barbecues, the restaurant outings, the visits to other cities, the football matches, the long, intimate discussions... I am happy for the encounters I had with you. I am also grateful to have met so many people from different nationalities, coming from all continents. It was so enriching... Among all these people, I particularly thank Grigor, Agnès, and Romain, who were especially present.

Finally, thank you to my family and friends for their support during these three years, particularly during the difficult phases. I have a special thought for my parents, thanks to whom I was able to achieve this journey. I also thank all my childhood friends from Reunion Island, especially Anthony, Adrien, and Arnaud, who have always reminded me how enduring our friendship is, despite the distance imposed by all my years of study on the mainland. I also thank Amandine, who fought to maintain our beautiful friendship, despite the ups and downs of life. I have also bonded with many people outside of work in recent years. These people have been a valuable support and a most pleasant company. I therefore thank my entire "week-end plage" group of friends from the Mines, who are all dear to my heart. I have a special thought for Meryem, Emmanuel, Théophile, Hélène, Clarisse, and Ines, with whom I spent

fabulous moments and who will remain lifelong friends. During the first year of my PhD, I had the chance to meet Alexis in a rather surprising way in Belfort, and I thank him for continuing to build this special friendship with me. I also had the pleasure of making wonderful connections through swing dancing in Marseille. I feel fortunate to have shared part of my life with Margaux, who is such an endearing and pleasant woman. I am also happy to have met Géraldine, the queen of techno parties, and Marina, with whom I had so many enjoyable conversations.

Contents

Nomenclature

Physical quantities

A_{act} active area (m^2)

A_T exhaust manifold throttle area (m^2)

a_w water activity in the pores of the CL

C molar concentration ($mol.m^{-3}$)

C_D throttle discharge coefficient

C_{scl} volumetric space-charge layer capacitance of the CCL ($F.m^{-3}$)

D diffusion coefficient of water in the membrane ($m^2.s^{-1}$)

D_c capillary diffusion coefficient ($kg.m^{-1}.s^{-1}$)

$D_{i/j}$ binary diffusivity of two species i and j in open space ($m^2.s^{-1}$)

E^0 standard-state reversible voltage (V)

E_{act} activation energy ($J.mol^{-1}$)

$ECSA$ electrochemical surface area ($cm^2_{Pt}.mg^{-1}_{Pt}$)

F Faraday constant ($C.mol^{-1}$)

f_{drop} liquid water induced voltage drop function

f_v water volume fraction of the membrane

H thickness (m)

h convective-conductive mass transfer coefficient ($m.s^{-1}$)

i current density per unit of cell active area ($A.m^{-2}$)

i_n internal current density ($A.m^{-2}$)

i_{lim} limit current density coefficient

J molar/mass transfer flow ($mol.m^{-2}.s^{-1}/kg.m^{-2}.s^{-1}$)

$J(s)$ Leverett function

K permeability (m^2)

k permeability coefficient in the membrane ($mol.m^{-1}.s^{-1}.Pa^{-1}$)

K_p/K_d proportionality/derivative constant of the back pressure valve controller ($m^2.s^{-1}.Pa^{-1}/m^2.Pa^{-1}$)

K_e acid-base equilibrium constant

$k_{i,j}$ nozzle orifice coefficient for i $\in \{sm, em\}$ and j $\in \{in, out\}$ ($kg.Pa^{-1}.s^{-1}$)

L_{gc} cumulated length of the gas channel (m)

L_{Pt} initial Pt loading of the electrode ($mg_{Pt}.cm^{-2}$)

M molecular weight ($kg.mol^{-1}$)

n number of moles (mol)

n_{cell} number of cells inside the simulated stack

n_{gdl} number of nodes inside each GDL

P pressure (Pa)

R universal gas constant ($J.mol^{-1}.K^{-1}$)

r_{cf} carbon fiber radius (m)

R_e/R_p electron/proton conduction resistance ($\Omega.m^2$)

r_f electrode roughness factor ($m^2_{Pt}.m^{-2}$)

S matter conversion ($mol.m^{-3}.s^{-1}$)

S_a/S_c stoichiometric ratio at the anode/cathode

S_h Sherwood number

S_{vl} phase transfer rate of condensation and evaporation ($mol.m^{-3}.s^{-1}$)

T_{fc} fuel cell temperature (K)

U voltage (V)

u velocity ($m.s^{-1}$)

V molar volume ($m^3.mol^{-1}$)

V_{sm}/V_{em} manifold volume (m^3)

W mass flow rate ($kg.s^{-1}/mol.s^{-1}$)

W_{gc} width of the gas channel (m)

x space variable (m)

x_v mole fraction of vapour

y_{O_2} molar fraction of O_2 in dry air

e capillary exponent

s liquid water saturation

s_{lim} limit liquid water saturation coefficient

α_c charge-transfer coefficient of the cathode

ΔH^0 standard enthalpy of reaction ($J.mol^{-1}$)

η overpotential (V)

γ rate constant (s^{-1})

$\gamma_{cond}/\gamma_{evap}$ overall condensation/evaporation rate constant for water ($s^{-1}/Pa^{-1}.s^{-1}$)

γ_{H_2}/γ_a heat capacity ratio of H_2 and dry air

γ_{sorp} sorption rate (s^{-1})

κ overpotential correction exponent

κ_{co} crossover correction coefficient

λ water content

μ dynamic viscosity ($Pa.s$)

ν_l liquid water kinematic viscosity ($m^2.s^{-1}$)

Φ relative humidity

ϕ local voltage (V)

ρ density ($kg.m^{-3}$)

σ surface tension of liquid water ($N.m^{-1}$)

σ_m conductivity of the membrane ($\Omega^{-1}.m^{-1}$)

τ pore structure coefficient

τ_{cp}/τ_{hum} air compressor/humidifier time constant (s)

θ_c contact angle of GDL for liquid water (°)

ε porosity

ε_c compression ratio

ε_{mc} volume fraction of ionomer in the CLs

ε_p percolation threshold porosity

Mathematical symbols

$\boldsymbol{\imath}$ unit vector along the x-axis

K_{shape} shape mathematical factor

$\dot{n}$ temporal derivative of n ($mol.s^{-1}$)

φ_{sp} Surface proportion function

α, β_1, β_2 fitted values for K_0

$a_{s_{lim}}, b_{s_{lim}}, a_{switch}, \mathtt{s}_{switch}$ fitted values for f_{drop}

$\triangleq$ equality by definition

∇ gradient notation

Subscripts and superscripts

a anode

aem anode exhaust manifold

asm anode supply manifold

c cathode

cap capillarity

cem cathode exhaust manifold

co crossover

$conv$ convective

cp compressor

csm cathode supply manifold

dif diffusion

eff effective

eq equilibrium

fc fuel cell

H^+ proton charge

H_2 dihydrogen

in inlet

l liquid

mem membrane

N_2 dinitrogen

O_2 dioxygen

out outlet

p production

$prod$ production

ref referenced

sat saturated

$sorp$ sorption

v vapor

vl vapor to liquid

w water

Abbreviation

acl/ACL anode catalyst layer

agc/AGC anode gas channel

$agdl/AGDL$ anode gas diffusion layer

ccl/CCL cathode catalyst layer

cgc/CGC cathode gas channel

$cgdl/CGDL$ cathode gas diffusion layer

cl/CL catalyst layer

EOD electro-osmotic drag

EOD electro-osmotic drag

gc/GC gas channel

gdl/GDL gas diffusion layer

$PEMFC$ proton exchange membrane fuel cell

Introduction

Background of energy transition

In the twenty-first century, there is a race against time to limit global warming to 1.5°C above pre-industrial levels, as agreed upon in the Paris Agreement by 192 Parties in December 2015 [1]. As a carbon-free, efficient, and widely applicable disruptive innovation, decarbonized hydrogen technologies have garnered increased attention [2, 3]. Indeed, these devices, which convert chemical energy into electricity and heat, stand out as highly promising candidates that can significantly impact various polluting sectors through relevant developments. For instance, they appear promising for powering heavy transport, generating stationary electricity, and providing backup power to data centers [4]. As a result, the development of hydrogen technology has become a national priority for many countries [2].

Benefits and drawbacks of hydrogen technologies

Among the different fuel cell technologies, PEMFC, which stands for Proton Exchange Membrane Fuel Cell, is the most promising for mobile applications [5]. This technology has reached a good level of maturity, although there is still significant room for improvement, and it is already being commercially available on a large scale. This work focuses on this technology.

It is useful to have an overview of the benefits and disadvantages of PEMFC technology compared to combustion engines and lithium batteries. Firstly, this technology is less polluting than combustion engines. There are very few emissions from "well to wheel" for fuel cell vehicles (FCVs) powered by hydrogen from decarbonized energy sources, similar to battery electric vehicles (BEVs), which is beneficial for human health in urban areas [6]. However, the CO2 equivalent impact over the life cycle is reduced by only a factor of two to four at best, similar to BEVs, while impacts on other sectors of the life cycle are increased [7, 8]. Therefore, none of these "green" technologies are entirely clean.

Another notable advantage of PEMFCs is their high energy efficiency, which is not constrained by the combustion of reactants. Without utilizing the produced heat, FCVs combined with electric motors have an efficiency of 50 to 65% in converting the chemical energy of the reactants into mechanical energy, which is higher than thermal systems that peak at 35-45%, but still lower than electric batteries combined with electric motors, which can achieve 80-85% of efficiency [6, 9–11]. Moreover, fuel cell systems are distinct from batteries in that they can cogenerate with the heat produced,

thereby improving the energy efficiency of the system. In contrast, the heat generated by batteries is too low and intermittent to be effectively recovered. Additionally, refueling hydrogen for FCVs is nearly as fast as refueling internal combustion engine vehicles (ICEVs), and significantly faster than recharging BEVs. This is because the energy contained in hydrogen and the fuel cell, acting as a converter, are decoupled, unlike in batteries where they are coupled [6]. For instance, a hydrogen bus takes slightly less than twenty minutes to refuel, whereas an electric bus with a capacity of 250 kWh requires 6 to 8 hours to recharge using a 30-40 kW charger, excluding fast charging, which accelerates battery degradation [12–14]. Furthermore, continuous electricity production is possible as long as there is a sufficient supply of hydrogen.

These significant advantages of PEMFC technology are counterbalanced by major drawbacks that scientific research is currently striving to mitigate. On the one hand, the lifespan of these converters is not yet satisfactory for widespread and long-term deployment. The European Union aims to double the lifespan of hydrogen buses to match that of thermal buses [15]. This issue is also present in BEVs [16]. Additionally, the manufacturing costs of fuel cells remain too high compared to thermal engines. Furthermore, FCVs require the use of rare materials, such as platinum, which is classified by the EU as a critical element for the economy and a material at risk of supply shortage since reserves are concentrated in very few countries [17], although the amounts used have been significantly reduced. This issue also applies to ICEVs, as platinum is a key component in catalytic converters. In 2021, the amount of platinum required for a PEMFC was 0.1–0.2 $g.kW^{-1}$, which represents between 10 and 20 grams of platinum per FCVs. In comparison, current ICEVs use between 2 and 8 grams of platinum in their exhaust systems [18]. The future goal is to achieve less than 0.1 $g.kW^{-1}$ by 2030 [6].

PEMFCs have other notable advantages and disadvantages. Hydrogen is a light molecule with a high mass energy density. This is advantageous for heavy-duty vehicles that need to carry large amounts of energy to achieve satisfactory autonomy without significantly increasing the weight, unlike BEVs, where autonomy and weight are difficult drawbacks to overcome [6]. However, PEMFCs have a low power density, lower than batteries [6], which necessitates an alternative energy source to handle power changes over the span of a few seconds. They also have a low volumetric energy density, much lower than that of petroleum or CNG, which requires energy consumption to compress hydrogen for mobile applications. This is a secondary issue for stationary applications where occupied volume is not critical.

PEMFCs offer additional advantages. They generate high current densities, reaching up to 3 $A.cm^2$ [6, 19], which enables the development of compact and easily integrable systems suitable for embedded applications. FCVs perform well below 0°C, significantly better than BEVs, which experience a considerable decrease in electrical capacity at low temperatures [6]. These vehicles require less maintenance compared to ICEVs, as they have fewer complex moving parts, do not need engine fluids or oil filters, feature regenerative braking systems, and lack a complex exhaust system [20]. Moreover, hydrogen is already supported by the chemical and refining industries, offering the opportunity for sustained growth backed by major companies [2]. Finally,

long-term seasonal storage is feasible with hydrogen for stationary applications due to its low self-discharge and the potential to reach the GW scale. This is not possible with batteries due to their self-discharge characteristics.

Regarding the drawbacks of PEMFCs, there are a few remaining issues to mention. These converters generate low voltages per cell, 0.65V nominally, which is significantly lower than batteries that typically offer 3.7V per cell [6]. It is also necessary to ensure proper safety around this technology, given that hydrogen is a highly flammable molecule and its high compression makes it susceptible to causing large explosions. However, the danger is similar to that of a gasoline tank or a traditional gas cylinder [18]. Additionally, fuel cells require numerous auxiliary components, which increases cost, volume, and complexity for installation, operation, and maintenance. Moreover, extensive infrastructure development is needed to enable hydrogen refueling, which is very expensive for public authorities [2]. Finally, current regulations limit the development of these technologies as they are often absent, lack clarity, are unsuitable for current projects, or are inconsistent across different sectors or countries. These regulations need to be reviewed and harmonized to support the industry [2].

Table 1 summarizes these characteristics.

Advantages of PEMFC	**Disadvantages of PEMFC**
Less pollution from "well to wheel"	Limited lifetime
Good energy efficiency	High costs
Possibility of cogeneration	Use of rare materials
Rapid recharging due to decoupling of energy and converter	Low power density (requiring an alternative energy source)
H_2 has a low density (lightweight)	Regulations need to be developed
H_2 has a high gravimetric energy density	H_2 has a low volumetric energy density
Generates high current densities	Generates low voltages
Good performance below 0°C	Safety concerns
Requires low maintenance	Requires numerous auxiliaries
Supported by an existing industry	Infrastructure development needed

Table 1. – Comparison of the advantages and disadvantages of PEMFC technology

Global objectives for the development of PEM fuel cells

As seen previously, PEMFCs face technological obstacles that need to be overcome for large-scale commercialization. It is first necessary to reduce the production costs of fuel cells. In 2022, the cost ranged between 50€ and 60€ per kW for cars, assuming a production scale of 500,000 units per year. The U.S. Department of Energy's target is 40€ per kW, which would correspond to 1,600€ for equipping a car with 30 to 40 kW of fuel cells with electric hybridization [18]. The European Union targets 50 €/kW by 2030

for stacks in heavy-duty vehicles [15]. Companies target similar costs for complete hydrogen systems and battery packs in 2030, considering the evolution of the battery sector [21].

Another important objective is to increase the lifespan of these systems. The European Union aims to double the lifespan of heavy-duty vehicles from 15,000 hours of operation, or approximately 8 years of operation, to 30,000 hours by 2030, or approximately 15 years of operation, which corresponds to a traditional thermal bus. These figures correspond to the durability of the fuel cell system based on the EOL (end-of-life) criterion. It is considered end-of-life when it has undergone a degradation of more than 10% of its initial power (a standard from the U.S. Department of Energy) or an H2 leakage rate exceeding the SAE2578 standard [15].

It is also necessary to operate PEMFCs at higher power and current densities. To achieve this, the European Union aims to reach 1.2 $W.cm^{-2}$ at 0.675 V by 2030 [15], while Japan targets 6 $kW.L^{-1}$ and 3.8 $A.cm^{-2}$ for the same year [6]. These objectives align with those of the scientific community, which aims to achieve a power of 6 $kW.L^{-1}$ with a current density of $3-4$ $A.cm^{-2}$ and a nominal voltage of $0.7-0.8$ V by 2030. For later, it is technically expected to reach a power of 9 $kW.L^{-1}$ with a current density of $4-5$ $A.cm^{-2}$ and a voltage of $0.8-0.9$ V [6]. These power objectives necessarily require improved fuel cell designs and operations, such as better water management within the cell, as it will be generated in greater quantities.

PEM fuel cell operation

Fuel cells are open thermodynamic systems that convert chemical energy into electricity. They function through electrochemical reactions, consuming reactants supplied from an external source [22] and expelling water produced within. PEM fuel cells take advantage of the electrochemical reaction between hydrogen and oxygen, $2H_2 + O_2 \rightarrow 2H_2O$, which, in addition to producing heat, can generate electricity if these reactants react cleverly. Indeed, a simple mixture of these reactants does not allow for the production of electricity and is even dangerous because it is highly flammable. A different approach must be taken to prevent their direct contact. To achieve this, a converter, the fuel cell, is used to enable the reaction of hydrogen with oxygen without combustion while recovering the electrical energy that this reaction generates [5, 23].

This converter consists of a set of cells, each made up of an assembly of solid layers. The juxtaposition of cells allows the power of the converter to be increased by adding the voltage produced by each of them. Figure 1 schematically represents a fuel cell with the different matter flows that pass through it (the same diagram is presented as a full-page landscape format in figure 1.1). A cell has a symmetrical structure around its membrane. It is composed of two bipolar plates (BP) at its ends, two electrodes each consisting of a gas diffusion layer (GDL) and a catalytic layer (CL), and finally a membrane in the middle. The anodic side of the cell corresponds to the area where hydrogen is transported, whereas the cathodic side corresponds to the area where

oxygen is transported [5, 23].

The membrane has two major roles within a PEM fuel cell. On one hand, it hermetically isolates hydrogen from oxygen, thereby preventing these gases from mixing. On the other hand, it facilitates the transport of protons from the anode to the cathode through its hydrophilic and hydrophobic domains, while remaining insulating to the passage of electrons. This is crucial for the chemical reaction $2H_2 + O_2 \rightarrow 2H_2O$ described below. The membranes used in PEMFCs are ionomers, which are polymers modified to include ions, usually sulfonic groups. Among the different types of membranes, the most commonly used are those based on perfluorosulfonic acid (PFSA), such as Nafion® [24]. A membrane must exhibit excellent proton conductivity, thermal and chemical stability, good mechanical resistance, flexibility, low gas permeability, and low resistance to water [24].

Bipolar plates are metal structures forming the skeleton of the fuel cell. Through these plates, the reactants are homogenized on the cell surface and penetrate the electrodes where the chemical reaction takes place. Moreover, they isolate the individual cells, conduct the current between cells, assist in the management of water and heat [24], and provide mechanical resistance to the cell assembly. They account for a significant portion of the cost (30%) and volume (70%) of the fuel cell [6]. Depending on the manufacturer and the desired trade-offs, they can be made of graphite, titanium, or stainless steel [25–27].

The electrodes correspond to the location where the chemical reaction occurs. More precisely, it takes place in the catalytic layer containing triple-point zones where the ionomer, the catalyst associated with its metallic support, and the void coexist. These triple-point zones are necessary for the reaction to occur because the ionomer acts as the transport medium for H^+ ions, the catalyst with its metallic support facilitates electron transport and accelerates the reaction, and the void acts as the transport medium for gaseous oxygen. All these matters must be transported to the same location for the chemical reaction to proceed, as described below [5, 23].

A catalyst is essential in fuel cells; without it, the power output would be too low for any practical use. In the case of a PEM fuel cell, platinum is typically used. However, to reduce costs, the electrode is not made of pure platinum but consists of a metallic support on which platinum nanoparticles are finely dispersed. This carbon-based metallic support allows the platinum nanoparticles to have a high dispersion (2-3 nm) and provides a porous, electronically conductive structure. This structure plays a crucial role in transporting reactants and electrons to the nanoparticles, as well as in removing gases and water produced [24]. The electrode layer where carbon and platinum coexist is called the catalytic layer, and the layer where only porous carbon is present is referred to as the gas diffusion layer. This latter layer also serves as mechanical support and provides electrical connection to the bipolar plates [6]. Finally, the compression between the electrode and the membrane leads to the penetration of the ionomer into the catalytic layers, allowing the formation of triple points.

Now that the various components of a fuel cell have been presented, the mechanism for converting the chemical energy contained in hydrogen and oxygen into electricity through the chemical reaction $2H_2 + O_2 \rightarrow 2H_2O$ can be explained. Hydrogen and

oxygen are separately introduced into the bipolar plates at the anode and cathode, where these gases are homogenized along the surface of the plates. Next, both gases diffuse into each electrode until they reach the catalytic layers. They are unable to mix because they are blocked by the membrane. At this stage, hydrogen molecules react by releasing their electrons and separating themselves into protons: $H_2 \rightarrow 2H^+ + 2e^-$, a process accelerated by the presence of the catalyst. This hydrogen reaction allows the protons (H^+) dissolved in the membrane to cross it in order to join the oxygen molecules in the cathodic catalytic layer. The electrons take a reverse path, moving toward the anodic bipolar plate, which is connected to the external electrical circuit of the cell and continues to the cathodic bipolar plate. They thus also reach the cathodic catalytic layer by another path. There, they react with oxygen to form oxide ions: $O_2 + 4e^- \rightarrow 2O^{2-}$, a reaction also accelerated by the catalyst. Then, the presence of protons and oxide ions in the same volume leads to the formation of water through the reaction: $2H^+ + O^{2-} \rightarrow H_2O$. These steps, taken together, correspond to the overall reaction $2H_2 + O_2 \rightarrow 2H_2O$. Finally, throughout this process, it is the movement of electrons through the external electrical circuit of the cell that generates electricity [5, 23].

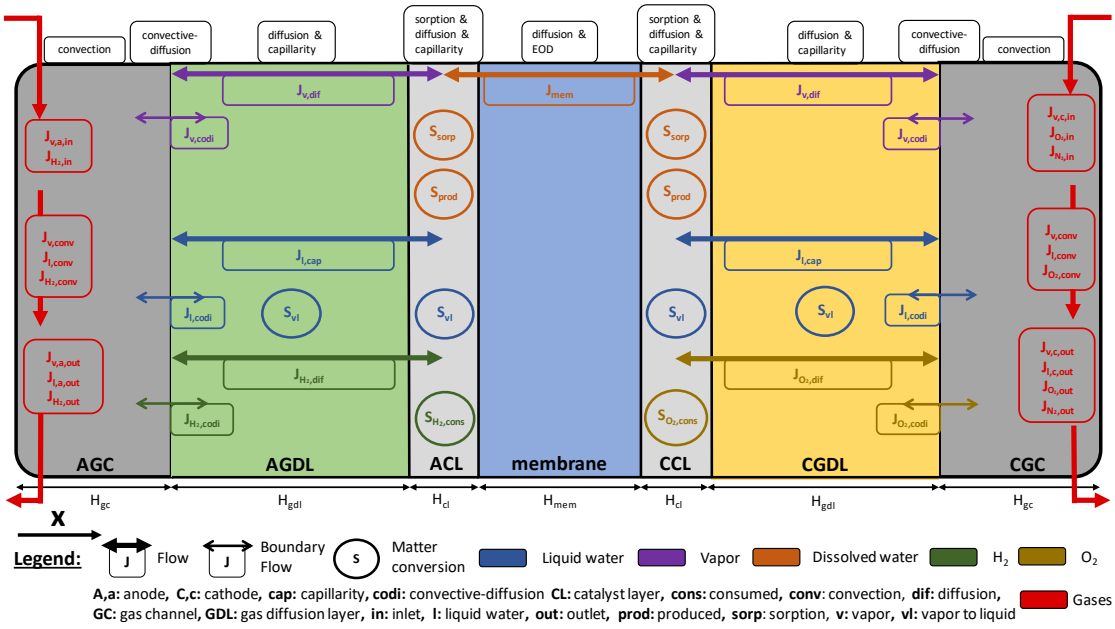

Figure 1. – Schematic of a single PEMFC with the matter flows illustrated

Finally, the fact that the gaseous reactants are inherently stored outside the fuel cell provides a significant advantage compared to other converters: it is possible to control the state of these gases to optimize the chemical reaction. For instance, an air compressor can be associated with the fuel cell to impose an oxygen input flow rate, a pump can be used to recirculate hydrogen at a precise flow rate to prevent losses of this expensive reactant, heat exchangers can control the incoming gas temperatures, humidifiers can regulate the moisture content of the incoming gases, and back-pressure

valves can manage the outgoing gas pressure. Manufacturers may combine these various auxiliaries as they see fit, depending on the desired performance and cost. The combination of a fuel cell and its auxiliaries is called a fuel cell system [5, 23].

Current state of open-source fuel cell modelling softwares

PEMFCs face challenges such as low power densities, high costs, and limited lifespan, factors that have impeded its broader adoption in the global market [6]. Enhancing power density can be handled with more effective water management, especially at high current density, where insights into water activity within each cell is valuable for refining their control. Introducing novel materials into the stack could potentially reduce production costs. Improving the lifespan involves considering degradation processes at a mesoscopic scale. In this regard, and in many other situations as well, fuel cell modeling emerges as an invaluable tool. Indeed, models provide insights that sensors might be unable to capture, particularly in cells where their slim thickness hinders sensor integration — a crucial aspect for control purposes. Virtual exploration of numerous materials and configurations via models significantly reduces the costs and time associated with experimental trials. Predicting stack degradation and evaluating the stack's remaining useful life relies on understanding the underlying physical phenomena, aspects effectively addressed through modeling.

In the current literature, a lack of physics-based PEM fuel cell models that are open to the community is observed. While some commercial software such as COMSOL Multiphysics®[28–30], Ansys Fluent®[31–34], or Wolfram Mathematica®[35, 36] allow such modeling, they are not open-source, require expensive licenses and offer limited possibilities for source code modification. The open-source publication of software is, however, a valuable aid to the community, as it not only prevents each research team from having to develop their own simulator from scratch, which is time-consuming, but also improves each software by subjecting it to international critique and allowing for collaborative development, thus enhancing and accelerating research. In this context, a research team from the Institute of Energy and Climate Research, IEK-3, has developed openFuelCell2, an open-source computational fluid dynamics toolbox for simulating fuel cells, based on the open-source library OpenFOAM®[37–40]. All these approaches yield very precise models which are suited for enhancing fuel cell design. However, they are computationally expensive which make them incompatible with embedded applications.

To the authors' knowledge, only two research teams have published PEM fuel cell models for control-command applications as open-source software, both programmed in Matlab. First, Pukrushpan et al. released a 0D dynamic and isothermal model of the fuel cell system in 2004, which includes the auxiliaries and requires very little computational power [41, 42]. The aim of this pioneering model was to be used in embedded applications while considering the dynamics of the auxiliaries. However, a physical model that accounts for spatial variations within each component of the

fuel cell system would enable more precise diagnosis of the internal states and better support control to optimize these states. Nevertheless, this work has paved the way for the construction of more detailed models. More recently, in 2019, Vetter et al. published a simple and compact software simulating the fuel cell in one-dimensional (1D) steady-state, non-isothermal conditions with two phases of water [43, 44]. Although the inclusion of one spatial dimension increases the model's accuracy, the lack of dynamic modeling and consideration of the auxiliaries makes this software incomplete for real-time use in embedded applications. However, it is important to note that this software is primarily intended as a simulation base for more accurate PEM fuel cell models, making it valuable for the community.

Objectives and scope of the thesis

The primary objective of this thesis is to construct a model of PEM fuel cell systems that can be used within embedded applications, such as hydrogen buses. It could thus enable better model-based control of fuel cell systems to improve their performance and longevity, thereby contributing to the development goals for this technology set by various countries and companies. The model to be developed should provide a good compromise between execution speed and accuracy, allowing for computation times compatible with the dynamics of vehicles while also providing the most precise results possible. This model should therefore simulate in real time the dynamic evolution of the key internal states of fuel cell systems, such as the liquid water within the different layers of each cell.

The first chapter of this thesis critically discusses the physics currently used to model PEM fuel cells. The second chapter relates the implementation of this science to produce a dynamic, one-dimensional (1D), biphasic, and isothermal model of the fuel cell system. The third chapter details the validation of this 1D model, the deployment of the associated open-source software named AlphaPEM, and the results produced. Finally, the fourth chapter introduces several seeds of innovation enabled by this model: improving the performance of the fuel cell by controlling its incoming humidity, producing EIS curves from this refined model, and conducting a mathematical analysis for automatic control.

1. Development of the physical model

Sommaire

1.1. Introduction to physical modelling

One of the prerequisites for developing physics-based models is a thorough understanding of the physics governing water, hydrogen, and oxygen transport in the stack, as well as voltage polarization. While Jiao et al. [45], O'Hayre et al. [23], and Dicks et al. [5] provided comprehensive reviews on matter transport and voltage polarization phenomena in 2011, 2016, and 2018, respectively, there is a need for a review that encompasses recent developments. Certain noteworthy and recent governing equations have been overlooked in these reviews and must be acknowledged. Indeed, many recent articles do not incorporate the latest propositions, even though they

offer greater precision in results or increased algorithmic stability. Disruptive errors are also spreading in the literature and need to be identified. Additionally, a more in-depth explanation of the background concerning governing laws and equations is essential. Often, multiple equations model the same phenomenon. Therefore, it is beneficial to synthesize them in a single work, providing a means to differentiate their usage based on the physics, experimental choices, and modeling considerations. Furthermore, a synthetic compilation of key constant values found throughout the literature is considered to gain insights into commonly accepted values, points of disagreement, and poorly considered values.

In this chapter, novel equations were introduced. Firstly, several expressions were combined to formulate new equations that exhibit enhanced stability, precision, or encompass a broader range of phenomena. Secondly, in an effort to simplify model generation and inspired by Pukrushpan et al.'s work [41], we proposed simplified boundary conditions at the gas channel's inlet and outlet. These conditions aim to yield preliminary results prior to modeling auxiliary systems. Lastly, we suggested new paths for future research. All provided governing laws and equations in this chapter are adaptable to any dynamic multi-dimensional two-phase model, with the final selected equations highlighted by frames. Figure 1.1 illustrates the matter flows considered in this work within a cell. The directional flows align with the stack's thickness, facilitating graphical representation. It's worth noting that flows in other spatial dimensions are feasible, albeit less significant within a cell.

In this chapter, based on an article published by the authors [46], transport of dissolved water within the Nafion®membrane is first examined. Subsequently, transport of liquid water in the catalyst layer (CL), gas diffusion layer (GDL), and gas channel (GC) is explored. Following this, vapor transport is delved, as well as the transport of hydrogen, oxygen, and nitrogen in all three regions. The study then addresses voltage polarization. In the appendices, additional equations are provided, constant values from the literature are synthesized, hypotheses considered in this work are outlined, and demonstrations are presented.

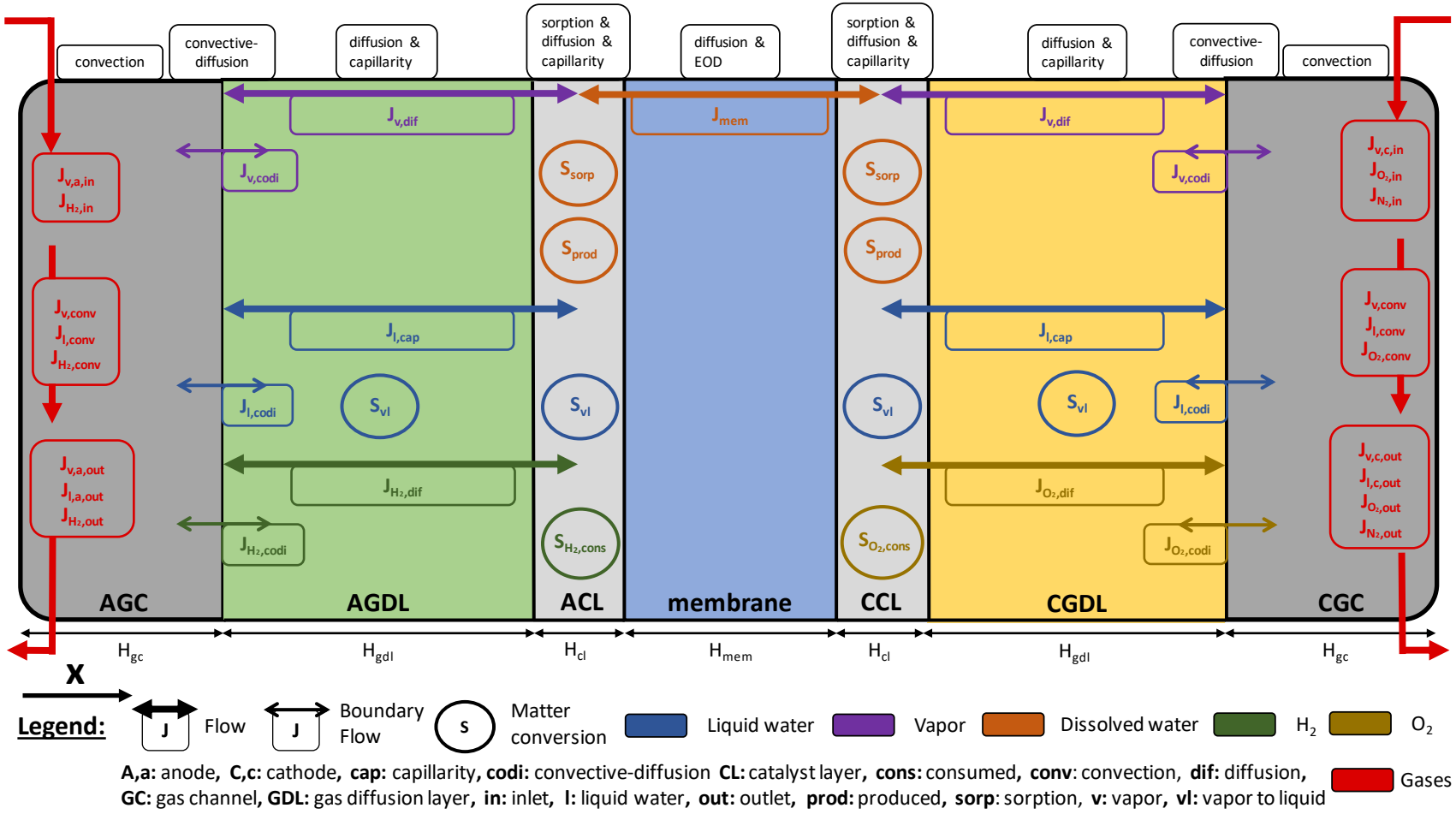

Figure 1.1. – Schematic of a single PEMFC with the matter flows illustrated

1.2. Matter transport physical modelling

1.2.1. Water transport in the membrane

Protons can be efficiently transported across the membrane only when a sufficient amount of dissolved water is present within it. Indeed, state-of-the art membranes like Nafion®exhibit significant ionic conductivity exclusively when in a hydrated state. Therefore, membrane hydration must be considered in the models to ensure the proper functioning of the cell.

Notably, in PEMFC studies, the active area has commonly served as the surface reference for various flows. Species evolve within different materials with distinct volume accessibility. Nonetheless, the active area, representing the surface of the MEA without the gasket, is a common surface shared by all materials, making it a reliable reference. Furthermore, it corresponds to the surface for defining current density. This choice of reference is valuable for accurately assessing molar transfer between elements, and consequently, the governing equations in this study incorporate constants such as porosity (ε) that enable to always consider the active area.

1.2.1.1. Water content: λ

In the Nafion®membrane, water is present in an unusual form. It is absorbed by the sulfonated side-chains ($-SO_3H$) in liquid phase [5]. Thus, it is interesting to quantify it using the water content variable (λ) which corresponds to the number of water molecules per charged site $SO_3^- H^+$ in the membrane.

$$\lambda \triangleq \frac{n}{n_{SO_3^- H^+}} \tag{1.1}$$

where n (mol) is the number of moles of water, $n_{SO_3^- H^+}$ (mol) is the number of moles of sulfonic acid group, and $\triangleq$ refers to an equality by definition.

Furthermore, λ must be considered in the catalyst layer (CL). A thin layer of ionomer adheres to the catalyst metal particles [5], and consequently, a fraction of the CL volume is comprised of the electrolyte. This necessitates the use of ε_{mc} in the governing equations, representing the ionomer volume fraction in the CL as defined in (1.2). It is then noteworthy to denote the location of the water content λ_{mem} in the membrane or λ_{cl} in the catalyst layer with an index. Although both are continuously linked, the governing equations differ, and this notation would simplify the writing of the differential equation for the dynamic behavior of λ. However, the omission of this index allows for a collective designation of both locations.

$$\varepsilon_{mc} \triangleq \frac{V_{\text{ionomer in CL}}}{V_{\text{CL}}} \tag{1.2}$$

1.2.1.2. Schroeder's paradox

In a Membrane Electrode Assembly (MEA), the membrane and catalyst layers are closely intertwined at their interface, allowing water to move between them. However, the paradox arised when considering the varying amounts of water absorption by the membrane, depending on whether the water is in a saturated vapour or in the pure liquid phase within the catalyst layer.

In the liquid phase, the membrane absorbs a significantly higher quantity of water. This apparent contradiction was puzzling because, in theory up to this point in time, dissolved water in the membrane should reach an equilibrium with water activity, which remains constant at 1 for both saturated vapour and pure liquid water. Consequently, both equilibriums should have been identical. This perplexing phenomenon is known as Schroeder's paradox, named after the researcher who discovered it in 1903. It is prevalent in various polymers, including perfluorosulfonic acid (PFSA) polymer, exemplified by Nafion®.

Although not fully understood, numerous studies have delved into this paradox. The presence of liquid water alters the morphology of the polymer, transitioning it from a strongly hydrophobic state to a hydrophilic one. In the case of liquid water, the hydrophilic sulfonated side-chains ($-SO_3H$) within Nafion®, initially located inside the material, can migrate to the membrane's surface, as depicted in Figure 1.2, facilitating the attraction and absorption of water. However, the absorption of vapour entails an additional step, requiring vapour condensation at the CL ionomer interface [45]. This phenomenon allows the understanding of three additional phenomena. Firstly, less water is absorbed at equilibrium in the vapour phase: $\lambda_{l,eq} > \lambda_{v,eq}$, as discussed in section 1.2.1.5. Secondly, it is easier for water to exit the membrane (desorption) than to enter (absorption), affecting the associated time constants. Finally, the liquid water sorption flow into the membrane is much faster than that of water vapour. These latter points are addressed in section 1.2.1.7.

While partially explained, this paradox continues to pose theoretical challenges for modeling, specifically when vapour and liquid water coexist, as stated in sections 1.2.1.5, 1.2.1.6, 1.2.1.8 and 1.2.1.7.

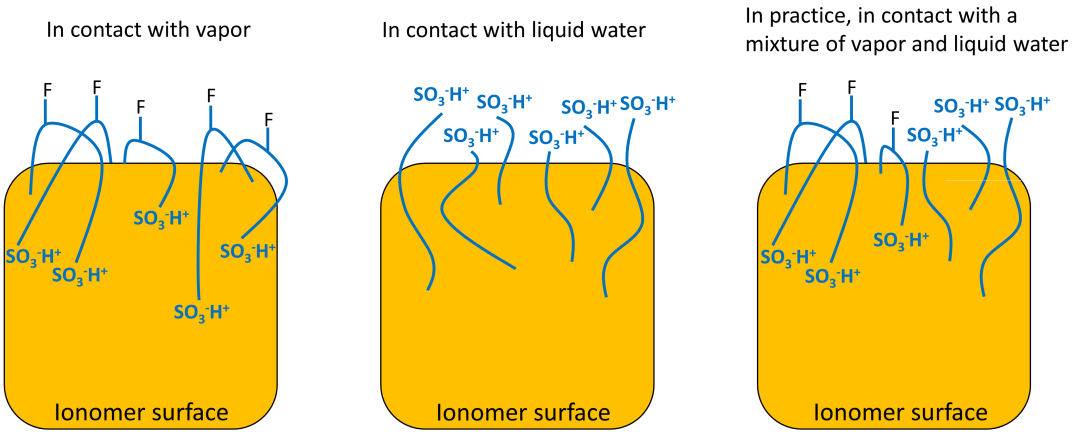

Figure 1.2. – Illustration of PFSA membrane surface morphology when it is in contact with vapour and liquid water [45].

1.2.1.3. Water flow in the membrane: J_{mem}

There are two dominant water transport mechanisms in the membrane: a diffusive flow and an electro-osmotic drag (EOD). The mathematical description of these two flows is initially expressed by the model of Weber and Newman [47, 48] from the concentrated solution theory [49]. However, their formulations involve complex mathematical expressions, incorporating theoretical variables like the chemical potential of water (μ), which are not practical for models at a mesoscopic scale. Consequently, their expressions have evolved into more functional forms while retaining all pertinent information.

Diffusive flow is expressed as a Fick-like expression [50], using the gradient of λ and an associated diffusion coefficient D, function of λ. EOD corresponds to the water molecule drag which is done by protons transport in the membrane. Protons travel in the membrane by hopping between adjacent water molecules (Grottus mechanism) or in the form of hydronium complexes H_3O^+ that cause them to drift (vehicle mechanism). Through this second phenomenon, protons carry water with them from the anode to the cathode [45, 51]. Springer et al. assumed in 1991 [50] that EOD is proportional to the current density and to the water content. Then, they found the corresponding constant, named EOD coefficient, and based on measurements in Nafion®117. Their work, shown in the expression of J_{mem} as (1.3), has been extensively used in the literature [45, 50, 52–55].

$$\boldsymbol{J_{mem}} = \frac{2.5}{22}\frac{i_{fc}}{F}\lambda\,\boldsymbol{\imath} - \frac{\rho_{mem}}{M_{eq}}D(\lambda)\,\boldsymbol{\nabla\lambda} \tag{1.3}$$

where J_{mem} $(mol.m^{-2}.s^{-1})$ is the water flow in the membrane, i_{fc} $(A.m^{-2})$ is the current density of the fuel cell per unit of cell active area, F $(C.mol^{-1})$ is the Faraday constant, ρ_{mem} $(kg.m^{-3})$ is the density of dry membrane, M_{eq} $(kg.mol^{-1})$ is the equivalent molar mass of ionomer calculated by its dry mass over the number of

moles of SO_3^-, D $(m^2.s^{-1})$ is the diffusion coefficient of water in the membrane, and $\boldsymbol{\imath}$ is a unit vector along the x-axis, which is the space variable in the direction of the thickness of the cell, as shown in Figure 1.1.

However, since 1991, significant enhancements in Nafion®membrane have been made [56] and the EOD on these new membranes may differ. It would thus be interesting to reproduce the EOD calculation in order to obtain more accurate models. The literature provides an alternative formulation for the EOD [45], although it is less employed and equally outdated. It is expressed as (1.4).

$$\boldsymbol{J_{EOD}} = \begin{cases} \frac{i_{fc}}{F}\,\boldsymbol{\imath}, & \lambda \leq 14 \\ [0.1875\lambda - 1.625]\,\frac{i_{fc}}{F}\,\boldsymbol{\imath}, & \lambda > 14 \end{cases} \tag{1.4}$$

where J_{EOD} $(mol.m^{-2}.s^{-1})$ is the EOD flow of water in the membrane.

Models other than that of Springer have been sparingly used for the flow of water through the membrane. They are mentioned in Dickinson et al. work [57].

1.2.1.4. Diffusion coefficient: D(λ)

The amount of water dissolved in the membrane significantly influences its diffusion coefficient. When the membrane is adequately hydrated, the polymer backbone molecules form water-filled micro-channels, with SO_3^- groups attached to their walls. Depending on the water content, the membrane exhibits varying numbers of water channels, mean radii, and forms [51], as shown in Figure 1.3. These structural characteristics directly impact water diffusion, benefiting from higher hydration levels through larger channels, reduced tortuosity, and diminished friction. Consequently, it is essential to account for this dependency when considering the diffusion coefficient, which cannot remain constant but should be expressed as a function of λ.

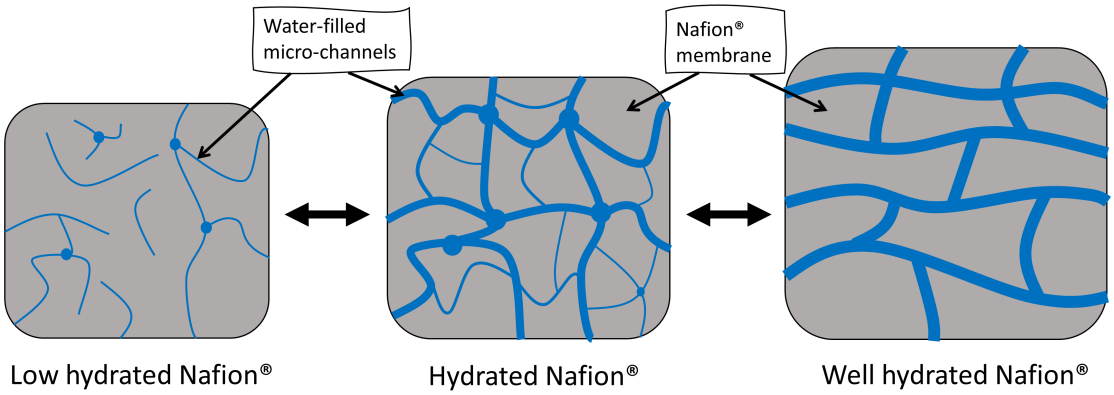

Figure 1.3. – Illustration of PFSA membrane morphology at different levels of hydration.

The diffusivity of dissolved water in the electrolyte is typically determined by fitting experimental data. The two commonly used expressions are based on Zawodzinski's data from 1991 [58]. The first expression, expressed as (1.5), was introduced

by Springer et al. in 1991 [45, 50]. The second expression, expressed as (1.6), was presented by Motupally et al. in 2000 [33, 45, 52, 55, 59, 60].

$$D(\lambda) = \begin{cases} 2.692661843 \times 10^{-10}, & \lambda \leq 2 \\ 10^{-10} e^{2416\left[\frac{1}{303} - \frac{1}{T_{fc}}\right]} \left[0.87\left[3-\lambda\right] + 2.95\left[\lambda - 2\right]\right], & 2 < \lambda \leq 3 \\ 10^{-10} e^{2416\left[\frac{1}{303} - \frac{1}{T_{fc}}\right]} \left[2.95\left[4-\lambda\right] + 1.642454\left[\lambda - 3\right]\right], & 3 < \lambda \leq 4 \\ 10^{-10} e^{2416\left[\frac{1}{303} - \frac{1}{T_{fc}}\right]} \left[2.563 - 0.33\lambda + 0.0264\lambda^2 - 0.000671\lambda^3\right], & 4 < \lambda < 17 \end{cases} \tag{1.5}$$

$$D(\lambda) = \begin{cases} 3.1 \times 10^{-7} \lambda \left[e^{0.28\lambda} - 1\right] e^{-\frac{2436}{T_{fc}}}, & \lambda < 3 \\ 4.17 \times 10^{-8} \lambda \left[161 e^{-\lambda} + 1\right] e^{-\frac{2436}{T_{fc}}}, & 3 \leq \lambda < 17 \end{cases} \tag{1.6}$$

where T_{fc} (K) is the fuel cell temperature. Notably, some recent papers have applied an inversion of the coefficient 2436 in the exponential [33, 45, 52]. Additionally, both of these expressions do not account for water content values greater than 17. The suitability of these relationships for higher λ values is therefore not guaranteed.

Upon examining figure 1.4, it becomes evident that the difference between the two correlations is non-negligible. However, no conclusive evidence points to one being more accurate than the other. Both correlations have found widespread use in PEMFC modeling [45, 50, 59]. However, the abrupt change in the diffusion coefficient poses challenges for numerical simulations. This peak arises from a correction procedure, which involves differentiating experimental data and may not be consistent with reality. Furthermore, the kinetics of channel formation within Nafion®membranes during water uptake, as well as the geometry of channels, remain insufficiently understood. However, as previously discussed, it is reasonable to assume that lower water content corresponds to a reduced mean pore radius in the membrane, hindering water diffusion [51]. Consequently, there should be no peak, and diffusivity must be a growing function of λ.

In 1998, Van Bussel et al. [61] conducted measurements that validated these physical considerations. Subsequently, Kulikovsky et al. fitted these values in 2003 and proposed a function expressed as (1.7)[33, 51, 60]. This equation appears to be more representative of the underlying physical phenomena. However, it has some drawbacks: the measurements were performed using outdated membranes, similar to the two previous equations [56]. Additionally, the temperature dependency was lost in this expression, which was fitted with data at 80°C.

$$\boxed{D(\lambda) = 4.1 \times 10^{-10} \left[\frac{\lambda}{25.0}\right]^{0.15} \left[1.0 + \tanh\left(\frac{\lambda - 2.5}{1.4}\right)\right]} \tag{1.7}$$

Figure 1.4 compares the three proposed equations for the diffusion coefficient at

80°C. The authors recommend using the Kulikovsky model [51], although further improvements could be made by incorporating temperature considerations and utilizing modern membranes in the measurements.

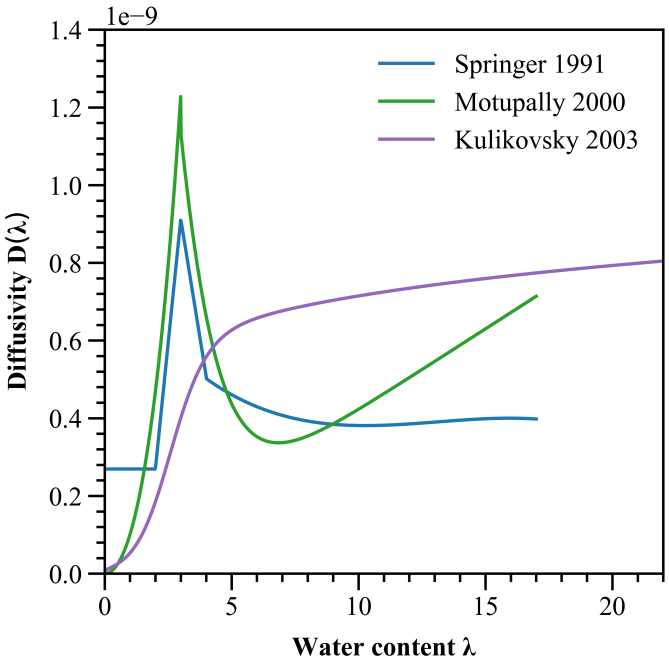

Figure 1.4. – Comparison of the three expressions of the diffusivity coefficient of the membrane at 80°C

1.2.1.5. Equilibrium water content of the membrane: λ_{eq} - an overview

To calculate the water sorption (S_{sorp}) between the membrane and the catalyst layer, it is essential to first comprehend the equilibrium water content of the membrane (λ_{eq}) and the water activity (a_{w}). However, the sorption process is complex, and the existing literature appears incomplete. An overview on λ_{eq} in this section, on a_w section 1.2.1.6 and on S_{sorp} section 1.2.1.7 are first presented based on the current litterature. Further, section 1.2.1.8 presents new proposals.

One effective method of quantifying the exchange flow between the membrane and the catalyst layer involves comparing the current water content in the catalyst layer, λ, with its equilibrium value, λ_{eq}. The equilibrium water content of the membrane λ_{eq} is a variable that is experimentally accessible, and is a function of the water activity a_w. Subsequently, $\lambda_{v,eq}$ must be differentiated from $\lambda_{l,eq}$. Here, $\lambda_{v,eq}$ refers to an equilibrium of the dissolved water with vapour, which has a certain activity a_w, whereas $\lambda_{l,eq}$ refers to an equilibrium with pure liquid water. The difference between $\lambda_{l,eq}$ and $\lambda_{v,eq}$ with saturated vapour is noticeable and is referred to as the Schroeder's paradox, as discussed in Section 1.2.1.2.

Two experiments widely accepted in the scientific community have been conducted to derive an equation for λ_{eq} from experimental data. The first experiment, proposed

by Springer et al. [50], utilized data provided by Zawodzinski et al. in 1991 [58]. This experiment focused exclusively on a Nafion®117 membrane, with measurements taken at 30°C for $\lambda_{v,eq}$ and 80°C for $\lambda_{l,eq}$. The equation is expressed as (1.8) [33, 41, 45, 50, 54, 55, 58, 60, 62].

The second experiment, proposed by Hinatsu et al. in 1994 [63], is expressed as (1.9) [57, 59, 63, 64]. This experiment provided an equation for $\lambda_{v,eq}$ that accurately fits data from various membrane types, including Nafion®115, Nafion®117, AC-12, and FL-12. It was conducted at the standard operating temperature of 80°C for PEMFCs. For $\lambda_{l,eq}$, the results varied based on the membrane type. It is the expression for Nafion®117 which is there considered. Additionally, a temperature dependency was incorporated into the equation. Considering that the experimental conditions proposed by Hinatsu et al. are more realistic than those of Springer et al., their results are preferable.

Zawodzinski et al. also conducted experiments at 80°C in 1993 [65], with the results expressed as an equation by Ye in 2007 [66]. However, it is the study by Hinatsu et al. which gained the widespread acceptance. Although these measurements are considered outdated for modern models due to advancements in membrane structures and experimental protocols over the last decade [56], they are still widely used. A graphical comparison of these expressions for $\lambda_{v,eq}$ is presented in figure 1.5.

$$\lambda_{eq}^{Springer} = \begin{cases} \lambda_{v,eq}(a_w) = 0.043 + 17.81a_w - 39.85a_w^2 + 36.0a_w^3, & a_w \in [0,1] \\ \lambda_{l,eq} = 16.8 \end{cases} \tag{1.8}$$

$$\lambda_{eq}^{Hinatsu} = \begin{cases} \lambda_{v,eq}(a_w) = 0.300 + 10.8a_w - 16.0a_w^2 + 14.1a_w^3, & a_w \in [0,1] \\ \lambda_{l,eq} = 10.0 + 1.84 \cdot 10^{-2} T_{fc} + 9.90 \cdot 10^{-4} T_{fc}^2, & T_{fc} \text{ in °C here} \end{cases} \tag{1.9}$$

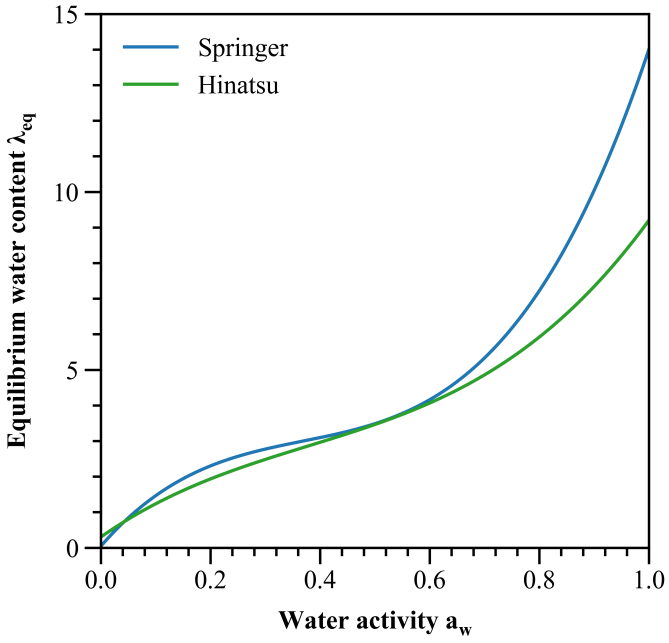

Figure 1.5. – Comparison between Springer's and Hinatsu's expressions for $\lambda_{v,eq}$.

Subsequently, numerous researchers have attempted to combine $\lambda_{v,eq}$ and $\lambda_{l,eq}$ into a single quantity, λ_{eq}. This choice is questioned section 1.2.1.8. To establish this connection, Springer et al. initially posited that their formulation for $\lambda_{v,eq}$ remains applicable at 80°C, despite the experimental measurements being conducted at 30°C [50]. This hypothesis is not necessary for the expression of Hinatsu. Then, Springer et al. correlated the water activity a_w with both vapour and liquid phases, although this is uncommon. For $a_w \in [0,1]$, only vapour was present, and for $a_w > 1$, liquid water coexisted with saturated vapour. Subsequently, they considered an activity value significantly exceeding 1 and concluded that $a_w = 3$ is a suitable value, resulting in the exclusive presence of pure liquid water occupying the entire cavity volume of the triple points zone. The arbitrary selection of $a_w = 3$ and the newly formulated expression for a_w associated with both vapour and liquid water were left unexplained in their study, posing challenges to the understanding of their model. However, these issues did not impede its prevalence in the literature, and an adapted expression for a_w has consequently been introduced, as discussed in section 1.2.1.6. Finally, a linear expression was arbitrarily employed to connect $\lambda_{v,eq}$ at $a_w = 1$ to $\lambda_{l,eq}$ at $a_w = 3$, as indicated in (1.10) [33, 41, 45, 50, 54, 55, 58, 60, 62]. In this model, the existence of $a_w \geq 3$ is deemed either improbable or impossible; hence, the value of 16.8 is retained for higher a_w, or higher values should not be considered [62]. Nonetheless, providing precise rules is challenging, given the incomplete and subjective nature of this framework. Nevertheless, this model persists in subsequent studies. The expression by Hinatsu et al. has been adjusted in the same manner at 80°C, resulting in (1.11).

$$\lambda_{eq}^{Springer}(a_w) = \begin{cases} 0.043 + 17.81a_w - 39.85a_w^2 + 36.0a_w^3, & a_w \in [0,1] \\ 14 + 1.4\,[a_w - 1]\,, & a_w \in]1,3] \end{cases} \tag{1.10}$$

$$\lambda_{eq}^{Hinatsu}(a_w) = \begin{cases} 0.300 + 10.8a_w - 16.0a_w^2 + 14.1a_w^3, & a_w \in [0,1] \\ 9.2 + 4.3\,[a_w - 1]\,, & a_w \in]1,3] \end{cases} \tag{1.11}$$

As evident, these equations are constructed in two parts, resulting in stiffness when $a_w = 1$. Consequently, oscillations occur during the implementation of the models. To enhance the numerical results, Bao et al. replaced the linear expression for $a_w \in]1,3]$ by Springer et al., presenting a unique and general equation for all a_w values [28]. The linear relationship between $\lambda_{eq}(a_w = 1)$ and $\lambda_{eq}(a_w = 3)$ being arbitrarily established, there appear to be no immediate obstacles to making this change. However, Bao et al. interpreted Springer's work differently, suggesting a discontinuity at $a_w = 3$, where λ_{eq} increases from 16.8 to 22 [28]. In the authors analysis, the value of 22 is provided for experiments conducted at 100°C, whereas 16.8 is evaluated at 80°C. Only one of them must be chosen depending on the working temperature, which is 80°C in this case. Thus, the authors slightly modified the expression proposed in [28] to obtain a more adapted equation, as expressed in (1.12).

$$\begin{aligned} \lambda_{eq} = {} & \frac{1}{2}\left[0.043 + 17.81a_w - 39.85a_w^2 + 36.0a_w^3\right] \cdot [1 - \tanh(100\,[a_w - 1])] \\ & + \frac{1}{2}\left[14 + 2.8\left[1 - \exp\left(-K_{\text{shape}}\,[a_w - 1]\right)\right]\right] \cdot [1 + \tanh(100\,[a_w - 1])] \end{aligned} \tag{1.12}$$

Various values of the mathematical factor K_{shape} enable the experimenter to depict either a smooth transition ($K_{\text{shape}} = 2$) or a sharp jump ($K_{\text{shape}} = 20$) between the "two ends of Schroeder's paradox" [28], as illustrated in figure 1.6. It is crucial to emphasize that this is formulated for modeling purposes only, and the physics considerations are disregarded at this point. This study recommends employing a small K_{shape}, such as $K_{\text{shape}} = 2$, to ensure that the model does not deviate excessively from the involved physics. At this stage, it becomes evident that a more robust theory on equilibrium water content needs formulation for enhanced utilization of $\lambda_{v,\text{eq}}$ and $\lambda_{l,\text{eq}}$.

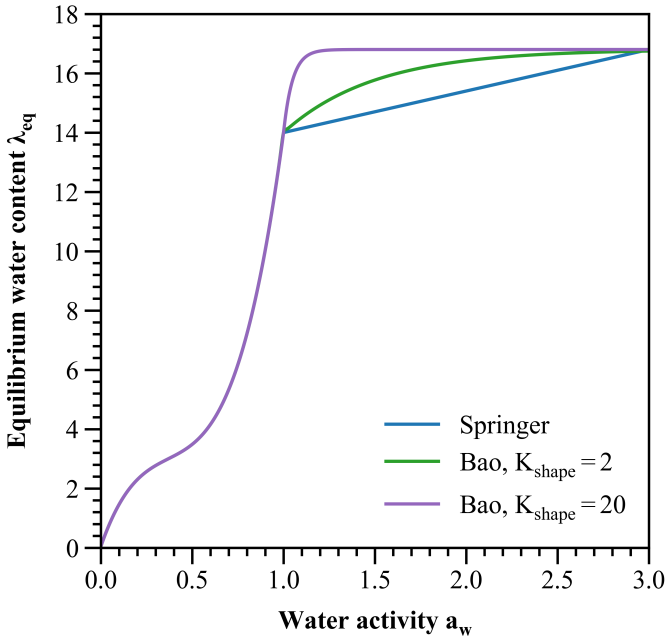

Figure 1.6. – Comparison between Springer's piece wise expression and Bao's function for water content equilibrium with different values of K_{shape}

Finally, the expression for λ_{eq} proposed in this study is expressed as (1.13). It is derived based on Hinatsu's equations at 80°C, following the form suggested by Bao et al. This expression is compared with the one of Springer et al. in figure 1.7.

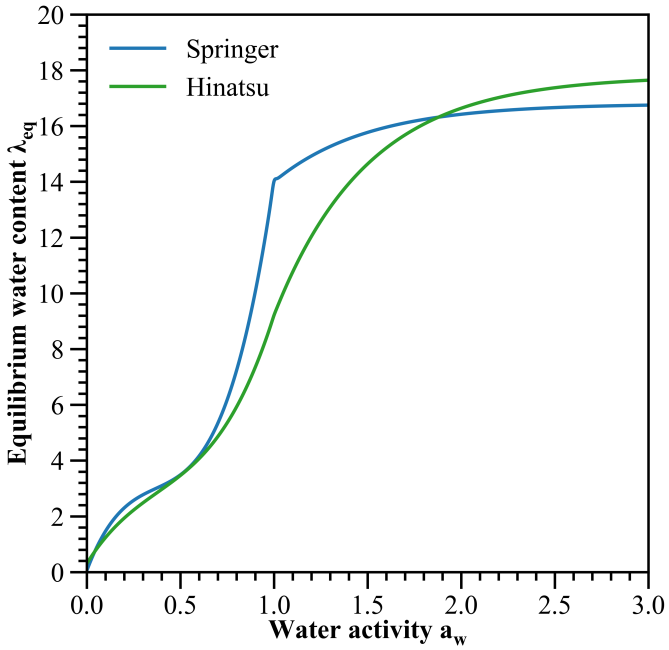

Figure 1.7. – Comparison between Springer's and Hinatsu's expressions for λ_{eq} at 80°C, using Bao's form.

$$\begin{aligned}\lambda_{eq} = &\frac{1}{2}\left[0.300 + 10.8a_w - 16.0a_w^2 + 14.1a_w^3\right]\cdot\left[1-\tanh\left(100\left[a_w-1\right]\right)\right] \\ &+\frac{1}{2}\left[9.2 + 8.6\left[1-\exp\left(-K_{\text{shape}}\left[a_w-1\right]\right)\right]\right]\cdot\left[1+\tanh\left(100\left[a_w-1\right]\right)\right]\end{aligned} \tag{1.13}$$

1.2.1.6. Water activity: a_w - an overview

The water activity, denoted as a_w, quantifies water's ability to humidify the membrane within the catalyst layer. According to Schroeder's paradox, the more condensed the water, the more favorable the humidification. In the literature, two commonly accepted definitions, (1.14) and (1.15), exist. However, the use of one against the other has never been explained, to the best of the authors knowledge. This section aims to provide an explanation for both of these definitions. Additionally, Section 1.2.1.8 introduces a novel approach.

The original definition, as expressed in (1.14), was initially proposed by Springer et al., [50] and pursued by Ge et al. [64]. When considering only vapour, a_w is equivalent to water humidity, a common consideration across various physics disciplines. However, it's noteworthy that a_w can surpass 1 and extend up to 3, indicating a mixture of vapour and liquid water. The value $a_w = 3$ specifically denotes pure liquid water.

$$a_w \triangleq \begin{cases} \frac{P}{P_{sat}} \underbrace{=}_{\text{ideal gas law}} \frac{C}{C_{sat}}, & \text{for pure vapour} \\ 3, & \text{for pure liquid water} \end{cases} \tag{1.14}$$

where P (Pa) is the vapour pressure, P_{sat} (Pa) is the vapour saturated pressure, C $(mol.m^{-3})$ is the vapour concentration, and C_{sat} $(mol.m^{-3})$ is the vapour saturated concentration.

The drawback of this model lies in the absence of an explanation regarding the characterization of a_w when its values exceed 1. It is implicitly assumed that the expression $\frac{P}{P_{sat}}$ is sufficient, but this assumption is questionable. When vapour is fully saturated at $a_w = 1$, condensation initiates, causing the vapour pressure to decrease and giving rise to liquid water. However, vapour continues to be supplied through the chemical reaction of hydrogen and oxygen. As condensation is not instantaneous, the input of vapour can eventually counterbalance condensation, leading to a pressure increase, resulting in $a_w > 1$. Nonetheless, the higher the $P > P_{sat}$, the more significant the amount of condensation (as discussed in section 1.2.2.7). Consequently, it is improbable for a_w to increase substantially. Springer et al. considered an arbitrary limit of 3 for a_w, corresponding to the water activity of pure liquid water. However, achieving this value is unlikely when considering only vapour in water activity a_w. Thus, while it is acceptable for $\frac{P}{P_{sat}} > 1$, it is unlikely to increase beyond 3.

In the literature, one extrapolation is widely used to incorporate both vapour and liquid water into a_w [33, 45, 54, 55]. This variable is reconstructed following specific rules. Initially, $a_w \in [0,3]$. Subsequently, $a_w \in [0,1]$ represents a vapour phase in the catalyst layer, while $a_w \in [1,3]$ indicates a mixture of vapour and liquid water. Finally, the value of a_w increases with the condensation of water. One mathematical expression that fulfills all these criteria is given by (1.15). However, it is not the sole mathematical approach meeting these conditions, and there is no evidence to suggest that (1.15) is the most accurate model for fuel cell modelling.

$$a_w \triangleq \frac{P}{P_{sat}} + 2\mathtt{s} \underbrace{=}_{\text{ideal gas law}} \frac{C}{C_{sat}} + 2\mathtt{s} \tag{1.15}$$

where $\mathtt{s}$ is the liquid water saturation (explained in 1.2.2.1).

Finally, there is another equation in the literature [52, 62] that is less commonly employed. This expression, denoted as (1.16), extrapolates the activity definition for water vapour from (1.14). In this formulation, liquid water is treated as a gas, and its "concentration" in the pore volume is considered. However, the authors strongly discourage the use of this equation for several reasons. Firstly, treating liquid water as a gas represents an overly restrictive assumption. Additionally, this equation is incompatible with Springer's model, even though it relies on it. Indeed, λ_{eq} is only applicable for activities between 0 and 3, with the value of 3 established solely for liquid water in the catalyst layer. However, in the case of this equation, for $s \in [0,1]$, a_w falls within the range $[0,5072]$. It is evident that this equation produces inaccurate results.

$$a_w \triangleq \frac{P_{\text{vapour+liquid}}}{P_{\text{sat}}} \underbrace{=}_{\text{ideal gas law}} \frac{C\,[1-\mathrm{s}] + \frac{\rho_{H_2O}}{M_{H_2O}}\mathrm{s}}{C_{\text{sat}}} \tag{1.16}$$

1.2.1.7. Water sorption at the ionomer/CL interface: S_{sorp} - an overview

At the interface between the ionomer and the CL, there is an exchange of water. This water exists in a dissolved form within the ionomer and in either vapour or liquid form in the CL. This water conversion, denoted as S_{sorp} in this study, represents either water absorption or desorption and occurs throughout the entire volume of the catalyst layer. It differs from a flow, which involves the transport of matter from one volume to another across a surface. This conversion takes place within a single volume and is therefore volumetric. Due to the discontinuity of matter at the interface, Fick's law does not accurately characterize this flow. More complex phenomena are at play, complicating the applicability of existing laws. Consequently, the caracteristic law for S_{sorp} has undergone refinement over the past decades [45, 53, 64]. In this section, the authors strive to articulate a clear and precise expression for the sorption term S_{sorp}, drawing on the insights from the most recent and original studies [54, 55, 64, 67].

First and foremost, the following general expression (1.17) is commonly accepted in the community [33, 45, 54, 55, 67, 68].

$$\boxed{S_{sorp} = \gamma_{sorp}\frac{\rho_{\text{mem}}}{M_{\text{eq}}}\left[\lambda_{\text{eq}} - \lambda\right]} \tag{1.17}$$

where γ_{sorp} (s^{-1}) is the sorption rate.

In this expression, λ_{eq} denotes the equilibrium value of λ. It functions as a virtual variable. Consequently, as long as λ deviates from λ_{eq}, a water flow persists between the membrane and the catalyst layer, endeavoring to achieve equilibrium.

The coefficient $\frac{\rho_{\text{mem}}}{M_{\text{eq}}}$ converts water content to membrane water concentration, enabling the expression of water flow. To eliminate the necessity of tracking membrane swelling in the model, Springer et al. adapted their extensively employed results to a dry membrane model [50].

Finally, the sorption rate coefficient reflects the velocity of this sorption. For a given gap between λ_{eq} and λ, the value of γ influences S_{sorp}, and renders the flow as more or less important. Determining γ in an actual PEMFC proved challenging, leading to the adoption of somewhat arbitrary values typically ranging from 0.1 to 100 s^{-1} in the literature [67]. The value $\gamma = 1.3s^{-1}$ is the most commonly encountered one [33, 45]. However, experiments have revealed that the sorption rate of water is not constant; rather, it depends on the volume fraction of water within the membrane, with distinct absorption and desorption rates. Ge et al. [64] introduced a more precise expression for γ_{sorp} in 2005. Subsequently, this expression underwent a slight modification by incorporating the H_{cl} term [32], as illustrated in (1.18) [54, 55, 64, 67].

$$\gamma_{sorp} = \begin{cases} \gamma_a = \frac{1.14 \cdot 10^{-5} f_v}{H_{cl}} e^{2416\left[\frac{1}{303} - \frac{1}{T_{fc}}\right]}, & \text{for an absorption flow} \\ \gamma_d = \frac{4.59 \cdot 10^{-5} f_v}{H_{cl}} e^{2416\left[\frac{1}{303} - \frac{1}{T_{fc}}\right]}, & \text{for a desorption flow} \end{cases} \tag{1.18a}$$

$$f_v = \frac{\lambda V_w}{V_{\text{mem}} + \lambda V_w} \tag{1.18b}$$

where f_v is the water volume fraction of the membrane, V_w ($m^3.mol^{-1}$) is the molar volume of water, and V_{mem} ($m^3.mol^{-1}$) is the molar volume of dry membrane.

There is one flaw in this equation. The coefficient ε_{mc}, discussed in section 1.2.1.1, should have been included in this equation to account for the volume fraction of the ionomer in the catalyst layer. Indeed, ε_{mc} is not universal and varies based on the stack design. Considering this variable is crucial for a more precise model. Including tortuosity considerations with ε_{mc}^{τ} would have been even more beneficial (as discussed in section 1.2.3.2).

It remains important to know if, in a biphasic state for water in the catalyst layer, S_{sorp} is a vapour, a liquid matter conversion, or both. Ge et al. provided insights into this matter. When liquid water is introduced, it comes into direct contact with the membrane. The water content of the membrane at the membrane/GDL interface is assumed to reach instant equilibrium with liquid water [64]. Thus, the expression for the sorption rate, γ_{sorp}, is valid only for vapour, and S_{sorp} necessarily denotes a vapour matter conversion. This observation is significant as it highlights, once again, the common yet inconsistent practice of combining $\lambda_{v,eq}$ and $\lambda_{l,eq}$ in the calculation of S_{sorp}, accomplished by introducing $\mathfrak{s}$ into a_w.

1.2.1.8. New interpretation of S_{sorp}, λ_{eq} and a_w

Previously, sections 1.2.1.5, 1.2.1.6, and 1.2.1.7 provided a comprehensive overview of the current utilization of λ_{eq}, a_w, and S_{sorp} in the literature, with their associated limitations highlighted. The present section introduces a novel approach to address these limitations.

Different phenomena give rise to distinct expressions for λ_{eq}. When vapour is in contact with the membrane, it is denoted as $\lambda_{v,eq}$. Conversely, when liquid water is in contact with the membrane, it is represented by $\lambda_{l,eq}$. Previous studies attempted to amalgamate them as a single entity, treating vapour and liquid water sorption as if they were identical. Consequently, the concepts of $\lambda_{v,eq}$ and $\lambda_{l,eq}$ were subsumed under λ_{eq}, and water activity was linked to both vapour and liquid water. However, these choices are here reconsidered for the reasons outlined in the previous sections. To address this, the authors propose distinguishing between two water sorption processes. One involves the conversion of vapour into condensed water, denoted as $S_{v,sorp}$. The other entails the conversion of liquid water into condensed water, denoted as $S_{l,sorp}$. As a result, $\lambda_{v,eq}$ and $\lambda_{l,eq}$ are no longer merged, and there is no longer a need to extrapolate the concept of water activity, which can remain equivalent to relative humidity in the CL. These expressions are provided in (1.19).

$$S_{v,sorp} = \left(1-\varphi_{sp}\right)\gamma_{v,sorp}\frac{\rho_{\text{mem}}}{M_{\text{eq}}}\left[\lambda_{\text{v,eq}}-\lambda_{cl}\right] \tag{1.19a}$$

$$S_{l,sorp} = \varphi_{sp}\gamma_{l,sorp}\left[\lambda_{\text{l,eq}}-\lambda_{cl}\right] \tag{1.19b}$$

where $\gamma_{v,sorp}$ is the sorption rate of vapour to condensed water, equal to the classic expression of γ_{sorp}, $\gamma_{l,sorp}$ is the sorption rate of liquid water to condensed water, and φ_{sp} is the surface proportion of liquid water at the CL ionomer interface.

However, this idea necessitates the identification of two novel quantities in future research. Firstly, $\gamma_{l,sorp}$ is currently unknown and requires experimental measurement. According to Ge et al. [64], the value of this sorption rate should be significantly higher than that of $\gamma_{v,sorp}$ to account for their hypothesis of instantaneous equilibrium. Secondly, φ_{sp} needs to be determined to properly balance these two water sorptions. These quantities are experimentally evaluated either without liquid water or without vapour. However, in a scenario involving the coexistence of these two quantities, it is essential to balance their access to the membrane. The authors propose considering the surface ratio of liquid water at the CL ionomer interface for φ_{sp}. Thus, φ_{sp} is a function of the volumetric ratio of liquid water $\mathtt{s}$. This function does not currently exist and could be the subject of future research. It is noteworthy that the inclusion of φ_{sp} might be circumvented if a three-dimensional model with sufficient precision to differentiate regions where liquid water resides from regions with vapour were available. However, constructing such a model would demand computational power to an extent that seems impractical to consider.

Finally, it remains to incorporate $S_{v,sorp}$ and $S_{l,sorp}$ into the matter balances for the water content λ_{cl}, the vapour concentration C, and the liquid water saturation $\mathtt{s}$.

1.2.1.9. Water production at the interface of the triple points: S_{prod}

Water is formed through the chemical reaction between hydrogen and oxygen at the triple point interface within the cathode catalyst layer. As redox reactions of oxygen and hydrogen are considered to be infinitely fast, water production is directly associated with i_{fc}, representing the current density generated by the fuel cell. Additionally, it is influenced by i_{sc}, corresponding to the short circuit current density, as discussed in section 1.3.3.3. This relationship is expressed in (1.20).

$$S_{\text{prod}} = \begin{cases} \frac{i_{fc}+i_{sc}}{2FH_{cl}}, & \text{in the CCL} \\ 0, & \text{elsewhere} \end{cases} \tag{1.20}$$

where S_{prod} $(mol.m^{-3}.s^{-1})$ is the water production in the membrane at the triple points zone, H_{cl} (m) is the catalyst layer thickness. It is unclear whether water is initially produced in vapour, liquid, or dissolved form in the membrane. Similar to Jiao et al. [45], the authors propose to implement it in a dissolved form. Nonetheless, it is straightforward to modify this assumption by relocating the matter conversion term to a different differential equation.

The stack also generates additional water due to the crossover of hydrogen and

oxygen, as discussed in section 1.2.5.2. This water generation is denoted as S_{co}. However, it is noteworthy that water can be produced in both the anode and cathode catalyst layers. This water production should be directly associated with the crossover flows, assuming these flows pass through the membrane instantaneously, as if it were of negligible thickness. Additionally, it is assumed that all the matter passing through undergoes instantaneous reaction to form water [69]. The corresponding equation is expressed in (1.21).

$$S_{co} = \begin{cases} 2 \cdot S_{O_2,co}, & \text{in the ACL} \\ S_{H_2,co}, & \text{in the CCL} \\ 0, & \text{elsewhere} \end{cases} \tag{1.21}$$

where $S_{i,co}$ $(mol.m^{-2}.s^{-1})$ is the crossover flow of molecule i (hydrogen or oxygen), discussed in 1.2.5.2.

Finally, the corrected expression of S_{prod} is expressed as (1.22).

$$S_{\text{prod}} = \begin{cases} 2k_{O_2} \frac{RT_{fc}}{H_{cl}} \nabla C_{O_2}, & \text{in the ACL} \\ \frac{i_{fc}+i_{sc}}{2FH_{cl}} + k_{H_2} \frac{RT_{fc}}{H_{cl}} \nabla C_{H_2}, & \text{in the CCL} \\ 0, & \text{elsewhere} \end{cases} \tag{1.22}$$

1.2.1.10. Water content dynamic behavior

In the membrane, water content is governed by the molar balances presented in equation 1.23a [52], along with the boundary condition given in equation 1.23b. The system involves two differential equations. Indeed, unlike the ionomer in the membrane, the ionomer in the catalyst layer represents only a fraction of the total volume. This factor affects the governing equation by introducing the CL ionomer volume fraction ε_{mc}. It is important to note that in this context, ε_{mc} is not associated with tortuosity; this relationship should only be considered in the context of expressing the transport flows.

$$\begin{cases} \frac{\rho_{\text{mem}}}{M_{\text{eq}}} \frac{\partial \lambda_{\text{mem}}}{\partial t} = -\nabla \cdot \boldsymbol{J_{mem}}, & \text{in the bulk membrane} \\ \frac{\rho_{mem}\varepsilon_{mc}}{M_{eq}} \frac{\partial \lambda_{cl}}{\partial t} = -\nabla \cdot \boldsymbol{J_{mem}} + S_{sorp} + S_{prod}, & \text{in the CL} \end{cases} \tag{1.23a}$$

$$\boldsymbol{J_{mem}^{cl,mem}} = \mathbf{0}, \text{at the ionomer border} \tag{1.23b}$$

1.2.2. Liquid water transport in the CL and GDL

1.2.2.1. Liquid water saturation: s

During the operation of a PEMFC, the water produced through chemical reactions, combined with the moisture in the incoming gas, often reaches a point of vapour saturation, leading to the formation of liquid water within the cell. It is crucial to regulate this quantity, as an excess may submerge the fuel cell, causing a drop in

voltage. On one hand, the triple points areas may be submerged in liquid water, introducing additional resistance to fuel transport to the catalysts. On the other hand, the presence of liquid water in the GDLs can impede the gas flow towards the CLs by increasing the material's tortuosity. To quantify the amount of liquid water, the liquid water saturation variable s is employed. The values of s range from 0 to 1, where 0 signifies the absence of liquid water and 1 indicates the exclusive presence of liquid water within the pore stack.

$$\mathrm{s} \triangleq \frac{V_{\text{liquid water}}}{V_{\text{pore}}} \tag{1.24}$$

Three phenomena govern the evolution of liquid water: capillarity, convection, and condensation/evaporation. Each of these phenomena is discussed in the following sections. Within the CL and the GDL, liquid water is mainly transported by a diffusive force known as capillarity. Referred to in this work as $J_{l,cap}$, this phenomenon is explored in detail in section 1.2.2.2. Additionally, a secondary flow, denoted as $J_{l,conv}$, arises from gas motions, leading to the hauling of liquid water and thus termed a convective flow. However, as examined in section 1.2.2.5, it is a minor flow compared to the capillary flow and is often disregarded. Darcy's law is employed to characterize both flows. Finally, liquid water at the GDL/GC border is considered equal to 0 due to its rapid expulsion in the GCs and the limited knowledge available on this subject. This is discussed in section 1.2.2.6.

1.2.2.2. Liquid water capillary flow in the CL and GDL: $J_{l,cap}$

The capillary flow, denoted as $J_{l,cap}$ and defined in (1.25), quantifies the capacity of liquid water generated within the electrode through vapour condensation to permeate it [45, 54, 60, 62, 66]. Capillarity represents a specific instance of diffusivity within the liquid phase. The equation is similar to Fick's law, incorporating a matter gradient $\boldsymbol{\nabla}\mathrm{s}$ and a variable diffusive coefficient D_{cap}. This relationship is given by Darcy's law, as demonstrated in A.4.1.

It is important to note that (1.25) is derived from experiments involving water permeation through beds of sand, representing a significant simplification compared to water permeation through the GDL. Despite this simplification, it currently stands as the most viable model in the literature [45]. Therefore, the development of more pertinent models is imperative. In this context, the porous environment is assumed to be homogeneous, with negligible deformation, and water flow must be slow enough to maintain a small Reynolds number under stationary conditions [70]. Gravity's impact is typically disregarded in the stack. Additionally, the flow expressed in (1.25) is historically in units of $kg.m^{-2}.s^{-1}$, whereas all other flows in PEMFC literature are presented in units of $mol.m^{-2}.s^{-1}$. This formulation is preserved in this review, with adjustments made to the differential equations to accommodate this distinction.

$$\begin{cases} \boldsymbol{J_{l,cap}} = -D_{cap}(\mathrm{s},\varepsilon)\,\boldsymbol{\nabla}\mathrm{s} \\ D_{cap}(\mathrm{s},\varepsilon) = \sigma\frac{K_0}{\nu_l}\left|\cos(\theta_c)\right|\sqrt{\frac{\varepsilon}{K_0}}\mathrm{s}^{\mathrm{e}}\left[1.417 - 4.24\mathrm{s} + 3.789\mathrm{s}^2\right] \end{cases} \tag{1.25}$$

where $\boldsymbol{J_{cap}}$ $(kg.m^{-2}.s^{-1})$ is the capillary flow, σ $(N.m^{-1})$ is the surface tension of liquid water, K_0 (m^2) is the intrinsic permeability, ν_l $(m^2.s^{-1})$ is the liquid water kinematic viscosity, θ_c (°) is the contact angle of GDL for liquid water, e is the capillary exponent, and $\boldsymbol{\nabla}$ is the gradient notation. To enhance the clarity of this expression, supplementary information is provided in (A.4.1).

It is noticeable that an absolute value was introduced on $\cos(\theta_c)$ in this study, a practice not commonly employed. This modification proves advantageous in ensuring a consistently positive diffusion coefficient D_{cap}, thereby preserving the negative sign typically associated with any mass balance. In existing literature, when $\cos(\theta_c)$ is negative, there are instances where the negative sign is occasionally omitted in the overall equation, complicating the proper understanding of the equation and impeding meaningful comparisons between different sources.

Moreover, the capillary exponent e serves as a novel parameter introduced in this study to account for various values of e found in the literature. Notably, the widely utilized cubic correlation assigns a value of 3 to e, originating from porous media such as sand/rock with typical porosities ranging from 0.1 to 0.4. Given the similarity between a PEMFC catalyst layer and sand/rock in terms of porosity and morphology, the liquid and gas permeabilities in the catalyst layer are computed using the aforementioned cubic correlations. However, recent research suggests that e should fall within the range of 4.0 to 5.0 for GDL porous materials characterized by high porosities ranging from 0.6 to 0.8. It is noted that the cubic correlation may tend to overestimate liquid permeability, especially at low liquid saturation [45, 54, 60, 66, 68]. These considerations are synthesized in (1.26).

$$\begin{cases} \mathsf{e} = 3, & \text{if } \varepsilon \in [0.1, 0.4] \\ \mathsf{e} \in [4,5], & \text{if } \varepsilon \in [0.6, 0.8] \end{cases} \tag{1.26}$$

Finally, it is important to note that $J_{l,cap}$ (as well as $J_{l,conv}$ in section 1.2.2.5) is based on Darcy's law, which applies only to creeping flow. While this assumption is reasonable within the GDL and the CL, modern stacks, which utilize complex flow-fields in the GC, such as the use of baffles, and operate under high current densities ($> 1 A.cm^{-2}$), may experience convective flows penetrating the GDL. In such critical conditions, Darcy's law becomes inadequate. Instead, Darcy-Forchheimer's law is employed to account for additional inertial effects. For further details, refer to the study by Kim et al. [19].

1.2.2.3. Intrinsic permeability: K_0

The intrinsic permeability, denoted as K_0, measures the porous material's capacity to facilitate the flow of fluids through it. This property is influenced by the material's porosity, the configuration and connectivity of its pores. It stands as an inherent physical characteristic of the material. The Tomadakis and Sotirchos (T&S) model is used to calculate intrinsic permeability within random fibrous and porous media [33, 71, 72]. It's worth noting persistent copying errors in the literature concerning this

equation. The formulation considered in this study in (1.27) aligns closely with the original expression [71].

$$K_0 = \frac{\varepsilon}{8\ln(\varepsilon)^2} \frac{\left[\varepsilon - \varepsilon_p\right]^{\alpha+2} r_{cf}^2}{\left[1-\varepsilon_p\right]^{\alpha} \left[\left[\alpha+1\right]\varepsilon - \varepsilon_p\right]^2} \tag{1.27}$$

where r_{cf} (m) is the carbon fibre radius, obtained at $4.6 \cdot 10^{-6}$ m [72] or $3.16 \cdot 10^{-6}$ m [33], ε_p is the percolation threshold porosity, obtained at 0.11 [33, 72], and α is a fitted value, obtained at 0.521 for in plane direction and at 0.785 for through plan direction [33, 72].

Another element that is often neglected in the literature must be considered in the calculation of the intrinsic permeability. This is the compression of the GDL, described by Bao et al. [73]. Indeed, when the cells are assembled together, a pressure is applied to them to ensure that the gases between each compartment are sealed. This compression causes deformations in the structure of the GDL and therefore causes changes in the transport properties within it [74]. It is therefore necessary to modify the previously proposed model. The advantage of the proposal by Bao et al. is that it fits any model for calculating the effective diffusivity before compression with the simple addition of an exponential coefficient to account for it. However, this study has a limitation. It can only be used for structures with a porosity of approximately 73% or 60%. Fortunately, this concerns a large part of the current GDL. Thus, the model of Tomadakis and Sotichos augmented by the work of Bao et al, which can be renamed by the TSB model, yields the following intrinsic permeability given equation 1.28.

$$\boxed{K_0 = \frac{\varepsilon}{8\ln(\varepsilon)^2} \frac{\left[\varepsilon - \varepsilon_p\right]^{\alpha+2} r_f^2}{\left[1-\varepsilon_p\right]^{\alpha} \left[\left[\alpha+1\right]\varepsilon - \varepsilon_p\right]^2} e^{\beta_1 \varepsilon_c}} \tag{1.28}$$

where β_1 is a fitted value which varies with the porosity and the matter diffusion direction according to the following table 1.1 and ε_c is the compression ratio of the GDL, which is defined as the ratio of the thickness reduction to the thickness of uncompressed GDL. According to Yim et al. [75], a value of 30% for ε_c, which corresponds to high GDL compression, is feasible and exhibits good performances. A minimum value of 15% should be given to ε_c for low GDL compression.

β_1	in-plane	through-plane
$\varepsilon \approx 0.6$	-5.07	-3.60
$\varepsilon \approx 0.73$	-3.51	-2.60

Table 1.1. – Different values of the fitted parameter β_1 according to the porosity and the diffusion direction of gases.

Table 1.2 presents a comparison between the value given by these equations and values found in other works.

	$K_0^{gdl}\,(m^2)$	$K_0^{cl}\,(m^2)$
TSB	$3.4 \cdot 10^{-13}$ ($\varepsilon = 0.6$)	$\emptyset$
T&S	10^{-12} ($\varepsilon = 0.6$)	$1.4 \cdot 10^{-14}$ ($\varepsilon = 0.25$)
Hu [53, 62]	$7 \cdot 10^{-13}$ ($\varepsilon = 0.5 - 0.6$)	$\emptyset$
Yang [55]	$3 \cdot 10^{-12}$ ($\varepsilon = 0.7$)	$3 \cdot 10^{-14}$ ($\varepsilon = 0.2$)
Wang [60]	$2 \cdot 10^{-15}$ ($\varepsilon = 0.5$)	$5 \cdot 10^{-17}$ ($\varepsilon = 0.12$)
Ye [66]	$23 \cdot 10^{-12}$ ($\varepsilon = 0.7$)	$2 \cdot 10^{-15}$ ($\varepsilon = 0.2$)
Meng [68]	10^{-12} ($\varepsilon = 0.6$)	10^{-13} ($\varepsilon = 0.12$)
Wang [76]	10^{-12} ($\varepsilon = 0.7$)	10^{-13} ($\varepsilon = 0.3$)

Table 1.2. – Comparison between the value given by Tamadakis and Sotirchos model and values found in other works

1.2.2.4. Water surface tension: σ

Surface tension is the force that preserves a fluid's specific geometry, corresponding to its minimal surface interface with another fluid, in this case, liquid water with air. This phenomenon enables the two fluids to minimize the energy at their interface. In this case, surface tension is solely a function of temperature, and can be calculated using equation 1.29 [77].

$$\sigma = 235.8 \times 10^{-3} \left[\frac{647.15 - T_{fc}}{647.15} \right]^{1.256} \left[1 - 0.625 \frac{647.15 - T_{fc}}{647.15} \right] \tag{1.29}$$

The equation produces a result of $\sigma = 0.0627\ N.m^{-1}$ at 80°C, closely aligning with the prevalent value found in PEMFC literature, which is $0.0625\ N.m^{-1}$ [33, 53–55, 62, 76].

1.2.2.5. Liquid water convective flow in the CL and GDL: $J_{l,conv}$

It is noteworthy that the convection flow of liquid water, denoted as $J_{l,conv}$, is not extensively addressed in prior studies. Certain models neglect this flow, such as the unsaturated flow theory (UFT) [78, 79], while others rigorously exclude it, like the multi-phase mixture model (M^2) [79]. In this study, $J_{l,conv}$ is finally neglected; nevertheless, a discussion is provided on it. This section explores various theories that allow for its omission and outlines resolution methods to be employed when it is deemed significant.

To comprehend $J_{l,conv}$, it is necessary to analyze the impact of gas motion on liquid water. The diffusive transport of gases carries liquid water molecules along with their motion. This transport, quantified by Darcy's law as is $J_{l,cap}$, is expressed as 1.30 [32, 45] and further demonstrated in A.4.1.

$$\boldsymbol{J_{l,conv}} = \frac{\rho_{H_2O}\mu_g}{\mu_l}\frac{\mathrm{s}^{\mathrm{e}}}{[1-\mathrm{s}]^{\mathrm{e}}}\boldsymbol{u_g} \tag{1.30}$$

where $\boldsymbol{J_{l,conv}}$ $(kg.m^{-2}.s^{-1})$ is the convective flow of liquid water, μ_g $(Pa.s)$ is the gas mixture dynamic viscosity, μ_l $(Pa.s)$ is the liquid water dynamic viscosity, and $\boldsymbol{u_g}$ $(m.s^{-1})$ is the gas mixture velocity.

The unsaturated flow theory (UFT) [78] justify the neglect of this flow by stating that the gas phase pressure remains constant throughout the porous media in a two-phase mixture. This reductionist assumption implies that the pressure variation of the liquid phase is equal to the capillary pressure variation. So, according to Darcy's law, gases are immobile in the porous medium, leading to $\boldsymbol{u_g} = \mathbf{0}$ (refer to demonstration A.4.1 for details). Consequently, the convective flow of liquid water is cancelled out. This theory has found widespread application in the field of fuel cell literature concerning two-phase flow through porous media. The UFT theory was excluded from this study due to the restrictive assumption of a constant gas pressure within the stack. Only the convective flow $J_{l,conv}$ was assumed negligible and consequently omitted from further consideration. Although this assumption may seem limiting, it is justified. Firstly, in terms of magnitude, the convective flow is relatively minor compared to the capillary flow. Additionally, liquid water is influenced by both vapour and fuel motions in the electrodes. Given that the vapour and fuel flows are comparable in magnitude and occur in opposite directions, they balance their influence on liquid water. Consequently, $\boldsymbol{u_g}$ is small, resulting in a minor convective flow.

The conventional approach to consider $\boldsymbol{J_{l,conv}}$, also known as the multi-phase approach [79], involves utilizing the Cauchy momentum equations to derive the velocity field within the MEA. In the dynamic behavior of liquid water saturation (1.33a), $J_{l,conv}$ is typically integrated by applying $\boldsymbol{\nabla}\cdot\left(\boldsymbol{J_{cap}}+\boldsymbol{J_{l,conv}}\right)$ instead of $\boldsymbol{\nabla}\cdot\boldsymbol{J_{cap}}$, following the methodology proposed by Wu et al. [32]. However, adopting this approach leads to the formulation of significantly more intricate equations and longer computational times. Neglecting $\boldsymbol{J_{l,conv}}$ helps circumvent this complexity, relying solely on the continuity equation within the MEA to model the system.

However, an alternative method has been developed to significantly reduce the number of equations inherent in the multi-phase approach, although Cauchy momentum equations are still required. This approach, known as the multi-phase mixture model (M²), treats water vapour and liquid water as a unified multi-phase mixture. As a result, the inter-phase interactions vanish, which eliminates both $J_{l,conv}$ and the terms related to the evaporation and condensation of water, represented by S_{vl} as discussed in section 1.2.2.7. The M² method maintains results accuracy comparable to the multi-phase approach without necessitating additional reduction assumptions. However, it does require minor adjustments to the present modeling structure by treating water as a singular entity, whether in a liquid or gaseous state. For a more

in-depth exploration of the M² model, refer to the study conducted by Wang et al [79].

1.2.2.6. Liquid water at the GDL/GC interface - a Dirichlet boundary condition

In the literature there are three major methods for modelling liquid water in the GC, and consequently, at the GDL/GC interface. The first, proposed by Pukrushpan et al. [41], involves considering liquid water as a spray flow, as only a small amount of liquid water is supposed to exist there. These liquid droplets are assumed to be finely dispersed (with zero volume) owing to the strong gaseous motion in the GC and to have transport properties identical to those of vapour.

Second, several studies have identified similarities between the porous structure of the GDL and the channels of the GC flow-field, although the order of magnitude of the sizes are not the same [55, 80–90]. Thus, they proposed to continue the use of the liquid water saturation variable s and to use Darcy's law, with a porosity equal to 1, for modelling liquid water transport, as dicussed previously in Section 1.2.2.2. This attempt further justified by the fact that liquid water can reach up to 10% of the total mass flow rate in the GC [91], which weakens the Pukrushpan hypothesis of a spray flow.

However, as long as 3D complex PEMFC flow-fields are modelled and high current densities are reached ($2 \sim 4\ A.cm^{-2}$), Darcy's law alone is not sufficient to consider liquid water transport. Thus, Darcy-Forchheimer's law is recommended instead [19]. This is an important consideration because the use of advanced GCs, for example baffles, is becoming the norm in modern fuel cells to achieve much higher power densities. In this scenario, GC geometry often result in gas flow penetrations into the GDL owing to strong convection. Consequently, extensive modelling is required to consider the 3D geometry of the GC and determine the location of the boundary between the convection-dominated flow within the GC core and the diffusion-dominated flow within the GDL core, which is not a flat boundary anymore. This high-level modelling, partially introduced by Kim et al. in 2017 [19], is not deeply discussed in this work.

To summarize, Pukrushpan's hypothesis is a relatively simplified perspective of reality. Indeed, regarding tiny liquid water droplets as a perfect gas is overly reductionist, despite their small size. Furthermore, it has been demonstrated that liquid water in the GC is not always in the form of a spray but sometimes exists in much condensed forms [91]. This hypothesis is therefore not recommended. Then, Darcy-Forchheimer's law requires sophisticated modelling, which is not considered in this study. Darcy's law, although compatible in the current stack model, does not fit well into models that consider all the auxiliaries in addition to the stack. To the best of the authors' knowledge, the auxiliaries are generally still modelled using simple equations wherein only gas flows are considered. Therefore, none of these models were adopted here.

Finally, it has been chosen here to not directly model liquid water in the GC, given the current difficulty in doing so and the potential issues it can pose when integrating stack and auxiliary models. To address this, an assumption is made: the configuration of the bipolar plates as well as the operating conditions allow for a good gas flow within

the GC, resulting in excellent removal of liquid water from the stack, preventing it from aggregating within the GC or even on its surface. Thus, liquid water is considered nonexistent in the GC, and a Dirichlet boundary condition is imposed at the GDL/GC interface, setting the liquid water saturation variable s to zero [92]. This boundary condition is presented in equation (1.31).

$$\mathrm{s} = 0, \text{at the GDL/GC border} \tag{1.31}$$

1.2.2.7. Water phase change rate: S_{vl}

In the stack, it is imperative to consider the mole variation of liquid water due to its evaporation or formation through vapour condensation. According to kinetic theory, assuming an ideal gas, neglecting interactions between individual molecules and employing constant overall phase change rates [45], the net matter transfer resulting from evaporation and condensation can be approximated. This is commonly expressed by the following equation (1.32) [33, 54, 55, 60, 66, 68, 76].

$$S_{vl} = \begin{cases} \gamma_{\text{cond}} \varepsilon \left[1 - \mathrm{s}\right] x_v \left[C_v - C_{\text{v,sat}}\right], & \text{if } C_v > C_{\text{v,sat}} \\ -\gamma_{\text{evap}} \varepsilon \mathrm{s} \frac{\rho_{H_2O}}{M_{H_2O}} R T_{fc} \left[C_{\text{v,sat}} - C_v\right], & \text{if } C_v \leq C_{\text{v,sat}} \end{cases} \tag{1.32}$$

where S_{vl} $(mol.m^{-3}.s^{-1})$ is the phase transfer rate of condensation and evaporation, indicating the amount of liquid water converted per units of volume and time, γ_{cond} (s^{-1}) is the overall condensation rate constant for water, γ_{evap} $(Pa^{-1}.s^{-1})$ is the overall evaporation rate constant for water, and x_v is the mole fraction of vapour.

Both constants γ_{cond} and γ_{evap} should be employed carefully, as they are reported in the literature using different units. Consequently, a direct comparison of their values is deemed inappropriate. Table A.2 in the appendix presents various sets of values found in the literature, where the evaporation rate typically surpasses the condensation rate. Notably, Hua Meng's proposed values, $\gamma_{cond} = 5 \cdot 10^3 s^{-1}$ and $\gamma_{evap} = 10^{-4} s^{-1} Pa^{-1}$, seem to be the most suitable. These values were well justified through numerical studies conducted in the work of Meng [68].

Finally, given that water phase change rates are significantly influenced by local conditions such as mass and heat transfer, the accuracy of the calculation at the macroscopic level remains debatable [45].

1.2.2.8. Liquid water saturation dynamic behavior

Considering all aforementioned phenomena, the dynamic behavior of liquid water can be expressed as given in (1.33a), along with its corresponding boundary conditions as indicated in (1.33b).

$$\rho_{H_2O} \varepsilon \frac{\partial \mathrm{s}}{\partial t} = -\nabla \cdot \boldsymbol{J_{cap}} + M_{H_2O} S_{vl} \tag{1.33a}$$

$$\begin{cases} \boldsymbol{J}_l^{cl,mem} = \mathbf{0}, \text{at the ionomer border} \\ \mathrm{s} = 0, \text{at the GDL/GC border} \end{cases} \tag{1.33b}$$

1.2.3. Vapour transport in the CL and GDL

1.2.3.1. Vapour diffusive flow in the CL and GDL: J_{dif}

Concentration gradients govern matter transport within the electrodes, with convection being neglected. This is due to the diminishing velocity of the gas stream near the GDL/GC boundary caused by frictional effects. In the absence of convective mixing, concentration gradients can arise within the stagnant gas of the electrode [23]. To describe this flow, a simple Fick equation is used, as depicted in (1.34).

$$\boldsymbol{J_{v,dif}} = -D_v^{eff} \boldsymbol{\nabla} C_v \tag{1.34}$$

where $J_{v,dif}$ is the vapour diffusive flow and D_v^{eff} is the vapour diffusion coefficient.

1.2.3.2. Effective diffusion coefficient of two species i and j: $D_{i/j}^{eff}$

The conventional binary diffusivity, denoted as $D_{i/j}$ and discussed in section 1.2.3.3, is typically calculated in an open space, which corresponds to an environment different from the matter transport within GDLs or CLs, both of which are porous solids. Consequently, it is necessary to adjust $D_{i/j}$ to incorporate the influence of its surroundings on matter transport. Therefore, the effective diffusivity of species i/j serves as a method to consider both the porosity and tortuosity of the material in which the species evolve, in addition to the space occupied by liquid water that constrains their movement. Tortuosity is introduced to characterize the additional hindrance to diffusion arising from a convoluted or tortuous flow path. Notably, the GDLs and the CLs exhibit disparate structures, leading to distinct flow behaviors within them. Furthermore, these structures are anisotropic, implying that their evolution is direction-dependent. Consequently, it becomes imperative to account for these variations in the mathematical expressions used to describe the effective diffusivity.

The Bruggeman model stands out as the most widely employed expression in the field [23, 33, 52, 54, 55, 72, 76, 93]. It introduces a pore structure coefficient denoted as τ, which characterizes the material's tortuosity. This coefficient exhibits a range of variability from 1.5 to 4.0 [23, 94], depending on the configuration of the pore structure. For example, highly 'maze-like' or meandering pore structures result in elevated tortuosity values [23]. Nevertheless, the Bruggeman model tends to overestimate the effective diffusion coefficient of GDLs [95], as it is based on the porosity of packed spherical particles rather than the cylindrical fibers constituting the GDLs. In contrast, Tomadakis and Sotirchos proposed an alternative model designed for randomly oriented fibrous porous media to characterise vapour infiltration through them [72]. Based on this, Nam et al. [93] proposed the adoption of the Bruggeman model for the CLs and the Tomadakis and Sotirchos model for the GDLs. They further adjusted

these models to incorporate liquid water saturation considerations. Consequently, the effective diffusion coefficient $D_{i/j}^{eff}$ is expressed in (1.35).

$$D_{i/j}^{eff} = \begin{cases} \varepsilon^{\tau}\,[1-\mathrm{s}]^{\tau}\,D_{i/j}, & \text{at the CL (Bruggeman model)} \\ \varepsilon\left[\frac{\varepsilon-\varepsilon_p}{1-\varepsilon_p}\right]^{\alpha}[1-\mathrm{s}]^2\,D_{i/j}, & \text{at the GDL (Tomadakis and Sotirchos model)} \end{cases} \tag{1.35}$$

where τ is the pore structure coefficient, commonly obtained at $\tau = 1.5$ for PEMFC [72], $D_{i/j}$ ($m^2.s^{-1}$) is the binary diffusivity of two species in open space, ε_p is the percolation threshold porosity, obtained at 0.11 [33, 72], and α is a fitted value, obtained at 0.521 for in plane direction and at 0.785 for through plan direction [33, 72].

ε_p represents the minimum porosity necessary within a porous material to allow for diffusion or permeation. Tomadakis and Sotirchos determined the percolation threshold porosity for a random, two-dimensional (2D) fibrous structure, determining it to be $\varepsilon_p = 0.11$. This conclusion was drawn by extrapolating the outcomes of their model [71, 72].

A distinct correlation for effective diffusivity also exists; nonetheless, it has been proven to be more accurate exclusively for fuel cells operating at elevated temperatures. PEMFCs are consequently unconcerned with this. This correlation is expressed as $D_{i/j}^{eff} = D_{i/j}\frac{\varepsilon_{gdl}}{\tau}$ [23].

Another aspect often overlooked in the literature is the compression of GDLs, as detailed by Bao et al. [73] and discussed in section 1.2.2.3. Consequently, a modification to the previously proposed model becomes necessary. It is important to clarify that this adjustment concerns only GDLs and not CLs. Due to the elastic properties of GDLs, they deform to a greater extent than CLs, where deformation can be disregarded. Thus, the Tomadakis and Sotichos model, enhanced by the contributions of Bao et al., renamed as the TSB model, provides the effective diffusion coefficient for the GDL, as given by 1.36.

$$\boxed{D_{i/j}^{eff} = \begin{cases} \varepsilon^{\tau}\,[1-\mathrm{s}]^{\tau}\,D_{i/j}, & \text{at the CL (Bruggeman model)} \\ \varepsilon\left[\frac{\varepsilon-\varepsilon_p}{1-\varepsilon_p}\right]^{\alpha}[1-\mathrm{s}]^2\,e^{\beta_2\varepsilon_c}D_{i/j}, & \text{at the GDL (TSB model)} \end{cases}} \tag{1.36}$$

where β_2 represents a fitted parameter that fluctuates based on porosity and the diffusion direction of gases, as outlined in table 1.3.

β_2	in-plane	through-plane
$\varepsilon \approx 0.6$	-2.05	-1.59
$\varepsilon \approx 0.73$	-1.04	-0.90

Table 1.3. – Different values of the fitted parameter β_2 according to the porosity and the diffusion direction of gases.

Finally, to ensure a comprehensive study, it is assumed that the electrolyte in the CLs exhibits tortuosity characteristics identical to those of the carbon structure.

1.2.3.3. Binary diffusion coefficient: $D_{i/j}$

As previously stated, diffusion coefficients are typically measured in open space. However, in PEMFCs, gas species are not alone during their transport in CLs and GDLs. They diffuse alongside other species, and this coexistence has an impact on their diffusion behavior. For the sake of simplicity, analyses often focus on only two gases simultaneously, with nitrogen assumed to have no interfering effect. As a result, when two species are transported jointly, they share the same diffusion coefficient. This is why $D_{i/j}$ is referred to as a binary diffusion coefficient.

For a binary system comprising gases i and j, $D_{i/j}$ is a function dependent on temperature, pressure, and the molecular weights of both species [23]. Two close expressions, derived from experimental data, can be found in the literature and are represented as (1.37) [23] and (1.38) [33, 55, 72, 76].

$$\boxed{\begin{cases} D_{H_2O/H_2} = 1.644 \cdot 10^{-4} \left[\frac{T_{fc}}{333}\right]^{2.334} \left[\frac{101325}{P}\right] \\ D_{H_2O/O_2} = 3.242 \cdot 10^{-5} \left[\frac{T_{fc}}{333}\right]^{2.334} \left[\frac{101325}{P}\right] \end{cases}} \tag{1.37}$$

The expressions (1.38), commonly employed in the literature, originate from a single source that does not provide a clear explanation of its calculation. Additionally, there is a disparity between D_{vc}, representing the vapour diffusion coefficient at the cathode, and D_{O2}, the dioxygen diffusion coefficient, in (1.38), despite both denoting the binary diffusivity of vapour and dioxygen in the GDLs, implying they should be equal. This disparity may be attributed to the presence of nitrogen in the fuel cell; however, these studies do not furnish explanations on this matter.

$$D_{H_2O/H_2} = 1.005 \cdot 10^{-4} \left[\frac{T_{fc}}{333}\right]^{1.75} \left[\frac{101325}{P}\right] \tag{1.38a}$$

$$\begin{cases} D_{vc} = 2.982 \cdot 10^{-5} \left[\frac{T_{fc}}{333}\right]^{1.75} \left[\frac{101325}{P}\right] \\ D_{O_2} = 2.652 \cdot 10^{-5} \left[\frac{T_{fc}}{333}\right]^{1.75} \left[\frac{101325}{P}\right] \end{cases} \tag{1.38b}$$

Table 1.4 provides a comparison between the two equations and data sourced from alternative references.

1.2.3.4. Vapour convective-diffusive flow at the GDL/GC interface: $J_{v,codi}$

To achieve a complete model of matter transports within the cell, it is imperative to account for the sorption flow between the GDL and GC. In this study, this flow is approximated by an alternative, easier to calculate, denoted as the vapour convective-diffusive flow at the GDL/GC interface and represented by $J_{v,codi}$. A subtle distinction

	$D_{va}\left(m^2 \cdot s^{-1}\right)$	$D_{vc}\left(m^2 \cdot s^{-1}\right)$	$D_{O_2}\left(m^2 \cdot s^{-1}\right)$
O'Hayre [23] (at 353 K and 1.5 atm)	$1.256 \cdot 10^{-4}$	$2.477 \cdot 10^{-5}$	$2.477 \cdot 10^{-5}$
Yang [55] (at 353 K and 1.5 atm)	$7.420 \cdot 10^{-5}$	$2.202 \cdot 10^{-5}$	$1.958 \cdot 10^{-5}$
Hu, Pasaogullari [53, 62] (at 353 K and 1.5 atm)	$5.457 \cdot 10^{-5}$	$2.236 \cdot 10^{-5}$	$1.806 \cdot 10^{-5}$
Jiao [45]	$1 \cdot 10^{-5}$	$1 \cdot 10^{-5}$	$\emptyset$
Nam, Bultel [93, 96]	$\emptyset$	$\emptyset$	$2.9 \cdot 10^{-5}$

Table 1.4. – Comparison between the values given by the mentioned expressions for the binary diffusion coefficients and values found in other works

exists between these two flows: $J_{v,codi}$ exclusively occurs within the GC, characterizing vapour flow from the GDL/GC interface on the GC side to the core of the GC. Conversely, the sorption flow characterizes vapour flow between two distinct layers, the GDL and the GC. It is reasonable to assume that concentrations at the two interface sides instantaneously balance. Consequently, in the absence of matter accumulation, the sorption flow at the GDL/GC interface equates to the convective-diffusive flow $J_{v,codi}$.

In the literature, $J_{v,codi}$ is commonly denoted as a convective flow [23]. However, the authors find this term to be potentially confusing and have opted to rename it as a convective-diffusive flow. Indeed, this flow arises from the coupling of convective mass transfer driven by the pressure difference between the GCs inlet and outlet, and diffusive mass transfer between the GCs interface and its core. These two flows mainly evolve orthogonally to each other. The mathematical expression for this phenomenon is provided in (1.39), derived from diffusive theory while incorporating characteristics of external convective flow [23, 97]. Further details on the derivation of this equation and the determination of the convective-diffusive mass transfer coefficient h_v can be found in A.4.2.

$$\boldsymbol{J_{v,codi}} = \begin{cases} h_v \left[C_{v,gc} - C_{v,gc}^{\text{inter}} \right] \boldsymbol{\imath}, \text{at the anode} \\ h_v \left[C_{v,gc}^{\text{inter}} - C_{v,gc} \right] \boldsymbol{\imath}, \text{at the cathode} \end{cases} \tag{1.39}$$

where h_v $(m.s^{-1})$ is the convective-diffusive mass transfer coefficient of vapour, $C_{v,gc}^{\text{inter}}$ $(mol.m^{-3})$ is the vapour concentration in the GC at its interface with the GDL, and $\boldsymbol{\imath}$ is a unit vector along the x-axis. Notably, h_v is not an "effective" coefficient, as convective-diffusive flow happens in the GC where vapour moves into an empty space.

To use equation (1.39), establishing a correlation between $C_{v,gc}^{\text{inter}}$, representing vapour concentration in the GC at its interface with the GDL, and $C_{v,gdl}^{\text{inter}}$, denoting vapour concentration in the GDL at its interface with the GC, is imperative. While $C_{v,gc}^{\text{inter}}$ remains unknown, $C_{v,gdl}^{\text{inter}}$ is accessible through the diffusion theory outlined

in 1.2.3.1. This requirement is similar to the relationship between λ_{eq} and a_w, albeit without matter conversion in this context. To date, a correlation of the form $C_{v,gc}^{\text{inter}} = f\left(C_{v,gdl}^{\text{inter}}\right)$ is not present in the existing literature. The authors encourage the scientific community to undertake experiments to determine this correlation. Meanwhile, the following simplification is suggested: $C_{v,gc}^{\text{inter}} = C_{v,gdl}^{\text{inter}}$, leading to equation (1.40).

$$\boxed{\boldsymbol{J_{v,codi}} = \begin{cases} h_v \left[C_{v,gc} - C_{v,gdl}^{\text{inter}}\right] \boldsymbol{\imath}, \text{at the anode} \\ h_v \left[C_{v,gdl}^{\text{inter}} - C_{v,gc}\right] \boldsymbol{\imath}, \text{at the cathode} \end{cases}} \tag{1.40}$$

where $C_{v,gdl}^{\text{inter}}$ $(mol.m^{-3})$ is the vapour concentration in the GDL at its interface with the GC.

Finally, an implicit assumption is considered when referring to a convective-diffusive flow. The dividing line, or boundary delineating the convective-dominated flow within the core of the GC and the diffusive-dominated flow within the core of the electrodes, is presumed to occur at the interface between the GC and the GDL. This assumption is reasonable for medium current density operation (approximately 1–1.5 $A.cm^{-2}$). However, its accuracy is contingent upon various factors, such as flow conditions, flow channel geometry, or electrode structure. For instance, under very low gas velocities in the GC, the diffusion layer may extend into the middle of the gas channels. Conversely, at extremely high gas velocities, convective mixing may infiltrate the electrode itself, causing the diffusion layer to recede. Nevertheless, precisely defining its location proves challenging, and determining the true diffusion layer thickness under such conditions necessitates sophisticated models [23], such as the one presented by Kim et al. [19]. These models are not incorporated into the scope of this study.

1.2.3.5. Water effective convective-diffusive mass transfer coefficient: h_v

To calculate h_v, it is common to use the Sherwood number S_h, establishing a connection between h_v and D_v as depicted in (1.41) [23]. The Sherwood number, a dimensionless parameter, is employed in mass-transfer operations to compare convective-diffusion with classical diffusion.

$$h_v = S_h \frac{D_v}{H_{gc}} \tag{1.41}$$

Then, by fitting the data provided by O'Hayre [23] with a correlation coefficient of $R^2 = 0.9869$, the authors derived the following expression for S_h, which exclusively depends on channel geometry. Nevertheless, equation (1.42) is applicable only under the assumption of uniform gas density along the channel.

$$S_h = 0.9247 \cdot \ln\left(\frac{W_{gc}}{H_{gc}}\right) + 2.3787, \text{for} \frac{W_{gc}}{H_{gc}} \in [0.2, 10.0] \tag{1.42}$$

where W_{gc} (m) is the width of the gas channel.

1.2.3.6. Vapour concentration dynamic behavior in the CL and GDL

After examining the aforementioned phenomena, the dynamic behavior of vapour concentration can be given. Equation (1.43a) represents a molar balance of vapour in the CL or the GDL, while (1.43b) aligns with the boundary conditions at the CL/membrane and the GDL/GC interfaces.

$$\varepsilon \frac{\partial}{\partial t}\left([1-s]\, C_v\right) = -\nabla \cdot \boldsymbol{J_{v,dif}} - S_{sorp} - S_{vl} \tag{1.43a}$$

$$\begin{cases} \boldsymbol{J_v^{cl,mem}} = \mathbf{0}, \text{at the ionomer border} \\ \boldsymbol{J_v^{gdl,gc}} = \boldsymbol{J_{v,codi}}, \text{at the GDL/GC border} \end{cases} \tag{1.43b}$$

1.2.4. Vapour transport in the GC

To complete water evolution in the stack, water concentrations in the gas channels must be considered.

1.2.4.1. Vapour convective flow in the GC : $J_{v,conv}$

The flow in the gas channels is convection dominated, and the driving force is the pressure at the flow channel inlets [45]. Within the GC, convection ensures that the gas streams are well mixed, preventing the occurrence of concentration gradients [23]. Then, GC being similar to a classical pipe, $J_{v,conv}$ is simply expressed as (1.44).

$$\boldsymbol{J_{v,conv}} = C_v \boldsymbol{u_g} \tag{1.44}$$

where $\boldsymbol{u_g}$ $(m.s^{-1})$ is the gas mixture velocity. It is assumed, as a hypothesis, that all gases evolve collectively at the same velocity and are not independent. However, $\boldsymbol{u_g}$ is not necessarily fixed. The calculation of the gas mixture velocity is not explicitly detailed in this study, as gas transport in flow-fields adheres to classical fluid mechanic equations and is highly dependent on the chosen geometry for the GC. Various GC configurations, such as interdigitated, serpentine, baffle, or porous flow fields, exist and continue to evolve over time. Each configuration has a significant and distinct impact on stack performance. However, the specifics of the gas mixture velocity calculation are beyond the scope of this study which does not delve into the detailed analysis of each configuration. However, it is essential to keep in mind that the choice of GC geometry plays a crucial role in gas transport within flow-fields.

1.2.4.2. Simplified vapour flows at the inlet and outlet of the GC: $J_{v,in/out}^{gc}$

In real conditions, gas flows at the inlet and outlet of the GC are dependent on the auxiliary system: the nozzles, manifolds, humidifiers, pump and compressor. Other components can also be added depending on the installation that is simulated.

Pukrushpan et al. proposed a very simple model involving these components [41], which has been refined by Xu et al. [98] and Shao and al. [99] while remaining simple. However, this significantly complicates the calculation of the inlet and outlet gas flows. Additionally, modeling the auxiliaries serves solely to determine the error and delay they introduce in the matter supply to the stack, in comparison to the operator's instructions. They are not necessary for modeling the stack's operation. Thus, during the building of a simulation, it is a better to have first a simplified model for these flows to check the accuracy of the matter transport simulated in the stack. The equations mentioned in this study are already numerous, complex, and dependent of one another. Thus, being able to verify the algorithm before using a more complex model is desirable. To this end, simplified equations inspired by Pukrushpan's work [41] for the inlet and outlet water flows at the GC are proposed here.

At the stack inlets, the flows are directly equal to the setpoints normally imposed on the reducer (for the anode) and the compressor (for the cathode). A demonstration of these expressions is provided in A.4.3 and A.4.4. To achieve this, it is simply assumed that the flows must be proportional to the consumed current, with a proportionality coefficient named stoichiometry S_a/S_c. It is considered that the gases are ideal, the channels of the GC are cubic, the incoming gases already have a humidity equal to the desired one Φ_{des}, and the pressure of the incoming gases is equal to the pressure at the GC inlet, with pressure losses being neglected. The equations are shown in (1.45).

At the stack outlets, the flows are not directly controlled by a machine, as it is the case at the inlets. They naturally evacuate the stack due to the pressure difference with the external environment. The outlet flows are therefore expressed based on this pressure difference. For simplicity, they are considered proportional to the latter, with $k_{em,\text{in}}$ the proportional constant. This is valid for compressible, adiabatic, and steady flows. The gases must also be ideal, and pressure losses neglected [41]. These are however strong assumptions. The back-pressure valve is indirectly modeled here by assuming that the outlet pressures of the gas channels directly match the desired pressures P_{des}. Finally, balances similar to those explained in A.4.3 and A.4.4 lead to equations (1.45).

$$\begin{cases} J_{v,\text{in}}^{agc} = \frac{\Phi_{a,\text{des}} P_{sat}}{P_{\text{agc,in}} - \Phi_{a,\text{des}} P_{sat}} \frac{A_{act}}{H_{gc} W_{gc}} \frac{S_a [i_{fc} + i_n]}{2F} \\ J_{v,\text{out}}^{agc} = \frac{\Phi_{agc,out} P_{sat}}{P_{agc,out}} \frac{k_{em,\text{in}}}{H_{gc} W_{gc} M_{agc,out}} \left[P_{agc,out} - P_{a,\text{des}} \right] \\ J_{v,\text{in}}^{cgc} = \frac{\Phi_{c,\text{des}} P_{sat}}{P_{\text{cgc,in}} - \Phi_{c,\text{des}} P_{sat}} \frac{1}{y_{O_2,ext}} \frac{A_{act}}{H_{gc} W_{gc}} \frac{S_c [i_{fc} + i_n]}{4F} \\ J_{v,\text{out}}^{cgc} = \frac{\Phi_{cgc,out} P_{sat}}{P_{cgc,out}} \frac{k_{em,\text{in}}}{H_{gc} W_{gc} M_{cgc,out}} \left[P_{cgc,out} - P_{c,\text{des}} \right] \end{cases} \tag{1.45}$$

where A_{act} (m^2) is the active area, Φ_{des} and P_{des} (Pa) are the desired humidity and pressure fixed by the user, P_{gc} is the GC total pressure, $y_{O_2,ext}$ is the molar fraction of O_2 in dry air, $M_{gc,out}$ is the molar mass of the gas mixture at the GC exit, and $k_{em,\text{in}}$ $(kg.s^{-1}.Pa^{-1})$ is the exhaust manifold inlet orifice constant, usually taken between $[3.5, 8.0] \times 10^{-6}$ $kg.s^{-1}.Pa^{-1}$ [41, 98].

1.2.4.3. Vapour dynamic behavior in the GC

Finally, assuming that no phase change occurs in the GC, the following dynamic behaviour of vapour concentration can be obtained. (1.46a) corresponds to a molar balance of vapour in the GC and (1.46b) matches the boundary conditions at the GDL/GC interface, inlet, and outlet of the GC.

$$\frac{\partial C_v}{\partial t} = -\boldsymbol{\nabla} \cdot \boldsymbol{J_{v,conv}} \tag{1.46a}$$

$$\begin{cases} \boldsymbol{J_v^{gdl,gc}} = \boldsymbol{J_{v,codi}}, \text{at the GDL/GC border} \\ J_v^{in/out,gc} = J_{v,\text{in/out}}^{gc}, \text{at the inlet/outlet of the GC} \end{cases} \tag{1.46b}$$

1.2.5. Hydrogen and oxygen transports

The behaviors of hydrogen and oxygen closely resemble vapor transport in the cell. Consequently, the following governing equations are presented without further explanations.

1.2.5.1. Hydrogen and oxygen flows: $J_{H_2,dif}$, $J_{H_2,codi}$, $J_{H_2,conv}$, $J_{O_2,dif}$, $J_{O_2,codi}$, $J_{O_2,conv}$

Hydrogen diffusive, convective-diffusive, convective flows, and inlet and outlet flows at the AGC are respectively expressed in (1.47).

$$\begin{cases} \boldsymbol{J_{H_2,dif}} = -D_{H_2}^{eff} \boldsymbol{\nabla} C_{H_2} \\ \boldsymbol{J_{H_2,codi}} = h_{H_2} \left[C_{H_2,\text{agc}} - C_{H_2,\text{agdl}}^{\text{inter}} \right] \boldsymbol{\imath} \\ \boldsymbol{J_{H_2,conv}} = C_{H_2} \boldsymbol{u_g} \\ J_{H_2,\text{in}} = \frac{A_{act}}{H_{gc} W_{gc}} \frac{S_a [i_{fc} + i_n]}{2F} \\ J_{H_2,\text{out}} = \frac{P_{\text{agc,out}} - \Phi_{\text{agc,out}} P_{sat}}{P_{\text{agc,out}}} \frac{k_{em,\text{in}}}{H_{gc} W_{gc} M_{agc,out}} \left[P_{agc,out} - P_{a,\text{des}} \right] \end{cases} \tag{1.47}$$

Oxygen diffusive, convective-diffusive, convective flows, and inlet and outlet flows at the CGC are respectively expressed in (1.48).

$$\begin{cases} \boldsymbol{J_{O_2,dif}} = -D_{O_2}^{eff} \boldsymbol{\nabla} C_{O_2} \\ \boldsymbol{J_{O_2,codi}} = h_{O_2} \left[C_{H_2,\text{cgdl}}^{\text{inter}} - C_{O_2,\text{cgc}} \right] \boldsymbol{\imath} \\ \boldsymbol{J_{O_2,conv}} = C_{O_2} \boldsymbol{u_g} \\ J_{O_2,\text{in}} = \frac{A_{act}}{H_{gc} W_{gc}} \frac{S_c [i_{fc} + i_n]}{4F} \\ J_{O_2,\text{out}} = y_{\text{cgc,out}} \frac{P_{\text{cgc,out}} - \Phi_{\text{cgc,out}} P_{sat}}{P_{\text{cgc,out}}} \frac{k_{em,\text{in}}}{H_{gc} W_{gc} M_{cgc,out}} \left[P_{cgc,out} - P_{c,\text{des}} \right] \end{cases} \tag{1.48}$$

1.2.5.2. Hydrogen and oxygen consumption at the interface of the triple points: $S_{H_2,cons}$

Hydrogen and oxygen consumption are respectively expressed as (1.49) and (1.50).

$$S_{H_2,cons} = \begin{cases} -\frac{i_{fc}}{2FH_{cl}}, & \text{in the ACL} \\ 0, & \text{elsewhere} \end{cases} \tag{1.49}$$

$$S_{O_2,cons} = \begin{cases} -\frac{i_{fc}}{4FH_{cl}}, & \text{in the CCL} \\ 0, & \text{elsewhere} \end{cases} \tag{1.50}$$

It is possible to incorporate mathematical terms into the equations (1.49) and (1.50) for accounting crossover effects. The membrane, chosen for its impermeability to gases, aims to prevent direct mixing of hydrogen and oxygen, which is crucial for electricity generation and safety. However, it is not perfectly impermeable, allowing a small gas transfer in both directions. Consequently, a portion of the hydrogen and oxygen, initially designated for participation in the fuel cell mechanism, instead traverse the membrane and react directly, forming water. Thus, a portion of the fuels is lost. This phenomenon is commonly known as crossover, and the equation describing the additional water production due to it is delineated in section 1.2.1.9.

The crossover flows, denoted as $S_{H_2,co}$ and $S_{O_2,co}$, are expressed in units of $mol.m^{-3}.s^{-1}$. It is more relevant to conceptualize them as volume flows since they traverse the membrane via the dispersed CL ionomer within the CL volume. The calculation of these flows classically involves the application of Fick's law across the two interfaces of the membrane [47, 69, 100–103], as illustrated in equations 1.51 and 1.52.

$$S_{H_2,co} = \begin{cases} k_{H_2} \frac{RT_{fc}}{H_{cl}} \nabla C_{H_2}, & \text{in the ACL} \\ 0, & \text{elsewhere} \end{cases} \tag{1.51}$$

$$S_{O_2,co} = \begin{cases} k_{O_2} \frac{RT_{fc}}{H_{cl}} \nabla C_{O_2}, & \text{in the CCL} \\ 0, & \text{elsewhere} \end{cases} \tag{1.52}$$

where k_i ($mol.m^{-1}.s^{-1}.Pa^{-1}$) is the permeability coefficient of molecule i (hydrogen or oxygen) in the membrane, and ∇C_i is the concentration gradient of molecule i at the two ends of the membrane.

An experimental expression for these permeability coefficients was proposed by Weber et al. in 2004 [47, 101, 102], providing the most accurate prediction to date with a coefficient function of both λ and T_{fc}. Kocha et al. conducted another experiment in 2006 [103], but did not account for the variation of λ in k_i. Gas permeability in PEM fuel cells strongly depends on membrane hydration level and temperature, leading to fluctuations in k_i with changes in operating conditions [103]. The Weber proposal is expressed by equations (1.53) and (1.54).

$$k_{H_2} = \begin{cases} \left[0.29 + 2.2 f_v(\lambda)\right] 10^{-14} \exp\left(\frac{E_{act,H_2,v}}{R}\left[\frac{1}{T_{ref}} - \frac{1}{T_{fc}}\right]\right) & if\, \lambda < \lambda_{l,eq} \\ 1.8 \cdot 10^{-14} \exp\left(\frac{E_{act,H_2,l}}{R}\left[\frac{1}{T_{ref}} - \frac{1}{T_{fc}}\right]\right) & if\, \lambda = \lambda_{l,eq} \end{cases} \tag{1.53}$$

$$k_{O_2} = \begin{cases} \left[0.11 + 1.9 f_v(\lambda)\right] 10^{-14} \exp\left(\frac{E_{act,O_2,v}}{R}\left[\frac{1}{T_{ref}} - \frac{1}{T_{fc}}\right]\right) & if\, \lambda < \lambda_{l,eq} \\ 1.2 \cdot 10^{-14} \exp\left(\frac{E_{act,O_2,l}}{R}\left[\frac{1}{T_{ref}} - \frac{1}{T_{fc}}\right]\right) & if\, \lambda = \lambda_{l,eq} \end{cases} \tag{1.54}$$

where $E_{act,H_2,v} = 2.1 \cdot 10^4 J.mol^{-1}$ and $E_{act,O_2,v} = 2.2 \cdot 10^4 J.mol^{-1}$ are the crossover activation energies of hydrogen and oxygen for an under saturated membrane, $E_{act,H_2,l} = 1.8 \cdot 10^4 J.mol^{-1}$ and $E_{act,O_2,l} = 2.0 \cdot 10^4 J.mol^{-1}$ are the crossover activation energies of hydrogen and oxygen for a liquid-equilibrated membrane, $T_{ref} = 303.15K$ is a referenced temperature, and f_v is the water volume fraction of the membrane described in 1.2.1.7.

After hydrogen and oxygen molecules traverse the membrane, their consumption needs to be considered, denoted as $S_{i,wasted}$. Existing equations in the literature simplify this process by assuming instantaneous passage of matter through the membrane, disregarding its thickness, and immediate reaction with its complementary molecule to form water [69]. Under this assumption, the equations can be expressed as (1.55) and (1.56).

$$S_{H_2,wasted} = \begin{cases} -2 \cdot S_{O_2,co}, & \text{in the ACL} \\ 0, & \text{elsewhere} \end{cases} \tag{1.55}$$

$$S_{O_2,wasted} = \begin{cases} -0.5 \cdot S_{H_2,co}, & \text{in the CCL} \\ 0, & \text{elsewhere} \end{cases} \tag{1.56}$$

Finally, the corrected formulations of $S_{i,cons}$, incorporating the short-circuited current density i_{sc}, are expressed in (1.57) and (1.58).

$$S_{H_2,cons} = \begin{cases} -\frac{i_{fc}+i_{sc}}{2FH_{cl}} - \frac{RT_{fc}}{H_{cl}}\left[k_{H_2}\nabla C_{H_2} + 2k_{O_2}\nabla C_{O_2}\right], & \text{in the ACL} \\ 0, & \text{elsewhere} \end{cases} \tag{1.57}$$

$$S_{O_2,cons} = \begin{cases} -\frac{i_{fc}+i_{sc}}{4FH_{cl}} - \frac{RT_{fc}}{H_{cl}}\left[k_{O_2}\nabla C_{O_2} + \frac{k_{H_2}}{2}\nabla C_{H_2}\right], & \text{in the CCL} \\ 0, & \text{elsewhere} \end{cases} \tag{1.58}$$

1.2.5.3. Hydrogen and oxygen concentration dynamic behavior in the CL and GDL

The hydrogen dynamic behaviour is given by the molar balance of H_2 in (1.59a) and the boundary conditions at the CL/membrane, GDL/GC interfaces, and inlet/outlet of the GC in (1.59b).

$$\begin{cases} \varepsilon \frac{\partial}{\partial t}\left([1-s]\, C_{H_2}\right) = -\nabla \cdot \boldsymbol{J_{H_2,dif}} + S_{H_2,cons}, & \text{in the anode} \\ \frac{\partial C_{H_2}}{\partial t} = -\nabla \cdot \boldsymbol{J_{H_2,conv}}, & \text{in the AGC} \end{cases} \tag{1.59a}$$

$$\begin{cases} \boldsymbol{J_{H_2}^{cl,mem}} = \mathbf{0}, & \text{at the CL/membrane border} \\ \boldsymbol{J_{H_2}^{gdl,gc}} = \boldsymbol{J_{H_2,codi}}, & \text{at the GDL/GC border} \\ J_{H_2}^{in/out,gc} = J_{H_2,\text{in/out}}, & \text{at the inlet/outlet of the GC} \end{cases} \tag{1.59b}$$

The oxygen dynamic behaviour is given by the molar balance of O_2 in (1.60a) and the boundary conditions at the CL/membrane, GDL/GC interfaces, and inlet/outlet of the GC in (1.60b).

$$\begin{cases} \varepsilon \frac{\partial}{\partial t}\left([1-s]\, C_{O_2}\right) = -\nabla \cdot \boldsymbol{J_{O_2,dif}} + S_{O_2,cons}, & \text{in the cathode} \\ \frac{\partial C_{O_2}}{\partial t} = -\nabla \cdot \boldsymbol{J_{O_2,conv}}, & \text{in the CGC} \end{cases} \tag{1.60a}$$

$$\begin{cases} \boldsymbol{J_{O_2}^{cl,mem}} = \mathbf{0}, & \text{at the CL/membrane border} \\ \boldsymbol{J_{O_2}^{gdl,gc}} = \boldsymbol{J_{O_2,codi}}, & \text{at the GDL/GC border} \\ J_{O_2}^{in/out,gc} = J_{O_2,\text{in/out}}, & \text{at the inlet/outlet of the GC} \end{cases} \tag{1.60b}$$

1.2.6. Nitrogen transport

For the modeling of nitrogen transport, it is crucial to assume homogeneity of N_2 throughout the stack (CCL, CGDL and CGC). This assumption facilitates the use of binary coefficients for the calculation of oxygen and water flows at the cathode. Consequently, in the following differential equation as depicted in (1.63), the control volume encompasses the cathode electrode and CGC volume. The internal nitrogen flow is disregarded, which is a reasonable assumption as no nitrogen is consumed in this process. Moreover, this study does not address N_2 crossover, as its relevance is confined to specific modeling tasks. For further details, please refer to [104].

Thus, nitrogen evolution fully depends on the inlet and outlet flows at the CGC. Similarly to vapor discussed in section 1.2.4, simplifications of these flows are suggested to obtain preliminary results before incorporating auxiliaries.

1.2.6.1. Simplified nitrogen concentration flows at the inlet and outlet of the CGC

The nitrogen inlet concentration flow in the stack is represented by (1.61), while the outlet concentration flow is denoted by (1.62). Demonstrations are provided in the appendix.

$$W_{N_2,\text{in}} = \frac{1 - y_{O_2,ext}}{y_{O_2,ext}} \frac{A_{act}}{H_{gc} W_{gc}} \frac{S_c \left[i_{fc} + i_n\right]}{4F} \tag{1.61}$$

$$W_{N_2,\text{out}} = \left[1 - y_{O_2,\text{cgc,out}}\right] \frac{P_{\text{cgc,out}} - \Phi_{\text{cgc,out}} P_{sat}}{P_{\text{cgc,out}}} \frac{k_{em,\text{in}}}{H_{gc} W_{gc} M_{cgc,out}} \left[P_{cgc,out} - P_{c,\text{des}}\right] \tag{1.62}$$

where L_{gc} is the cumulated length of the gas channel.

1.2.6.2. Nitrogen concentration dynamic behavior in the cathode

The nitrogen dynamic behaviour in the cathode is expressed as (1.63).

$$\frac{\mathrm{dC_{N_2}}}{\mathrm{dt}} = W_{N_2,\text{in}} - W_{N_2,\text{out}} \tag{1.63}$$

1.3. Voltage physical modelling

In the literature, the current density i_{fc} is typically imposed independently of other variables, with the resulting voltage then being calculated or measured. However, it is important to acknowledge that under extreme conditions, such as severe fuel starvation or intense membrane drying, it becomes impractical to maintain a fixed current density, leading to the stack ceasing operation. Utilizing a model that consistently imposes a fixed current density may yield inaccurate results, including negative voltages. Since this study does not consider such extreme scenarios, it is crucial to work with acceptable values for both operating conditions and current density.

1.3.1. The apparent voltage: U_{cell}

To determine the apparent voltage U_{cell} in a fuel cell, various phenomena must be taken into account. Initially, the equilibrium voltage U_{eq} defines the maximum energy available in the reaction $H_2(g) + \frac{1}{2}O_2(g) \rightarrow H_2O\ (l)$ through thermodynamics. This equation also implicitly contributes to concentration losses, arising from insufficient fuel stored in the CLs due to gas diffusion limitations, which cannot counterbalance excessive fuels demand at high current density. This aspect is elaborated upon in section 1.3.2.

Consequently, multiple voltage losses need consideration. The overpotential η encompasses kinetic losses from the redox reactions, fuel crossover, internal short circuit, and contributes to concentration losses. Kinetic losses serve to accelerate the rate-limiting step from redox reactions, ensuring molecules in the CLs are appropriately directed to triple point areas and decomposed into ions. Voltage losses from fuel crossover and internal short circuits result from membrane imperfections, allowing a portion of fuels and electrons to pass through, translating to an energy loss. This discussion is presented in section 1.3.3.

Finally, both the electrical resistances of protons R_p and electrons R_e counterbalance the equilibrium voltage. These voltage losses originate from the transport of electric charges which experience resistances from the materials in which they move. They result from microscopic collisions between electric charges and materials. The resistances associated with protons, denoted as R_p, are distinguished from those associated with electrons, denoted as R_e, because the charges and materials are different. Indeed, the transport of protons through the membrane and CLs to the triple point areas is much more resistant than the transport of electrons through the GDLs and bipolar plates, which are good electrical conductors. An expression for R_p is provided in section 1.3.5. However, to the best of the authors' knowledge, there is no widely disseminated expression for R_e in the literature. This quantity is generally either neglected or considered as an undetermined parameter that must be calibrated with experimental data from the specific fuel cell under study.

Based on this theory, the following relation (1.64) is obtained for calculating the apparent cell voltage [5, 23, 45, 52]:

$$U_{cell} = U_{eq} - \eta_c - i_{fc}\left[R_p + R_e\right] \tag{1.64}$$

where U_{cell} (V) is the cell voltage, U_{eq} (V) is the equilibrium voltage, η_c (V) is the cathode overpotential, R_p $(\Omega.m^2)$ is the area specific resistance of the protons, and R_e $(\Omega.m^2)$ is the area specific resistance of the electrons.

1.3.2. Equilibrium potential at the cathode U_{eq}

The theoretical maximum energy extractable from chemical reactions is represented by the Gibbs free energy, grounded in thermodynamics. Subsequently, it is reformulated to adopt the expression of a potential, denoted as the equilibrium potential U_{eq} or the Nernst equation, as shown in 1.65. In literature, the convention is to designate the anode potential as zero. As a result, the equilibrium voltage is equivalent to the cathode equilibrium potential [23, 28, 33, 41, 45, 76, 105].

$$U_{eq} = V_{eq}^{c} = E^0 - 8.5\cdot10^{-4}\left[T_{fc} - 298.15\right] + \frac{RT_{fc}}{2F}\left[\ln\left(\frac{RT_{fc}C_{H_2,\text{acl}}}{P_{\text{ref}}}\right) + \frac{1}{2}\ln\left(\frac{RT_{fc}C_{O_2,\text{ccl}}}{P_{\text{ref}}}\right)\right] \tag{1.65}$$

where E^0 (V) is the standard-state reversible voltage taken at $E^0 = 1.229V$, P_{ref} (Pa) is the reference pressure taken at 10^5 Pa, $C_{H_2,\text{acl}}$ and $C_{O_2,\text{ccl}}$ $(mol.m^{-3})$ are the H_2 concentration at the anode catalyst layer and the O_2 concentration at the cathode catalyst layer, respectively. These concentrations should be taken into account at the CLs, where reactions occur and chemical energy is converted [106]. By doing so, U_{eq} contributes to calculating the concentration drop, as any reduction in fuel concentrations in the CLs will consequently decrease the apparent voltage. Further details are discussed in section 1.3.4.

1.3.3. The overpotential at the cathode η_c

The overpotential is a complex quantity that encompasses various voltage drops. All equations describing overpotential currently rely on the Butler-Volmer theory, derived from transition state theory applied to single-electron transfer reactions [107]. However, redox reactions are more complex, and this assumption is simplifying. Consequently, employing the Butler-Volmer theory to model overpotential entails limitations, such as the inability to account for potential effects of electrode flooding or membrane drying on the overpotential. Furthermore, current knowledge about overpotential is restricted, without the existence of widely accepted alternative theories. Consequently, several researchers have proposed modifications to the Butler-Volmer equation to incorporate other phenomena [28, 33, 52]. However, these ideas have been criticized by others [108]. Section 1.3.3.1 explores the Tafel equation, based on the conventional Butler-Volmer theory, while section 1.3.3.2 discusses the proposed modifications to the equation.

1.3.3.1. A fair use of the Butler-Volmer theory

The oxidation reaction of hydrogen at the anode is significantly faster than the reduction reaction of oxygen at the cathode. Therefore, it is common to neglect the overpotential resulting from this chemical reaction at the anode compared to the overpotential at the cathode $\left(i_{0,a} >> i_{0,c}\right)$. Then, applying the Butler-Volmer equation at the cathode for the oxygen reduction reaction leads to equation 1.66 [108].

$$i_{fc} + i_n = i_{0,c}\left(\exp\left(\alpha_c \frac{F}{RT_{fc}}\eta_c\right) - \exp\left(-\beta_c \frac{F}{RT_{fc}}\eta_c\right)\right) \tag{1.66}$$

where i_n $(A.m^{-2})$ is the internal current density, $i_{0,c}^{ref}$ is the exchange current density at the cathode, α_c and β_c are charge-transfer coefficients of the cathode, and R $(J.mol^{-1}.K^{-1})$ is the universal gas constant.

Subsequently, it is generally assumed in the literature that the negative exponential term is negligible [50, 108]. Indeed, in practice, this term is nearly zero for almost the entire range of current density values, except at very low currents where $i \approx i_{0,c}$. Moreover, simplifying this term significantly reduces the complexity of the Butler-Volmer equation, allowing η_c to be easily isolated from the equation and $i_{0,c}$ to be expressed as a function of oxygen concentration, while taking into account the warnings provided by Dickinson et al. [108]. By doing so, the Butler-Volmer theory leads to a simplified equation known as the Tafel equation, expressed in (1.67). This equation references the pioneering work of Swiss chemist Julius Tafel, who derived it from empirical data.

Given the omnipresence of Tafel equation, the original Butler-Volmer equation is not deeply discussed here. It is however important to note that Dickinson et al. [108] have identified a major misuse of the Butler-Volmer equation, which has been widely propagated in the literature, and renamed the Bernardi-Verbrugge formulation. This formulation contains a single concentration-dependence term, utilizing oxygen concentration, which is applied equally between the two processes of oxidation and reduction (each modeled by an exponential), contradicting the essence of the Butler-Volmer equation. This error is concealed in practice by the simplifying assumption of neglecting hydrogen overpotential, but it is crucial not to build a model on the wrong foundation. The authors therefore urge the community to exercise caution in choosing litterature equations.

$$\boxed{i_{fc} + i_n = i_{0,c}^{ref}\left[\frac{C_{O_2,ccl}}{C_{O_2}^{ref}}\right]^{\kappa_c} \exp\left(\frac{F\alpha_c}{RT_{fc}}\eta_c\right)} \tag{1.67}$$

where $i_{0,c}^{ref}$ is the referenced exchange current density at the cathode for a given oxygen concentration $C_{O_2}^{ref}$, $C_{O_2}^{ref}$ $(mol.m^{-3})$ is the reference concentration of oxygen, and κ_c is the overpotential correction exponent.

In equations (1.66) and (1.67), the internal current density i_n is used to consider the fuel crossover in the membrane and the electronic short circuit [5, 109]. It is deeply explained in section 1.3.3.3.

The exchange current density, denoted as $i_{0,c}$, serves to measure the number of chemical reactions occurring at equilibrium within the triple point regions of the CCL, when the fuel cell is not generating current. This quantity is normalized to a current density, as the difference between this value and the imposed current density on the fuel cell provides a measure of the requirement to accelerate the redox reaction and, consequently, the associated kinetic losses. $i_{0,c}$ is at least a function of the oxygen concentration in the CCL. This dependency is explicitly expressed in the Tafel equation provided in (1.67), and further detailed in (1.68). Therefore, $i_{0,c}^{ref}$ corresponds to the exchange current density measured at a reference oxygen concentration $C_{O_2}^{ref}$. In this study, the overpotential correction exponent denoted as κ_c is introduced. Indeed, numerous exponent values can be found in the literature, typically ranging between $[0.25, 4.0]$ [28, 33, 52, 94, 105, 108], but none of these values appears to be dominant. Then, the authors propose considering κ_c as an undetermined parameter which should be estimated for each specific fuel cell stack.

$$i_{0,c} = i_{0,c}^{ref} \left[\frac{C_{O_2,ccl}}{C_{O_2}^{ref}} \right]^{\kappa_c} \tag{1.68}$$

The term $exp\left(\frac{F\alpha_c}{RT_{fc}}\eta_c\right)$ serves as the final component connecting the current density i_{fc} to the overpotential η_c. The parameter α_c, commonly known as the 'charge-transfer coefficient,' represents the proportion of the electrical energy utilized to modify the rate of an electrochemical reaction by altering the activation barrier. Its value is contingent upon the specific reaction and electrode material, but it must fall within the 0–1.0 range. Typically, for most electrochemical reactions, α_c falls within the approximate range of 0.2–0.5. At the oxygen electrode, there is greater variability in the charge-transfer coefficient, ranging from about 0.1–0.5 in most scenarios. In the case of 'symmetric' reactions, α_c is generally considered as 0.5 [5, 23].

Furthermore, it is crucial to incorporate $C_{O_2,ccl}$ in the calculation of η_c since the overpotential manifests in the triple point region [106]. This indirectly contributes to the modeling of concentration losses, as discussed in 1.3.4.

Finally, for improved precision in calculating the model voltage or addressing specific issues such as electrode flooding, it is essential to move away from the use of the Butler-Volmer equation. Instead, adopting a rigorous multi-step mechanism-based model is crucial. However, further extensive research is needed before effectively implementing such a model [108]. The addition of terms to the Tafel equation is a temporary proposition embraced by many researchers while awaiting more advanced models. These propositions are detailed in Section 1.3.3.2. Nonetheless, Dickinson et al. [108] caution against the uselessness of such an approach. Since the Butler-Volmer theory is inherently simple and reductionist, there is no reason to believe that such

manipulations can be effective. There is a risk of rendering the model more unstable and complex without achieving any significant gains.

1.3.3.2. Manipulations on the Butler-Volmer equation

There is a need to consider temperature variations in the CCL [28, 33, 110], membrane drying [28], CCL flooding [33, 52, 99, 110] and electrochemical surface area reduction over time [106, 111–113] when calculating overpotential. Since these requirements are not addressed by a robust theory, empirical coefficients have been suggested by the community to modify the Tafel equation derived from the simple Butler-Volmer theory. Several of these proposals have been synthesized in (1.69). Each of these coefficients can be used independently, depending on the desired application.

$$\begin{cases} i_{fc} + i_n = i_{0,c} \exp\left(\frac{F\alpha_c}{RT_{fc}}\eta_c\right) \\ i_{0,c} = i_{0,353}^{ref} a_+^{1-2\alpha_c} \left[1 - s_{ccl}\right]^{1.5} r_f(t) \exp\left(\frac{E_{act}}{R}\left[\frac{1}{T_{ref}} - \frac{1}{T_{fc}}\right]\right) \left[\frac{C_{O_2,ccl}}{C_{O_2}^{ref}}\right]^{\kappa_c} \\ r_f(t) = ECSA(t) \cdot L_{Pt} \\ a_+ = \frac{[\lambda_{ccl}+1] - \sqrt{[\lambda_{ccl}+1]^2 - 4\lambda_{ccl}\left[1-\frac{1}{K_e}\right]}}{2\left[1-\frac{1}{K_e}\right]} \\ K_e = K_e^0 \exp\left(-\frac{\Delta H^0}{R}\left[\frac{1}{T_{fc}} - \frac{1}{298}\right]\right) \end{cases} \tag{1.69}$$

where $i_{0,353}^{ref}$ $(A.m^{-2})$ is the referenced exchange current density at the cathode for a given oxygen concentration $C_{O_2}^{ref}$, a humidified membrane, a dry electrode, an initial electrode roughness factor and at $353.15K$. r_f $(m_{Pt}^2.m^{-2})$ is the electrode roughness factor, representing the ratio of the active platinum surface area to the flat surface area of the electrode. This active platinum surface is non-planar, defined in three dimensions as the sum of surfaces where redox reactions are accelerated by the catalyst within the electrode's pores. r_f is on the order of a hundred [112] and is commonly decomposed to reveal the electrochemical surface area ($ECSA$ in $cm_{Pt}^2.mg_{Pt}^{-1}$), a more practical quantity widely used in the literature. ECSA accounts for the active surface area surrounding a mass of platinum, facilitating the development of models for the evolution of this active surface. Its value is on the order of a hundred $cm_{Pt}^2.mg_{Pt}^{-1}$ for a PEMFC [112]. L_{Pt} $(mg_{Pt}.cm^{-2})$ corresponds to the initial platinum loading of the electrode, a fixed quantity over time, typically around 0.5 $mg_{Pt}.cm^{-2}$ [112]. Then, a_+ is the activity of solvated protons, E_{act} $(J.mol^{-1})$ is the activation energy term, T_{ref} (K) is the referenced temperature taken at 353.15 K, K_e is the acid-base equilibrium constant, K_e^0 is the standard acid-base equilibrium constant, and ΔH^0 $(J.mol^{-1})$ is the standard enthalpy of reaction.

The solvated protons' activity, denoted as a_+, serves as a metric to examine the impact of a notably dry membrane on the exchange current density. This analysis is carried out for analysing start operation and current ignition [28]. Additionally, as

illustrated in figure 1.8, when $T = 353K$ and $\lambda > 1$, the value of a_+ is approximately 1. Consequently, it exerts negligible influence on the equation for a hydrated membrane.

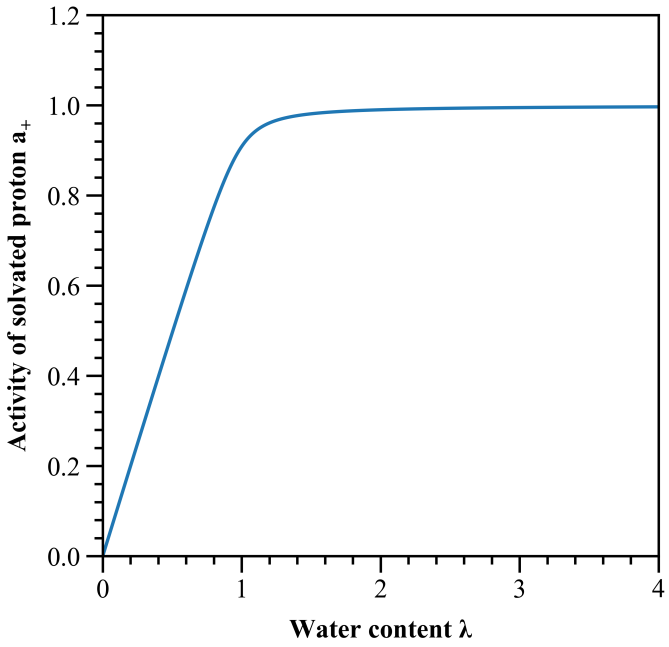

Figure 1.8. – Plot of the activity of the solvated protons function of the water content

The purpose of $(1 - s_{ccl})^{1.5}$ is to account for the impact of flooding on the cell voltage by examining the covering effect of liquid water on the active area of the catalyst. When the liquid saturation at the CCL increases, the active area of the catalyst becomes covered by liquid water, leading to a drop in cell voltage. Several formulations have been proposed for this coefficient [33, 52, 99, 110], yet none has been experimentally validated.

The purpose of the electrode roughness factor r_f is to account for the diminishing active surface area of platinum over time within the electrode on the cell voltage [106, 111–113]. Several degradation phenomena contribute to this decrease in the platinum's active surface, such as the oxidation of the platinum surface. Various degradation models available in the literature could be employed to quantify the evolution of ECSA over time [114–116]. The details of these models, however, are not covered in this work and merit a specific discussion.

Another dependency of $i_{0,c}$ is highlighted here: temperature [28, 33, 110]. Similar to the approach taken for the concentration dependency, a referenced constant $i^{ref}_{0,353}$ is identified, representing the exchange current density measured at a reference oxygen concentration $C^{ref}_{O_2}$ and at a specified temperature, typically set at 353 K. The temperature dependence is then expressed through the coefficient $\exp\left(\frac{E_{act}}{R}\left[\frac{1}{T_{ref}} - \frac{1}{T_{fc}}\right]\right)$.

Finally, it is crucial to highlight that η_c is associated with indeterminate parameters, $i^{ref}_{0,353}$ and κ_c, due to the limitations of current knowledge. These parameters have to be

calibrated based on experimental data. The utilization of predefined values for them is not feasible, given their dependence on the particular fuel cell being employed.

1.3.3.3. Internal current density: crossover and short circuit

In the fuel cell, a small amount of matter naturally permeates the membrane, even though it is designed to be impermeable. This dissipation of chemical energy within the stack results in a voltage drop. This matter can be either oxygen or hydrogen, termed as crossover, or in the case of electrons, it is identified as an electronic short circuit. Together, these two phenomena contribute to the internal current density, as formulated in 1.70.

$$i_n = i_{co,H_2} + i_{co,O_2} + i_{sc} \tag{1.70}$$

where $i_{co,i}$ $(A.m^{-2})$ is the internal crossover current density of the molecule i (hydrogen or oxygen) and i_{sc} $(A.m^{-2})$ is the internal short circuit current density.

During a crossover, the matter which was expected to react following the fuel cell mechanism instead permeates the membrane and interacts with its complementary molecule by direct contact. Consequently, both the matter and the electrons it carries are lost. The volume flow of matter through the membrane during this crossover, denoted as $S_{i,co}$ and discussed in section 1.2.5.2, can be correlated with a flow of lost electrons for the calculation of i_{co}. This relationship is expressed in (1.71).

$$\begin{cases} i_{co,H_2} = 2FH_{cl}S_{H_2,co} = 2Fk_{H_2}RT_{fc}\nabla C_{H_2} \\ i_{co,O_2} = 4FH_{cl}S_{O_2,co} = 4Fk_{O_2}RT_{fc}\nabla C_{O_2} \end{cases} \tag{1.71}$$

The way $i_{co,i}$ is introduced into the equation for η_c in (1.67) needs clarification. As crossover corresponds to a matter loss in the cell, it is expressed in the gas transport equations. Thus, it is already indirectly included in $C_{O_2,ccl}$. However, the calculation of the equilibrium potential U_{eq} also utilizes the value of $C_{O_2,ccl}$. Therefore, the theoretically maximum energy extractable by redox reactions is biased by the crossover. To account for this energy loss, it should be necessary to add the value of $C_{O_2,ccl}$ to U_{eq} along with the oxygen concentration lost due to crossover. Another method widely employed in the literature and proposed in (1.67), considered equivalent and more practical, involves adding $i_{co,i}$ to i_{fc} in the calculation of η_c. This means that additional fictitious current is required to compensate for the crossover loss, thereby increasing the overpotential value. However, the equivalence of these two methods is questionable. Transferring information that should be contained in U_{eq} to η_c is not straightforward. Future research should be conducted to better incorporate crossover effects in voltage calculations.

During an electronic short circuit across the membrane, the reaction between oxygen and hydrogen occurs as expected on both sides of the membrane. However, the electrons released by hydrogen do not traverse the external circuit. Consequently, they do not contribute to i_{fc} and manage to pass through the membrane, even though it is designed to resist their passage. There is limited literature on this topic. The equation

presented here, standardized since the work of Giner-Sanz et al. [100] for broader applicability and expressed as (1.72), includes several assumptions that significantly constrain its utility. This experimental study was conducted using a single commercial Nafion®117 membrane and employed linear voltammetry. The measurements were carried out under constant temperature and relative humidity of the incoming gases. The pressures at the anode and cathode were the only variables and were adjusted independently, without the necessity for their equality. Consequently, it was assumed that pressure is the crucial variable for calculating i_{sc}, although, in reality, temperature should also be considered. Additionally, pressure variations are relatively small, ranging between 1.12–1.45 bar at the cathode and only between 1.01–1.06 bar at the anode. Given these significant limitations, further extensive experimental tests are necessary to refine these results [100].

$$\begin{cases} i_{sc} = \frac{U_{cell}}{r_{sc}} \\ r_{sc} = 1.79 \cdot 10^{-2} \left[\frac{P_{agc}}{101325}\right]^{-9.63} \left[\frac{P_{cgc}}{101325}\right]^{0.38} \end{cases} \tag{1.72}$$

where r_{sc} ($\Omega.m^2$) is the area specific short circuit resistance.

Giner-Sanz et al. proposed a physical explanation for the correlation between the inlet pressures of the stack and the internal electronic short circuit. Elevating the gas pressure in a PEMFC can induce two opposing effects on the short-circuit resistance. On one hand, it may increase the effective interfacial contact area between layers, thereby reducing resistance. On the other hand, it can lead to porosity and morphological changes, which may increase or decrease resistance depending on the specific characteristics of the PEMFC. Whether an increase in pressure will result in heightened or diminished resistance depends on the relative significance of these two effects. Nonetheless, further research is needed to validate this hypothesis [100].

Next, the authors provide an explanation of how electronic short circuits affect voltage. As the redox reactions proceed as normal, oxygen molecules that receive electrons traversing the membrane are still attracted to the triple point regions to form ions. Thus, the electronic short circuit phenomenon leads to overpotential, yet does not contribute to i_{fc}. Therefore, it is acceptable to calculate overpotential by adding i_{sc} to i_{fc}.

It is noteworthy, as mentioned by O'Hayre et al. [23], and in contrast to the proposition by Dicks et al. [5], that adding i_n to i_{fc} should not be done when calculating electronic and proton resistances. These resistances are only associated with the external current density and do not encompass internal losses.

Finally, the internal current density is weak, approximately 0.01–0.05 $A \cdot cm^{-2}$. Under normal working conditions, it is highly negligible. However, at low current density, its impact becomes significant. It is responsible for the reduced value of the open circuit voltage of fuel cells, which is approximately 0.95 V, whereas the Nernst potential is around 1.2 V. Therefore, accurate modeling of these losses is crucial for developing PEMFC models that faithfully replicate the experimental behavior of PEMFCs operating at low current densities.

1.3.4. Concentration losses

Under high loads or suboptimal operating conditions, the concentrations of O_2 and H_2 within the CLs may significantly decrease, resulting in a voltage loss. Indeed, these are the fuel concentrations within the CLs that mainly influence the voltage in the cell, as reflected in the mathematical expression for U_{cell}. Various factors could contribute to this phenomenon, commonly known as concentration loss.

Diffusion between the GC and the CL may result in concentration losses. While effective control of the auxiliary system can stabilize fuel concentrations in the GC, an increase in fuel consumption at the CL inherent to the rise in current density, diminishes fuel concentration at the CL. Indeed, achieving matter equilibrium requires fuel supply to equal consumption. As the main mechanism of matter transport in the MEA is diffusion, and with concentrations in the GCs stabilized, enhancing the supply flow necessitates reducing fuel concentrations in the CLs. The extent of this concentration loss depends on the diffusion characteristics of the stack, load, and operating conditions [23].

Then, across the width of the stack, inhomogeneities can lead to a partial concentration drop near the stack outlet. While diffusion alone may effectively fill the initial active sites near the GC inlets, it may be insufficient for those located in proximity to the outlets. This is because, as the gas mixture traverses the channels of the bipolar plates, it becomes depleted in fuel, consequently diminishing the diffusion capabilities of fuels within the stack. Given that the dimensions across the width are significantly larger than those along the depth, lateral diffusion alone may prove insufficient to compensate for this shortfall [23].

Additionally, the crossover of N_2 through the membrane may result in a loss of H_2 concentration, as its accumulation leads to a reduction in the partial pressure of H_2 in the gas mixture, at a constant total pressure in the GC. However, this challenge can be addressed by strategically employing an ejector at the anode outlet, which expels gases when the presence of N_2 is substantial.

Furthermore, in the absence of an effective drainage system, the accumulation of liquid water can impede oxygen flow to the catalyst sites, leading to a loss of concentration. Under fixed operating conditions, it is common for this concentration loss to occur at lower current densities than those required to saturate the diffusion capabilities of the fuel cell in the absence of liquid water. Hence, the occurrence of liquid water is a critical point for concentration loss.

To account for all these phenomena, the following expression (1.73) [5, 23, 41, 105, 117, 118] is mainly used in the literature as another voltage loss to add in (1.64).

$$\Delta V_{conc} = \frac{RT}{2F} ln\left(\frac{i_{lim}}{i_{lim} - i_{fc}}\right) \tag{1.73}$$

where i_{lim} $(A.m^{-2})$ is the limiting current density. However, (1.73) represents a simplified approach to concentration losses. It proves valuable solely for black box and equivalent electrical models where concentrations at the CLs remain inaccessible.

Additionally, a significant drawback is its dependence on experimental data. The value of i_{lim} varies with stack technology and operating conditions, and no universal expressions exist to define it. Consequently, it lacks the precision needed to predict concentration losses accurately under changing operating conditions, imposing limitations on its applicability.

Nevertheless, when PEMFC is spatially modeled, some of the information regarding concentration losses already exists. Indeed, it is embedded in the fuel concentrations at the CLs. This is why $C_{O_2,ccl}$ is used in both the equilibrium potential U_{eq} (see 1.3.2) and the overpotential η_c (see 1.3.3) [106]. These two equations contribute to representing the concentration drop in the voltage calculation, albeit indirectly. The modeling of mass transport directly represents this phenomenon. However, current models do not satisfactorily simulate the impact of liquid water on fuel transport to triple point areas. Therefore, it is still necessary to use (1.73) to fully consider the concentration drop, although improvements in models should lead to its elimination.

1.3.5. Proton conductive resistance

1.3.5.1. Proton conductivity of the membrane: σ_m

The proton conductivity, denoted by σ, is commonly defined as shown in (1.74).

$$\frac{1}{R_p} \triangleq \sigma \frac{dS}{dx} \tag{1.74}$$

A confusing convention exists in the literature on PEMFC. The term "resistance" (R_p) is intended to represent the area-specific resistance (r_p) in units of $\Omega.m^2$. Theoretically, we should have $r_p = R_p dS$. However, in the litterature, the resistance is referred to as the area-specific resistance, and the symbol R_p is still used, leading to the statement "$r_p = R_p$". Consequently, due to this ambiguous convention, the authors adopt the following definition for the local proton conductivity (see equation (1.75)).

$$\frac{1}{R_p} = \frac{\sigma}{dx} \tag{1.75}$$

Then, to determine the resistance R_p, Springer et al. experimentally derived an expression for proton conductivity in the membrane σ_m in 1991 [50]. This expression has since become widely adopted in the literature [28, 33, 45, 52, 54, 55, 62, 66, 76], and is represented by (1.76).

$$\sigma_m = \begin{cases} [0.5139\lambda - 0.326] \exp\left(1268 \left[\frac{1}{303.15} - \frac{1}{T_{fc}}\right]\right), & \text{for } \lambda \geq 1 \\ 0.1879 \exp\left(1268 \left[\frac{1}{303.15} - \frac{1}{T_{fc}}\right]\right), & \text{for } \lambda < 1 \end{cases} \tag{1.76}$$

The linear term $0.5139\lambda - 0.326$ is derived from measurements at 30°C, while the exponential component enables the extension to other temperature ranges. An ac-

tivation energy, $E_{\text{act}} = 10542\ J.mol^{-1}$, was measured and assumed to be independent of λ. Subsequently, the coefficient 1268 was computed using the equation $1268 = \frac{E_{act}}{R} = \frac{10542}{8.314}$. Additionally, when the quantity of water molecules per charge site is below one ($\lambda < 1$), the conductivity is presumed to remain constant. The graphical representation of this function is illustrated in figure 1.9.

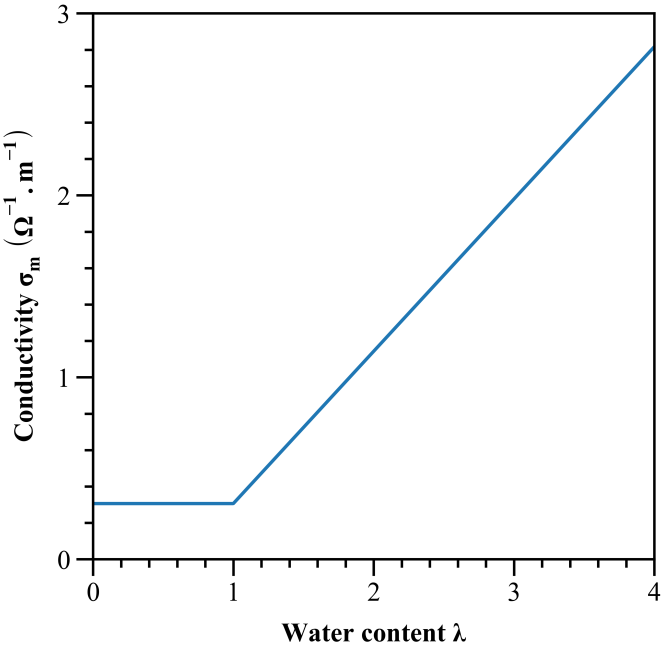

Figure 1.9. – Shape of the conductivity σ_m function of the water content λ at $T_{fc} = 343.15K$

In certain papers, there was an innacurate modification of this expression when $\lambda < 1$, employing a linear decrease with λ as illustrated in (1.77) [66]. The aim was to "avoid negative conductivity". While the intention was to rectify the expression for σ_m, which exhibits negative values when the expression for $\lambda \geq 1$ is applied to $\lambda < 1$, this approach is flawed. The constant term in (1.76) is mentioned in Springer's original work [50], albeit only in the text and not in the equation, potentially causing confusion. Moreover, while it is reasonable to expect conductivity to decrease with λ for a 117 Nafion®membrane, attributing $\sigma_m = 0\ \Omega^{-1}.m^{-1}$ when $\lambda = 0$ seems excessive, suggesting a perfect insulator under feasible conditions.

$$\sigma_m = 0.1879\lambda \exp\left(1268\left[\frac{1}{303.15} - \frac{1}{T_{fc}}\right]\right), \text{for } \lambda < 1 \tag{1.77}$$

The expression (1.76) is limited in its applicability to modern models due to its creation with outdated membranes [56]. While recent models do exist [57], they have not gained widespread acceptance in the literature due to various shortcomings. These include reliance on outdated data, lack of accessibility to the data used, or restriction of the equation's applicability to single-phase systems without liquid water.

Consequently, the community expects a robust, well-documented study for σ_m with minimal limitations across a broad range of membranes.

Moreover, (1.76) has the disadvantage of being constructed in two parts, resulting in a discontinuous derivative. This characteristic could potentially introduce parasitic oscillations in models, especially when the discontinuity occurs around $\lambda \approx 1$. To circumvent this issue, it is possible to opt for the expression proposed by Ramousse et al. [119], as given by (1.78). However, it is worth noting that this expression relies on outdated and hardly accessible data. Additionally, it yields $\sigma_m = 0\ \Omega^{-1}.m^{-1}$ when $\lambda = 0$. A comparative analysis of the Springer and Ramousse expressions is illustrated in Figure 1.10.

$$\begin{cases} \sigma_m = \left[0.0013\lambda^3 + 0.0298\lambda^2 + 0.2658\lambda\right] \exp\left(E_A\left[\frac{1}{353} - \frac{1}{T_{fc}}\right]\right) \\ E_A = 2640\exp\left(-0.6\lambda\right) + 1183 \end{cases} \tag{1.78}$$

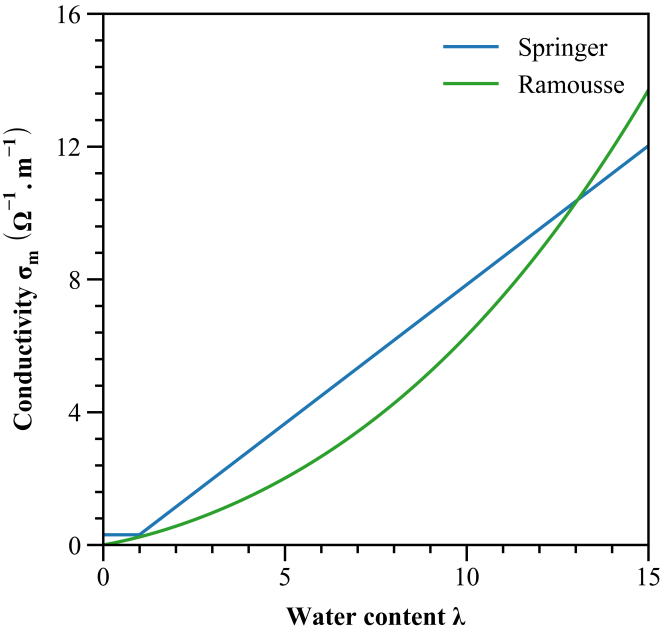

Figure 1.10. – Comparison between Springer and Ramousse expressions for the conductivity at $T_{fc} = 343.15K$

1.3.5.2. Proton conductivity resistance: R_p

The proton conductivity resistance R_p encompasses both the proton resistance within the membrane and the proton resistance within the ionomer of the CCL. The proton resistance within the ionomer of the ACL is neglected because the hydrogen oxidation reaction is fast, and gas diffusion resistances for pure H2 are minor. As a result, the reaction current occurs near the membrane, establishing a short route for proton transport and minimizing voltage loss at the anode [120].

Springer's relationship characterizes the conductivity in the membrane but does not address the CCL ionomer's conductivity. For this purpose, previous authors assumed that the ionomer within the CCL exhibits a conductivity equivalent to that of the membrane, but adjusted by a factor $\frac{\varepsilon_{mc}}{\tau}$ to account for both the dispersion of the ionomer within the CCL (represented by ε_{mc}) and its tortuosity (denoted by τ) [52, 120, 121]. In this context, tortuosity is represented using a different form than the one introduced in section 1.2.3.2: ε_{mc}^{τ}. The authors did not find reasons for this choice, and it remains unclear whether substituting $\frac{\varepsilon_{mc}}{\tau}$ with ε_{mc}^{τ} produces acceptable results. This aspect will require further clarification in future research. Hence, the following equation (1.79) for R_p is proposed, using ε_{mc}^{τ} proposition to remain coherent with what was proposed section 1.2.3.2.

$$R_p = R_{mem} + R_{ccl} = \int_{mem} \frac{dx}{\sigma_m} + \int_{ccl} \frac{dx}{\varepsilon_{mc}^{\tau}\sigma_m} \tag{1.79}$$

1.4. Summary of the developed physical model

This chapter attempted to synthesise and document the matter transport and voltage polarisation governing laws proposed in the literature. New laws, being the combination of several ideas presented in the literature, have also been presented. Certain expressions were discussed in detail, as they were more representative of the physics phenomena at stake. For brevity, tables 1.5, 1.6, and 1.7 compile the partial differential equations and spotlighted matter transport expressions. Tables 1.8 and 1.9 compile the spotlight flow coefficients, while table 1.10 compile the spotlighted voltage polarization expressions. Finally, certain perspectives are discussed in this last section.

From this chapter, it is noted that more investigations are needed to model more clearly and precisely the processes at stake. In particular, explorations should be undertaken to improve the water sorption at the triple points in a biphasic state, the matter sorption at the GDL/GC interface, and the flooding impact on the voltage. Better modelling of these processes requires more targeted experimental investigation at both the material and cell levels.

The values of involved parameters are determinative for model performance. As shown in tables A.2 and A.3, different parameters are selected and used in both mater transport and voltage polarisation models. The unclarified selection and use conditions of these parameters could lead to poor model performance, and even model invalidity. In addition, most of the available experimental data dedicated to model identification in the literature are outdated. The data were mainly extracted from experiments at the beginning of the 1990s. When more recent expressions are given, they are often based on outdated experimental or hardly accessible data, or usable only with strong limitations. Thus, a strong well documented study with few limitations over a large brand of fuel cells must be conducted to update the electro-osmotic drag, equilibrium water content, capillary pressure, and protonic conductivity expressions. The components have evolved during the last years and the modern measurement protocols have become more precise [56]. It is therefore highly necessary to update the database dedicated to model parameter identification. Overall, the limitations of the identified model parameters should be well noted in the model development and use stages.

However, the authors recognise that doing these precise experimentations is very challenging. This explains why the equations in the literature are not unified, as they were done by different teams on different stacks and under different experimental conditions. It is therefore difficult to separate equations that model the same physical phenomenon. It also remains to be demonstrated that these equations from different experimental conditions remain valid in combination in a global model.

The development of both the matter and voltage polarisation models involves multiscale physicochemical phenomena. The global operating conditions can only be controlled and assigned at the macroscopic level. However, the matter transport and electrochemical processes are concerned at microscale to mesoscale. Most existing models were developed without considering the link between the different scales. For

instance, processes at the microscale to mesoscale are often concerned with modelling the mass transport along the MEA and GDL. The corresponding models were thus often built using the data from ex-situ characterisations without considering the impacts of dynamic macroscopic operating parameters. It is questionable that the developed model can still conserve the performance when the multiscale interactions must be considered, which is the condition in practice. Thus, to achieve more reliable models, experiments and model development must be undertaken with multiscale characterisations and analysis. In these experiments, it is often necessary to combine macroscopic in-situ characterisations at the stack/system level and ex-situ microscopic characterisations at the component/cell level. Moreover, the in-situ and operando characterisation techniques are promising tools to gather the relevant microscopic data during operation [122].

As discussed in this chapter, the matter transport models, developed based on different theories, are governed by partial differential equations (PDEs) based on the Navier-Stokes equations. It is mainly the conservation equations which were used, as most flows are Fick-like ones [123]. However, for more complex models that consider multidimensional space (from 2D to 3D) or that consider convective flows within the GDL and CL, it is necessary to add the Navier-Stokes momentum balance equations to obtain a solvable model. These PDEs, in most cases, can be solved only by numerical simulations [124]. The high computation complexity renders it difficult to upscale the developed models in terms of space and time. In addition, the PDEs governed models are naturally not able to satisfy the requirements of certain model applications. For instance, inferring material properties must solve inverse problems, that is, calculating model parameters from online measured data. The inverse problems of PDEs and molecular simulations are prohibitively expensive and require complex formulations, and new algorithms [125]. Moreover, the models represented by PDEs cannot handle the noisy boundary data [126]. This results in the development of reduced-order modelling (ROM) that seeks to build low-dimensional models for efficient solutions with noisy boundary data [127]. Particularly, recent studies have shown that machine learning can be adopted as an efficient ROM tool and provide robust and efficient model resolutions [128].

The reviewed matter transport and voltage polarisation models are essential for optimisation of cell design, materials preparation, and operating conditions. It should be noted that different uses of the models recall different requirements for model order reduction, simplification, and formulation [129]. Nowadays, the analysis and optimisation of high-power fuel cell stacks/systems and the prediction of performance degradation has become increasingly important for fuel cell large deployment. In these large spatial-tempo scale applications, how to maintain the high-fidelity model performance without losing the model efficiency remains a challenging issue [130].

To proceed further, a one-dimensional dynamic two-phases model is built and discussed in the following chapters. It is an interesting application to observe the deeper simplifications that were made to adapt the equations of this chapter for a control-command use.

Dynamical models	Matter flow expressions
Dissolved water in the membrane	
$\begin{cases} \frac{\rho_{\text{mem}}}{M_{\text{eq}}} \frac{\partial \lambda_{\text{mem}}}{\partial t} = -\boldsymbol{\nabla} \cdot \boldsymbol{J_{mem}}, \text{in the bulk membrane} \\ \frac{\rho_{mem} \varepsilon_{mc}}{M_{eq}} \frac{\partial \lambda_{cl}}{\partial t} = -\boldsymbol{\nabla} \cdot \boldsymbol{J_{mem}} + S_{sorp} + S_{prod}, \text{in the CL} \end{cases}$ (1.23a) $\boldsymbol{J_{mem}^{cl,mem}} = \boldsymbol{0}$, at the ionomer border (1.23b)	$S_{\text{prod}} = \begin{cases} 2k_{O_2} \frac{RT_{fc}}{H_{cl}} \nabla C_{O_2}, & \text{in the ACL} \\ \frac{i_{fc}+i_{sc}}{2FH_{cl}} + k_{H_2} \frac{RT_{fc}}{H_{cl}} \nabla C_{H_2}, & \text{in the CCL} \\ 0, & \text{elsewhere} \end{cases}$ (1.22) $S_{sorp} = \gamma_{sorp} \frac{\rho_{\text{mem}}}{M_{\text{eq}}} \left[\lambda_{\text{eq}} - \lambda\right]$ (1.18) $\boldsymbol{J_{mem}} = \frac{2.5}{22} \frac{i_{fc}}{F} \lambda \, \boldsymbol{\imath} - \frac{\rho_{mem}}{M_{eq}} D(\lambda) \boldsymbol{\nabla \lambda}$ (1.3)
Liquid water in the GDL and the CL	
$\rho_{H_2O} \varepsilon \frac{\partial \mathrm{s}}{\partial t} = -\boldsymbol{\nabla} \cdot \boldsymbol{J_{l,cap}} + M_{H_2O} S_{vl}$ (1.33a) $\begin{cases} \boldsymbol{J_l^{cl,mem}} = \boldsymbol{0}, \text{at the ionomer border} \\ \mathrm{s} = 0, \text{at the GDL/GC border} \end{cases}$ (1.33b)	$S_{vl} = \begin{cases} \gamma_{\text{cond}} \varepsilon \left[1 - \mathrm{s}\right] x_v \left[C_v - C_{\text{v,sat}}\right], & \text{if } C_v > C_{\text{v,sat}} \\ -\gamma_{\text{evap}} \varepsilon \mathrm{s} \frac{\rho_{H_2O}}{M_{H_2O}} RT_{fc} \left[C_{\text{v,sat}} - C_v\right], & \text{if } C_v \leq C_{\text{v,sat}} \end{cases}$ (1.32) $\boldsymbol{J_{l,cap}} = -\sigma \frac{K_0}{\nu_l} \left|\cos(\theta_c)\right| \sqrt{\frac{\varepsilon}{K_0}} \mathrm{s}^{\mathrm{e}} \left[1.417 - 4.24\mathrm{s} + 3.789\mathrm{s}^2\right] \boldsymbol{\nabla} \mathrm{s}$ (1.25)
Vapour in the GDL and the CL	
$\varepsilon \frac{\partial}{\partial t} \left(\left[1 - \mathrm{s}\right] C_v\right) = -\boldsymbol{\nabla} \cdot \boldsymbol{J_{v,dif}} - S_{sorp} - S_{vl}$ (1.43a) $\begin{cases} \boldsymbol{J_v^{cl,mem}} = \boldsymbol{0}, \text{at the ionomer border} \\ \boldsymbol{J_v^{gdl,gc}} = \boldsymbol{J_{v,codi}}, \text{at the GDL/GC border} \end{cases}$ (1.43b)	$\boldsymbol{J_{v,dif}} = -D_v^{eff} \boldsymbol{\nabla C_v}$ (1.34) $\boldsymbol{J_{v,codi}} = \pm h_v \left[C_{v,gc} - C_{v,gdl}^{\text{inter}}\right] \boldsymbol{\imath}$ (1.40)

Table 1.5. – Synthesis of the partial differential equations and the spotlighted matter transport expressions (1/3)

Dynamical models	Matter flow expressions
Vapour in the GC	
$\frac{\partial C_v}{\partial t} = -\boldsymbol{\nabla}\cdot\boldsymbol{J_{v,conv}}$ (1.46a)	$\boldsymbol{J_{v,conv}} = C_v\boldsymbol{u_g}$ (1.44)
	$J^{agc}_{v,\text{in}} = \frac{\Phi_{a,\text{des}}P_{sat}}{P_{\text{agc,in}}-\Phi_{a,\text{des}}P_{sat}}\frac{A_{act}}{H_{gc}W_{gc}}\frac{S_a[i_{fc}+i_n]}{2F}$ (1.45)
	$J^{agc}_{v,\text{out}} = \frac{\Phi_{agc,out}P_{sat}}{P_{agc,out}}\frac{k_{em,\text{in}}}{H_{gc}W_{gc}M_{agc,out}}\left[P_{agc,out}-P_{a,\text{des}}\right]$ (1.45)
	$J^{cgc}_{v,\text{in}} = \frac{\Phi_{c,\text{des}}P_{sat}}{P_{\text{cgc,in}}-\Phi_{c,\text{des}}P_{sat}}\frac{1}{y_{O_2,ext}}\frac{A_{act}}{H_{gc}W_{gc}}\frac{S_c[i_{fc}+i_n]}{4F}$ (1.45)
$\begin{cases}\boldsymbol{J^{gdl,gc}_v} = \boldsymbol{J_{v,codi}}, \text{at the GDL/GC border}\\ J^{in/out,gc}_v = J^{gc}_{v,\text{in/out}}, \text{at the inlet/outlet of the GC}\end{cases}$ (1.46b)	$J^{cgc}_{v,\text{out}} = \frac{\Phi_{cgc,out}P_{sat}}{P_{cgc,out}}\frac{k_{em,\text{in}}}{H_{gc}W_{gc}M_{cgc,out}}\left[P_{cgc,out}-P_{c,\text{des}}\right]$ (1.45)
Hydrogen in the GDL and the CL	
$\varepsilon\frac{\partial}{\partial t}\left([1-\mathrm{s}]\,C_{H_2}\right) = -\boldsymbol{\nabla}\cdot\boldsymbol{J_{H_2,dif}} + S_{H_2,cons}$ (1.59a)	$S_{H_2,cons} = \begin{cases}-\frac{i_{fc}+i_{sc}}{2FH_{cl}} - \frac{RT_{fc}}{H_{cl}}\left[k_{H_2}\nabla C_{H_2} + 2k_{O_2}\nabla C_{O_2}\right], \text{ACL}\\ 0, \text{elsewhere}\end{cases}$ (1.57)
$\begin{cases}\boldsymbol{J^{cl,mem}_{H_2}} = \boldsymbol{0}, \text{at the CL/membrane border}\\ \boldsymbol{J^{gdl,gc}_{H_2}} = \boldsymbol{J_{H_2,codi}}, \text{at the GDL/GC border}\end{cases}$ (1.59b)	$\boldsymbol{J_{H_2,dif}} = -D^{eff}_{H_2}\boldsymbol{\nabla}C_{H_2}$ (1.47)
	$\boldsymbol{J_{H_2,codi}} = h_{H_2}\left[C_{H_2,\text{agc}} - C^{\text{inter}}_{H_2,\text{cgdl}}\right]\boldsymbol{\imath}$ (1.47)
Hydrogen in the GC	
$\frac{\partial C_{H_2}}{\partial t} = -\boldsymbol{\nabla}\cdot\boldsymbol{J_{H_2,conv}}$ (1.59a)	$\boldsymbol{J_{H_2,conv}} = C_{H_2}\boldsymbol{u_g}$ (1.47)
	$J_{H_2,\text{in}} = \frac{A_{act}}{H_{gc}W_{gc}}\frac{S_a[i_{fc}+i_n]}{2F}$ (1.47)
$\begin{cases}\boldsymbol{J^{gdl,gc}_{H_2}} = \boldsymbol{J_{H_2,codi}}, \text{at the GDL/GC border}\\ J^{in/out,gc}_{H_2} = J_{H_2,\text{in/out}}, \text{at the inlet/outlet of the GC}\end{cases}$ (1.59b)	$J_{H_2,\text{out}} = \frac{P_{\text{agc,out}}-\Phi_{\text{agc,out}}P_{sat}}{P_{\text{agc,out}}}\frac{k_{em,\text{in}}}{H_{gc}W_{gc}M_{agc,out}}\left[P_{agc,out}-P_{a,\text{des}}\right]$ (1.47)

Table 1.6. – Synthesis of the partial differential equations and the spotlighted matter transport expressions (2/3)

Dynamical models	Matter flow expressions
Oxygen in the GDL and the CL	
$\varepsilon \frac{\partial}{\partial t}\left([1-s]\, C_{O_2}\right) = -\boldsymbol{\nabla}\cdot \boldsymbol{J_{O_2,dif}} + S_{O_2,cons}$ (1.60a)	$S_{O_2,cons} = \begin{cases} -\frac{i_{fc}+i_{sc}}{4FH_{cl}} - \frac{RT_{fc}}{H_{cl}}\left[k_{O_2}\nabla C_{O_2} + \frac{k_{H_2}}{2}\nabla C_{H_2}\right], \text{CCL} \\ 0, \text{elsewhere} \end{cases}$ (1.58)
$\begin{cases} \boldsymbol{J_{O_2}^{cl,mem}} = \mathbf{0}, \text{at the CL/membrane border} \\ \boldsymbol{J_{O_2}^{gdl,gc}} = \boldsymbol{J_{O_2,codi}}, \text{at the GDL/GC border} \end{cases}$ (1.60b)	$\boldsymbol{J_{O_2,dif}} = -D_{O_2}^{eff}\boldsymbol{\nabla} C_{O_2}$ (1.48)
	$\boldsymbol{J_{O_2,codi}} = h_{O_2}\left[C_{O_2,\text{cgdl}}^{\text{inter}} - C_{O_2,\text{cgc}}\right]\boldsymbol{\imath}$ (1.48)
Oxygen in the GC	
$\frac{\partial C_{O_2}}{\partial t} = -\boldsymbol{\nabla}\cdot \boldsymbol{J_{O_2,conv}}$ (1.60a)	$\boldsymbol{J_{O_2,conv}} = C_{O_2}\boldsymbol{u_g}$ (1.48)
$\begin{cases} \boldsymbol{J_{O_2}^{gdl,gc}} = \boldsymbol{J_{O_2,codi}}, \text{at the GDL/GC border} \\ J_{O_2}^{in/out,gc} = J_{O_2,\text{in/out}}, \text{at the inlet/outlet of the GC} \end{cases}$ (1.60b)	$J_{O_2,\text{in}} = \frac{A_{act}}{H_{gc}W_{gc}}\frac{S_c[i_{fc}+i_n]}{4F}$ (1.48)
	$J_{O_2,\text{out}} = y_{O_2,\text{cgc,out}}\frac{P_{\text{cgc,out}} - \Phi_{\text{cgc,out}}P_{sat}}{P_{\text{cgc,out}}}\frac{k_{em,\text{in}}}{H_{gc}W_{gc}M_{cgc,out}}\left[P_{cgc,out} - P_{c,\text{des}}\right]$ (1.48)
Nitrogen	
$\frac{\mathrm{dC_{N_2}}}{\mathrm{dt}} = W_{N_2,\text{in}} - W_{N_2,\text{out}}$ (1.63)	$W_{N_2,\text{in}} = \frac{1-y_{O_2,ext}}{y_{O_2,ext}}\frac{A_{act}}{H_{gc}W_{gc}}\frac{S_c[i_{fc}+i_n]}{4F}$ (1.61)
	$W_{N_2,\text{out}} = \left[1-y_{O_2,\text{cgc,out}}\right]\frac{P_{\text{cgc,out}} - \Phi_{\text{cgc,out}}P_{sat}}{P_{\text{cgc,out}}}\frac{k_{em,\text{in}}}{H_{gc}W_{gc}M_{cgc,out}}\left[P_{cgc,out} - P_{c,\text{des}}\right]$ (1.62)

Table 1.7. – Synthesis of the partial differential equations and the spotlighted matter transport expressions (3/3)

Coefficients associated to the dissolved water in the membrane

$$a_w(C,\mathrm{s}) = \frac{C}{C_{sat}} + 2\mathrm{s} \quad (1.15)$$

$$D(\lambda) = 4.1\times10^{-10}\left[\frac{\lambda}{25.0}\right]^{0.15}\left[1.0+\tanh\left(\frac{\lambda-2.5}{1.4}\right)\right] \quad (1.7)$$

$$\begin{aligned}\lambda_{eq} = {} & \frac{1}{2}\left[0.300+10.8a_w-16.0a_w^2+14.1a_w^3\right]\cdot\left[1-\tanh\left(100\left[a_w-1\right]\right)\right] \\ & +\frac{1}{2}\left[9.2+8.6\left[1-\exp\left(-K_{\text{shape}}\left[a_w-1\right]\right)\right]\right]\cdot\left[1+\tanh\left(100\left[a_w-1\right]\right)\right]\end{aligned} \quad (1.13)$$

$$f_v(\lambda) = \frac{\lambda V_w}{V_{\text{mem}}+\lambda V_w} \quad (1.18)$$

$$\gamma_{sorp}(\lambda,T) = \begin{cases}\frac{1.14\cdot10^{-5}f_v(\lambda)}{H_{cl}}e^{2416\left[\frac{1}{303}-\frac{1}{T_{fc}}\right]}, & \text{absorption flow}\\ \frac{4.59\cdot10^{-5}f_v(\lambda)}{H_{cl}}e^{2416\left[\frac{1}{303}-\frac{1}{T_{fc}}\right]}, & \text{desorption flow}\end{cases} \quad (1.18)$$

Coefficients associated to liquid water in the GDL and the CL

$$\begin{cases}\mathrm{e}=3, & \text{if } \varepsilon\in[0.1,0.4]\\ \mathrm{e}\in[4,5], & \text{if } \varepsilon\in[0.6,0.8]\end{cases} \quad (1.26)$$

$$K_0(\varepsilon) = \frac{\varepsilon}{8\ln(\varepsilon)^2}\frac{\left[\varepsilon-\varepsilon_p\right]^{\alpha+2}r_f^2}{\left[1-\varepsilon_p\right]^{\alpha}\left[\left[\alpha+1\right]\varepsilon-\varepsilon_p\right]^2}e^{\beta_1\varepsilon_c} \quad (1.28)$$

$$\sigma(T) = 235.8\times10^{-3}\left[\frac{647.15-T_{fc}}{647.15}\right]^{1.256}\left[1-0.625\frac{647.15-T_{fc}}{647.15}\right] \quad (1.29)$$

Table 1.8. – Synthesis of the spotlight flow coefficients (1/2)

Coefficients associated to vapour in the GDL and the CL	
$h_v = S_h \frac{D_v}{H_{gc}}$ (1.41)	$D_{i/j}^{eff} = \begin{cases} \varepsilon^{\tau} [1-s]^{\tau} D_{i/j}, & \text{in the CL} \\ \varepsilon \left[\frac{\varepsilon-\varepsilon_p}{1-\varepsilon_p}\right]^{\alpha} [1-s]^2 e^{\beta_2 \varepsilon_c} D_{i/j}, & \text{in the GDL} \end{cases}$ (1.36)
$S_h = 0.9247 \cdot \ln\left(\frac{W_{gc}}{H_{gc}}\right) + 2.3787$ (1.42)	$\begin{cases} D_{H_2O/H_2} = 1.644 \cdot 10^{-4} \left[\frac{T_{fc}}{333}\right]^{2.334} \left[\frac{101325}{P}\right] \\ D_{H_2O/O_2} = 3.242 \cdot 10^{-5} \left[\frac{T_{fc}}{333}\right]^{2.334} \left[\frac{101325}{P}\right] \end{cases}$ (1.37)
Coefficients associated to H_2 and O_2 in the CL	
$k_{H_2} = \begin{cases} \left[0.29 + 2.2 f_v(\lambda)\right] 10^{-14} \exp\left(\frac{E_{act,H_2,v}}{R}\left[\frac{1}{T_{ref}} - \frac{1}{T_{fc}}\right]\right) & if\ \lambda < \lambda_{l,eq} \\ 1.8 \cdot 10^{-14} \exp\left(\frac{E_{act,H_2,l}}{R}\left[\frac{1}{T_{ref}} - \frac{1}{T_{fc}}\right]\right) & if\ \lambda = \lambda_{l,eq} \end{cases}$ (1.53)	
$k_{O_2} = \begin{cases} \left[0.11 + 1.9 f_v(\lambda)\right] 10^{-14} \exp\left(\frac{E_{act,O_2,v}}{R}\left[\frac{1}{T_{ref}} - \frac{1}{T_{fc}}\right]\right) & if\ \lambda < \lambda_{l,eq} \\ 1.2 \cdot 10^{-14} \exp\left(\frac{E_{act,O_2,l}}{R}\left[\frac{1}{T_{ref}} - \frac{1}{T_{fc}}\right]\right) & if\ \lambda = \lambda_{l,eq} \end{cases}$ (1.54)	

Table 1.9. – Synthesis of the spotlight flow coefficients (2/2)

Spotlighted voltage polarization expressions	
The apparent voltage	$U_{cell} = U_{eq} - \eta_c - i_{fc}\left[R_p + R_e\right]$ (1.64)
The equilibrium potential	$U_{eq} = E^0 - 8.5\cdot 10^{-4}\left[T_{fc} - 298.15\right] + \frac{RT_{fc}}{2F}\left[\ln\left(\frac{RT_{fc}C_{H_2,\text{acl}}}{P_{\text{ref}}}\right) + \frac{1}{2}\ln\left(\frac{RT_{fc}C_{O_2,\text{ccl}}}{P_{\text{ref}}}\right)\right]$ (1.65)
The overpotential	$\eta_c = \frac{RT_{fc}}{\alpha_c F} ln\left(\frac{i_{fc}+i_n}{i_{0,c}^{ref}\left[\frac{C_{O_2,ccl}}{C_{O_2}^{ref}}\right]^{\kappa_c}}\right)$ (1.67) $\quad i_n = i_{co,H_2} + i_{co,O_2} + i_{sc}$ (1.70) $\begin{cases} i_{sc} = \frac{U_{cell}}{r_{sc}} \\ r_{sc} = 1.79\cdot 10^{-2}\left[\frac{P_{agc}}{101325}\right]^{-9.63}\left[\frac{P_{cgc}}{101325}\right]^{0.38} \end{cases}$ (1.72) $\quad \begin{cases} i_{co,H_2} = 2Fk_{H_2}\nabla P_{H_2} \\ i_{co,O_2} = 4Fk_{O_2}\nabla P_{O_2} \end{cases}$ (1.71)
The proton resistance	$\sigma_m = \begin{cases} [0.5139\lambda - 0.326]\exp\left(1268\left[\frac{1}{303.15} - \frac{1}{T_{fc}}\right]\right), & \text{for } \lambda \geq 1 \\ 0.1879\exp\left(1268\left[\frac{1}{303.15} - \frac{1}{T_{fc}}\right]\right), & \text{for } \lambda < 1 \end{cases}$ (1.76) $R_p = \int_{mem}\frac{dx}{\sigma_m} + \int_{ccl}\frac{dx}{\varepsilon_{mc}^{\gamma}\sigma_m}$ (1.79)

Table 1.10. – Synthesis of the spotlighted voltage polarization expressions

2. Implementation of the 1D numerical model

Sommaire

2.1. Diversity of the numerical model possibilities

Ideally, it would be advisable to always utilize the most accurate PEMFC models that capture the 3D and dynamic characteristics of the stack. These models are considered the most precise available, although the current limits of understanding of fuel cell physics constrains their accuracy. However, these models [32, 33], which rely on commercial software, demand significant computational resources and processing time, making them incompatible with embedded applications. To mitigate this computational burden, partial spatial reductions have been proposed. This involves combining, for example, a 3D model of the gas channels (GC) and gas diffusion layers (GDL) with a 1D model of the catalytic layers (CL) and membrane, forming a so-called "3D+1D" model [31]. Similarly, "2D+1D" models have also been introduced

[35, 131]. Other researchers have suggested pseudo-3D ("P3D") models, which, in practice, correspond to multilayered 2D models [132], or simply models exclusively in 2D [28, 29]. Reductive assumptions have also been incorporated, such as stationary, isothermal models with a single phase for water. While these models effectively reduce computational load while maintaining precision in the stack's internal states, they still rely on commercial software and remain too time-consuming for practical use in embedded conditions. They require, for instance, several hours on a high-performance desktop computer to yield results in the case of stationary models. On the other hand, there are highly simplified models that can run quickly on any computer. These are the lumped-parameter models. Among them, the so-called "0D" models physically represent the matter evolution but without modeling the spatial variations within each component. They provide a dynamic view of matter transport as well as a direct representation of the auxiliaries that enable stack control. The foundational work of Pukrushpan et al. [41], whose model is accessible in open-source, has been widely disseminated. However, it is valuable to consider the spatial evolution of the stack's internal states along its thickness because matter variations are significant, and the physical phenomena occurring there are different. To achieve sufficiently precise control of PEMFCs, it seems crucial to retain at least this spatial direction.

To consider the distributed parameters along the stack thickness, 1D, "1D+0D," and "1D+1D" models have been studied. The "1D+0D" [133] and "1D+1D" models [110, 134–137] from the literature are either fast but stationary [133–135] or dynamic but employ numerical solution methods that excessively slow down the model [110, 136, 137], rendering them incomplete for dynamic control design in both cases. As for the 1D models [52, 98, 99, 138–141], some are also (partially) stationary [138–140]. Others incompletely represent matter transports within the MEA [98] or neglect to include the modeling of auxiliaries or bipolar plates [139, 141]. Finally, some models, such as these proposed by Y. Shao et al. and L. Xu et al. [52, 99], are the ones closest to the set objectives: they are fast, dynamic, biphasic, account for the balance of plant and provide sufficiently precise information on all internal states of the stack. However, it is worth noting that their proposed liquid water modeling necessitates the introduction of simplifying assumptions, such as quasi-static equilibrium or an infinite evaporation rate. It is essential to alleviate these assumptions by incorporating insights from alternative 1D models [141] that consider liquid water without resorting to such reductive assumptions. This ensures the credibility of the model predictions.

One objective of this chapter is to overcome the drawbacks of the above modelings by developing a comprehensive model of the PEM fuel cell system that eliminates the previous simplifying assumptions regarding the evolution of liquid water, while still maintaining its speed qualities. This model is 1D, dynamic, biphasic, and isothermal. In the developed model, certain involved equations are revised or improved, incorporating findings from recent research and extending upon the authors' work. Some original equations have been added and discussed concerning auxiliary variables and voltage calculation to make the model more comprehensive and realistic. In particular, a novel coefficient, named the limit liquid water saturation coefficient (s_{lim}), is introduced to better model the voltage drop at high current densities, establishing a

connection between this current density limit and the internal states as well as operating conditions of the cell. In the appendices, hypotheses considered in this work are outlined. Ultimately, this open-source model has been designed to be adopted and extended by other researchers to expedite research in this field. In particular, the coupling of physics-based models like this one with machine learning-based models appears highly promising for producing even faster models while maintaining a very high level of accuracy [125, 142, 143].

2.2. 1D matter transport numerical implementation

The model developed in this study, and published by the authors [144], is oriented to real-time diagnosis and control purposes. It is therefore needed to take into account both execution speed and accuracy. For instance, regarding the mass transfer process, the model is expected to predict the next tens to hundreds seconds within a few seconds. This enables the controllers to perform multiple model-base predictions within a single control period so that a model predictive control paradigm can be deployed. However, these predictions must also be sufficiently accurate to support the model based diagnosis and control to avoid unintentionally putting the stack in a faulty state or a highly degraded condition, as well as preventing hydrogen waste.

To fulfill these requirements, a one-dimensional (1D) model has been proposed. To achieve efficient gas and water management-related control, real-time access to the dynamically varying spatial distribution of internal states within the fuel stack is necessary. These states encompass the concentrations of reactants and products, the proportion of liquid or dissolved water in the membrane, and the flow of matter throughout the stack. These variables primarily evolve in the thickness direction of the stack, which is why a 1D model was selected. Furthermore, the condensation of water vapor within the stack is important to consider as flooding must be closely monitored. As a result, the model accounts for two states of water molecules: vapor and liquid, making it a two-phase model. Lastly, it is important to note that the model assumes isothermal conditions and considers that all cell exhibit identical behavior throughout the entire stack. These significant assumptions were made to simplify the complexity of developing the model and are expected to be eliminated in future model versions.

For the model resolution, a finite-difference method is employed to discretize the partial differential equations governed model and transform it into an ordinary differential equations (ODE) governed one. The number and positions of nodes were set appropriately to simplify the model resolution to the utmost extent without losing accuracy. An adaptable numerical method is then applied to solve the transformed ODE.

In the sequel, the finite-difference method, the numerical solution, and the transformed model are presented successively. The balance of plant modeling is discussed in section 2.3.

2.2.1. Finite-difference model and its numerical solution

2.2.1.1. Finite-difference modeling method

Finite-difference modeling involves dividing a system into discrete nodes, with each node representing a specific volume within the system. Within each region, all quantities are assumed to be homogeneous. The value at the center of each volume is then extrapolated to the entire one. Consequently, each node is positioned at the center of its respective region. Therefore, by decreasing the size of the volumes, the

simplifying assumption becomes less significant, resulting in a more accurate model.

Within a PEM single cell, there are seven distinct zones. The anode consists of a GDL and a CL. It is in contact with a gas channel (GC) on one side and a membrane on the other side. The configuration is similar on the cathode side, and a single membrane separates the anode from the cathode within the same cell. Each of these zones is composed of different materials or experiences the flow of different molecules. To accurately represent these structures and the matter flow within them, each zone must be assigned a separate node at minimum since each node homogenizes the quantities present within it. Therefore, a minimum of seven nodes is required, corresponding to the seven zones under consideration.

Then, it is also necessary to include an additional node at each GDL, specifically at the boundary with the bipolar plate. These additional nodes are required to account for the material discontinuity between the GDL and the GC, which results in sorption flows between them. Including these nodes accurately captures the sorption flows and ensures the model properly represents this phenomenon.

Furthermore, due to the difference in thickness between the GDL and the CL, it is not enough to only use 9 nodes. Indeed, for the sake of numerical stability, it is advisable to have distances between the nodes of the discretization scheme that are of the same order of magnitude. Ideally, each GDL should have a number of nodes, denoted as n_{gdl}, equal to $\lfloor \frac{H_{gdl}}{H_{cl}} \rfloor$. However, this results in a large number of nodes within the cell, with n_{gdl} generally exceeding 20. Given the number of variables interacting in the GDL, this has a significant computational time cost. In line with the compromise approach of this study, the authors thus propose to take $n_{gdl} = \lfloor \frac{H_{gdl}}{2H_{cl}} \rfloor$.

Finally, figure 2.1 was generated to illustrate both the overall flows and matter conversions, including their notations, and the placement of model nodes within a PEM single cell.

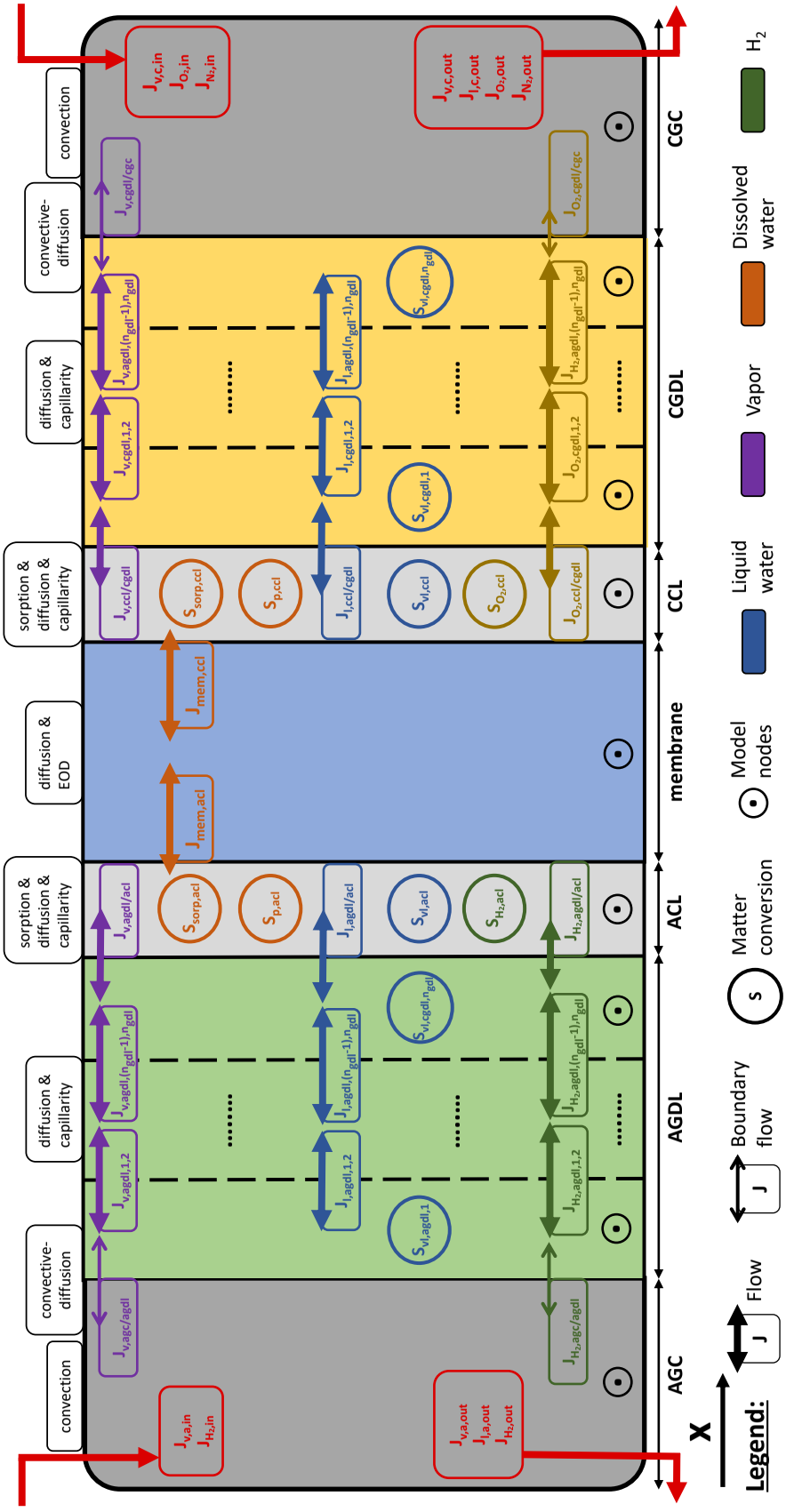

Figure 2.1. – 1D modeling of matter transport phenomena in a PEM single cell divided into several nodes

2.2.1.2. Numerical solution method

To solve the finite-difference model, the 'BDF' (Backward Differentiation Formula) method, available in the '`solve_ivp`' function of Python's scipy.integrate module, has been utilized [145]. This method offers several advantages.

Firstly, it is an implicit method that guarantees the convergence of results, which is particularly valuable for this model as it involves a stiff problem with high sensitivity to parameters. Indeed, the various physical phenomena in the fuel stack are interconnected. For instance, the consumption of hydrogen leads to the production of dissolved water, which subsequently influences the amount of water vapor or liquid water present. Furthermore, matters evolve at different timescales in the whole fuel cell system. Gases, for example, move much faster compared to liquid water in the stack. This complexity gives rise to a stiff problem that necessitates meticulous numerical solving techniques.

Secondly, this 'BDF' method employs a non-constant step size, automatically identifying regions of significant changes that require smaller time steps, as well as regions with more gradual changes where larger time steps can be used. This results in a significant reduction in computation time.

Finally, it is important to remember that only methods that can handle stiff problems can be used to solve the proposed model, which excludes most explicit methods.

2.2.2. The flows and differential equations at stake

2.2.2.1. Adaptation of mathematical expressions to the finite-difference model

To solve the system of differential equations that describes the matter transports in the stack, certain simplifications have been applied to tailor the mathematical expressions to the proposed finite-difference model.

Firstly, the spatial gradients $\boldsymbol{\nabla}$ have been approximated using a partial spatial derivative through the thickness of the cell, denoted as $\frac{\partial}{\partial x}\boldsymbol{\imath}$, where $\boldsymbol{\imath}$ is a unit vector pointing from the anode to the cathode direction. This simplification is valid because the main circulation of matter occurs along this spatial direction, x. The notation ∂ is retained to indicate that the quantities involved are dependent on other variables, such as time t. Subsequently, this partial derivative $\frac{\partial}{\partial x}$ is replaced by a finite difference between two nodes. These successive simplifications are illustrated in Equation (2.1), which describes the diffusion of water vapor in the anode:

$$\boldsymbol{J_{dif}} = -D_v^{eff}\boldsymbol{\nabla}C_v \approx -D_v^{eff}\frac{\partial C_v}{\partial x}\boldsymbol{\imath} \approx -2D_v^{eff}\frac{C_{v,acl} - C_{v,agdl,n_{gdl}}}{H_{gdl}/n_{gdl} + H_{cl}}\boldsymbol{\imath} \tag{2.1}$$

where $C_{agdl,n_{gdl}}$ is the vapor concentration at the n_{gdl}-th node of the AGDL.

Furthermore, in the calculation of flow between two nodes, many parameters or variables need to be averaged. For instance, in the case of water vapor diffusion mentioned earlier, the effective diffusion coefficient D_v^{eff} is dependent on several

factors, including liquid water saturation s, porosity ε, pressure P, and temperature T: $D_v^{eff}(s,\varepsilon,P,T)$. These four quantities, among others, vary spatially. However, when studying the flow between two nodes, it is necessary to assign a single symmetric value for D_v^{eff}. The proposed approach is to average the variables and parameters of two consecutive nodes. Thus, secondary variables and parameters are introduced, as seen in (2.2) with $\mathtt{s}_{agdl,acl}$, $\varepsilon_{agdl,acl}$, $P_{agdl,acl}$ and $T_{agdl,acl}$. In this study, the spatial variation of temperature is implied, although the model assumes an isothermal condition. This is made to facilitate the future implementation of heat transfers.

$$\begin{cases} \boldsymbol{J_{dif}} = -D_v^{eff}(\mathtt{s},\varepsilon,P,T)\boldsymbol{\nabla} C_v \approx -2D_v^{eff}(\mathtt{s}_{agdl,acl},\varepsilon_{agdl,acl},P_{agdl,acl},T_{agdl,acl})\frac{C_{v,acl}-C_{v,agdl,n_{gdl}}}{H_{gdl}/n_{gdl}+H_{cl}}\boldsymbol{\imath} \\ \mathtt{s}_{agdl,acl} = \frac{\mathtt{s}_{agdl,n_{gdl}}+\mathtt{s}_{acl}}{2}, \varepsilon_{agdl,acl} = \frac{\varepsilon_{agdl}+\varepsilon_{acl}}{2}, \\ P_{agdl,acl} = \frac{P_{agdl,n_{gdl}}+P_{acl}}{2}, T_{agdl,acl} = \frac{T_{agdl,n_{gdl}}+T_{acl}}{2} \end{cases} \tag{2.2}$$

2.2.2.2. Expression of the physical phenomena involved

After incorporating the previously discussed modifications, the differential equations and matter transport expressions can be represented as shown in tables 2.1, 2.2, 2.3 and 2.4. It should be noted that here the parameter L_{gc} represents the cumulative length of the gas channel, which is the total distance traveled by the gases as they circulate through the bipolar plates. Additionally, the flow coefficients that are functions of internal states have been adjusted for this model and are provided in table 2.5. Finally, general parameters for modeling the cell are furnished in table 2.6, while the cell's specific parameters contingent upon the cell type should be identified independently. This will be discussed in section 3.1.2.

Dynamical models

Liquid water in the GDL and the CL

$$\forall i \in [\![2, n_{\text{gdl}}-1]\!] : \rho_{H_2O}\varepsilon_{gdl}\frac{d\mathrm{s}_{agdl,i}}{dt} = \frac{J_{l,agdl,(i-1),i} - J_{l,agdl,i,(i+1)}}{H_{gdl}/n_{gdl}} + M_{H_2O}S_{vl,agdl,i}$$

$$\rho_{H_2O}\varepsilon_{gdl}\frac{d\mathrm{s}_{agdl,n_{gdl}}}{dt} = \frac{J_{l,agdl,(n_{gdl}-1),n_{gdl}} - J_{l,agdl,acl}}{H_{gdl}/n_{gdl}} + M_{H_2O}S_{vl,agdl,n_{gdl}}$$

$$\rho_{H_2O}\varepsilon_{cl}\frac{d\mathrm{s}_{acl}}{dt} = \frac{J_{l,agdl,acl}}{H_{cl}} + M_{H_2O}S_{vl,acl}$$

$$\rho_{H_2O}\varepsilon_{cl}\frac{d\mathrm{s}_{ccl}}{dt} = \frac{-J_{l,ccl,cgdl}}{H_{cl}} + M_{H_2O}S_{vl,ccl}$$

$$\rho_{H_2O}\varepsilon_{gdl}\frac{d\mathrm{s}_{cgdl,1}}{dt} = \frac{J_{l,ccl,cgdl} - J_{l,cgdl,1,2}}{H_{gdl}/n_{gdl}} + M_{H_2O}S_{vl,cgdl,1}$$

$$\rho_{H_2O}\varepsilon_{gdl}\frac{d\mathrm{s}_{cgdl,i}}{dt} = \frac{J_{l,cgdl,(i-1),i} - J_{l,cgdl,i,(i+1)}}{H_{gdl}/n_{gdl}} + M_{H_2O}S_{vl,cgdl,i}$$

Boundary conditions: $\mathrm{s}_{agdl,1} = 0$, $\mathrm{s}_{cgdl,n_{gdl}} = 0$

Vapor in the GDL and the CL

$$\forall i \in [\![2, n_{\text{gdl}}-1]\!] :$$

$$\varepsilon_{gdl}\left[1-\mathrm{s}_{agdl,1}\right]\frac{dC_{v,agdl,1}}{dt} = \frac{J_{v,agc,agdl} - J_{v,agdl,1,2}}{H_{gdl}/n_{gdl}} - S_{vl,agdl,1}$$

$$\varepsilon_{gdl}\left[1-\mathrm{s}_{agdl,i}\right]\frac{dC_{v,agdl,i}}{dt} = \frac{J_{v,agdl,(i-1),i} - J_{v,agdl,i(i+1)}}{H_{gdl}/n_{gdl}} - S_{vl,agdl,i}$$

$$\varepsilon_{gdl}\left[1-\mathrm{s}_{agdl,n_{gdl}}\right]\frac{dC_{v,agdl,n_{gdl}}}{dt} = \frac{J_{v,agdl,(n_{gdl}-1),n_{gdl}} - J_{v,agdl,acl}}{H_{gdl}/n_{gdl}} - S_{vl,agdl,n_{gdl}}$$

$$\varepsilon_{cl}\left[1-\mathrm{s}_{acl}\right]\frac{dC_{v,acl}}{dt} = \frac{J_{v,agdl,acl}}{H_{cl}} - S_{sorp,acl} - S_{vl,acl}$$

$$\varepsilon_{cl}\left[1-\mathrm{s}_{ccl}\right]\frac{dC_{v,ccl}}{dt} = -\frac{J_{v,ccl,cgdl}}{H_{cl}} - S_{sorp,ccl} - S_{vl,ccl}$$

$$\varepsilon_{gdl}\left[1-\mathrm{s}_{cgdl,1}\right]\frac{dC_{v,cgdl,1}}{dt} = \frac{J_{v,ccl,cgdl} - J_{v,cgdl,1,2}}{H_{gdl}/n_{gdl}} - S_{vl,cgdl,1}$$

$$\varepsilon_{gdl}\left[1-\mathrm{s}_{cgdl,i}\right]\frac{dC_{v,cgdl,i}}{dt} = \frac{J_{v,cgdl,(i-1),i} - J_{v,cgdl,i,(i+1)}}{H_{gdl}/n_{gdl}} - S_{vl,cgdl,i}$$

$$\varepsilon_{gdl}\left[1-\mathrm{s}_{cgdl,n_{gdl}}\right]\frac{dC_{v,cgdl,n_{gdl}}}{dt} = \frac{J_{v,cgdl,(n_{gdl}-1),n_{gdl}} - J_{v,cgdl,cgc}}{H_{gdl}/n_{gdl}} - S_{vl,cgdl,n_{gdl}}$$

Hydrogen in the GDL and the CL

$$\forall i \in [\![2, n_{\text{gdl}}-1]\!] :$$

$$\varepsilon_{gdl}\left[1-\mathrm{s}_{agdl,1}\right]\frac{dC_{H_2,agdl,1}}{dt} = \frac{J_{H_2,agc,agdl} - J_{H_2,agdl,1,2}}{H_{gdl}/n_{gdl}}$$

$$\varepsilon_{gdl}\left[1-\mathrm{s}_{agdl,i}\right]\frac{dC_{H_2,agdl,i}}{dt} = \frac{J_{H_2,agdl,(i-1),i} - J_{H_2,agdl,i,(i+1)}}{H_{gdl}/n_{gdl}}$$

$$\varepsilon_{gdl}\left[1-\mathrm{s}_{agdl,n_{gdl}}\right]\frac{dC_{H_2,agdl,n_{gdl}}}{dt} = \frac{J_{H_2,agdl,(n_{gdl}-1),n_{gdl}} - J_{H_2,agdl,acl}}{H_{gdl}/n_{gdl}}$$

$$\varepsilon_{cl}\left[1-\mathrm{s}_{acl}\right]\frac{dC_{H_2,acl}}{dt} = \frac{J_{H_2,agdl,acl}}{H_{cl}} + S_{H_2,acl}$$

Oxygen in the GDL and the CL

$$\forall i \in [\![2, n_{\text{gdl}}-1]\!] :$$

$$\varepsilon_{cl}\left[1-\mathrm{s}_{ccl}\right]\frac{dC_{O_2,ccl}}{dt} = \frac{-J_{O_2,ccl,cgdl}}{H_{cl}} + S_{O_2,ccl}$$

$$\varepsilon_{gdl}\left[1-\mathrm{s}_{cgdl,1}\right]\frac{dC_{O_2,cgdl,1}}{dt} = \frac{J_{O_2,ccl,cgdl} - J_{O_2,cgdl,1,2}}{H_{gdl}/n_{gdl}}$$

$$\varepsilon_{gdl}\left[1-\mathrm{s}_{cgdl,i}\right]\frac{dC_{O_2,cgdl,i}}{dt} = \frac{J_{O_2,cgdl,(i-1),i} - J_{O_2,cgdl,i,(i+1)}}{H_{gdl}/n_{gdl}}$$

$$\varepsilon_{gdl}\left[1-\mathrm{s}_{cgdl,n_{gdl}}\right]\frac{dC_{O_2,cgdl,n_{gdl}}}{dt} = \frac{J_{O_2,cgdl,(n_{gdl}-1),n_{gdl}} - J_{O_2,cgdl,cgc}}{H_{gdl}/n_{gdl}}$$

Table 2.1. – Synthesis of the differential equations and the associated matter transport expressions in the stack (1/4)

Matter flow expressions
Liquid water in the GDL and the CL
$\forall i \in [\![1, n_{\text{gdl}}-1]\!] : J_{l,agdl,i,(i+1)} = \sigma(T_{fc}) \frac{K_0(\varepsilon_{gdl})}{\nu_l} \cos(\theta_{c,gdl}) \sqrt{\frac{\varepsilon_{gdl}}{K_0(\varepsilon_{gdl})}} \mathsf{s}^{\mathsf{e}}_{agdl,i,(i+1)} \left[1.417 - 4.24\mathsf{s}_{agdl,i,(i+1)} + 3.789\mathsf{s}^2_{agdl,i,(i+1)}\right] \frac{\mathsf{s}_{agdl,(i+1)} - \mathsf{s}_{agdl,i}}{H_{gdl}/n_{gdl}}$
$J_{l,agdl,acl} = 2\sigma(T_{fc}) \frac{K_0(\varepsilon_{gdl,cl})}{\nu_l} \cos(\theta_{c,gdl,cl}) \sqrt{\frac{\varepsilon_{gdl,cl}}{K_0(\varepsilon_{gdl,cl})}} \mathsf{s}^{\mathsf{e}}_{agdl,acl} \left[1.417 - 4.24\mathsf{s}_{agdl,acl} + 3.789\mathsf{s}^2_{agdl,acl}\right] \frac{\mathsf{s}_{acl} - \mathsf{s}_{agdl,n_{gdl}}}{H_{gdl}/n_{gdl} + Hcl}$
$J_{l,ccl,cgdl} = 2\sigma(T_{fc}) \frac{K_0(\varepsilon_{gdl,cl})}{\nu_l} \cos(\theta_{c,gdl,cl}) \sqrt{\frac{\varepsilon_{gdl,cl}}{K_0(\varepsilon_{gdl,cl})}} \mathsf{s}^{\mathsf{e}}_{ccl,cgdl} \left[1.417 - 4.24\mathsf{s}_{ccl,cgdl} + 3.789\mathsf{s}^2_{ccl,cgdl}\right] \frac{\mathsf{s}_{cgdl,1} - \mathsf{s}_{ccl}}{H_{gdl}/n_{gdl} + Hcl}$
$J_{l,cgdl,i,(i+1)} = \sigma(T_{fc}) \frac{K_0(\varepsilon_{gdl})}{\nu_l} \cos(\theta_{c,gdl}) \sqrt{\frac{\varepsilon_{gdl}}{K_0(\varepsilon_{gdl})}} \mathsf{s}^{\mathsf{e}}_{cgdl,i,(i+1)} \left[1.417 - 4.24\mathsf{s}_{cgdl,i,(i+1)} + 3.789\mathsf{s}^2_{cgdl,i,(i+1)}\right] \frac{\mathsf{s}_{cgdl,(i+1)} - \mathsf{s}_{cgdl,i}}{H_{gdl}/n_{gdl}}$
$S_{vl} = \begin{cases} \gamma_{\text{cond}} \varepsilon (1-\mathsf{s}) x_v \left(C_v - C_{\text{v,sat}}\right), & \text{if } C_v > C_{\text{v,sat}} \\ -\gamma_{\text{evap}} \varepsilon \mathsf{s} \frac{\rho_{H_2O}}{M_{H_2O}} R T_{fc} \left(C_{\text{v,sat}} - C_v\right), & \text{if } C_v \leq C_{\text{v,sat}} \end{cases}$
Vapor in the GDL and the CL
$J_{v,agc,agdl} = h_a(P_{agc,agdl}, T_{fc}) \left[C_{v,agc} - C_{v,agdl,1}\right]$
$J_{v,agdl,i,(i+1)} = -D_{a,eff}(\mathsf{s}_{agdl,i,(i+1)}, \varepsilon_{gdl}, P_{agdl,i,(i+1)}, T_{fc}) \frac{C_{v,agdl,(i+1)} - C_{v,agdl,i}}{H_{gdl}/n_{gdl}}$
$J_{v,agdl,acl} = -2D_{a,eff}(\mathsf{s}_{agdl,acl}, \varepsilon_{agdl,acl}, P_{agdl,acl}, T_{fc}) \frac{C_{v,acl} - C_{v,agdl,n_{agdl}}}{H_{gdl}/n_{gdl} + H_{cl}}$
$J_{v,ccl,cgdl} = -2D_{c,eff}(\mathsf{s}_{ccl,cgdl}, \varepsilon_{ccl,cgdl}, P_{ccl,cgdl}, T_{fc}) \frac{C_{v,cgdl,1} - C_{v,ccl}}{H_{gdl}/n_{gdl} + H_{cl}}$
$J_{v,cgdl,i,(i+1)} = -D_{c,eff}(\mathsf{s}_{cgdl,i,(i+1)}, \varepsilon_{gdl}, P_{cgdl,i,(i+1)}, T_{fc}) \frac{C_{v,cgdl,(i+1)} - C_{v,cgdl,i}}{H_{gdl}/n_{gdl}}$
$J_{v,cgdl,cgc} = h_c(P_{cgdl,cgc}, T_{fc}) \left[C_{v,cgdl,n_{cgdl}} - C_{v,cgc}\right]$

Table 2.2. – Synthesis of the differential equations and the associated matter transport expressions in the stack, with $i \in [\![1, n_{\text{gdl}}-1]\!]$ (2/4)

Matter flow expressions
Hydrogen in the GDL and the CL
$J_{H_2,agc,agdl} = h_a(P_{agc,agdl}, T_{fc}) \left[C_{H_2,agc} - C_{H_2,agdl,1}\right]$
$J_{H_2,agdl,i,(i+1)} = -D_{a,eff}(\mathtt{s}_{agdl,i,(i+1)}, \varepsilon_{gdl}, P_{agdl,i,(i+1)}, T_{fc}) \frac{C_{H_2,agdl,(i+1)} - C_{H_2,agdl,i}}{H_{gdl}/n_{gdl}}$
$J_{H_2,agdl,acl} = -2D_{a,eff}(\mathtt{s}_{agdl,acl}, \varepsilon_{agdl,acl}, P_{agdl,acl}, T_{fc}) \frac{C_{H_2,acl} - C_{H_2,agdl,n_{gdl}}}{H_{gdl}/n_{gdl} + H_{cl}}$
$S_{H_2,acl} = -\frac{i_{fc}}{2FH_{cl}} - \frac{RT_{fc}}{H_{cl}H_{mem}} \left[k_{H_2}\left(\lambda_{mem}, T_{fc}\right) C_{H_2,acl} + 2k_{O_2}\left(\lambda_{mem}, T_{fc}\right) C_{O_2,ccl}\right]$
Oxygen in the GDL and the CL
$S_{O_2,ccl} = -\frac{i_{fc}}{4FH_{cl}} - \frac{RT_{fc}}{H_{cl}H_{mem}} \left[k_{O_2}\left(\lambda_{mem}, T_{fc}\right) C_{O_2,ccl} + \frac{k_{H_2}(\lambda_{mem}, T_{fc})}{2} C_{H_2,acl}\right]$
$J_{O_2,ccl,cgdl} = -2D_{c,eff}(\mathtt{s}_{ccl,cgdl}, \varepsilon_{ccl,cgdl}, P_{ccl,cgdl}, T_{fc}) \frac{C_{O_2,cgdl,1} - C_{O_2,ccl}}{H_{gdl}/n_{gdl} + H_{cl}}$
$J_{O_2,cgdl,i,(i+1)} = -D_{c,eff}(\mathtt{s}_{cgdl,i,(i+1)}, \varepsilon_{gdl}, P_{cgdl,i,(i+1)}, T_{fc}) \frac{C_{O_2,cgdl,(i+1)} - C_{O_2,cgdl,i}}{H_{gdl}/n_{gdl}}$
$J_{O_2,cgdl,cgc} = h_c(P_{cgdl,cgc}, T_{fc}) \left[C_{O_2,cgdl,n_{gdl}} - C_{O_2,cgc}\right]$

Table 2.3. – Synthesis of the differential equations and the associated matter transport expressions in the stack, with $i \in [\![1, n_{\text{gdl}} - 1]\!]$ (3/4)

Dynamical models	Matter flow expressions
Dissolved water in the membrane	
$\frac{\rho_{mem}\varepsilon_{mc}}{M_{eq}}\frac{d\lambda_{acl}}{dt} = -\frac{J_{\lambda,mem,acl}}{H_{cl}} + S_{sorp,acl} + S_{p,acl}$	$S_{\mathrm{p},acl} = 2k_{O_2}\left(\lambda_{mem}, T_{fc}\right)\frac{RT_{fc}}{H_{cl}H_{mem}}C_{O_2,ccl}$
	$S_{sorp,acl} = \gamma_{sorp}(\lambda_{acl}, T_{fc})\frac{\rho_{\mathrm{mem}}}{M_{\mathrm{eq}}}\left[\lambda_{\mathrm{eq}}(C_{v,acl}, \mathtt{s}_{acl}, T_{fc}) - \lambda_{acl}\right]$
$\frac{\rho_{mem}}{M_{eq}}\frac{d\lambda_{mem}}{dt} = \frac{J_{\lambda,mem,acl} - J_{\lambda,mem,ccl}}{H_{mem}}$	$J_{\lambda,mem,acl} = \frac{2.5}{22}\frac{i_{fc}}{F}\lambda_{acl,mem} - \frac{2\rho_{mem}}{M_{eq}}D(\lambda_{acl,mem})\frac{\lambda_{mem}-\lambda_{acl}}{H_{mem}+H_{cl}}$
	$J_{\lambda,mem,ccl} = \frac{2.5}{22}\frac{i_{fc}}{F}\lambda_{mem,ccl} - \frac{2\rho_{mem}}{M_{eq}}D(\lambda_{mem,ccl})\frac{\lambda_{ccl}-\lambda_{mem}}{H_{mem}+H_{cl}}$
$\frac{\rho_{mem}\varepsilon_{mc}}{M_{eq}}\frac{d\lambda_{ccl}}{dt} = \frac{J_{\lambda,mem,ccl}}{H_{cl}} + S_{sorp,ccl} + S_{p,ccl}$	$S_{sorp,ccl} = \gamma_{sorp}(\lambda_{ccl}, T_{fc})\frac{\rho_{\mathrm{mem}}}{M_{\mathrm{eq}}}\left[\lambda_{\mathrm{eq}}(C_{v,ccl}, \mathtt{s}_{ccl}, T_{fc}) - \lambda_{ccl}\right]$
	$S_{\mathrm{p},ccl} = \frac{i_{fc}}{2FH_{cl}} + k_{H_2}\left(\lambda_{mem}, T_{fc}\right)\frac{RT}{H_{cl}H_{mem}}C_{H_2,acl}$
Vapor in the GC	
$\frac{\mathrm{d}C_{v,agc}}{\mathrm{dt}} = \frac{J_{v,a,\mathrm{in}} - J_{v,a,\mathrm{out}}}{L_{gc}} - \frac{J_{v,agc,agdl}}{H_{gc}}$	$J_{v,a,\mathrm{in}} = \frac{\Phi_{asm}P_{sat}(T_{fc})}{P_{asm}}\frac{W_{asm,out}}{H_{gc}W_{gc}M_{asm}}$
	$J_{v,a,\mathrm{out}} = \frac{\Phi_{agc}P_{sat}(T_{fc})}{P_{agc}}\frac{W_{aem,in}}{H_{gc}W_{gc}M_{agc}}$
$\frac{\mathrm{d}C_{v,cgc}}{\mathrm{dt}} = \frac{J_{v,c,\mathrm{in}} - J_{v,c,\mathrm{out}}}{L_{gc}} + \frac{J_{v,cgdl,cgc}}{H_{gc}}$	$J_{v,c,\mathrm{in}} = \frac{\Phi_{csm}P_{sat}(T_{fc})}{P_{csm}}\frac{W_{csm,out}}{H_{gc}W_{gc}M_{csm}}$
	$J_{v,c,\mathrm{out}} = \frac{\Phi_{cgc}P_{sat}(T_{fc})}{P_{cgc}}\frac{W_{cem,in}}{H_{gc}W_{gc}M_{cgc}}$
Hydrogen and oxygen in the GC	
$\frac{\mathrm{d}C_{H_2,agc}}{\mathrm{dt}} = \frac{J_{H_2,\mathrm{in}} - J_{H_2,\mathrm{out}}}{L_{gc}} - \frac{J_{H_2,agc,agdl}}{H_{gc}}$	$J_{H_2,\mathrm{in}} = \frac{P_{asm} - \Phi_{asm}P_{sat}(T_{fc})}{P_{asm}}\frac{W_{asm,out}}{H_{gc}W_{gc}M_{asm}}$
	$J_{H_2,\mathrm{out}} = \frac{P_{agc} - \Phi_{agc}P_{sat}(T_{fc})}{P_{agc}}\frac{W_{aem,in}}{H_{gc}W_{gc}M_{agc}}$
$\frac{\mathrm{d}C_{O_2,cgc}}{\mathrm{dt}} = \frac{J_{O_2,\mathrm{in}} - J_{O_2,\mathrm{out}}}{L_{gc}} + \frac{J_{O_2,cgdl,cgc}}{H_{gc}}$	$J_{O_2,\mathrm{in}} = y_{O_2,ext}\frac{P_{csm} - \Phi_{csm}P_{sat}(T_{fc})}{P_{csm}}\frac{W_{csm,out}}{H_{gc}W_{gc}M_{csm}}$
	$J_{O_2,\mathrm{out}} = y_{O_2,cgc}\frac{P_{cgc} - \Phi_{cgc}P_{sat}(T_{fc})}{P_{cgc}}\frac{W_{cem,in}}{H_{gc}W_{gc}M_{cgc}}$
Nitrogen	
$\frac{\mathrm{d}C_{N_2}}{\mathrm{dt}} = \frac{J_{N_2,\mathrm{in}} - J_{N_2,\mathrm{out}}}{L_{gc}}$	$J_{N_2,\mathrm{in}} = \left(1 - y_{O_2,ext}\right)\frac{P_{csm} - \Phi_{csm}P_{sat}(T_{fc})}{P_{csm}}\frac{W_{csm,out}}{H_{gc}W_{gc}M_{csm}}$
	$J_{N_2,\mathrm{out}} = \left(1 - y_{O_2,cgc}\right)\frac{P_{cgc} - \Phi_{cgc}P_{sat}(T_{fc})}{P_{cgc}}\frac{W_{cem,in}}{H_{gc}W_{gc}M_{cgc}}$

Table 2.4. – Synthesis of the differential equations and the associated matter transport expressions in the stack (4/4)

Coefficients associated to the dissolved water in the membrane

$$a_w(C_v, \mathrm{s}) = \frac{C_v}{C_{v,sat}} + 2\mathrm{s} \tag{2.3}$$

$$D(\lambda) = 4.1 \times 10^{-10} \left[\frac{\lambda}{25.0}\right]^{0.15} \left[1.0 + \tanh\left(\frac{\lambda - 2.5}{1.4}\right)\right] \tag{2.4}$$

$$\lambda_{eq}^{cl} = \frac{1}{2}\left(0.300 + 10.8a_w - 16.0a_w^2 + 14.1a_w^3\right) \cdot (1 - \tanh\left[100\left(a_w - 1\right)\right]) + \frac{1}{2}\left(9.2 + 8.6\left(1 - \exp\left[-K_{\text{shape}}\left(a_w - 1\right)\right]\right)\right) \cdot (1 + \tanh\left[100\left(a_w - 1\right)\right]) \tag{2.5}$$

$$f_v(\lambda) = \frac{\lambda V_w}{V_{\text{mem}} + \lambda V_w} \tag{2.6}$$

$$\gamma_{sorp}(\lambda, T_{fc}) = \begin{cases} \frac{1.14 \cdot 10^{-5} f_v(\lambda)}{H_{cl}} e^{2416\left[\frac{1}{303} - \frac{1}{T_{fc}}\right]}, & \text{absorption flow} \\ \frac{4.59 \cdot 10^{-5} f_v(\lambda)}{H_{cl}} e^{2416\left[\frac{1}{303} - \frac{1}{T_{fc}}\right]}, & \text{desorption flow} \end{cases} \tag{2.7}$$

Coefficients associated to liquid water in the GDL and the CL

$$K_0(\varepsilon) = \frac{\varepsilon}{8\ln(\varepsilon)^2} \frac{\left[\varepsilon - \varepsilon_p\right]^{\alpha+2} r_f^2}{\left[1 - \varepsilon_p\right]^{\alpha} \left[\left[\alpha + 1\right]\varepsilon - \varepsilon_p\right]^2} e^{\beta_1 \varepsilon_c} \tag{2.8}$$

$$\sigma(T_{fc}) = 235.8 \times 10^{-3} \left[\frac{647.15 - T_{fc}}{647.15}\right]^{1.256} \left[1 - 0.625\frac{647.15 - T_{fc}}{647.15}\right] \tag{2.9}$$

Coefficients associated to vapor inside the GDL and the CL

$$\begin{cases} D_{a,eff}\left(\mathrm{s}, \varepsilon, P, T_{fc}\right) = \varepsilon\left[\frac{\varepsilon - \varepsilon_p}{1 - \varepsilon_p}\right]^{\alpha} \left[1 - \mathrm{s}\right]^2 e^{\beta_2 \varepsilon_c} D_a\left(P, T_{fc}\right) \\ D_{c,eff}\left(\mathrm{s}, \varepsilon, P, T_{fc}\right) = \varepsilon\left[\frac{\varepsilon - \varepsilon_p}{1 - \varepsilon_p}\right]^{\alpha} \left[1 - \mathrm{s}\right]^2 e^{\beta_2 \varepsilon_c} D_c\left(P, T_{fc}\right) \end{cases} \tag{2.10}$$

$$\begin{cases} D_a\left(P, T_{fc}\right) = 1.644 \cdot 10^{-4} \left[\frac{T_{fc}}{333}\right]^{2.334} \left[\frac{101325}{P}\right] \\ D_c\left(P, T_{fc}\right) = 3.242 \cdot 10^{-5} \left[\frac{T_{fc}}{333}\right]^{2.334} \left[\frac{101325}{P}\right] \end{cases} \tag{2.11}$$

$$h_i(P, T_{fc}) = S_h \frac{D_i(P, T_{fc})}{H_{gc}} \;\; \forall\, \mathrm{i} \in \{a, c\} \tag{2.12}$$

$$S_h = 0.9247 \cdot \ln\left(\frac{W_{gc}}{H_{gc}}\right) + 2.3787 \tag{2.13}$$

Coefficients associated to H_2 and O_2 in the CL

$$k_{H_2}\left(\lambda, T_{fc}\right) = \begin{cases} \kappa_{co}\left[0.29 + 2.2 f_v\left(\lambda\right)\right] 10^{-14} \exp\left(\frac{E_{act,H_2,v}}{R}\left[\frac{1}{T_{ref}} - \frac{1}{T_{fc}}\right]\right) & if\, \lambda < 17.6 \\ \kappa_{co} 1.8 \cdot 10^{-14} \exp\left(\frac{E_{act,H_2,l}}{R}\left[\frac{1}{T_{ref}} - \frac{1}{T_{fc}}\right]\right) & if\, \lambda \geq 17.6 \end{cases} \tag{2.14}$$

$$k_{O_2}\left(\lambda, T_{fc}\right) = \begin{cases} \kappa_{co}\left[0.11 + 1.9 f_v\left(\lambda\right)\right] 10^{-14} \exp\left(\frac{E_{act,O_2,v}}{R}\left[\frac{1}{T_{ref}} - \frac{1}{T_{fc}}\right]\right) & if\, \lambda < 17.6 \\ \kappa_{co} 1.2 \cdot 10^{-14} \exp\left(\frac{E_{act,O_2,l}}{R}\left[\frac{1}{T_{ref}} - \frac{1}{T_{fc}}\right]\right) & if\, \lambda \geq 17.6 \end{cases} \tag{2.15}$$

Table 2.5. – Synthesis of the flow coefficients

Symbol	Name (Unit)	Value
Cell model parameters		
ρ_{mem}	Density of the dry membrane ($kg.m^{-3}$)	1980
M_{eq}	Equivalent molar mass of ionomer ($kg.mol^{-1}$)	1.1
ε_{cl}	Porosity of the catalyst layer	0.25
$\theta_{c,gdl}$	Contact angle of GDL for liquid water (rad)	$\frac{2}{3}\pi$ (120°)
$\theta_{c,cl}$	Contact angle of CL for liquid water (rad)	1.66 (95°)
γ_{cond}	Overall water condensation rate constant (s^{-1})	$5 \cdot 10^3$
γ_{evap}	Overall water evaporation rate constant ($Pa^{-1}.s^{-1}$)	10^{-4}
K_{shape}	Mathematical factor governing λ_{eq} smoothing	2
Physical constants		
F	Faraday constant ($C.mol^{-1}$)	96485
R	Universal gas constant ($J.mol^{-1}.K^{-1}$)	8.314

Table 2.6. – Synthesis of the general parameters for the cell modeling

2.3. 0D balance of plant numerical implementation

2.3.1. An anodic recirculation PEMFC system

In this work, the focus was on considering a fuel cell system rather than examining a single cell only. This approach enables the observation of the auxiliary components' impact on the fuel cells' internal states and performance, which is crucial for control design. Within this investigation, a conventional fuel cell system for vehicles is studied and depicted in figure 2.2. Specifically, on the anode side, there is a hydrogen storage tank where H_2 is maintained at a desired temperature T. It is connected to a pressure relief valve that delivers pure H_2 to the supply manifold of the anodic chamber. At the outlet of this chamber, there is an exhaust manifold connected both to an electronic purge valve and to a pump that recirculates H_2 back to the supply anode manifold. On the cathode side, a compressor supplies ambient air to the stack, passing successively through a heat exchanger, a humidifier, and a supply cathode manifold. At the outlet of the cathodic chamber, an exhaust manifold is directly linked to an electronic back pressure valve. Finally, this valve releases the gases into the atmosphere, without recovering heat or water from the exhaust air.

Thus, with this setup, the fuel cell can be controlled by the user. On the anode side, the inlet pressure is regulated by the pressure relief valve, and the inlet flow by the recirculation pump. It is also assumed here that the hydrogen within its reservoir is maintained at the desired temperature. On the cathode side, the temperature and humidity of the incoming gases are controlled through the heat exchanger and the humidifier. The compressor dictates an inlet flow, and the back-pressure valve regulates the pressure within the cell.

Remark: This configuration is a simplified version of the one predominantly employed in embedded applications. Yet, during the model validation phase, a modified anode gas supply configuration, similar to the cathode, is utilized to have more flexible control over the operating conditions. This approach is frequently employed in laboratory settings.

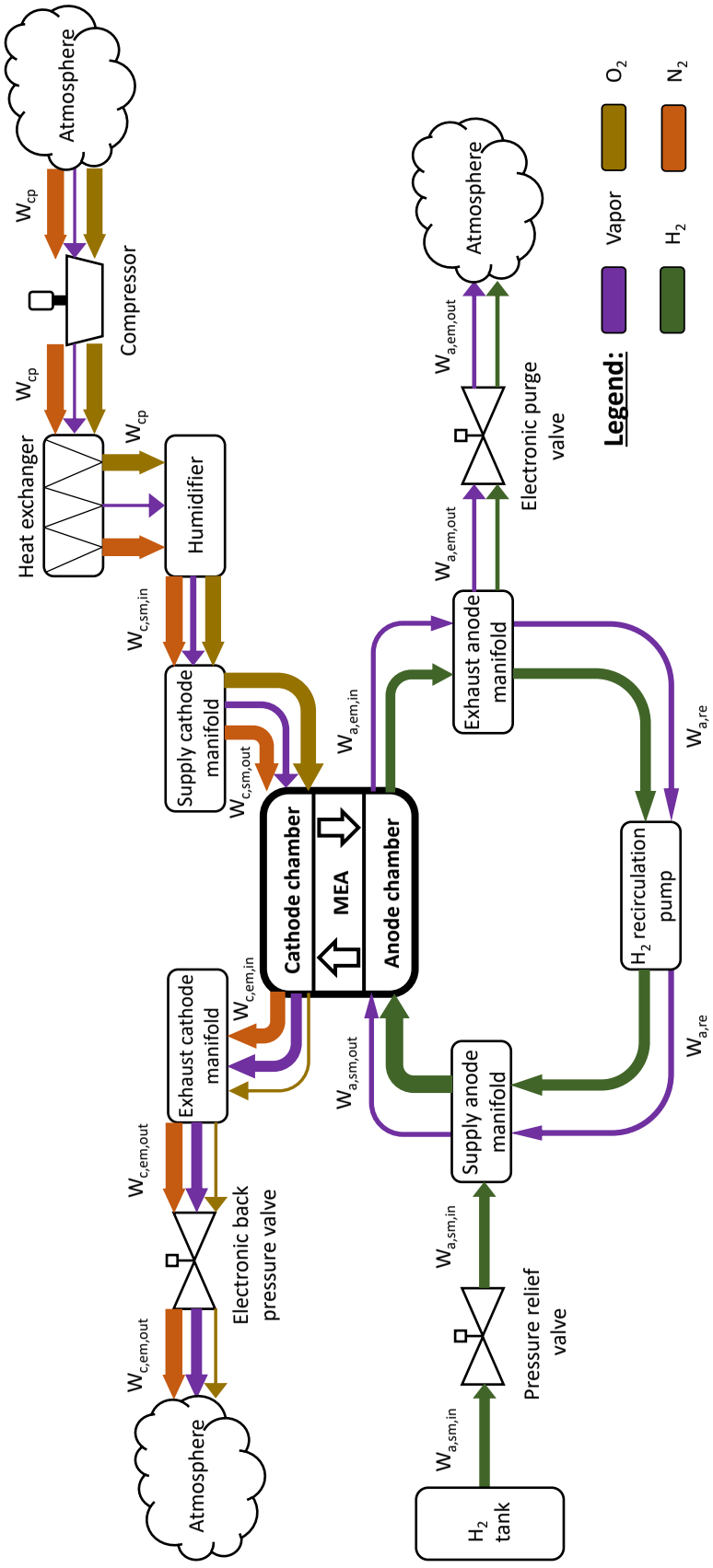

Figure 2.2. – The studied simplified structure of a PEMFC system, consisting of a forced-convective cathode and anodic recirculation.

2.3.2. A 0D, dynamic and isothermal model of the auxiliary system

For this study, the aim is not to extensively model the auxiliary system. A simple approach is proposed, based on the foundational work of Pukrushpan et al. [41] and in line with the works of Liangfei Xu et al. [98], Y. Shao et al. [99] and Ling Xu et al. [52]. These works already provide a clear explanation of the auxiliaries' modeling, and readers are encouraged to refer to them for a more detailed understanding. In the present thesis, the equations derived from these works are directly adopted, with some additions and modifications detailed below. It is worth noting that the mathematical quantity describing the material flows in auxiliaries is traditionally denoted as W and is in $kg.s^{-1}$, unlike the flows in the cells which are traditionally denoted as J, are calculated per area, and primarily molar ($mol.m^{-2}.s^{-1}$).

Several simplifying assumptions have been considered here for the modeling of this auxiliary system:

— Each of the mentioned components is modeled in 0D, meaning the internal parameters in each component are homogeneous.
— The current model is isothermal, implying that the temperature T_{fc} is assumed constant throughout the fuel cell system. Thus, the heat exchanger is disregarded here. This assumption is significant, but is expected to be eliminated in future works.
— Pressure losses along fuel cell gas channels are not modeled.
— The liquid water separator is not modeled. It is assumed that water droplets evacuate so rapidly and efficiently that they do not exist in the auxiliaries. Similarly, any condensation within the auxiliary components is presumed to be promptly removed.
— The H_2 tank and its pressure relief valve are not directly modeled. It is assumed that this reservoir is infinite, and its valve is perfectly regulated to continuously produce a flow at a constant controlled pressure $P_{a,des}$ at the inlet of the supply anode manifold.
— The electronic purge valve is inactive in this study and so $k_{purge} = 0$ in (2.37).
— The dynamic behavior of the compressor and humidifier is simplified at first order considering the desired steady-state flows $W_{cp,des}$ and $W_{c,inj,des}$, along with the time constants τ_{cp} and τ_{hum}.
— It is assumed that the pressure at the compressor outlet equals the pressure in the supply manifold of the cathode: $P_{cp} = P_{csm}$.
— It is considered that the recirculation pump reaches its steady state instantly, being much faster than other devices.

Certain additions have also been made compared to the existing auxiliary models, such as calculating the humidities in the manifolds (following the same principles stated by Pukrushpan et al. [41]) and controlling the back pressure valve to set the pressure in the stack. The cathode back pressure valve is modeled using a proportional derivative controller as shown in (2.31). This is an original idea presented in this paper. The throttle area of this valve, denoted as $A_{bp,c}$, with $A_{bp,c} \in [0, A_T]$, is controlled to

affect the quantity of matter exiting the cell and thereby influencing the upstream pressure, P_{cgc} here. Then, the proportionality constant K_p is set by considering that the valve takes two seconds to fully open or close and that, during this period, the pressure can change by 0.1 bar. The derivative constant K_d is obtained empirically.

The linearization of several flows is employed in (2.32), (2.34), (2.36), (2.41) and (2.42). The exhaust manifolds outflows, in (2.37) and (2.43), are not linearized because the pressure difference between the interior of the fuel cell system and the external environment can be significant. Additionally, it has been assumed here that the outflow is necessarily subcritical to avoid the additional instability associated with the piecewise-defined function proposed by Pukrushpan et al. [41]. Furthermore, it should be noted that there are persistent errors in the literature regarding these equations, specifically the omission of the molar mass under the square root and the confusion between sonic and supersonic flows [41, 52, 98]. Finally, in these equations, γ_{H_2} and γ_a are considered constants, their value changing only slightly with the alteration of flow composition.

Knowing these hypotheses and based on the previously mentioned works [41, 52, 98, 99], it is possible to construct the system of differential equations, presented in tables 2.10 and 2.11, which describes the studied auxiliary system. Additionally, the molar masses equations and the balance of plant parameters are provided in tables 2.7, 2.8, and 2.9.

Molar masses equations
$$M_{asm} = \frac{\Phi_{asm} P_{sat}\left(T_{fc}\right)}{P_{asm}} M_{H_2O} + \frac{P_{asm} - \Phi_{asm} P_{sat}\left(T_{fc}\right)}{P_{asm}} M_{H_2} \quad (2.16)$$
$$M_{aem} = \frac{\Phi_{aem} P_{sat}\left(T_{fc}\right)}{P_{aem}} M_{H_2O} + \frac{P_{aem} - \Phi_{aem} P_{sat}\left(T_{fc}\right)}{P_{aem}} M_{H_2} \quad (2.17)$$
$$M_{csm} = \frac{\Phi_{csm} P_{sat}\left(T_{fc}\right)}{P_{csm}} M_{H_2O} + y_{O_2,ext} \frac{P_{csm} - \Phi_{csm} P_{sat}\left(T_{fc}\right)}{P_{csm}} M_{O_2} + \left(1 - y_{O_2,ext}\right) \frac{P_{csm} - \Phi_{csm} P_{sat}\left(T_{fc}\right)}{P_{csm}} M_{N_2} \quad (2.18)$$
$$M_{agc} = \frac{\Phi_{agc} P_{sat}\left(T_{fc}\right)}{P_{agc}} M_{H_2O} + \frac{P_{agc} - \Phi_{agc} P_{sat}\left(T_{fc}\right)}{P_{agc}} M_{H_2} \quad (2.19)$$
$$M_i = \frac{\Phi_i P_{sat}\left(T_{fc}\right)}{P_i} M_{H_2O} + y_{O_2,i} \frac{P_i - \Phi_i P_{sat}\left(T_{fc}\right)}{P_i} M_{O_2} + \left(1 - y_{O_2,i}\right) \frac{P_i - \Phi_{cgc} P_{sat}\left(T_{fc}\right)}{P_i} M_{N_2}, i \in \{cem, cgc, ext\} \quad (2.20)$$

Table 2.7. – Synthesis of the molar masses equations

Symbol	Name (Unit)	Value
External environmental parameters		
T_{ext}	Outside temperature (K)	298
P_{ext}	Outside pressure (Pa)	101325
Φ_{ext}	Outside relative humidity	0.4
$y_{O_2,ext}$	Molar fraction of O_2 in ambient dry air	0.2095

Table 2.8. – Synthesis of the necessary parameters for the balance of plant modeling (1/2)

Symbol	Name (Unit)	Value
Auxiliary system model parameters		
τ_{cp}	Air compressor time constant (s)	1 [98]
τ_{hum}	Humidifier time constant (s)	5 [98]
K_p	Proportionality constant of the back pressure valve controller ($m^2.s^{-1}.Pa^{-1}$)	$5 \cdot 10^{-8}$
K_d	Derivative constant of the back pressure valve controller ($m^2.Pa^{-1}$)	10^{-8}
C_D	Throttle discharge coefficient	0.05 [98]
$k_{sm,in}$	Nozzle orifice coefficient at the inlet supply manifold ($kg.Pa^{-1}.s^{-1}$)	$1.0 \cdot 10^{-5}$
$k_{sm,out}$	Nozzle orifice coefficient at the outlet supply manifold ($kg.Pa^{-1}.s^{-1}$)	$8.0 \cdot 10^{-6}$ [98]
Auxiliary system physical parameters		
n_{cell}	Number of cells inside the stack	5
V_{sm}	Supply manifold volume (m^3)	$7.0 \cdot 10^{-3}$ [98]
V_{em}	Exhaust manifold volume (m^3)	$2.4 \cdot 10^{-3}$ [98]
A_T	Exhaust manifold throttle area (m^2)	$1.18 \cdot 10^{-3}$ [98]
Physical constants		
γ_{H_2}	Heat capacity ratio of H_2 at 100°C	1.404
γ_a	Heat capacity ratio of dry air at 100°C	1.401
M_{H_2}	Molar mass of H_2 ($kg.mol^{-1}$)	$2 \cdot 10^{-3}$
M_{H_2O}	Molar mass of H_2O ($kg.mol^{-1}$)	$1.8 \cdot 10^{-2}$
M_{O_2}	Molar mass of O_2 ($kg.mol^{-1}$)	$3.2 \cdot 10^{-2}$
M_{N_2}	Molar mass of N_2 ($kg.mol^{-1}$)	$2.8 \cdot 10^{-2}$

Table 2.9. – Synthesis of the necessary parameters for the balance of plant modeling (2/2)

Dynamical models

Manifolds at the anode

$$\frac{dP_{asm}}{dt} = \frac{RT_{fc}}{V_{sm}M_{asm}}\left[W_{asm,in} + W_{are} - n_{cell}W_{asm,out}\right] \tag{2.21}$$

$$\frac{dP_{aem}}{dt} = \frac{RT_{fc}}{V_{em}M_{aem}}\left[n_{cell}W_{aem,in} - W_{are} - W_{aem,out}\right] \tag{2.22}$$

$$\frac{d\Phi_{asm}}{dt} = \frac{RT_{fc}}{V_{sm}P_{sat}\left(T_{fc}\right)}\left[W_{v,asm,in} - J_{v,a,in}H_{gc}W_{gc}n_{cell}\right] \tag{2.23}$$

$$\frac{d\Phi_{aem}}{dt} = \frac{RT_{fc}}{V_{em}P_{sat}\left(T_{fc}\right)}\left[J_{v,a,out}H_{gc}W_{gc}n_{cell} - W_{v,asm,in} - W_{v,aem,out}\right] \tag{2.24}$$

Manifolds at the cathode

$$\frac{dP_{csm}}{dt} = \frac{RT_{fc}}{V_{sm}M_{csm}}\left[W_{csm,in} - n_{cell}W_{csm,out}\right] \tag{2.25}$$

$$\frac{dP_{cem}}{dt} = \frac{RT_{fc}}{V_{em}M_{cem}}\left[n_{cell}W_{cem,in} - W_{cem,out}\right] \tag{2.26}$$

$$\frac{d\Phi_{csm}}{dt} = \frac{RT_{fc}}{V_{sm}P_{sat}\left(T_{fc}\right)}\left[W_{v,csm,in} - J_{v,c,in}H_{gc}W_{gc}n_{cell}\right] \tag{2.27}$$

$$\frac{d\Phi_{cem}}{dt} = \frac{RT_{fc}}{V_{em}P_{sat}\left(T_{fc}\right)}\left[J_{v,c,out}H_{gc}W_{gc}n_{cell} - W_{v,cem,out}\right] \tag{2.28}$$

Air compressor, humidifiers and back-pressure valve

$$\frac{dW_{cp}}{dt} = \frac{W_{cp,des} - W_{cp}}{\tau_{cp}} \tag{2.29}$$

$$\frac{dW_{c,inj}}{dt} = \frac{W_{c,inj,des} - W_{c,inj}}{\tau_{hum}} \tag{2.30}$$

$$\frac{dA_{bp,c}}{dt} = \begin{cases} 0, & \text{if } A_{bp,c} \geq A_T \text{ and } \frac{dA_{bp,c}}{dt} > 0 \\ 0, & \text{if } A_{bp,c} \leq 0 \text{ and } \frac{dA_{bp,c}}{dt} < 0 \\ -K_p\left[P_{c,des} - P_{cgc}\right] + K_d\frac{dP_{cgc}}{dt}, & \text{else} \end{cases} \tag{2.31}$$

Table 2.10. – Synthesis of the differential equations and the associated matter transport expressions in the auxiliary system (1/2)

Matter flow expressions

Manifolds at the anode

$$W_{asm,in} = k_{sm,in}\left[P_{a,des} - P_{asm}\right] \tag{2.32}$$

$$W_{v,asm,in} = \frac{\Phi_{aem} P_{sat}\left(T_{fc}\right)}{M_{aem} P_{aem}} W_{are} \tag{2.33}$$

$$W_{asm,out} = k_{sm,out}\left[P_{asm} - P_{agc}\right] \tag{2.34}$$

$$W_{are} = n_{cell} M_{aem} \frac{P_{aem}}{P_{aem} - \Phi_{aem} P_{sat}\left(T_{fc}\right)} \frac{\left[S_a - 1\right]\left[i_{fc} + i_n\right] A_{act}}{2F} \tag{2.35}$$

$$W_{aem,in} = k_{em,in}\left[P_{agc} - P_{aem}\right] \tag{2.36}$$

$$W_{aem,out} = k_{purge} \frac{C_D A_T P_{aem}}{\sqrt{R T_{fc}}} \left(\frac{P_{ext}}{P_{aem}}\right)^{\frac{1}{\gamma_{H_2}}} \sqrt{M_{agc} \frac{2\gamma_{H_2}}{\gamma_{H_2} - 1}\left[1 - \left(\frac{P_{ext}}{P_{aem}}\right)^{\frac{\gamma_{H_2}-1}{\gamma_{H_2}}}\right]} \tag{2.37}$$

$$W_{v,aem,out} = \frac{\Phi_{aem} P_{sat}\left(T_{fc}\right)}{M_{aem} P_{aem}} W_{aem,out} \tag{2.38}$$

Manifolds at the cathode

$$W_{csm,in} = W_{cp} + W_{c,inj} \tag{2.39}$$

$$W_{v,csm,in} = \frac{\Phi_{ext} P_{sat}\left(T_{ext}\right)}{M_{ext} P_{ext}} W_{cp} + \frac{1}{M_{H_2O}} W_{c,inj} \tag{2.40}$$

$$W_{csm,out} = k_{sm,out}\left[P_{csm} - P_{cgc}\right] \tag{2.41}$$

$$W_{cem,in} = k_{em,in}\left[P_{cgc} - P_{cem}\right] \tag{2.42}$$

$$W_{cem,out} = \frac{C_D A_{bp,c} P_{cem}}{\sqrt{R T_{fc}}} \left(\frac{P_{ext}}{P_{cem}}\right)^{\frac{1}{\gamma a}} \sqrt{M_{cgc} \frac{2\gamma_a}{\gamma_a - 1}\left[1 - \left(\frac{P_{ext}}{P_{cem}}\right)^{\frac{\gamma a - 1}{\gamma a}}\right]} \tag{2.43}$$

$$W_{v,cem,out} = \frac{\Phi_{cem} P_{sat}\left(T_{fc}\right)}{M_{cem} P_{cem}} W_{cem,out} \tag{2.44}$$

Air compressor, humidifiers and back-pressure valve

$$W_{cp,des} = n_{cell} M_{ext} \frac{P_{ext}}{P_{ext} - \Phi_{ext} P_{sat}\left(T_{ext}\right)} \frac{1}{y_{O_2,ext}} \frac{S_c\left[i_{fc} + i_n\right] A_{act}}{4F} \tag{2.45}$$

$$W_{c,inj,des} = W_{c,v,des} - W_{v,hum,in} \tag{2.46}$$

$$W_{c,v,des} = M_{H_2O} \frac{\Phi_{c,des} P_{sat}\left(T_{fc}\right)}{P_{cp}} \frac{W_{cp}}{M_{ext}} \tag{2.47}$$

$$W_{v,hum,in} = M_{H_2O} \frac{\Phi_{ext} P_{sat}\left(T_{ext}\right)}{P_{ext}} \frac{W_{cp}}{M_{ext}} \tag{2.48}$$

Table 2.11. – Synthesis of the differential equations and the associated matter transport expressions in the auxiliary system (2/2)

2.3.3. Flaws of this balance of plant model

The model proposed for the auxiliaries has several flaws. First, the only equations in the literature that are practically applicable for calculating the manifold inflow or outflow rates based on a pressure difference are those of the form given in (2.32), (2.34), (2.36), (2.41) and (2.42). There are other equations derived from the Bernoulli's principle, such as the one proposed by Pukrushpan [41] and used in (2.37) and (2.43). However, these equations, in addition to assuming steady and incompressible flow, which is not valid in the present case, introduce a square root of the pressure difference. This square root function imposes a direction to the flow, as the pressure difference has to be positive, preventing symmetric considerations. This is problematic because, around initial conditions, the flows can be temporarily and briefly reversed. Gas could enter the GC through the outlet manifold, or gas could exit the GC towards the inlet manifold. Square root is also a source of numerical instability when solving the equations. Equations (2.32), (2.34), (2.36), (2.41) and (2.42), on the other hand, are obtained by linearizing the aforementioned Bernoulli principle. While it solves the asymmetry issue, the linearization requires that the pressure difference on both sides of the orifice must be very small, which may not be the case in practice. To the best of the authors' knowledge, no superior models for these flows currently exist.

2.4. Voltage numerical implementation

2.4.1. General expressions

The voltage polarization expressions are adapted for this model and given in table 2.12. Two significant scientific additions are noteworthy here: κ_{co} and s_{lim}. They have been implemented to enable the model to more accurately simulate reality when comparing results with the experimental data. A discussion dedicated to them can be found in sections 2.4.2 and 2.4.3. Finally, general parameters for modeling the cell voltage are furnished in table 2.13, while the cell's voltage specific parameters contingent upon the cell type used are delineated in section 3.1.2.

<table>
<tr><th colspan="2">Voltage polarization expressions</th></tr>
<tr><td>The apparent voltage</td><td>$$U_{cell} = U_{eq} - \eta_c - i_{fc}\left[R_p + R_e\right] \quad (2.49)$$</td></tr>
<tr><td>The equilibrium potential</td><td>$$U_{eq} = E^0 - 8.5\cdot 10^{-4}\left[T_{fc} - 298.15\right] + \frac{RT_{fc}}{2F}\left[\ln\left(\frac{RT_{fc}C_{H_2,acl}}{P_{\text{ref}}}\right) + \frac{1}{2}\ln\left(\frac{RT_{fc}C_{O_2,ccl}}{P_{\text{ref}}}\right)\right] \quad (2.50)$$</td></tr>
<tr><td>The overpotential</td><td>$$\eta_c = \frac{1}{f_{drop}(\mathtt{s},P)}\frac{RT_{fc}}{\alpha_c F} ln\left(\frac{i_{fc}+i_n}{i_{0,c}^{ref}}\left[\frac{C_{O_2}^{ref}}{C_{O_2,ccl}}\right]^{\kappa_c}\right) \quad (2.51)$$ $$\mathtt{s}_{lim} = a_{\mathtt{s}_{lim}} P_{des} + b_{\mathtt{s}_{lim}} \quad (2.52)$$ $$f_{drop}(\mathtt{s},P) = \frac{1}{2}\left[1.0 - tanh\left[\frac{4\mathtt{s}_{ccl} - 2\mathtt{s}_{lim} - 2\mathtt{s}_{switch}}{\mathtt{s}_{lim} - \mathtt{s}_{switch}}\right]\right] \quad (2.53)$$ $$\mathtt{s}_{switch} = a_{switch}\cdot \mathtt{s}_{lim} \quad (2.54)$$ $$\begin{cases} i_{co,H_2} = 2Fk_{H_2}\left(\lambda_{mem}, T_{fc}\right) RT_{fc}C_{H_2,acl} \\ i_{co,O_2} = 4Fk_{O_2}\left(\lambda_{mem}, T_{fc}\right) RT_{fc}C_{O_2,ccl} \end{cases} \quad (2.55)$$ $$i_n = i_{co,H_2} + i_{co,O_2} \quad (2.56)$$</td></tr>
<tr><td>The proton resistance</td><td>$$R_p = R_{mem} + R_{ccl} \quad (2.57)$$ $$R_{mem} = \begin{cases} \frac{H_{mem}}{[0.5139\cdot\lambda_{mem} - 0.326]\exp\left(1268\left[\frac{1}{303.15} - \frac{1}{T_{fc}}\right]\right)}, & \text{if } \lambda_{mem} \geq 1 \\ \frac{H_{mem}}{0.1879\exp\left(1268\left[\frac{1}{303.15} - \frac{1}{T_{fc}}\right]\right)}, & \text{if } \lambda_{mem} < 1 \end{cases} \quad (2.58)$$ $$R_{ccl} = \begin{cases} \frac{H_{cl}}{\varepsilon_{mc}^{\tau}[0.5139\cdot\lambda_{ccl} - 0.326]\exp\left(1268\left[\frac{1}{303.15} - \frac{1}{T_{fc}}\right]\right)}, & \text{if } \lambda_{ccl} \geq 1 \\ \frac{H_{cl}}{0.1879\varepsilon_{mc}^{\tau}\exp\left(1268\left[\frac{1}{303.15} - \frac{1}{T_{fc}}\right]\right)}, & \text{if } \lambda_{ccl} < 1 \end{cases} \quad (2.59)$$</td></tr>
</table>

Table 2.12. – Synthesis of the numerical expressions for voltage polarization

Cell voltage model parameters		
Symbol	**Name (Unit)**	**Value**
$C_{O_2,ref}$	Reference concentration of O_2 $(mol.m^{-3})$	3.39
α_c	Cathode transfer coefficient	0.5
E_0	Standard-state reversible voltage (V)	1.229
P_{ref}	Reference pressure (Pa)	10^5
E_{act}	Activation energy $(J.mol^{-1})$	$73.2 \cdot 10^3$

Table 2.13. – Synthesis of the general parameters for the cell voltage modeling

2.4.2. New parameter: the crossover correction coefficient κ_{co}

Expressing the crossover of reactants in fuel cell models is useful for several reasons. First, it is essential for accurately considering the open-circuit voltage in cells and thus obtaining a proper representation of the polarization curve. Furthermore, this information could be valuable to the operator in cases where the cell is temporarily idle. In fact, it is possible to assess the need to flush the anode of any remaining hydrogen, which can lead to cell degradation, when the shutdown is brief and so the quantity of material crossing the membrane is potentially not significant. In such cases, a decision must be made between degradation resulting from purging with ambient air and degradation arising from material crossover.

However, the most notable mathematical expression in the literature, which characterizes this phenomenon, dates back to 2004 [47]. According to the authors' results, this expression is not sufficient to describe the complexity of the crossover in recent stacks. To address this issue, and while awaiting further experiments, the authors propose adding a corrective parameter, denoted here as κ_{co}, to the permeability coefficients of hydrogen and oxygen in the membrane κ_{H_2} and κ_{O_2}. This modification has been directly incorporated into equations (1.53) and (1.54). κ_{co} is undetermined and requires calibration to be identified for the specific stack under investigation. Further details on the calibration stage are discussed in section 3.1.2.

2.4.3. New physical quantity: the limit liquid water saturation coefficient s_{lim}

To the authors' knowledge, current models struggle to physically incorporate concentration drop during the simulation of polarization curves. Thus, the most commonly used approach so far does not leverage the fuel cell's physics to explain this drop, but rather involves artificially introducing a new element into the equations. For instance, (2.60) is a widely known equation which has been used to quantify the concentration voltage loss [5, 23, 41, 105, 117, 118]. In this equation, i_{lim} is introduced to define the limit current density at which the concentration drop becomes inevitable. In most studies, i_{lim} is commonly considered as a constant. However, operational

conditions invariably influence its value, consequently altering the current density level at which the concentration drop manifests. i_{lim} therefore should be regarded as a function of the operational conditions, for which the link has yet to be identified.

$$U_{conc} = \frac{RT}{2F} ln\left(\frac{i_{lim}}{i_{lim} - i_{fc}}\right) \tag{2.60}$$

Next, it is necessary to clarify the use of the coefficient i_{lim} for modeling purposes. As soon as more complex models than lumped-parameter models are employed and internal state data within the catalytic layers are available, the physical representation of i_{lim} changes. It ceases to remain the sole mathematical element in the voltage equations that delineate concentration losses arising from gas diffusion limitations within the cell. This limitation occurs when the concentration of oxygen or hydrogen drops to zero within their respective catalytic layers, and the physical and operating conditions do not permit further supply to this region to counterbalance material consumption at high currents. Indeed, this information is already encompassed within the equilibrium potential and overpotential equations for spatially distributed models, where oxygen and hydrogen concentrations within the catalytic layers can be expressed. This is seen in this work equations (2.50) and (2.51). However, in most models, it remains necessary to retain i_{lim} empirically because the current state of the art is not mature enough to take into account all the physical phenomena that impact voltage at high current densities. Indeed, at high currents, liquid water emerges within the cell. This matter subsequently impacts the transport of oxygen and hydrogen to the triple point zones, making it more challenging. This results in a voltage drop [134] for current densities lower than if there were no liquid water present. However, this has not been physically modeled in the existing literature, and i_{lim} serves as an imperfect attempt to address this because it is detached from the physical variable that explains this phenomenon: the saturation in liquid water $\mathtt{s}$.

Here, we propose a new coefficient, named limit liquid water saturation coefficient $\mathtt{s}_{lim}$, which is indirectly added to the Butler-Volmer equation in (2.51) to physically consider the impact of catalyst layer flooding on its voltage. U_{conc} is no longer useful. A physical interpretation of this coefficient will be proposed in the authors' future work. This proposition allows for a better connection between the equations and physics, which is valuable as it enables the observation, diagnosis and control of the factor responsible for the concentration drop: $\mathtt{s}$. Additionally, this proposal easily links $\mathtt{s}_{lim}$ to operating conditions in (2.52), which is valuable for considering the stack beyond the arguable optimal conditions imposed by manufacturers.

The proposed contribution here involves adding a new quantity to the Butler-Volmer equation: the liquid water induced voltage drop function f_{drop}. This function, expressed in (2.53) and shown in figure 2.3, equals to 0 when the liquid water saturation of the cathodic catalytic layer $\mathtt{s}_{ccl}$ exceeds the limit value of $\mathtt{s}_{lim}$, resulting in an increase in overvoltage and, ultimately, a drop in voltage. When $\mathtt{s}_{ccl}$ is sufficiently far from this limit, there is no impact of liquid water on the voltage, and therefore, f_{drop} equals 1. In between, f_{drop} strictly decreases towards 0. Indeed, experimentally, the concentration drop is not abrupt and extends over a few tenths of amperes per

square centimeter. This is expressed by the fact that liquid water begins to significantly impact the voltage from a certain value of s, and this impact worsens with its increase until the stack stops. Thus, it is necessary to determine a boundary value for s at which the voltage begins to drop, even before reaching s_{lim}. The authors propose considering s_{switch}, which takes a percentage of s_{lim} as the boundary value for the start of voltage drop, as expressed in (2.54). The proportionality coefficient a_{switch} is an undetermined parameter of the model. Furthermore, f_{drop} is built as a continuous and infinitely differentiable function, which is useful to avoid any fluctuations during numerical resolution.

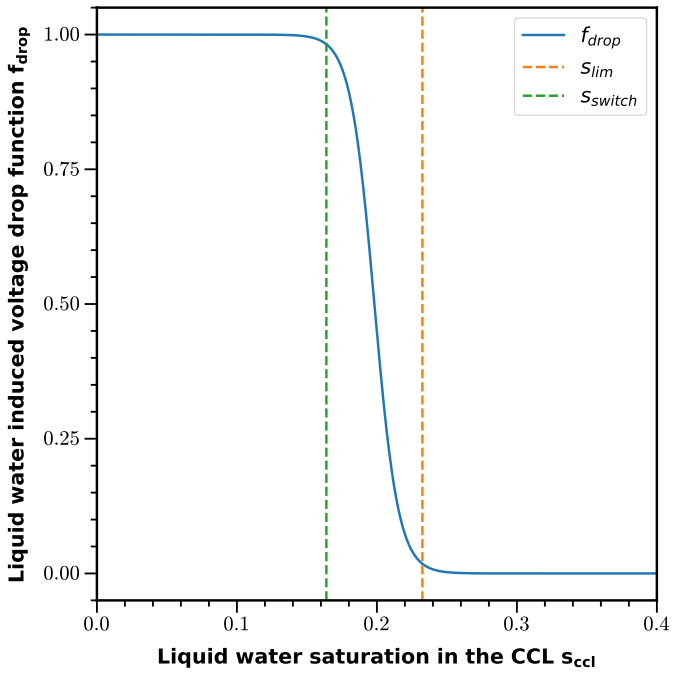

Figure 2.3. – Plot of the liquid water induced voltage drop function, expressed as a function of the liquid water saturation in the CCL, for $P_{des} = 2.5$ bar, $a_{s_{lim}} = 0.05$, $b_{s_{lim}} = 0.1075$ and $a_{switch} = 0.705$

Finally, given that s is interpreted as a hindrance to the arrival of gases in the triple point areas, it is evident that s_{lim} depends on the internal geometry of the stack materials, particularly the GDLs and CLs. Thus, its value inherently relies on the employed technology, making it impossible to establish a universal value. Even a slight modification in the porosity of the stack components would affect it. Therefore, it stands as a parameter specific to fuel cell design. Furthermore, it has been observed that s_{lim} varies with the operating conditions. It is a linear function of the desired gas pressure set by the operator P_{des}, as demonstrated by the model validation section 3.1.2. Hence, its proposed expression in (2.52) involves $a_{s_{lim}}$ and $b_{s_{lim}}$ as two new undetermined parameters. The dependence of s_{lim} on other operating conditions will be studied in future work.

2.5. Summary of the developed numerical model

Multi-physics models allow increasing the available information to better control PEM fuel cells, which is valuable considering the impossibility of placing sensors inside a cell. Currently, most existing models either provide a very detailed description of the internal states of the cell but require a very high computational cost, such as computational fluid dynamics models, or are fast but provide summary information about the cell, such as lumped-parameter models. This chapter aims to find a better compromise to combine result accuracy and execution speed. Thus, a one-dimensional, dynamic, two-phase, isothermal, and finite-difference model of the PEMFC system has been developed. It remains compatible with embedded applications and provides more precision than lumped-parameter models.

In addition, a new coefficient has been introduced to replace the limit current density coefficient (i_{lim}). This coefficient, the limit liquid water saturation coefficient (s_{lim}), also determines the voltage drop at high current densities. s_{lim} offers the added advantage of establishing a physical connection between this voltage drop, the internal states of the cell, and the operating conditions. Moreover, this parameter has been proven to be a function of the pressure imposed by the operators P_{des}.

To proceed further, in the following chapters, an experimental validation of the model is presented, an open-source software with a graphical user interface implementing this model is provided to the community, and a physical interpretation of s_{lim} is proposed.

3. Validation and practical applications of the model

Sommaire

3.1. Validation of the model

3.1.1. Calibration procedure

3.1.1.1. Overview

Experimental validation is essential to ensure that the decisions based on the model accurately reflect reality within an acceptable margin of error. Given that each fuel cell is unique and the physics of fuel cells is not yet fully understood, a set of undetermined parameters must be adjusted to align the model with the actual cell. Therefore, validation must be conducted for each system used, even if the model has previously been validated on other cells.

Experimental validation is carried out in two phases. The first phase involves calibrating the undetermined parameters of the model using a set of experimental data. The second phase is dedicated to verifying the results by comparing the model against a different set of experimental data from the same cell, with the undetermined parameters kept fixed. This approach, using different sets of experimental data, is crucial

for robust validation, although many studies rely solely on a single polarization curve, which is insufficient [94].

To enhance the robustness of the validation, a diverse set of experimental data is required, including polarization curves obtained under varying operating conditions. Electrochemical impedance spectroscopy (EIS) curves can also complement this analysis by providing detailed information about system dynamics. Additionally, cyclic voltammetry curves and spatial current density distribution curves are traditional tools used for characterizing the cell.

3.1.1.2. Calibration of undetermined parameters

Undetermined parameters refer to mathematical constants whose values are not universally defined across all fuel cell systems. These may include physical constants not disclosed by manufacturers, such as the porosity of the gas diffusion layer (ε_{gdl}), or theoretical constants that are not yet well understood, like the tortuosity coefficient (τ). Additionally, some uncertain parameters may act as correction coefficients or exponents, introduced to adjust existing equations until further experimental data becomes available, such as the corrective exponent for overpotential (κ_c). Each model possesses its own set of undetermined parameters that require specific identification by the modeler.

The calibration process is challenging due to the high number of undetermined parameters and the broad range of potential values for each. An effective approach involves using optimization algorithms, such as genetic algorithms, which, however, necessitate a large number of simulations - often exceeding one hundred thousand. To expedite the calibration process, parallel computation on multiple CPU cores and the use of a computing cluster are crucial. To make this approach feasible for a computationally expensive model, a faster, simplified model containing most of the original undetermined parameters can be temporarily used, such as AlphaPEM. Additionally, manual parameter adjustment may be required to fine-tune the calibration. The automatic calibration is addressed in section 3.2.

Manual calibration requires fewer simulations compared to automatic calibration, but can be tedious and time-consuming. To improve efficiency, undetermined parameters can be classified based on their effects on characteristic curves, thereby simplifying the procedure into more manageable steps. Table 3.1 categorizes the undetermined parameters of this work 1D model according to their impact on three types of voltage losses related to polarization curves: activation losses, ohmic losses, and mass transport losses. Each of these losses affects the curve in a specific way, enabling the calibration to be broken down into distinct steps. A "++" symbol indicates a significant impact, "+" indicates a moderate impact, and the absence of a symbol indicates no impact. This classification was inspired by Xie et al. work [94].

The vertical order of these undetermined parameters in table 3.1 has been carefully chosen to match the authors' recommendation for manual parameter modification order. Bounds have also been suggested to limit the search for each parameter. However, these bounds are only indicative and subjective, based on the authors' experience.

The following methodology should be regarded as a clarification on parameter calibration to enhance its efficiency. However, it may require adjustments, especially if the model employed undetermined parameters distinct from those used in this study. In such cases, it can serve as a foundational source of inspiration for creating one's own procedure. The calibration outlined in this study is as follows:

— It is preferable to adjust activation losses first, as this helps bring the simulated curve closer to the experimental data. For this purpose, the parameter $i_{0,ca}$ should be modified first, its impact on the curve being significant. Next, adjusting the parameter κ_{co} is necessary to obtain the correct open circuit voltage. Since κ_{co} also has a slight influence on activation losses, it may be necessary to revise $i_{0,ca}$ again before proceeding to the next step.

— Then, it is recommended to adjust ohmic losses to achieve the desired slope. For this purpose, it is suggested to start by modifying κ_c since it has a major impact on the curve. However, it also affects activation losses, so it may be necessary to slightly adjust again the two previous parameters. Subsequently, τ and ϵ_{mc} should be modified, as their impact are mainly on ohmic losses and are moderate. Finally, R_e allows for fine-tuning the curve for a direct slope adjustment of a few degrees.

— Lastly, the mass transfer losses step is reached. It is the most difficult part of the calibration procedure. It is recommended to first vary e as there are only three possible values, each with a different impact on the curve. Then, ϵ_c has a significant effect mainly on mass transfer losses, which is valuable for completing the calibration. Subsequently, both ϵ_{cl} and ϵ_{gdl} can be adjusted cautiously for more advanced calibration. Since ϵ_{gdl} can also affect ohmic losses, additional adjustments may be needed. Finally, the s_{lim} coefficients are new mathematical elements that allow for a more precise refinement of the mass transfer losses. It is necessary to use at least two polarization curves at different pressures for their calibration. These coefficients are highly sensitive to any changes but significantly and exclusively impact the mass transfer losses, which enables the finalisation of the calibration.

Finally, to the best of the authors' knowledge, it is unclear whether calibrating undetermined parameters in a PEM fuel cell model using polarization curves yields a unique set of values. It is crucial to ensure that only one specific configuration of the undetermined parameters leads to a particular polarization curve, thereby guaranteeing the model's reliability.

Undetermined physical parameters	Symbol	Default value	Typical values	Voltage loss relevance		
				Act.	Ohm.	Mass
Referenced cathode exchange current density ($A.m^{-2}$)	$i_{0,c}^{ref}$	$120 \times H_{cl}$	[0.001, 500]	++		
Crossover correction coefficient ($mol.m^{-1}.s^{-1}.Pa^{-1}$)	κ_{co}	1	[0.01, 40]	++		
Overpotential correction exponent	κ_c	2	[0, 100]	+	++	+
Pore structure coefficient	τ	1.5	[1.0, 4.0]		++	
CL volume fraction of ionomer	ε_{mc}	0.25	[0.15, 0.4]		++	
Electron conduction resistance ($\Omega.m^2$)	R_e	10^{-6}	$[5 \cdot 10^{-7}, 5 \cdot 10^{-6}]$		+	
Capillary exponent	e	4	$[3,5] \in \mathbb{N}$		+	++
GDL compression ratio	ε_c	0.2	[0.15, 0.3]			++
GDL porosity	ε_{gdl}	0.6	[0.55, 0.8]		++	++
s_{lim} coefficients (bar^{-1}, ∅, ∅)	$a_{s_{lim}}$, $b_{s_{lim}}$, a_{switch}	0.05, 0.1, 0.7	[0, 1]			++

Table 3.1. – Classification of the undetermined parameters of this model for calibration based on polarization curves

3.1.1.3. Verification of results

After calibrating the undetermined parameters, a final verification step is necessary to validate the model. This step involves assessing the model's consistency under conditions different from those used during calibration, by employing new experimental data without adjusting the undetermined parameters. However, even if this step is successful, the validation may still be incomplete. For instance, relying solely on polarization curves tests only the static aspects of the model and overlooks its dynamic behavior. Additionally, specific experimental conditions might lead to partial utilization of the model's underlying physics, such as the omission of liquid water in scenarios with high input stoichiometries. Thus, validation based on a limited dataset may be insufficient. To mitigate these limitations, it is essential to use a broad range

of experimental data.

This verification process is crucial even when the operating conditions of the system are specified by the manufacturer. Relying solely on a calibrated but unverified model can lead to misleading conclusions. For example, a single polarization curve may be accurately reproduced by the model, even if the internal states are poorly simulated. Typically, the experimental data used for validation operates on a different scale than the simulated data. Voltage is a macroscopic quantity representing the entire cell, while for instance the concentrations of each chemical species are mesoscopic and can vary spatially within the cell. Consequently, although voltage is influenced by mesoscopic phenomena, some information is lost during this scale transition. Since mesoscopic quantities are generally not measurable - except for current density and temperature - only voltage can be used for model validation. Thus, without rigorous validation, the reliability of the model's results cannot be ensured.

3.1.2. Validation of the model's static behavior

The developed model, including the matter flows, the voltage, and the auxiliaries, is implemented in Python. The corresponding programs are organized into a software package named AlphaPEM, which is freely accessible as open-source [146].

To validate the static behavior of the proposed model, a 1 kW EH-31 stack from EH Group [147], dated 2022, was utilized. The physical parameters of the stack, shown in table 3.2, were either measured in the laboratory or estimated based on conventional dimensions mentioned in the literature. Manufacturers seldom disclose these data; they typically provide only operating conditions. Subsequently, for this validation, experimental data on the same stack for different operational conditions are necessary. Here, polarization curves are employed as reference data. Among the operational conditions, it is the pressure within the stack (equal at the anode and cathode sides: $P_{a,des} = P_{c,des} = P_{des}$) that is altered, while other operational conditions remain constant. Their respective values are listed in table 3.3.

This validation only concerns the model's static behavior, since it solely relies on data representing the static states of the stack. To assess the dynamism of the model, forthcoming experiments will incorporate electrochemical impedance spectroscopy (EIS) curves. Additionally, this validation remains partial due to its utilization of operating conditions that do not fully capture the diversity of potential states within the stack, as discussed in section 3.1.3.

Symbol	Accessible physical parameter	Measured value	Estimated value
A_{act}	Active area (m^2)	$8.5 \cdot 10^{-3}$	/
H_{mem}	Membrane thickness (m)	/	$2 \cdot 10^{-5}$
H_{cl}	Catalyst layer thickness(m)	/	10^{-5}
H_{gdl}	Gas diffusion layer thickness (m)	/	$2 \cdot 10^{-4}$
H_{gc}	Gas channel thickness (m)	/	$5 \cdot 10^{-4}$
W_{gc}	Gas channel width (m)	$4.5 \cdot 10^{-4}$	/
L_{gc}	Gas channel cumulated length (m)	9.67	/

Table 3.2. – Synthesis of the accessible physical parameters for the experimental fuel cell

Symbol	Manufacturer operating conditions	Value
T_{fc}	Cell temperature (K)	347.15
P_{des}	Desired cell pressure (4 scenarios) (bar)	1.5 / 2.0 / 2.25 / 2.5
S_a / S_c	Stoichiometries (anode/cathode)	1.2 / 2.0
$\Phi_{a,des}$ / $\Phi_{c,des}$	Desired entrance humidities (anode/cathode)	0.4 / 0.6

Table 3.3. – Synthesis of the manufacturer operating conditions for the EH-31 experimental fuel cell

The model validation process begins by calibrating the undetermined parameters. This calibration involves utilizing two sets of experimental polarization curves derived from the same cell but under distinct operating conditions. These sets serve as a reference for fine-tuning these parameters until achieving convergence between the model's results and the observed experimental outcomes. Here, the maximum voltage deviations ΔU_{max} between the model and experimental curves are below 1.2 %, indicating an excellent calibration. These curves are depicted in figure 3.1 (the two dashed curves, at 2.0 and 2.25 bar), and their corresponding calibrated values are provided in table 3.4. Subsequently, the second validation step involves comparing the model outcomes with new experimental data obtained from the same cell, without altering any of the calibrated parameters, under varying operating conditions. It is also noted that the tested data is under operating pressure outside the pressure range used for calibrating the model parameters. The model overfitting can therefore be excluded in the validation phase. Similarly, the maximum voltage deviation ΔU_{max} between the model and experimental curves is low, below 1.8 %. This result is shown in figure 3.1 (the solid line curve at 2.5 bar). Hence, the model's static behavior has been validated through experimentation.

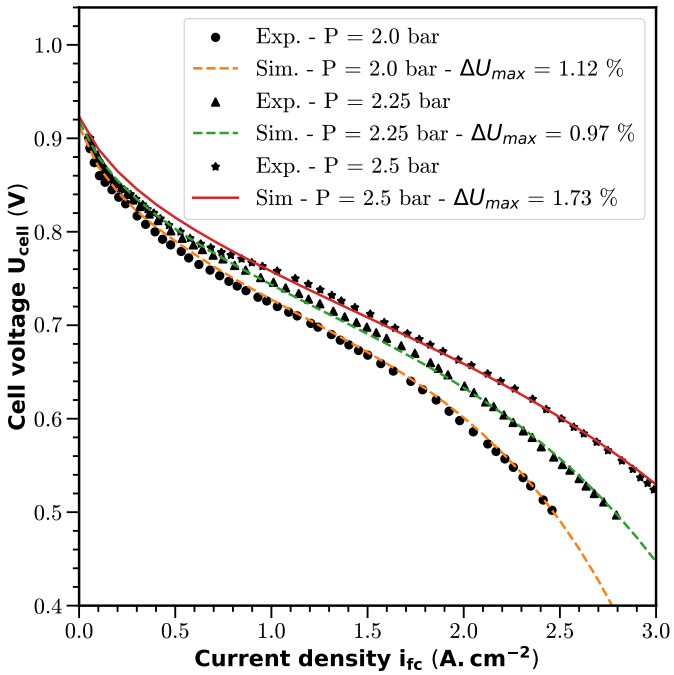

Figure 3.1. – Comparison of polarization curves between simulation and experiment to validate the model's static behavior.

Symbol	Undetermined physical parameters	Calibrated value
$i_{0,c}^{ref}$	Referenced cathode exchange current density ($A.m^{-2}$)	2.79
κ_{co}	Crossover correction coefficient ($mol.m^{-1}.s^{-1}.Pa^{-1}$)	27.2
κ_c	Overpotential correction exponent	1.61
τ	Pore structure coefficient	1.02
ε_{mc}	volume fraction of ionomer in the CLs	0.399
R_e	Electron conduction resistance ($\Omega.m^2$)	$5.70 \cdot 10^{-7}$
e	Capillary exponent	5
ε_c	GDL compression ratio	0.271
ε_{gdl}	GDL porosity	0.701
$a_{s_{lim}}$, $b_{s_{lim}}$, a_{switch}	s_{lim} coefficients (bar^{-1}, ∅, ∅)	0.056, 0.105, 0.637

Table 3.4. – Synthesis of the calibrated undetermined parameters for the EH-31 experimental fuel cell

3.1.3. Limits of the model

Despite the excellent agreements observed in section 3.1.2 between the experimental and model results at pressures of 2.0, 2.25, and 2.5 bar, the comparison is less favorable at a lower pressure of 1.5 bar, as illustrated in figure 3.2. Specifically, the

error remains low for current densities below 1.3 $A.cm^{-2}$, with ΔU_{max} = 1.5 % within this range, but increases significantly for higher current densities.

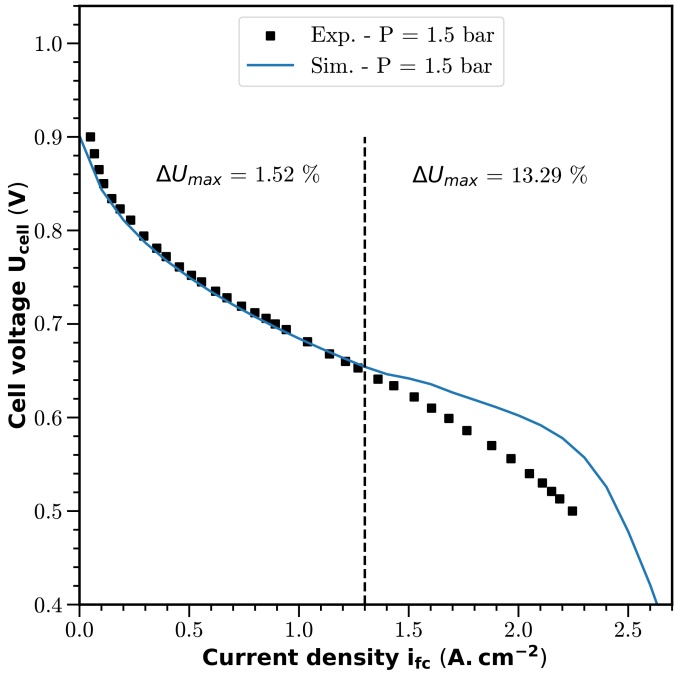

Figure 3.2. – Comparison of polarization curves between simulation and experiment at 1.5 bar.

This variation arises from the condensation of water within the cell, starting exactly from i_{fc} = 1.3 $A.cm^{-2}$, whereas liquid water was consistently present for all current density levels in previous experiments. It is plausible that the limited theoretical understanding of water sorption in catalytic layers causes inaccurate simulation of the transition from a humid gas without condensed water to a gas saturated with vapor and with liquid water. This could result in the significant errors observed in this simulated voltage. Thus, the authors urge the scientific community to enhance the theory describing the evolution of water in its various states within each cell.

It is also conceivable that this deviation arises from the methodology employed by stack manufacturers in experimentally measuring the polarization curve. If the measurement is conducted dynamically rather than statically, it could impact the results. Dynamic measurement of the polarization curve involves initially balancing the stack at a nominal operating point, then rapidly sweeping through the entire current density range without achieving perfect equilibrium for each current density. Consequently, if the stack lacks adequate time for proper balancing, the amount of liquid water at a given current density might differ compared to a static scenario, resulting in disparities in the measured concentration drop. This effect could be particularly pronounced at a pressure of 1.5 bar, as the nominal operating point might not initially yield liquid water, for instance, if sets at 1.0 $A.cm^{-2}$, unlike in other

considered scenarios. Hence, new polarisation curve tests with assured equilibrium at each current density point would be imperative to verify this hypothesis.

Additionally, it is crucial to acknowledge the limited scope of validating a PEM fuel cell model solely based on three polarization curves. These curves, which vary only in pressure from 2.0 to 2.5 bar, fail to encompass the full range of physical scenarios occurring within one cell. Indeed, the transition between a humid gas without liquid water and a gas saturated with vapor containing liquid water is notably absent with these operating conditions. Consequently, the accuracy of the results is contingent upon specific conditions, rendering the model unreliable for all scenarios. It would be beneficial to develop a routine, under specified operating conditions, that ensures comprehensive coverage of all relevant physical phenomena within the cell, for its static validation with polarization curves.

3.2. AlphaPEM open-source software

This thesis introduces AlphaPEM, the first open-source, isothermal, two-phase, 1D dynamic model for PEM fuel cell systems [146]. It is designed for real-time model-based diagnosis and control implementation within embedded systems, balancing precision and execution speed. It simulates the dynamic evolution of internal states of the fuel cell, its auxiliaries, and the resultant voltage based on the operating conditions and imposed current density. This software package is written in Python for its readability and ease of writing. It is deployed in open-source with GNU General Public License v3.0 [148]. The modular design of the code allows for easy addition of new features, such as incorporating heat transfer within the fuel cell. Despite the complex physics involved, the code is well-written following the informatics standards [149] and documented to facilitate its uptake and continuous improvement by the community. AlphaPEM is implemented as a Python class to ease its open-source distribution, leveraging SciPy's classical solver for ordinary differential equations (ODEs). The finite difference problem is solved using SciPy's 'solve_ivp' function [145], employing the implicit 'BDF' method due to the stiff nature of the problem arising from nonlinearities and coupled variables in the ODE system.

The AlphaPEM software package quickly simulates the internal states and voltage dynamics of PEM fuel cell systems for all current densities and operating conditions imposed on it. In particular, it is possible to apply a step current density or use current profiles to generate polarization curves or electrochemical impedance spectroscopy (EIS) curves. The package includes databases from various real fuel cells [33, 94, 150, 151] to facilitate its adoption and allows users to freely insert characteristics of other fuel cells. An automated program for calibrating undetermined parameters is included in AlphaPEM. These parameters are calibrated using the genetic algorithm 'geneticalgorithm2' [152], a maintained fork of the widely-used open-source Python program 'geneticalgorithm' [153]. A graphical user interface is also included to facilitate initial use before delving into the code. Finally, AlphaPEM can be used to compare the results of similar models or assist in the calibration of undetermined parameters in more precise models for which computational time does not allow for accurate calibration within a reasonable timeframe.

To use AlphaPEM, it is necessary to install a certain number of packages beforehand.

```
1 git clone https://github.com/gassraphael/AlphaPEM.git # clone the
      repository
2 cd AlphaPEM                  # navigate to the project directory
3 python3 -m venv env          # creation of a new python environment
4 source env/bin/activate      # activation of the environment
5 pip install --upgrade pip # update the Python package manager pip
6 pip install numpy scipy matplotlib              # required packages
7 pip install colorama geneticalgorithm2          # required packages
8 python3 -m pip install git+https://github.com/RedFantom/ttkthemes
```

3.2.1. Software architecture

The software architecture of AlphaPEM consists of five directories, each containing several Python files. The root of the software package contains the 'main.py' and 'GUI.py' files. One of these two files must be run to operate the simulator, as they both control the entire software. The 'main.py' file is used for the standard operation of AlphaPEM for programmers. The 'GUI.py' file, which is optional, provides a graphical user interface (GUI) for AlphaPEM to facilitate its use without delving into the program's details. All basic functionalities are included in the GUI without requiring any modifications to other files. However, the GUI does not allow for the calibration of undetermined parameters. The program's results are saved in the '/results' directory.

Next, the directory '/model' contains all the Python files related to the model's physics, such as 'dif_eq.py', which includes the system of differential equations to be solved. The file 'AlphaPEM.py' contains a class of the same name that represents PEM fuel cell simulators. An object of the AlphaPEM class takes as arguments the set of parameters defining a given fuel cell system, its operating conditions, the imposed current density, and the computing parameters. It returns the evolution of the voltage and all internal states over time. A 'control.py' file is also present, which contains the instructions for dynamically controlling the operating conditions of the fuel cell using the information provided by the model.

The '/modules' directory contains all the Python files that serve as modules for other files. Indeed, to improve the readability of the previous programs, some of the less essential instructions have been written as separate functions and placed in these module files. Each of these module files is named to directly refer to the file it is associated with. For example, 'flows_modules.py' is used in 'flow.py'. Additionally, a file named 'transitory_functions.py' is present in this directory and is used in most other programs in the package. It contains a set of mathematical functions that have physical significance for the model, such as the saturation pressure of water vapor.

Finally, the directory '/calibration' contains all the information necessary for calibrating the undetermined parameters of the model. The file 'parameter_calibration.py' includes the program for performing the calibration, the file 'experimental_values' contains the experimental information of the fuel cell system that the simulator must represent, the file 'run.sh' contains the instructions to send to the computing cluster to perform the calibration, and the directory '/calibration/results' contains the calibration results.

Figure 3.3 represents the structure of AlphaPEM, highlighting the dependencies between the Python files. Each box represents a Python file, with an associated number indicating its location within the software package. An arrow from file A to file B indicates that information from file A are imported into file B. The colors associated with certain boxes and their outgoing arrows improve readability and specifically indicate where these files are imported. This is necessary due to the program's complex overall structure. The boxes that remain black indicate no ambiguity regarding the destination of their arrows. To further enhance readability, the arrows conventionally point from bottom to top or are horizontal. Thus, the files most frequently used by

other parts of the program are located towards the bottom of the diagram, while the files executed by the user to start the program are at the top.

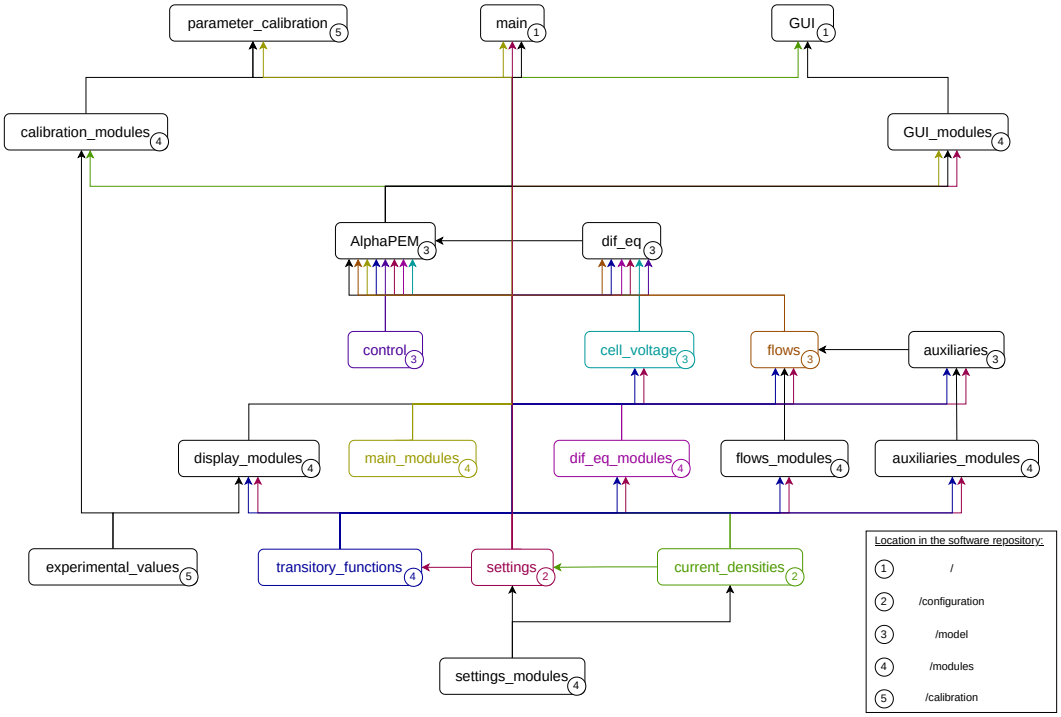

Figure 3.3. – The main structure of AlphaPEM.

3.2.2. Software functionalities

The usage of the software package AlphaPEM is illustrated by the graphical user interface present in the file '/GUI.py' and displayed in figure 3.4. All the features offered by this GUI are accessible through the files '/main.py' and '/configuration/settings.py'. A fuel cell is characterized by the operating conditions under which it is run (temperature, pressures, stoichiometries and humidities at both anode and cathode), its accessible physical parameters (such as the active area), and its undeterminated physical parameters (such as the tortuosity of the GDL). All these parameters can be adjusted by the user, and predefined configurations based on existing cells can be selected in the 'Fuel cell:' dropdown menu.

Other adjustable parameters exist, here hidden in the GUI to avoid overloading the display. On one hand, the current density parameters allow for the adjustment of the shape of the step current density, or the current density required to create polarization or EIS curves. On the other hand, the computing parameters enable modification of numerical settings, such as the number of points in the numerical model placed in the gas diffusion layer, or the purge times of the stack.

Next, different simulation options can be selected from the 'Model possibilities' menu. It is possible to configure the auxiliaries of the studied fuel cell system as follows: a 'no auxiliaries' system, where matter flows are instantly adjusted to the correct operating conditions at the fuel cell inlet and all gases are evacuated without recirculation; a 'closed cathode with anodic recirculation' system, where the remaining humidified hydrogen at the fuel cell outlet is re-injected at the inlet; or a 'closed cathode with flow-through anode' system, where the anode configuration resembles that of the cathode, with humidified fuel inserted in excess at the inlet and directly evacuated at the outlet. Depending on the selected configuration, the physical modeling of auxiliaries is adjusted, impacting the boundary conditions of the fuel cell system's cells.

Additional options include enabling or disabling control over the operating conditions, choosing the presence or absence of an anode purge, selecting a synthetic or detailed display of results, and displaying results either only at the end of the simulation or with frequent updates during the calculation.

Finally, once these choices are made, the user can generate the model results, which include the internal states (discussed section 3.3) and the voltage of the fuel cell stack, either from a current density step, or a current density producing a polarization curve or an EIS curve. The GUI limits the simulation possibilities to these three types of current densities, but from the source code, it is possible to use any physically acceptable function.

To enable AlphaPEM to simulate a new fuel cell, it is necessary to calibrate certain undetermined physical parameters so that the software results can correspond to the actual cell. Indeed, there are several physical parameters dependent on the specific fuel cell used that are difficult to obtain without the manufacturer's information, such as the porosity of the gas diffusion layers. These parameter values can be approximated using experimental data from the fuel cells. To do this, the user can perform automated calibration of the undetermined parameters using the AlphaPEM Python file '/calibration/parameter_calibration.py'. This functionality is not available from the GUI. It is necessary to input the experimental values of polarization curves under different operating conditions in the file '/calibration/experimental_values' (at least three curves), as well as the operating conditions and accessible physical parameters of the studied fuel cell system in the file '/modules/calibration_modules'.

This automated calibration uses a genetic algorithm. The parameters of this algorithm have been adjusted for this specific optimization problem to achieve a good balance between the accuracy of the calibration and execution speed. These parameters are shown in table 3.5. Only the population size and the maximum number of iterations can be modified to match the available computing capacity. It is preferable to have the population size between 100 and 200 individuals and to choose a number that is a multiple of the number of available CPU cores to utilize them fully, as the calculations are parallelized for each member of the same population. The number of iterations should be as large as possible, typically around 1000 to 1500 generations for effective calibration. It is worth noting that the calibration can be resumed from where it previously stopped, allowing multiple computation sessions to finally achieve

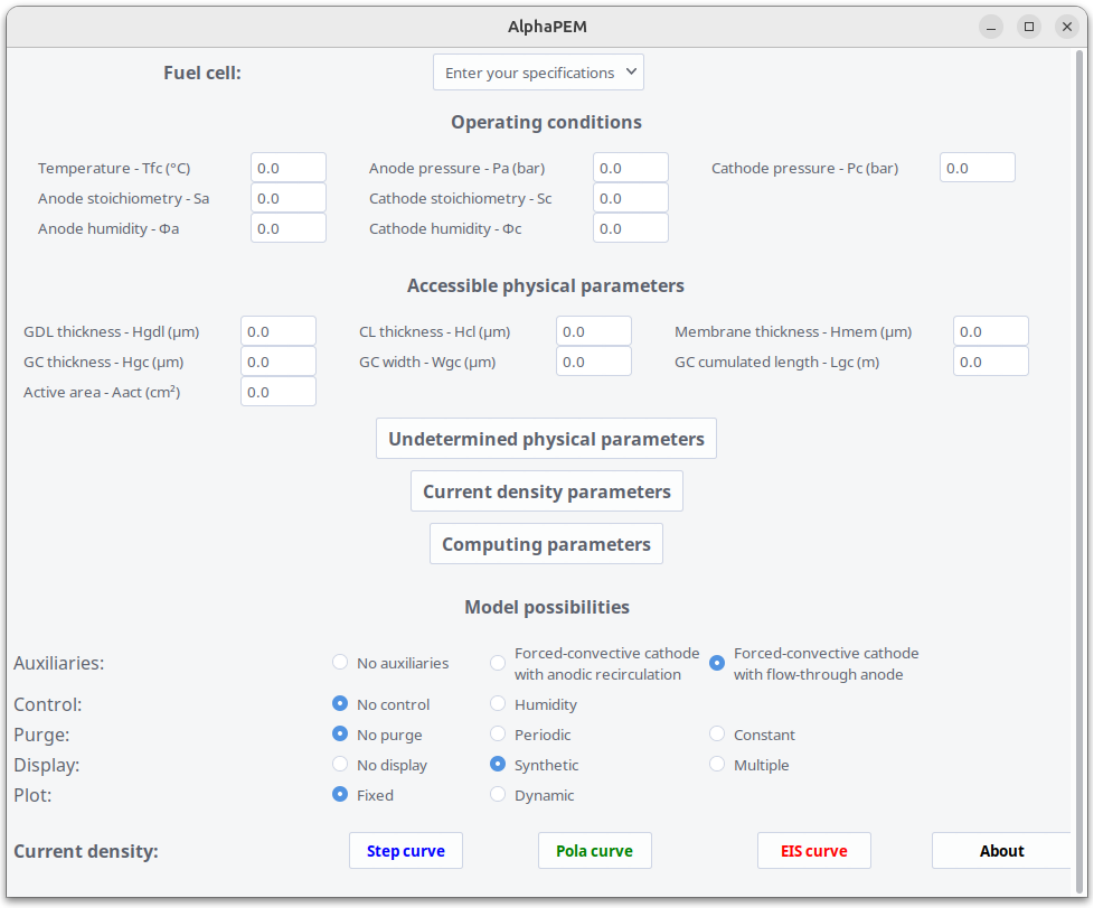

Figure 3.4. – AlphaPEM graphical user interface.

a satisfactory result.

Finally, it is preferable to use a computing cluster with many CPU cores for calibration. As an example, the authors successfully performed a calibration with a maximum error of 1.06% between the experimental and simulated data, after two weeks of calculations on a server equipped with 80 Intel(R) Xeon(R) Gold 6338 CPU cores @ 2.00GHz.

3.2.3. Software computational efficiency

1000s current density step simulation was conducted on a workstation featuring an Intel Core i9-11950H @ 2.60 GHz processor and required 17s of computation time. Simulating a polarization curve takes 9s. Therefore, the model implemented within AlphaPEM operates within the same order of magnitude as other 1D simulators mentioned in the literature [52], is two orders of magnitude faster than a 1D model from commercial software like COMSOL Multiphysics®[52], and four to five orders of magnitude faster than 1D+1D, 3D+1D, or 3D models from the literature [94, 132, 137]. The computation times obtained by AlphaPEM are thus compatible with uses in

Parameters	Values
Number of iteration	1500
Population size	160
Mutation probability	$0.33/nb\_undetermined\_parameters$
Elit ratio	$1/population\_size$
Parents portion	0.2
Crossover type	'one_point'
Mutation type	'uniform_by_x'
Selection type	'roulette'

Table 3.5. – Optimised genetic algorithm parameters for AlphaPEM.

embedded applications.

3.3. Tracking internal state variables

Under an arbitrary dynamic operating condition, the developed model enables monitoring within a cell of the water evolution, whether in the form of vapor, liquid, or dissolved matter in the membrane, characterized respectively by the variables C_v, $\mathfrak{s}$, or λ. It also tracks the evolution of dihydrogen, dioxygen, and nitrogen, characterized by the variables C_{H_2}, C_{O_2}, and C_{N_2}. These variables are evaluated at several nodes within the cell, and the variables with indices agdl or cgdl refer to the node in the center of the corresponding GDL. Additionally, data regarding matter flows between these nodes (J) are also accessible. Furthermore, the evolution of pressures P and humidities Φ within the auxiliary manifolds can also be tracked. Finally, the cell voltage over time U_{cell} is calculated from these internal states.

Several results of the calibrated model are shown in figures 3.5, 3.6 and 3.8, under pressure P_{des} = 2.0 bar. In this study case, a step-shape current density is applied, ranging from 0 $A.cm^{-2}$ to 0.5 $A.cm^{-2}$ at the start of the experiment, and then from 0.5 $A.cm^{-2}$ to 1.5 $A.cm^{-2}$ at 500s, as seen in figure 3.5a. The variables are initialized to the values they would have in steady-state conditions, with zero current density, if they were subjected to the pressure, humidity, and temperature of the desired operating conditions. For simplicity, it is assumed that the variables within each cell are initially subject to the average of the anodic and cathodic pressures and humidity. The experiment virtually lasts 1000s.

The advantage of performing a double step-shape current density is to eliminate the need for initial condition values in the analysis of the results. Indeed, the first step-shape current density allows the system to reach a steady state within the fuel cell, with a waiting time of 500 seconds. Since the fuel cell is controlled, it will always reach the same steady state regardless of its initial conditions, which only influence its transition to this stationary state. Thus, after around 500 seconds, the fuel cell operates in a state with realistic internal values. The second step-shape current density can then be studied under standardized conditions.

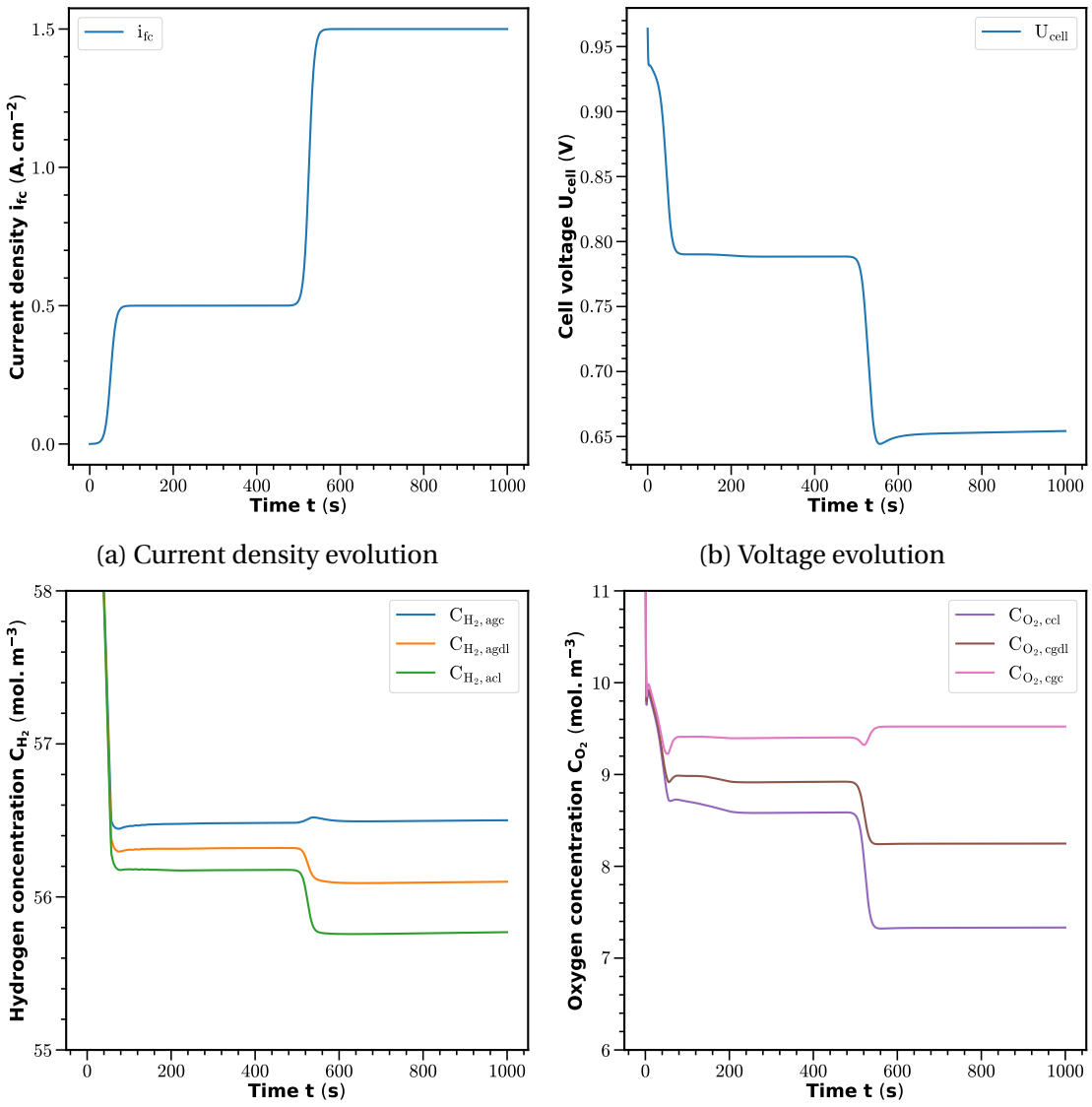

(a) Current density evolution

(b) Voltage evolution

(c) Hydrogen evolution

(d) Oxygen evolution

Figure 3.5. – Internal states of a PEM fuel cell system for two current density steps, computed by AlphaPEM (1/3).

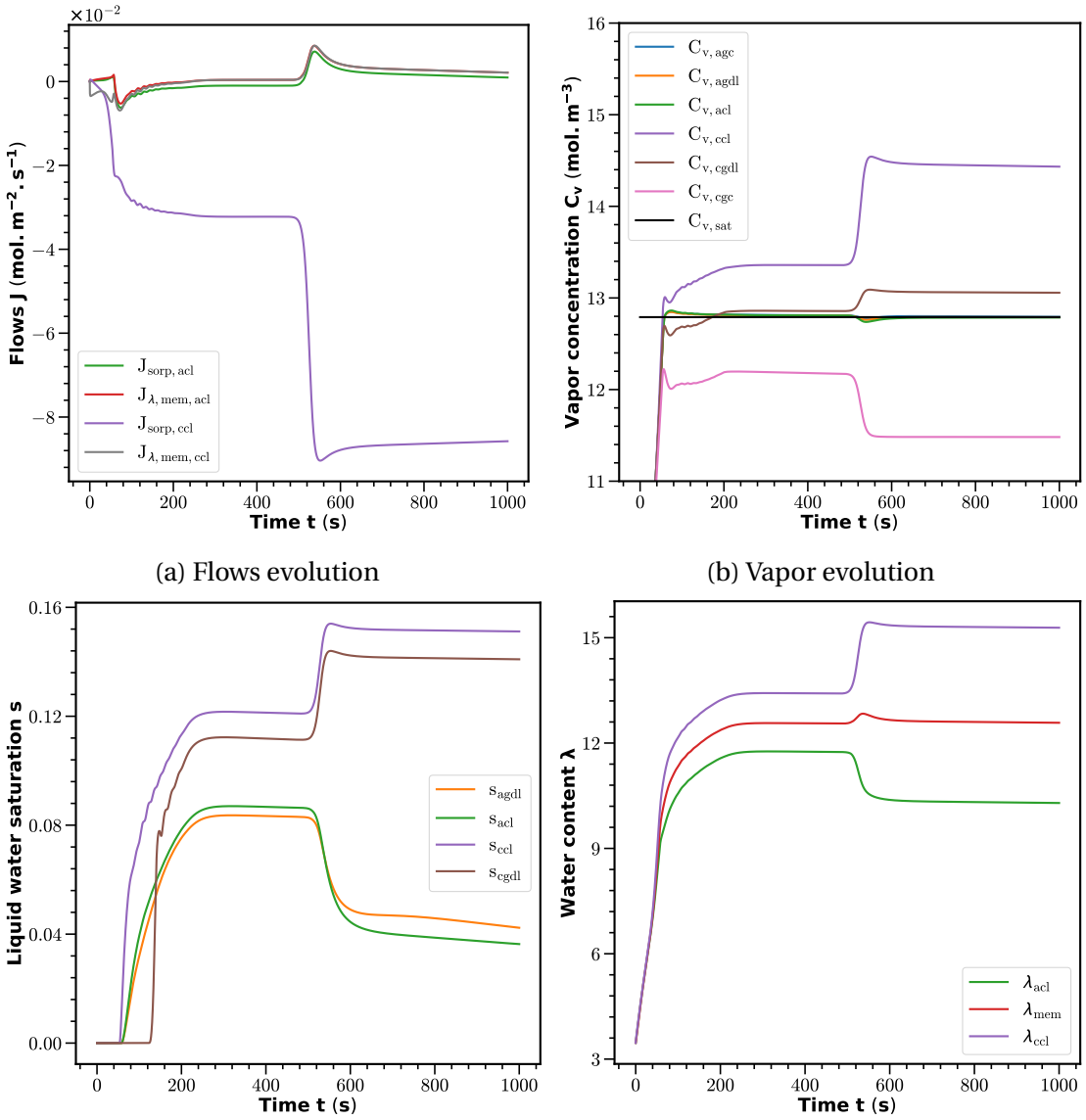

(a) Flows evolution

(b) Vapor evolution

(c) Liquid water evolution

(d) Dissolved water evolution

Figure 3.6. – Internal states of a PEM fuel cell system for two current density steps, computed by AlphaPEM (2/3).

The results generally follow the expected pattern within the cell: an increase in current density leads to increased flows, reduced reactants, and increased water content. However, it is necessary to further examine certain variables to clarify their behavior. Firstly, the reactants in the bipolar plates, characterized by $C_{H_2,agc}$ and $C_{O_2,cgc}$ figures 3.5c and 3.5d, do not exhibit significant changes and tend to slightly increase, unlike the reactants in the membrane electrode assembly (MEA) $C_{H_2,agdl}$, $C_{H_2,acl}$, $C_{O_2,cgdl}$ and $C_{O_2,ccl}$. This can be explained by the fact that $C_{H_2,agc}$ and $C_{O_2,cgc}$ are less sensitive to the chemical activity within the MEA, as the stack is designed to stabilize the pressure within the bipolar plates using a backpressure valve. The slight

fluctuations are attributed to changes in the composition of this gas mixture, with a decrease in vapor concentration ($C_{v,agc}$ and $C_{v,cgc}$ figure 3.6b) occurring at high currents due to its expulsion by the increased gas flow rates involved.

Then, it is surprising that the behavior of water at the anode differs from that at the cathode, regardless of its form (vapor with $C_{v,agdl}$ and $C_{v,acl}$ figure 3.6b, liquid with s_{agdl} and s_{acl} figure 3.6c, or dissolved with λ_{agdl} and λ_{acl} figure 3.6d): it decreases with current density (except at low currents < 0.5 $A.cm^{-2}$ where it increases with current density, even after leaving the initial state). This can be explained by the existence of two opposing phenomena. On one hand, more water is created at the cathode with increasing current and passes through the membrane towards the anode. On the other hand, the flow of gases circulating in the bipolar plates also increases, making it easier to remove water from the MEA. As these flows are of the same order of magnitude, it is not easy to predict the evolution of water vapor in the anode. This depends on several parameters, such as the stoichiometry and geometric parameters like the thicknesses of the membrane and the thicknesses of the MEA. To illustrate this point, the same experiment was repeated with a threefold reduction in the thickness of the membrane and the catalytic layer, significantly reducing the resistance of the membrane to the passage of water from the cathode to the anode. Thus, the decrease in liquid water at the anode side is no longer visible and has been replaced by an increase, as shown in Figure 3.7.

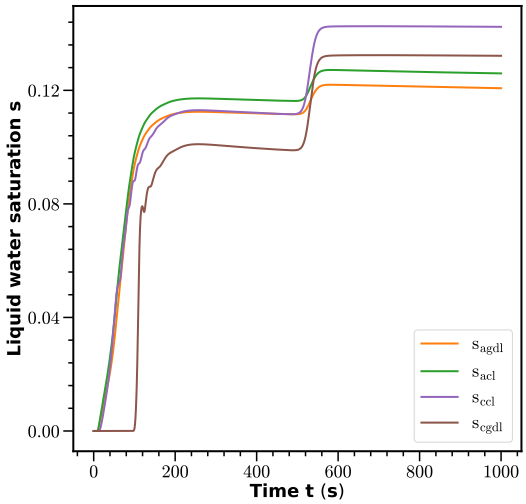

Figure 3.7. – Evolution of liquid water within the cell for a membrane and a catalytic layer three times thinner.

Furthermore, the impact of auxiliary dynamics is particularly evident in the evolution of oxygen concentrations with $C_{O_2,cgc}$ figure 3.5d, or equivalently P_{cgc} figure 3.8a (which influences $C_{O_2,cgdl}$ and $C_{O_2,ccl}$), leading to fluctuations in concentrations with each change in current density. This phenomenon does not occur when the cell is modeled without auxiliaries. However, in this model, the other variables are less affected than $C_{O_2,cgc}$ by the presence of auxiliaries.

However, there is a fluctuation in most internal states when a current density step is crossed, especially concerning water (see $C_{v,ccl}$ figure 3.6b for example). It is characterized by a slight overshoot in the equilibrium value. This can be explained by the sudden increase in current that causes a sudden production of water in the cell. The discharge of this water is not sudden and possesses some inertia, leading to a transient over-accumulation of matter, namely a peak. This observed dynamic phenomenon is of interest, considering that the amount of water can affect the cell's voltage and potentially damage it. Thus, in energy management strategies, it might be interesting to slow down this increase in current density attributed to the fuel cell by temporarily compensating the energy demand with other electricity sources, such as batteries. Consequently, these observed peaks will disappear.

Next, liquid water saturation sometimes evolves with slight fluctuations, notably observed figure 3.6c around $200s$ for s_{ccl} and s_{cgdl}. These fluctuations subsequently impact other variables, such as $C_{v,cgdl}$, $C_{v,cgc}$, $S_{sorp,acl}$, $J_{\lambda,mem,acl}$, $S_{sorp,ccl}$, and $J_{\lambda,mem,ccl}$. These are minor numerical errors resulting from an insufficiently high number of nodes in each GDL, as discussed in section 2.2.1.1. Here, it was chosen not to use an excessively high number of nodes to avoid significantly increasing computation times, even at the cost of a slight loss in precision in the results. Indeed, quadrupling n_{gdl} is necessary to achieve nearly perfectly smooth results, which triples the computation times.

It is also noteworthy to observe that water vapor concentrations C_v can exceed the saturation vapor value $C_{v,sat}$ figure 3.6b. This can be explained by the dynamic equilibrium at stake. On one hand, surpassing the water vapor saturation threshold triggers the condensation of this vapor into liquid water. However, this condensation is not instantaneous and depends on a time constant γ_{cond} embedded within the model. On the other hand, the stack continues to produce large amounts of water that feed into the water vapor. Indeed, in this model, it has been assumed that water production occurs necessarily in a dissolved manner. The current state of research does not allow us to determine in what form water appears immediately after the chemical redox reaction between hydrogen and oxygen [45, 46]. A choice must therefore be made. Furthermore, in this model, the water flows between the membrane and the catalytic layer necessarily occur between a dissolved form and a vapor form. Only thereafter is condensation possible. Water production in the cell therefore directly involves vapor water supply. The supply flow of water vapor and condensation thus oppose each other, resulting in a dynamic equilibrium that can exceed the saturation vapor point, as long as the cell operates. If the time constant associated with condensation, γ_{cond}, is increased sufficiently, this phenomenon disappears, and C_{sat} becomes the actual limit of the water vapor concentration. However, the value chosen for γ_{cond} in the authors' model corresponds to that recommended by Hua Meng in a dedicated study [68]. Thus, this oversaturation phenomenon is acceptable.

Inside the auxiliaries, it is also remarkable to note that the pressure difference between the manifolds and the bipolar plates, shown figure 3.8a, is low in this model, on the order of 1 to $10Pa$, which is not realistic. This stems, on the one hand, from the unmodeled pressure losses, and on the other hand, from the choice of equations

(2.32), (2.34), (2.36), (2.41), and (2.42) which concern the incoming or outgoing matter flows from the manifolds and are based on simplifying assumptions. This is an aspect that needs improvement in the model.

Moreover, it is interesting to discuss the evolution of humidity in the auxiliaries, as shown in the curve 3.8b. The supply manifold receives a controlled water flow which is at the desired humidity level, while also delivering a water flow to the cell. It stabilizes at a value lower than the desired humidity. This is a consequence of the chosen humidity control strategy, which focuses on the water flow entering the supply manifold rather than the humidity level within the supply manifold itself. Additionally, it can be observed that the humidity in the exhaust manifold stabilizes at the same level as the humidity in the gas channel. This humidity also corresponds to that of the flow exiting the cell, as the current model is one-dimensional.

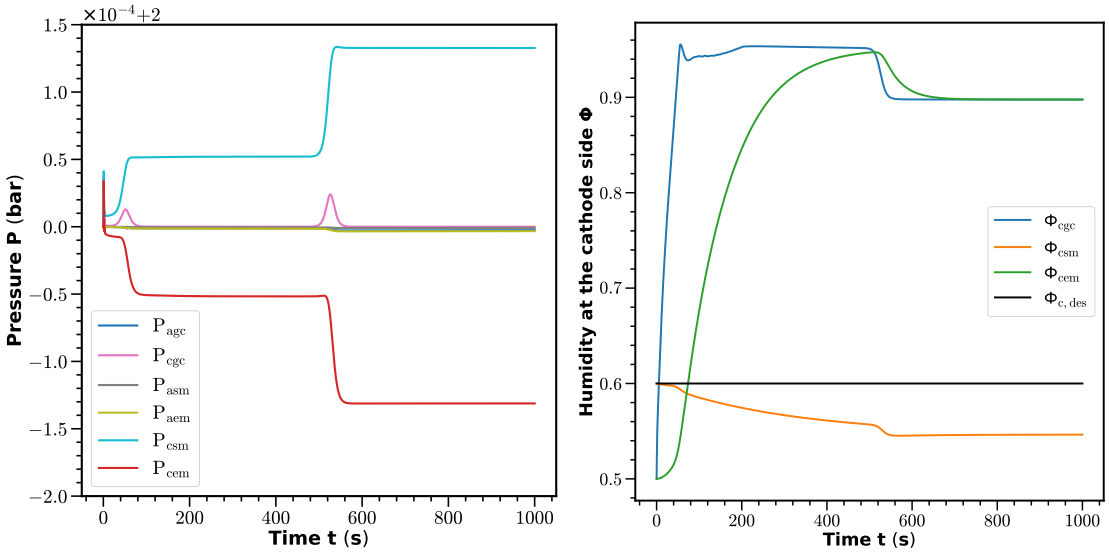

(a) Pressures evolution

(b) Humidity evolution at the cathode side

Figure 3.8. – Internal states of a PEM fuel cell system for two current density steps, computed by AlphaPEM (3/3).

3.4. Summary of validation and software implementation

This chapter presents AlphaPEM, an open-source, user-friendly, and modular software package in Python, designed for PEM fuel cell modeling for embedded applications. This framework is based on the 1D finite difference, dynamic, biphasic, and isothermal model of PEM fuel cell systems proposed in the previous chapter. Its static behavior has been validated against several published experimental polarization curves. It employs a solver using an implicit numerical method to solve the system of differential equations.

In practice, AlphaPEM provides real-time access to the internal states and the voltage of the fuel cell systems and can generate polarization and EIS curves. It can also automatically calibrate the model's undetermined parameters to fit any real fuel cell system. This model runs two orders of magnitude faster than 1D models from the commercial software Comsol Multiphysics and up to five orders of magnitude faster than 3D models from the literature. This simulator, therefore, paves the way for improving the real-time control of the operating conditions of fuel cell systems to enhance their performance and longevity.

To proceed further, in the following chapters, propositions for improvement and reuse of this model are given, such as enhancing cell performance through inlet humidity control, details on EIS curve modelling and its use for having an EIS analysis tool, and finally a state-space representaton of a reduced version of the model.

4. Propositions for improvement and reuse of the model

Sommaire

In this chapter, various seeds of innovations enabled by the model developed during this thesis are proposed for exploration. These different proposals correspond to ongoing exploratory work under development and validation. They may serve as a foundation for future research.

4.1. Introduction of the limit liquid water saturation coefficient (s_{lim})

In section 2.4.1, the limit liquid water saturation coefficient s_{lim} was introduced into the overpotential equation, with an initial description provided in section 2.4.3. Here, a physical interpretation is proposed to concretely understand why liquid water affects

the overpotential. The limitations of such an interpretation are also discussed. Finally, a theoretical proposal to improve fuel cell performance by controlling its incoming humidity is explored using this new coefficient s_{lim}.

4.1.1. Theory of s_{lim}

A potential physical explanation for the voltage drop induced by the presence of liquid water in the fuel cell is proposed in this section. It is inspired by an environmental scanning electron microscope (ESEM) image provided by Gerteisen et al. [154]. This explanation is the basis for the decision to implement s_{lim} in the overpotential equation (2.51) and not elsewhere. The phenomenon proposed here requires looking into the catalyst layers, inside their pores. In a healthy environment, that is, without the presence of liquid water and without significant degradation of the cells, hydrogen and oxygen can easily reach their respective triple point zones to initiate the chemical reaction. The fuel cell is designed for this purpose. However, this forced displacement, illustrated in Figure 4.1a, comes at a cost: part of the cell's voltage is sacrificed. This is the overpotential. Nevertheless, the accessibility of each triple point zone is not uniform locally. Some are easily accessible, meaning they incur less overpotential, while others are more challenging to reach. The former are represented by green arrows, the latter by red arrows.

However, when liquid water appears, the areas that were previously easily accessible may become difficult to access, depending on the local geometry and where the water has condensed. This can significantly increase the overpotential, even without liquid water quantity being very high. Indeed, at this scale, water doesn't fill the pores like a glass of water filling up linearly from bottom to top. Water condenses on the material, forming tiny droplets across the pore surface, as depicted in figure 4.1b. These droplets may interconnect and initiate their movement out of the pore by following the capillary pressure gradient. In certain areas, they remain unconnected, forming immobile liquid water. As a result, several pathways that were previously easily accessible now necessitate traversing water droplets before reaching the triple point zones. Subsequently, hydrogen or oxygen must dissolve into the liquid water. This circumstance potentially renders the triple point zones difficult to access, thereby impacting the overpotential. The authors suggest that an average amount of liquid water, measured by the liquid water saturation variable `s`, between 20% and 40%, depending on the cells and operating conditions, can cause the voltage to drop to 0. It is not necessary for the cell to be completely flooded, meaning having a liquid water quantity almost equal to 100% of the pores volume, for the voltage drop to occur.

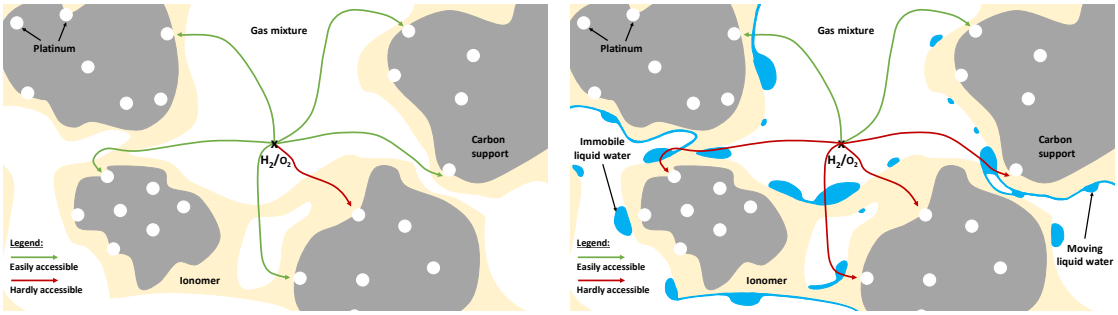

(a) Accessibility of triple point zones without liquid water

(b) Accessibility of triple point zones in a partially flooded environment

Figure 4.1. – Accessibility of triple point zones by H_2 and O_2 within the pores of their respective catalytic layer

This physical explanation presents a new perspective on the commonly termed "concentration drop" region within the polarization curves. When fuel cells become flooded before reaching their intrinsic gas diffusion limits during increased current density, which is typically the scenario, the observed voltage drop is no longer due to concentration drop, as the matter remains within the catalyst layers. Instead, it is caused by an activation drop intensified by the presence of liquid water at high current densities.

4.1.2. Limits of s_{lim}

Two criticisms can be made to the previous physical explanation. Firstly, oxygen and hydrogen can dissolve in liquid water and cross this water barrier. To author's knowledge, it is not currently known to what extent this resistance is significant. It might be negligible or could represent just one among several phenomena involving liquid water that cause a voltage drop within the cell. The second criticism arises from the work of Dickinson et al. [108], as highlighted in 1.3.3.1, which advises against the common practice of modifying the Butler-Volmer equation to obtain model results closer to experimental data, as has been done here. Indeed, the Butler-Volmer equation serves as a significant approximation of the redox reaction occurring within the fuel cell, as it theoretically applies to a single-step reaction, while the redox equations in the electrodes involve multiple steps. Given the inherently simplistic and reductionist nature of the Butler-Volmer theory, there is no substantiated indication that such modifications would be effective. Introducing such alterations may pose a potential risk of augmenting the model's instability and complexity without delivering tangible benefits.

There is another perspective that can explain this voltage drop, observed due to a partial presence of liquid water. However, this view requires a more complex implementation within the equations and has therefore not been considered in this study. This other perspective requires looking into the gas diffusion layers, inside their pores. The structure within these pores differs from that of the catalyst layers,

yet the proposed principle remains the same. Without liquid water, gas transport is straightforward, whereas with liquid water, even if it only partially fills the pores, gas transport becomes more challenging. However, in this scenario, gases do not need to be transported to the GDL borders; they simply traverse this structure. Thus, the resistance to transportation arises not because gases need to dissolve in the liquid water to traverse it (or marginally), but because they must navigate around it. Since the pore volume is only partially submerged, paths leading to the CLs still exist. Consequently, gas trajectories are significantly disrupted, potentially explained by a notable increase in tortuosity. This can be viewed as a structural change in the GDLs, resulting in an increase in their tortuosity. Moreover, considering that the GDLs' thickness is on average twenty times greater than that of the CLs, this cumulative impact could be significant, potentially rivaling or even surpassing the previously proposed explanation.

In this physical description, voltage drop corresponds to a concentration drop, whereas previously the impact of liquid water in the CLs resulted in increased activation losses at high current densities. Indeed, with a more challenging matter transport, the effective gas diffusion coefficient within the GDLs, $D_{i/j}^{eff}$, drops. This reduces the maximum flows of reactants that can be supplied to the CLs and consequently leads to concentration losses at high current densities. Thus, there is no need to modify the equations governing the cell voltage to consider this physical phenomenon, which allows to remain in line with the cautions expressed by Dickinson et al. [108]. Solely adjusting the effective gas diffusion coefficient in the GDLs is adequate to indirectly consider the concentration losses magnified by liquid water.

However, incorporating the effect of liquid water into diffusion equations is not straightforward. Indeed, as discussed in 1.2.3.2, Tomadakis and Sotirchos model is the current reference in the litterature concerning gas diffusion in GDLs. In this model, tortuosity is linked to porosity through equation (4.1) in an environment devoid of liquid water [72].

$$\tau = \left(\frac{1-\varepsilon_p}{\varepsilon-\varepsilon_p}\right)^{\alpha} \tag{4.1}$$

where τ is the GDL tortuosity, ε is the GDL porosity, ε_p is the GDL percolation threshold porosity, and α is a fitted value. Given that this model was constructed without considering liquid water, modifying it to yield results consistent with the observed voltage drop is not evident. A dedicated study is necessary in this regard, particularly because altering the gas diffusion coefficient significantly impacts the overall stack behavior.

In conclusion, it is proposed in this paper to modify the cell overvoltage equation to simply, but accurately, represent the voltage drop at high current densities caused by the presence of liquid water. This choice may be further complemented in the future, as knowledge relative to fuel cells advances. Nevertheless, it appears to be a beneficial step in model development.

4.1.3. Enhancing cell performance through inlet humidity control

Currently, fuel cells operate under fixed operating conditions recommended by manufacturers. This stems from the fact that the cell is highly sensitive to these parameters and can easily fail, notably becoming flooded or dried out. It is not recommended to manually modify these operating conditions that have been designed to ensure proper cell functioning in most situations. However, maintaining fixed operating conditions inevitably implies limitations in the use of the fuel cell. For instance, at high current densities, the voltage drops rapidly with increased current density due to the formation of liquid water that gradually floods the cell. However, the humidity of the gases entering the cell remains constant, whereas it would be logical to reduce it to prevent this phenomenon and enable the cell to access higher current density ranges without additional loss of voltage. Nevertheless, altering the humidity setpoint without precisely monitoring the impact of this action on the remaining water quantity in the cell may result in membrane drying, which would also degrade the voltage. Therefore, it is essential to understand the internal states of the cell through a model in order to modify its operating conditions and enhance its capabilities. To the authors' knowledge, such an approach has not yet been proposed in the literature. This work therefore constitutes a contribution to the improvement of fuel cells.

Here, we theoretically demonstrate a simple rule-based control over the incoming gas humidities using AlphaPEM model. The fuel cell system utilized in this experiment is based on the EH-31 cell calibrated in section 3.1.2, with a pressure of $P_{des} = 2.0$ bar and a closed cathode with flow-through anode. The proposed control operates as follows. Every 20 seconds, the internal states of the stack are analyzed. If the liquid water saturation in the CCL exceeds a threshold, denoted as $s_{ccl} > s_{max}$, and the water content in the membrane surpasses a certain value, denoted as $\lambda_{mem} > \lambda_{min}$, there is a risk of cell flooding initiation, and the incoming gas humidity must decrease. It is suggested here to reduce this humidity by 0.01 units within the accessible range of values. If both aforementioned variables are collectively lower than their threshold, there is a risk of cell dehydration, and the incoming gas humidity is increased by 0.01 units, within its accessible range. In the other two situations, no action is taken. Specifically, if $s_{ccl} > s_{max}$ and $\lambda_{mem} \leq \lambda_{min}$, then the stack risks being flooded at the cathode and dehydrated at the membrane simultaneously. There is no action that can be taken on incoming humidity to resolve this situation. Finally, having $s_{ccl} \leq s_{max}$ and $\lambda_{mem} > \lambda_{min}$ represents the desired internal condition: the stack is neither flooded nor dehydrated. Lastly, the determination of fixed values for s_{max} and λ_{min} is not a straightforward task. It is likely that these values depend on the studied stack or other operating conditions. However, it seems reasonable to have $s_{max} \in [0.10, 0.15]$ and $\lambda_{min} \in [5, 10]$ to allow for a margin before faults occur, based on the authors' expertise. In this work, $s_{max} = 0.55 \cdot s_{lim}$ and $\lambda_{min} = 8$ [141] were chosen.

The results derived from controlling the humidity of inlet gas are depicted in figure 4.2 through polarization, cell power density, and cell efficiency curves, where cell efficiency is calculated using equation 4.2.

$$\eta_{fc} = \frac{U_{cell} \cdot i_{fc}}{U_{eq}\left(i_{fc} + i_n\right)} \tag{4.2}$$

These results exhibit significant promise for prospective real-world applications. In the specific scenario under examination, the attainable current density range (typically deemed applicable for a cell voltage exceeding $0.5V$) sees a notable increase of 68%, while the peak power density attainable by the cell notably rises by 66% with only a 2% decrease in cell efficiency. On the other hand, the previous peak power can be achieved in the new configuration with a 20% cell efficiency gain. Nonetheless, these promising results must be greeted with caution pending the realization of laboratory experiments that will enable the assessment of their value. Indeed, It is likely that this model is incomplete and that other unmodeled phenomena might contribute to voltage concentration losses, thereby potentially diminishing the aforementioned gains.

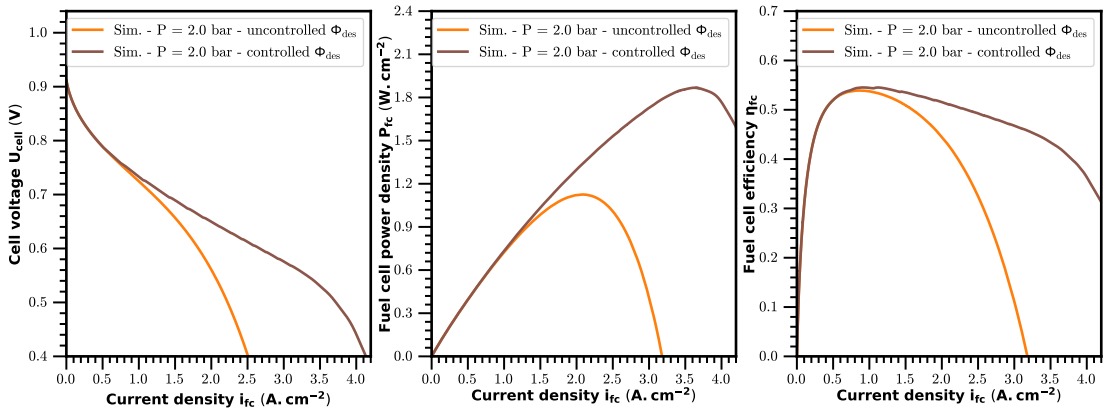

Figure 4.2. – Comparison of polarization, electrical power and system efficiency curves for a fuel cell system with a closed cathode with flow-through anode, with and without controlled entrance humidity.

For information purposes, the variations in inlet gas humidity Φ_{des}, liquid water saturation s, and water content λ during the generation of the curves in figure 4.2 are depicted in figures 4.3 and 4.4.

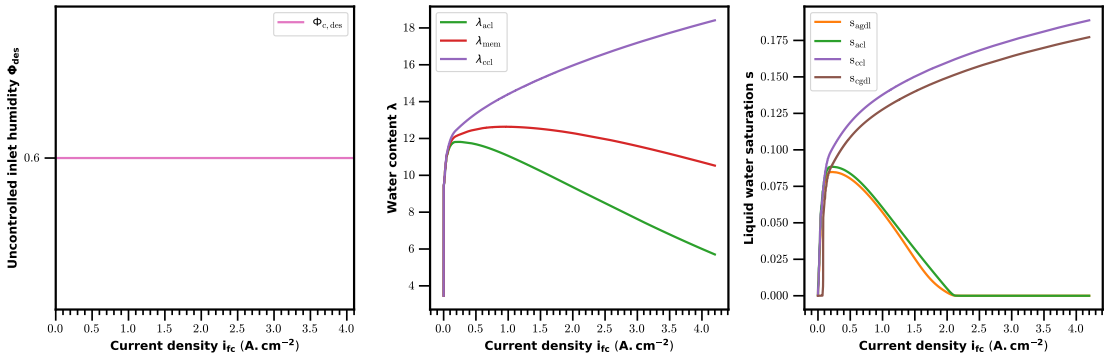

Figure 4.3. – Analysis of internal states in fuel cell polarization curve generation without humidity setpoint variation.

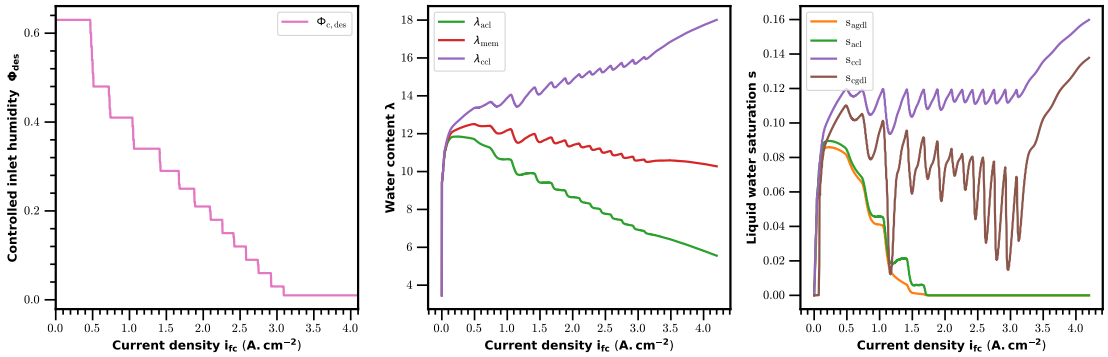

Figure 4.4. – Analysis of internal states in fuel cell polarization curve generation with humidity setpoint variation.

Remark: The control method presented here is a basic rule-based approach, with unoptimized controller parameters. The intention is to demonstrate the model's potential in aiding control design, with controller optimization being outside the scope of this study.

4.2. EIS curve modelling

EIS curves are widely used tools in the scientific community for characterizing fuel cells. Indeed, these curves allow the identification of the contribution of each of the simultaneous physical phenomena underlying the operation of fuel cells, and which have different time scales, to their overall performance [155, 156]. Furthermore, these curves can be obtained experimentally in a non-invasive and in situ way, while the fuel cell is operating for other purposes, providing real-time information on electrochemical behavior [156]. Thus, by knowing the signature of a healthy cell, it is possible to precisely identify the source of defaults in a faulty cell by analyzing the deviations of its EIS curve from that of the healthy cell [157–159]. Similarly, EIS curves can be used to monitor the degradation of a fuel cell by analyzing its shift relative to the initial curves. Additionally, these curves help identify the most limiting physical phenomena in the operation of a given fuel cell, thereby guiding efforts to improve performance on the most critical points [155]. Finally, EIS curves provide elements for evaluating the internal states of the fuel cell from these experimental data, such as the water content λ, which is linked to the high frequency resistance of the EIS [155]. However, the interpretation of EIS remains challenging due to the overlap of processes with similar time scales and the complexity of the involved physical phenomena [155, 156].

The modeling of EIS curves using physics-based models, in addition to their experimental acquisition, is interesting for several reasons. First, it serves as a tool to validate the dynamic behavior of models, whereas polarization curves limit validation to static properties, as discussed in section 3.1. Then, this modeling can serve as an EIS analysis tool. On the one hand, the noise inherent in experimental EIS data is eliminated. On the other hand, simulations can isolate specific physical processes, helping to precisely characterize the impact of each process that shares the same time scale and whose effects, therefore, overlap in reality. This is particularly useful for isolating diffusive effects in experimental EIS curves, which are typically masked by other physical phenomena due to their low impedance. Additionally, the equipment currently used to obtain EIS curves is heavy, bulky, and expensive. Therefore, having a calibrated model that performs the same task allows this tool to be integrated into embedded systems, despite the dependence of the results on the underlying theory. Finally, modeling EIS curves using physics-based models is more reliable than using equivalent circuit models, allowing for a deeper interpretation of the results [160, 161].

In this section, a discussion is presented regarding the simulation of EIS curves made possible by the AlphaPEM model. However, this work is still ongoing, as a comparison between the model and experimental data has not yet been conducted, and potential applications of such simulations to improve the performance and durability of fuel cells are being developed for future works.

4.2.1. Proton charge conservation equation

To properly model an EIS curve using AlphaPEM, it is necessary to consider a dynamic that has not yet been addressed in this work: the movement of protonic

charges H_+ within the CCL. This physical phenomenon is significant for EIS, as it governs the plotting of the high-frequency semicircle. The proton charge conservation equation, adapted for a fuel cell's CCL and highlighted in equation (4.3), introduces this dynamic [162–164]. Furthermore, this equation involves a new and undetermined parameter, C_{scl}, the volumetric space-charge layer capacitance of the CCL, which can be calibrated using two experimental EIS curves under different operating conditions. In order to obtain preliminary results while waiting for the generation of experimental curves, C_{scl} is set to $2 \cdot 10^7$ $F.m^{-3}$, which corresponds to a physically acceptable value for a porous electrode PEM fuel cell [164].

In this work, the capacitive phenomenon related to the accumulation of H_+ charges at the ionomer boundary in the CCL, as opposed to the accumulation of negative charges on the electrode surface, has been designated as a "space-charge layer" rather than a "double layer," as is frequently used in the literature. Indeed, this term, common in the electrochemical community, is appropriate when the studied system contains a liquid electrolyte whose solvent forms a Stern layer in addition to the diffusion layer of H_+ charges mentioned above. However, in the case of a solid electrolyte, such as that present in a PEM fuel cell, there is no Stern layer, making it inappropriate to refer to a double-layer phenomenon. Therefore, the term "space-charge layer" is preferred to describe this similar phenomenon.

Moreover, it should be noted that the addition of equation (4.3) to the model will have minimal impact on its temporal behavior, with only its high-frequency behavior being influenced. In fact, the charging time of the double layer in a PEM fuel cell is on the order of 10^{-6} seconds [164], which is imperceptible on the timescales typically employed in practice. During the temporal behavior, the proton charge reaches a steady state almost instantaneously; thus, this equation simplifies to the one previously used to calculate the overpotential: equation (1.69).

$$\boxed{C_{scl} H_{cl} \frac{\partial \eta_c}{\partial t} = i_{fc} + i_n - i_{0,c} \cdot exp\left(\frac{F\alpha_c}{RT_{fc}} \eta_c\right), \text{in the CCL}} \tag{4.3}$$

where C_{scl} $(F.m^{-3})$ is the volumetric space-charge layer capacitance of the CCL.

This equation is frequently used in the literature without providing a detailed demonstration. However, it seems necessary to the authors to elaborate on the calculation leading to this balance in order to fully understand the mechanisms of this physics. First, the universal proton charge conservation equation, which is not specific to the CCL, is written locally as equation (4.4). This equation has been directly reduced for a problem with a single spatial dimension x.

$$\frac{\partial C_{H^+}}{\partial t} = -\frac{\partial i_{H^+}}{\partial x} - S_{H^+} \tag{4.4}$$

where C_{H^+} $(C.m^{-3})$ is the proton charge concentration, i_{H^+} $(A.m^{-2})$ is the local proton current density and S_{H^+} $(A.m^{-3})$ is the consumption of proton charges.

Next, it is necessary to position oneself within the CCL and observe the various specificities that come into play. On one hand, a space-charge layer forms by H^+ at

the interface of the polymer electrolyte and the negatively charged electrode [162, 164]. These regions of the CCL locally behave like capacitors, and the capacitor behavior law can therefore be applied: $C_{H^+} = C_{scl}\phi$, where ϕ corresponds to the local voltage between the two terminals of a capacitor [165]. Here, C_{scl} is considered independent of ϕ. Thus, this equation, which is based on proton charge conservation, transforms into an equation governing the dynamics of local voltage evolution. Additionally, it is assumed that the consumption of protonic charges S_{H^+} follows the Butler-Volmer law, discussed in section 1.3.3, which can also be seen as the rate of conversion of the ionic current into the electronic one in the CL [163]. Thus, the proton charge conservation equation can be rewritten according to equation (4.5).

$$C_{scl}\frac{\partial \phi}{\partial t} = -\frac{\partial i_{H^+}}{\partial x} - i_* \exp\left(\frac{F\alpha_c}{RT_{fc}}\eta_c\right) \tag{4.5}$$

where i_* is the volumetric exchange current density at the cathode, for which $\int_0^{H_{cl}} i_*\, dx = i_{0,c}$.

Moreover, it is worth noting that $i_{H^+}(x=0) = i_{fc}$, because the proton flow crossing the membrane, before reaching the CCL, is exactly equal to the electron flux through the electrical circuit, as both charges originate from the electrochemical reaction $H_2 \rightarrow 2H^+ + 2e^-$. However, to remain consistent with the assumptions made in section 1.3.3.3, it is assumed that $i_{H^+}(x=0) = i_{fc} + i_n$ holds true to account for the crossover and short circuit in the fuel cell. Similarly, $i_{H^+}(x = H_{cl}) = 0$ since the proton charges are consumed as they travel through the CCL and cannot exit it. Additionally, assuming that local variations in concentrations are negligible in the CCL, it is possible to write that $\phi = \eta_c$ [162]. Finally, given that proton transport in the CCL is rapid, it can be assumed that η is independent of x [164]. Thus, by integrating equation (4.5) over the thickness of the CCL, equation (4.3) is recovered. The demonstration is complete.

4.2.2. EIS curve simulation using AlphaPEM

4.2.2.1. General results

Figure 4.5 shows the generation of EIS curves by the AlphaPEM model, which simulates the EH group fuel cell system [150] discussed in section 3.1.2, with a desired pressure of $P_{des} = 2.0$ bar. The auxiliary system modeled contains an open anode circuit, identical to the cathode circuit, in order to precisely control all operating conditions and to avoid the additional complexity that a recirculation configuration would introduce. The characteristic frequencies of all the identified phenomena are reported in figure 4.5a and discussed in section 4.2.2.2. As previously mentioned, it would be necessary to compare these curves with experiments in order to calibrate the undetermined parameter C_{scl}, which significantly influences these results, as well as to validate this simulation. This work will be carried out in future studies. In the meantime, it is still possible to qualitatively assess the trend of these curves and conclude that they have the expected shape and that their values fall within typical ranges as in the litterature [5, 164, 166, 167].

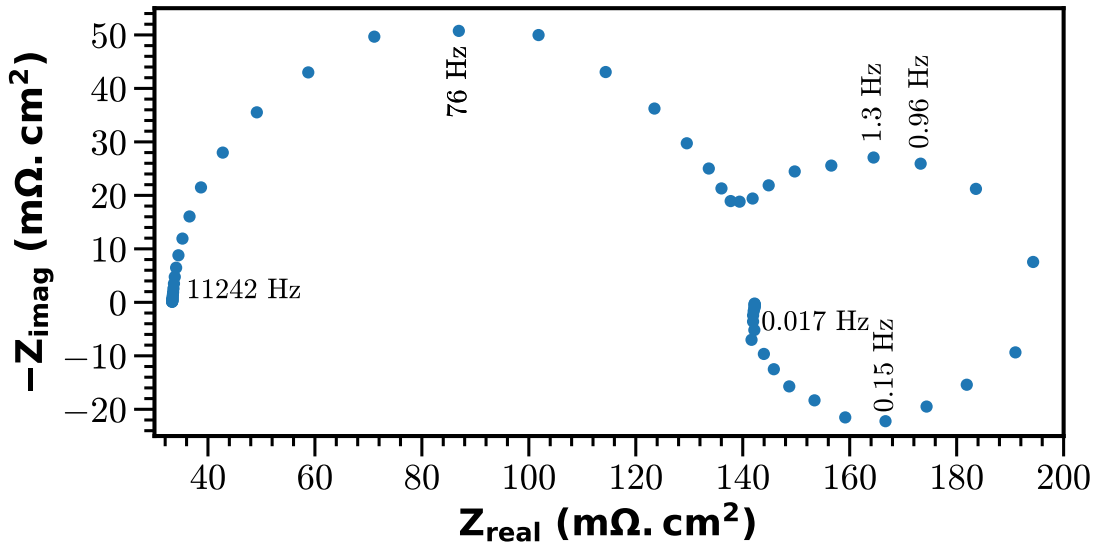

(a) Nyquist diagram

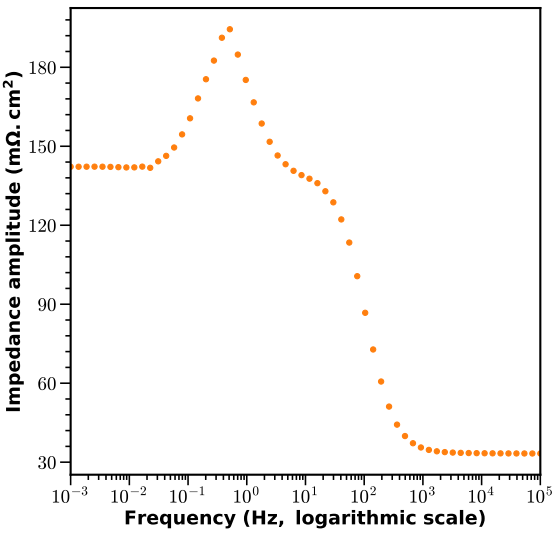

(b) Bode magnitude diagram

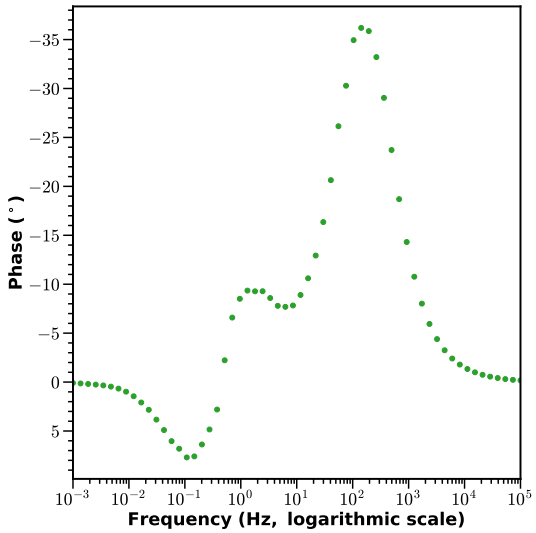

(c) Bode phase diagram

Figure 4.5. – EIS curves computing by AlphaPEM simulating EH-31 fuel cell system [150] at 2.0 bar

4.2.2.2. Results derived from reduced physics

To better understand the Nyquist diagram in figure 4.5a, AlphaPEM was modified to reduce the physics it models. By removing only the modeling of the auxiliaries, discussed in section 2.3, the Nyquist diagram becomes the one shown in figure 4.6a. By removing only the modeling of proton charge dynamics, discussed in subsection 4.2.1, the Nyquist diagram becomes the one shown in figure 4.6b. Finally, by removing both models together and retaining only the diffusive phenomena, the Nyquist diagram becomes the one shown in figure 4.6c.

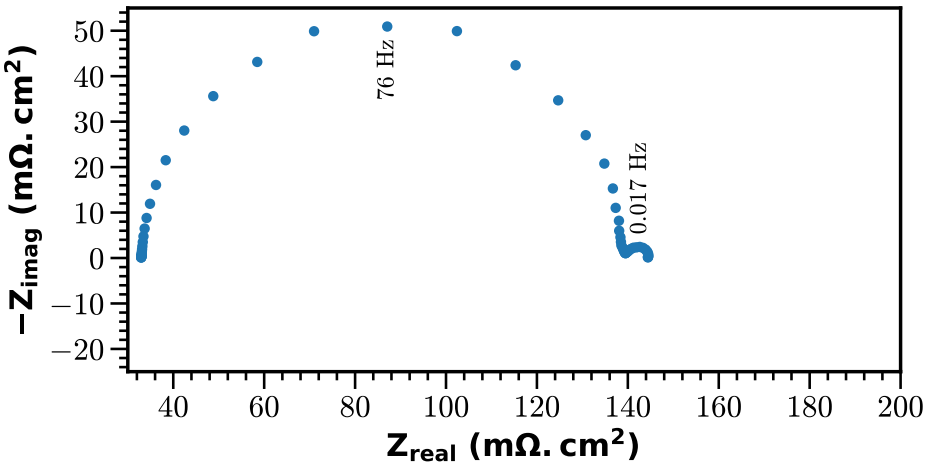

(a) Nyquist diagram without auxiliairies

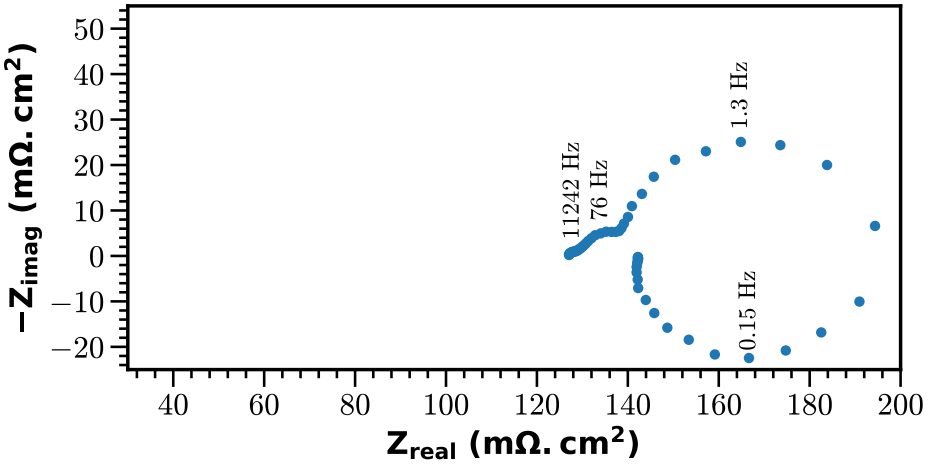

(b) Nyquist diagram without proton charge dynamic behavior

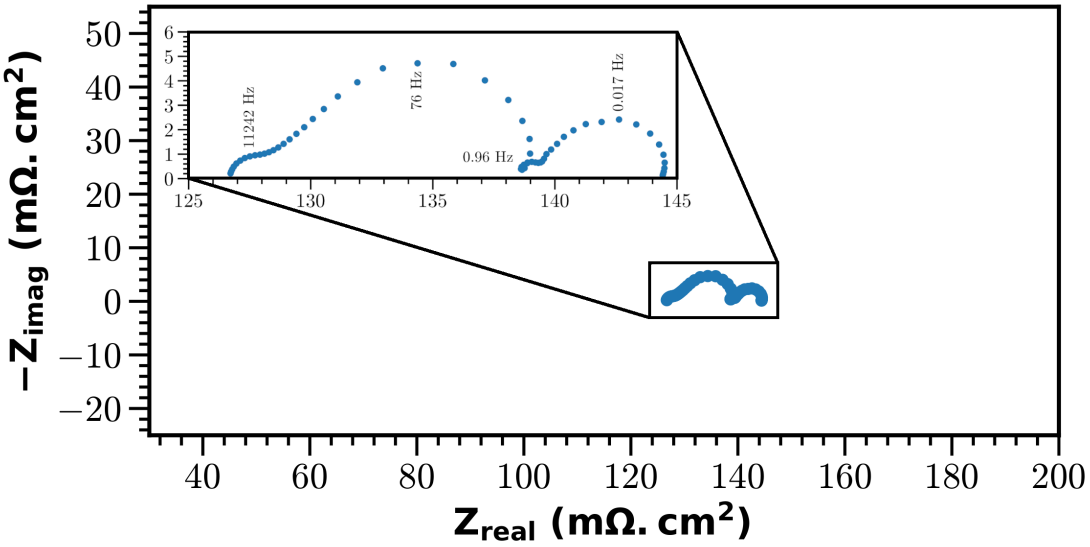

(c) Nyquist diagram without proton charge dynamic behavior and without auxiliaries

Figure 4.6. – Comparison of Nyquist diagrams by reducing AlphaPEM physics

From these observations, it can be concluded that the high-frequency semicircle is made by proton charge dynamics, as expected [168]. The second almost complete circle at medium and low frequencies, which takes both positive and negative values, highlights capacitive and inductive effects and is mainly influenced by auxiliary dynamics. To the authors' knowledge, the modeling and physical understanding of this inductive effects at low frequencies is novel and has been expected by the scientific community in PEM fuel cells [169]. Lastly, matter diffusive transport within the cell does impact the EIS curves, producing four small semicircles at different frequencies over a wide interval. The characteristic signature of diffusive phenomena is recognizable by semicircles having a 45° angle with respect to the x-axis at their highest frequency points [170]. This differentiation into four arcs likely arises from the three diffusion phenomena (gas, liquid water, and water dissolved in the membrane) [168]. However, these diffusive effects have small impedance and are overshadowed by the impacts of the other dynamics in the global Nyquist plot, figure 4.5a, as already observed in the literature [156].

Once these observations are made, it is important to note that the model developed in this thesis does not account for convective mass transport or heat transfer. However, these two physical phenomena introduce dynamics that impact the EIS [164] and should therefore be implemented to achieve a simulation that is more representative of reality.

4.2.2.3. Results derived from reduced auxiliary systems

To go further, the two arcs at medium and low frequencies caused by the modeling of AlphaPEM auxiliaries are actually produced only by the inlet auxiliaries. Indeed, by directly imposing ideal inlet flows to the fuel cell while keeping the outlet auxiliary system as modeled, the resulting Nyquist plot corresponds to the one without auxiliaries, as shown in figure 4.6a. Thus, the dynamics of the backpressure valves and the outlet manifolds are negligible at this scale and do not contribute any inductive effects.

Three dynamic phenomena are present at the fuel cell inlet in this model: the flow rate of the compressors, flow rate of the humidifiers, and the accumulation of matter in the inlet manifolds. Since the humidifiers' flow rate depends on that of the compressors, it is not easy to separate their dynamics, and these two components are therefore considered together. It is possible to model the EIS by imposing ideal matter flows directly in the inlet manifold, which is equivalent to having compressors and humidifiers that respond instantly to the current setpoint. This results in the curve shown in figure 4.7a. A noticeable change in the medium and low-frequency arcs can be observed, with modifications in their radii and characteristic frequencies. However, capacitive and inductive effects are still present.

On the other hand, by maintaining the dynamics of the compressors and humidifiers but removing the inlet manifolds (i.e., injecting the corresponding flows directly into the fuel cell's bipolar plates), the curve in figure 4.7b is obtained. This curve closely resembles the one obtained with the manifolds, shown in figure 4.5a: the capacitive and inductive effects at the medium and low-frequency range remain. However, by

combining the two reductions of the inlet auxiliary model proposed here, figure 4.6a is obtained, and these capacitive and inductive effects are eliminated. Thus, the dynamics of the compressors and humidifiers, as well as the presence of a manifold at the fuel cell inlet, can independently cause capacitive and inductive effects at medium and low frequencies.

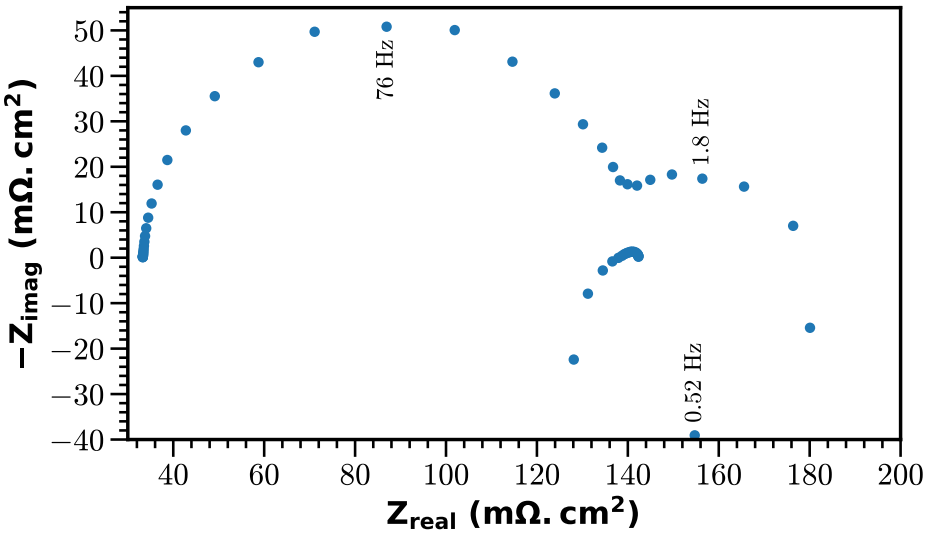

(a) Nyquist diagram with ideal inlet flow and with inlet manifold

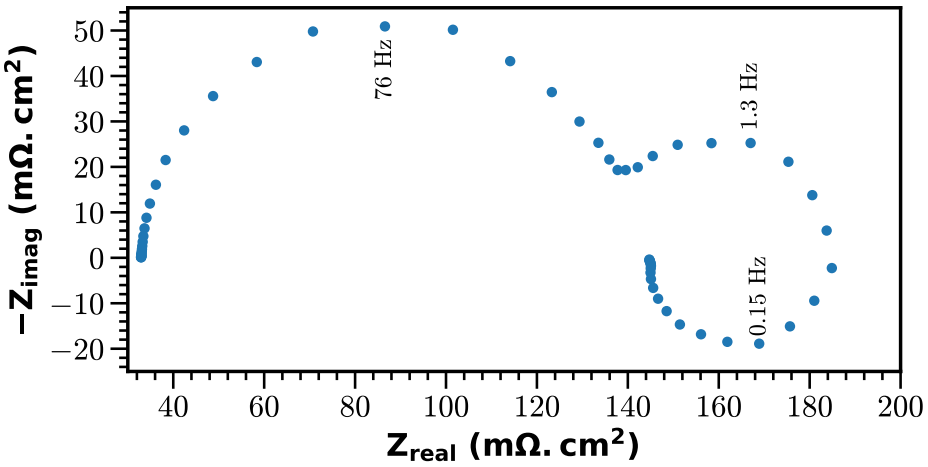

(b) Nyquist diagram without ideal inlet flow and without inlet manifold

Figure 4.7. – Comparison of Nyquist diagrams by reducing the physics of AlphaPEM auxiliary system

It is possible to interpret these results. First, it is necessary to discuss, in general terms, the inductive effects observed at low frequencies. Firstly, the term 'inductive' is used because the observed behavior is identical to that of an inductor. Given that the community that established the theory of EIS was composed of electricians, this term has remained to describe a negative arc on the Nyquist diagram. However, this may

involve physical phenomena that have nothing to do with an electrical inductor, as it is the case here. Secondly, in the presence of an inductive effect, the phase shift of the response to the input signal is positive. However, this should not be interpreted as a response that leads the input signal in time, as if it could predict the input in advance and adjust to it, which is, of course, impossible. The understanding of this phenomenon is more subtle. Indeed, the system evolves around an equilibrium point with a small and regular perturbation. Thus, the response can follow the rhythm imposed by the input and shift either backward (resulting in a capacitive effect) or forward (resulting in an inductive effect). It is this positive or negative shift relative to a regular rhythm that allows understanding why an inductive effect can be observed.

Next, the inlet collectors act as buffer reservoirs between the cell and the incoming flows into the fuel cell system. These intermediate volumes, which fill and empty according to the pressures in the cell and the incoming flows, influence the dynamic evolution of concentrations in the CCL, and thus affect the voltage. Their behavior is complex, and depending on the excitation frequency, they can result on either a capacitive or inductive effect on the voltage. When these collectors are removed and the evolution of the inlet flows is non-ideal, modeled by first-order systems, it is the volume of the channels in the bipolar plates that acts as a buffer volume between the CCL and the incoming flows into the cell, similarly causing capacitive and inductive effects.

Finally, as shown in figure 4.8, when the air compressor time constant τ_{cp} is multiplied by 10, the characteristic frequency of the inductive arc is also divided by 10, suggesting a mathematical relationship between these two quantities.

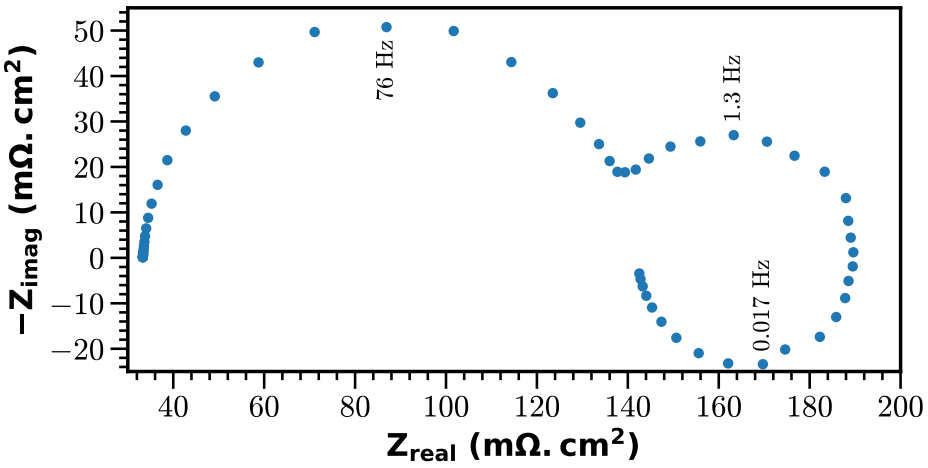

Figure 4.8. – Nyquist diagram with τ_{cp} multiplied by 10

4.2.2.4. Results derived from diffusion-only model

To better understand the obtained diffusion arcs, other physical phenomena can be modified or removed one by one, and the resulting changes in the corresponding EIS curves can be analyzed, starting from the model without the auxiliaries and

the space charge layer, represented in figure 4.6c. Thus, figure 4.9a represents this diffusion-only model with a 30% increase in the diffusion coefficients, figure 4.9b shows the model with the removal of dissolved water transport in the membrane, and figure 4.9c represents the model without liquid water transport in the cell. Each of these three modifications impacts the EIS curve, but the effect is not localized to a single arc: the three arcs at lower frequencies are significantly affected by each modification. Moreover, an inductive effect is notably more pronounced in figure 4.9c, while it disappears completely in figure 4.9b. The high-frequency arc is only slightly affected by these changes. Therefore, it is not straightforward to associate each diffusion arc with a specific diffusion phenomenon, as it appears that each arc is influenced by several of these phenomena. A more in-depth study would be useful so that experimental EIS curves could be better used to characterize diffusion phenomena in PEM fuel cells, provided that such small variations can be isolated experimentally.

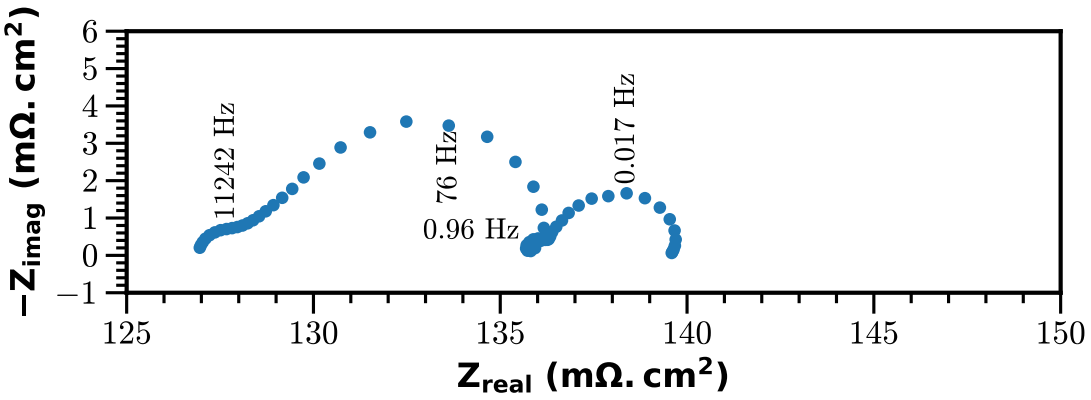

(a) Nyquist diagram from diffusion-only model with a 30% increase in diffusion coefficients

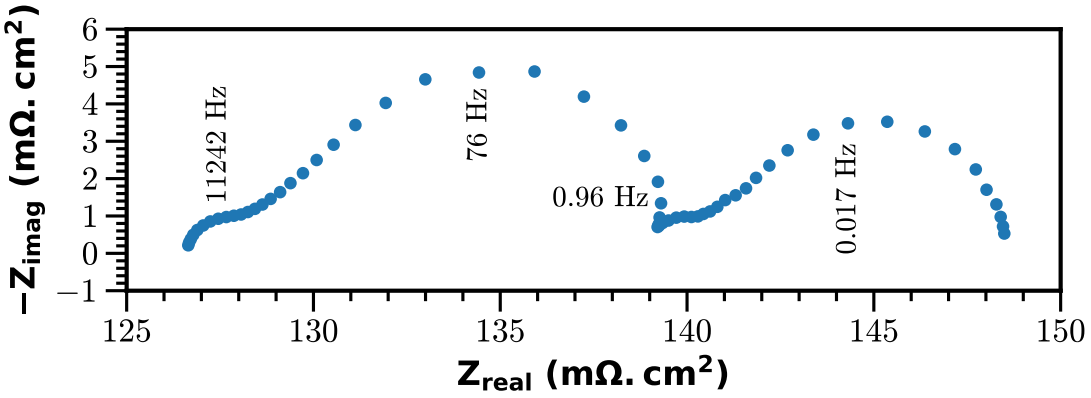

(b) Nyquist diagram from diffusion-only model excluding dissolved water diffusion into the membrane

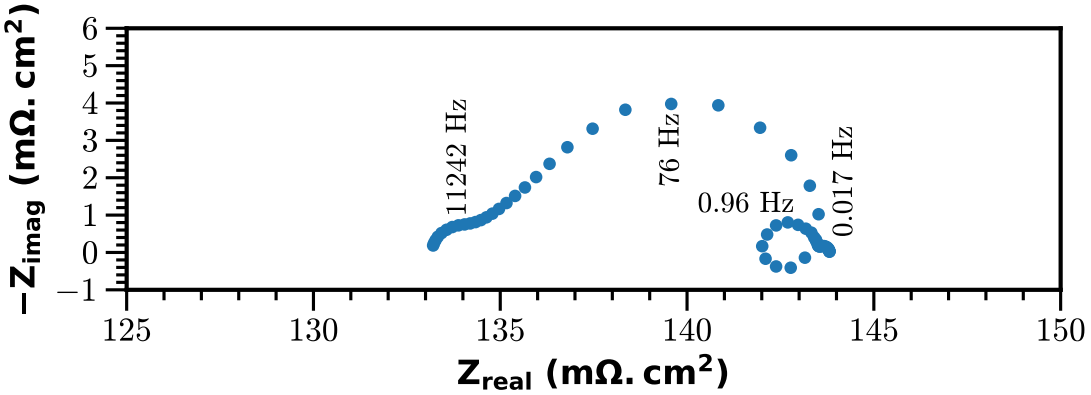

(c) Nyquist diagram from diffusion-only model without liquid water permeation

Figure 4.9. – Comparison of Nyquist diagrams from diffusion-only model

4.3. State-space representation of a reduced version of the model

Fuel cells are devices whose performance depends on the control of their operating conditions. It is therefore useful to use a model with a good balance of speed and accuracy, such as AlphaPEM, which links these operating conditions to the internal states of the cell, in order to assess the impact of the former on the latter. However, it is necessary to reformulate the model presented in this thesis into a state-space representation to make it compatible with a predictive control framework. Consequently, the notations used have been converted to those of the automatic control domain. Given the complexity of this task, the transformation of AlphaPEM was carried out using a simplified version of the model.

In addition to enabling in-depth control and command of fuel cells, this work could provide mathematical proof of the stability and uniqueness of the model's solutions. It could thus lead to the revision of some empirical equations to better reconcile the demands of physics and numerical resolution, thereby improving stability. Indeed, given the increasing importance of these models in embedded applications, ensuring their reliability is essential for human and material safety. Furthermore, mathematical analysis would allow for the verification of whether it is possible, from a limited number of measurable physical quantities, to recover all the internal states of the fuel cell.

This work serves as a preparatory step, establishing a foundation for future studies. Subsequent research will build upon this groundwork, further refining the model and exploring its applications in control-command systems.

4.3.1. Methodological and conceptual framework

4.3.1.1. Notations and conventions

The following notations and conventions have been adopted to formulate the model into a state-space representation.

— The model to be established is $\dot{X} = f(X, u, \theta, e)$, where u represents the system inputs, i.e., operating conditions, θ represents the parameters (either determined or undetermined), and e represents the exogenous inputs.
  — $u = [P_{a,des}, P_{c,des}, S_a, S_c, \Phi_{a,des}, \Phi_{c,des}]$,
  with $\left(P_{a,des}, P_{c,des}\right) \in [10^5, 3 \cdot 10^5]^2 Pa$, $(S_a, S_c) \in [1,3]^2$,
  $\left(\Phi_{a,des}, \Phi_{c,des}\right) \in [0,1]^2$.
  — An element of θ is generically denoted θ_i, with $i \in [\![1,31]\!]$. θ_i is a vector of parameters.
  — e = i_{fc}, the current density, with $i_{fc} \in [0.5 \cdot 10^4, 2 \cdot 10^4]$ $A.m^{-2}$.
— The variables of the system of differential equations, called internal states, are contained in a vector of real vectors X.

  - The $p \in \mathbb{N}$ elements of X are denoted $X_i \in \mathbb{R}^{n_i}$, with $i \in [\![1, p]\!]$ and $n_i \in \mathbb{N}$. We have $X = \left(X_1, X_2, ..., X_p\right)$.
  - The n_i elements of each X_i are denoted x_j.
  - Each vector X_i can only be related in the system of differential equations to the previous vector X_{i-1} and the next vector X_{i+1}, if they exist. In practice, each X_i corresponds to a spatial zone in the stack.
- Functions, such as δ_ω, are used to empirically describe physical quantities.
  - They take as an argument a variable z which is a combination of the x_j, for example $z = \frac{x_3}{1+(x_5)^2}$.
  - Functions defined by an uppercase letter, such as Ψ_ω, invoke another function in their expression, usually denoted with the same lowercase letter ψ_ω.
  - Bolded variables and parameters refer to a vector.
- Parentheses () represent the evaluation of a function, whereas brackets [] represent factorization.
- The following establishes the link between the mathematical notations and the physical notations concerning the system variables:

X_1	X_2	X_3	X_4	X_5	X_6	X_7
$x_1 = C_{H_2,agc}$ $x_8 = C_{v,agc}$	$x_2 = C_{H_2,agdl}$ $x_9 = C_{v,agdl}$ $x_{14} = \mathtt{s}_{agdl}$	$x_3 = C_{H_2,acl}$ $x_{10} = C_{v,acl}$ $x_{15} = \mathtt{s}_{acl}$ $x_{18} = \lambda_{acl}$ $x_{20} = \lambda_{mem}$	$x_4 = C_{O_2,ccl}$ $x_{11} = C_{v,ccl}$ $x_{16} = \mathtt{s}_{ccl}$ $x_{19} = \lambda_{ccl}$	$x_5 = C_{O_2,cgdl}$ $x_{12} = C_{v,cgdl}$ $x_{17} = \mathtt{s}_{cgdl}$	$x_6 = C_{O_2,cgc}$ $x_{13} = C_{v,cgc}$	$x_7 = C_{N_2}$

with $C_{H_2} \in [0,80]$ $mol.m^{-3}$, $C_{O_2} \in [0,20]$ $mol.m^{-3}$, $C_{N_2} \in [20,60]$ $mol.m^{-3}$, $C_v \in [8,20]$ $mol.m^{-3}$, $\mathtt{s} \in [0, \mathtt{s}_{max}]$, $\lambda \in [\lambda_{min}, \lambda_{max}[$, $\mathtt{s}_{max} \in [0.2, 0.5]$, $\lambda_{min} \in [5,10]$ et $\lambda_{max} \in [15,25]$.

4.3.1.2. Hypotheses

The following hypotheses were established to simplify the model and provide a preliminary state-space representation that is as straightforward as possible to manipulate, while maintaining a physical, dynamic, and one-dimensional model.

- The system is considered isothermal (all temperatures are constant). The constant temperature $\left(T_{fc}\right)$ is therefore excluded from the system inputs, and its expression in the model is incorporated into the constants. (H1)
- Auxiliaries, crossover, and charge transport are not modeled. Ideal matter flows enter and exit the stack. (H2)
- A single spatial point is considered in each gas diffusion layer (GDL). The physical phenomena occurring there are similar, so this does not result in a reduction of the physics. However, it could affect the system's stability. (H3)

— It is assumed that the dynamic evolution of $\mathtt{s}$ is much faster compared to that of the gas concentrations C, so it is possible to consider $\overbrace{[1-\mathtt{s}]\,C}^{\cdot} = [1-\mathtt{s}]\,\dot{C}$. (H4)

— The coefficient of gas depression from the bipolar plate channels: $D_{agc,out}\left(C_{H_2,agc}, C_{v,agc}\right)$ or $D_{cgc,out}\left(C_{O_2,cgc}, C_{N_2}, C_{v,cgc}\right)$, present in the expression $J_{gc,out} = D_{gc,out}\left[P_{agc,out} - P_{des}\right]$, is considered constant due to its evolution shown in figure 4.10. (H5)

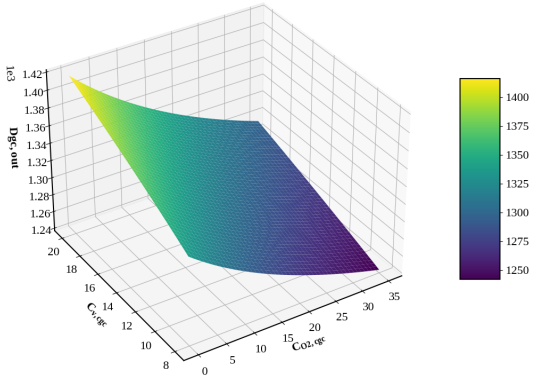

Figure 4.10. – Evolution of $D_{cgc,out}$, for a fixed value of $C_{N_2} = 48\ mol.m^{-3}$

4.3.2. System of differential equations

The system of differential equations formulated in state-space form is given by equations 4.6 to 4.25.

$$\dot{x}_1 = -\pi_{\theta_1}(x_1+x_2+x_8+x_9)[x_1-x_2] - \frac{\theta_2 \cdot x_1}{x_1+x_8}[\theta_3[x_1+x_8]-u_1] + \theta_4 \cdot u_3 \cdot e \tag{4.6}$$

$$\dot{x}_2 = \Pi_{\theta_5}(x_2+x_3+x_9+x_{10}, x_{14}+x_{15})\frac{x_3-x_2}{1-x_{14}} + \pi_{\theta_6}(x_1+x_2+x_8+x_9)\frac{x_1-x_2}{1-x_{14}} \tag{4.7}$$

$$\dot{x}_3 = -\Pi_{\theta_7}(x_2+x_3+x_9+x_{10}, x_{14}+x_{15})\frac{x_3-x_2}{1-x_{15}} - \frac{\theta_8 \cdot e}{1-x_{15}} \tag{4.8}$$

$$\dot{x}_4 = \Pi_{\theta_9}(x_4+x_5+2x_7+x_{11}+x_{12}, x_{16}+x_{17})\frac{x_5-x_4}{1-x_{16}} - \frac{\theta_{10} \cdot e}{1-x_{16}} \tag{4.9}$$

$$\dot{x}_5 = -\Pi_{\theta_{11}}(x_4+x_5+2x_7+x_{11}+x_{12}, x_{16}+x_{17})\frac{x_5-x_4}{1-x_{17}} - \pi_{\theta_{12}}(x_5+x_6+2x_7+x_{12}+x_{13})\frac{x_5-x_6}{1-x_{17}} \tag{4.10}$$

$$\dot{x}_6 = \pi_{\theta_{13}}(x_5+x_6+2x_7+x_{12}+x_{13})[x_5-x_6] - \frac{\theta_{14} \cdot x_6}{x_6+x_7+x_{13}}[\theta_3[x_6+x_7+x_{13}]-u_2] + \theta_{15} \cdot u_4 \cdot e \tag{4.11}$$

$$\dot{x}_7 = -\frac{\theta_{14} \cdot x_7}{x_6+x_7+x_{13}}[\theta_3[x_6+x_7+x_{13}]-u_2] + \theta_{16} \cdot u_4 \cdot e \tag{4.12}$$

$$\dot{x}_8 = -\pi_{\theta_1}(x_1+x_2+x_8+x_9)[x_8-x_9] - \frac{\theta_2 \cdot x_1}{x_1+x_8}[\theta_3[x_1+x_8]-u_1] + \theta_4 \cdot \rho_{\boldsymbol{\theta_{17}},u_5}(x_1+x_8) \cdot u_3 \cdot e \tag{4.13}$$

$$\dot{x}_9 = \Pi_{\theta_5}(x_2+x_3+x_9+x_{10}, x_{14}+x_{15})\frac{x_{10}-x_9}{1-x_{14}} + \pi_{\theta_6}(x_1+x_2+x_8+x_9)\frac{x_8-x_9}{1-x_{14}} - \delta_{\boldsymbol{\theta_{18}}}(x_2, x_9, x_{14})\frac{1}{1-x_{14}} \tag{4.14}$$

$$\dot{x}_{10} = -\Pi_{\theta_7}(x_2+x_3+x_9+x_{10}, x_{14}+x_{15})\frac{x_{10}-x_9}{1-x_{15}} - \Psi_{\boldsymbol{\theta_{19}}}(x_{10}, x_{18})\frac{\alpha_{\boldsymbol{\theta_{20}}}(x_{10})-x_{18}}{1-x_{15}} - \delta_{\boldsymbol{\theta_{18}}}(x_3, x_{10}, x_{15})\frac{1}{1-x_{15}} \tag{4.15}$$

$$\dot{x}_{11} = \Pi_{\theta_9}(x_4 + x_5 + 2x_7 + x_{11} + x_{12}, x_{16} + x_{17}) \frac{x_{12} - x_{11}}{1 - x_{16}} - \Psi_{\boldsymbol{\theta_{19}}}(x_{11}, x_{19}) \frac{\alpha_{\boldsymbol{\theta_{20}}}(x_{11}) - x_{19}}{1 - x_{16}} - \delta_{\boldsymbol{\theta_{18}}}(x_4 + x_7, x_{11}, x_{16}) \frac{1}{1 - x_{16}} \tag{4.16}$$

$$\dot{x}_{12} = -\Pi_{\theta_{11}}(x_4 + x_5 + 2x_7 + x_{11} + x_{12}, x_{16} + x_{17}) \frac{x_{12} - x_{11}}{1 - x_{17}} - \pi_{\theta_{12}}(x_5 + x_6 + 2x_7 + x_{12} + x_{13}) \frac{x_{12} - x_{13}}{1 - x_{17}} - \delta_{\boldsymbol{\theta_{18}}}(x_5 + x_7, x_{12}, x_{17}) \frac{1}{1 - x_{17}} \tag{4.17}$$

$$\dot{x}_{13} = \pi_{\theta_{13}}(x_5 + x_6 + 2x_7 + x_{12} + x_{13})[x_{12} - x_{13}] - \frac{\theta_{14} \cdot x_{13}}{x_6 + x_7 + x_{13}}[\theta_3[x_6 + x_7 + x_{13}] - u_2] + \theta_{21} \cdot \rho_{\boldsymbol{\theta_{17}}, u_6}(x_6 + x_7 + x_{13}) \cdot u_4 \cdot e \tag{4.18}$$

$$\dot{x}_{14} = \beta_{\boldsymbol{\theta_{22}}}(x_{14} + x_{15}) \cdot [x_{15} - x_{14}] + \delta_{\boldsymbol{\theta_{23}}}(x_2, x_9, x_{14}) - \beta_{\boldsymbol{\theta_{24}}}(x_{14}) \cdot x_{14} \tag{4.19}$$

$$\dot{x}_{15} = -\beta_{\boldsymbol{\theta_{25}}}(x_{14} + x_{15}) \cdot [x_{15} - x_{14}] + \delta_{\boldsymbol{\theta_{23}}}(x_3, x_{10}, x_{15}) \tag{4.20}$$

$$\dot{x}_{16} = \beta_{\boldsymbol{\theta_{25}}}(x_{16} + x_{17}) \cdot [x_{17} - x_{16}] + \delta_{\boldsymbol{\theta_{23}}}(x_4 + x_7, x_{11}, x_{16}) \tag{4.21}$$

$$\dot{x}_{17} = -\beta_{\boldsymbol{\theta_{22}}}(x_{16} + x_{17}) \cdot [x_{17} - x_{16}] + \delta_{\boldsymbol{\theta_{23}}}(x_5 + x_7, x_{12}, x_{17}) - \beta_{\boldsymbol{\theta_{24}}}(x_{17}) \cdot x_{17} \tag{4.22}$$

$$\dot{x}_{18} = \phi_{\boldsymbol{\theta_{26}}}(x_{18} + x_{20}) \cdot [x_{20} - x_{18}] + \Psi_{\boldsymbol{\theta_{27}}}(x_{10}, x_{18}) \cdot \left[\alpha_{\boldsymbol{\theta_{20}}}(x_{10}) - x_{18}\right] - \theta_{28} \cdot e \cdot [x_{18} + x_{20}] \tag{4.23}$$

$$\dot{x}_{19} = -\phi_{\boldsymbol{\theta_{26}}}(x_{19} + x_{20}) \cdot [x_{19} - x_{20}] + \Psi_{\boldsymbol{\theta_{27}}}(x_{11}, x_{19}) \cdot \left[\alpha_{\boldsymbol{\theta_{20}}}(x_{11}) - x_{19}\right] + \theta_{28} \cdot e \cdot [x_{19} + x_{20}] + \theta_{29} \cdot e \cdot \tag{4.24}$$

$$\dot{x}_{20} = -\phi_{\boldsymbol{\theta_{30}}}(x_{18} + x_{20}) \cdot [x_{20} - x_{18}] + \phi_{\boldsymbol{\theta_{30}}}(x_{20} + x_{19}) \cdot [x_{19} - x_{20}] + \theta_{31} \cdot e \cdot [x_{18} - x_{19}] \tag{4.25}$$

This system of differential equations relies on constants that are synthesized in Tables 4.1 and 4.2.

Notation	Physical Expression	Order of Magnitude	Remarks
θ_1	$\frac{2}{R \cdot T_{fc} \cdot {H_{gc}}^2} \left[0.9247 \cdot ln\left(\frac{W_{gc}}{H_{gc}}\right) + 2.3787\right] \cdot 1.644 \cdot 10^{-4} \cdot \left(\frac{T_{fc}}{333}\right)^{2.334} \cdot 101325$	$[10^3, 10^6]$	
θ_2	$\frac{k_{em,in}}{H_{gc} \cdot W_{gc} \cdot L_{gc}} \frac{x_1 + x_8}{M_{H_2} \cdot x_1 + M_{H_2O} \cdot x_8}$	$[10^2, 10^5]$	The hypothesis (H5) is applied here.
θ_3	$R \cdot T_{fc}$	10^3	
θ_4	$\frac{A_{act}}{2 \cdot F \cdot H_{gc} \cdot W_{gc} \cdot L_{gc}}$	$[10^{-2}, 10^{-1}]$	
θ_5	$\frac{[\varepsilon_{gdl} + \varepsilon_{cl}] \cdot e^{\beta_2 \cdot \varepsilon_c}}{R \cdot T_{fc} \cdot H_{gdl} \cdot [H_{gdl} + H_{cl}] \cdot \varepsilon_{gdl}} \left(\frac{\frac{\varepsilon_{gdl} + \varepsilon_{cl}}{2} - 0.11}{1 - 0.11}\right)^{0.785} \cdot 1.644 \cdot 10^{-4} \cdot \left(\frac{T_{fc}}{333}\right)^{2.334} \cdot 101325$	$[10^3, 10^5]$	
θ_6	$\frac{2}{R \cdot T_{fc} \cdot H_{gc} \cdot H_{gdl} \cdot \varepsilon_{gdl}} \left[0.9247 \cdot ln\left(\frac{W_{gc}}{H_{gc}}\right) + 2.3787\right] \cdot 1.644 \cdot 10^{-4} \cdot \left(\frac{T_{fc}}{333}\right)^{2.334} \cdot 101325$	$[10^3, 10^7]$	
θ_7	$\frac{[\varepsilon_{gdl} + \varepsilon_{cl}] \cdot e^{\beta_2 \cdot \varepsilon_c}}{R \cdot T_{fc} \cdot H_{cl} \cdot [H_{gdl} + H_{cl}] \cdot \varepsilon_{cl}} \left(\frac{\frac{\varepsilon_{gdl} + \varepsilon_{cl}}{2} - 0.11}{1 - 0.11}\right)^{0.785} \cdot 1.644 \cdot 10^{-4} \cdot \left(\frac{T_{fc}}{333}\right)^{2.334} \cdot 101325$	$[10^4, 10^7]$	
θ_8	$\frac{1}{2 \cdot F \cdot H_{cl} \varepsilon_{cl}}$	$[10^{-1}, 10^0]$	
θ_9	$\frac{[\varepsilon_{gdl} + \varepsilon_{cl}] \cdot e^{\beta_2 \cdot \varepsilon_c}}{R \cdot T_{fc} \cdot H_{cl} \cdot [H_{gdl} + H_{cl}] \cdot \varepsilon_{cl}} \left(\frac{\frac{\varepsilon_{gdl} + \varepsilon_{cl}}{2} - 0.11}{1 - 0.11}\right)^{0.785} \cdot 3.242 \cdot 10^{-5} \cdot \left(\frac{T_{fc}}{333}\right)^{2.334} \cdot 101325$	$[10^2, 10^4]$	
θ_{10}	$\frac{1}{4 \cdot F \cdot H_{cl} \cdot \varepsilon_{cl}}$	$[10^{-2}, 10^0]$	
θ_{11}	$\frac{[\varepsilon_{gdl} + \varepsilon_{cl}] \cdot e^{\beta_2 \cdot \varepsilon_c}}{R \cdot T_{fc} \cdot H_{gdl} \cdot [H_{gdl} + H_{cl}] \cdot \varepsilon_{gdl}} \left(\frac{\frac{\varepsilon_{gdl} + \varepsilon_{cl}}{2} - 0.11}{1 - 0.11}\right)^{0.785} \cdot 3.242 \cdot 10^{-5} \cdot \left(\frac{T_{fc}}{333}\right)^{2.334} \cdot 101325$	$[10^2, 10^4]$	
θ_{12}	$\frac{2}{R \cdot T_{fc} \cdot H_{gc} \cdot H_{gdl} \cdot \varepsilon_{gdl}} \left[0.9247 \cdot ln\left(\frac{W_{gc}}{H_{gc}}\right) + 2.3787\right] \cdot 3.242 \cdot 10^{-5} \cdot \left(\frac{T_{fc}}{333}\right)^{2.334} \cdot 101325$	$[10^2, 10^6]$	
θ_{13}	$\frac{2}{R \cdot T_{fc} \cdot {H_{gc}}^2} \left[0.9247 \cdot ln\left(\frac{W_{gc}}{H_{gc}}\right) + 2.3787\right] \cdot 3.242 \cdot 10^{-5} \cdot \left(\frac{T_{fc}}{333}\right)^{2.334} \cdot 101325$	$[10^2, 10^5]$	
θ_{14}	$\frac{k_{em,in}}{H_{gc} \cdot W_{gc} \cdot L_{gc}} \frac{x_6 + x_7 + x_{13}}{M_{O_2} \cdot x_6 + M_{N_2} \cdot x_7 + M_{H_2O} \cdot x_{13}}$	$[10^1, 10^4]$	The hypothesis (H5) is applied here.
θ_{15}	$\frac{A_{act}}{4 \cdot F \cdot H_{gc} \cdot W_{gc} \cdot L_{gc}}$	$[10^{-3}, 10^{-2}]$	
θ_{16}	$\frac{1 - y_{O_2,ext}}{y_{O_2,ext}} \frac{A_{act}}{4 \cdot F \cdot H_{gc} \cdot W_{gc} \cdot L_{gc}}$	$[10^{-2}, 10^{-1}]$	

Table 4.1. – Summary table of the constants used in the system of differential equations with their orders of magnitude (1/2).

Notation	Physical Expression	Order of Magnitude
$\boldsymbol{\theta_{17}}$	$\left(P_{sat}\left(T_{fc}\right), R \cdot T_{fc}, P_{sat}\left(T_{fc}\right)\right)$	$\left(10^4, 10^3, 10^4\right)$
$\boldsymbol{\theta_{18}}$	$\left(\gamma_{cond}, \frac{P_{sat}(T_{fc})}{RT_{fc}}, \frac{\gamma_{evap} \cdot RT_{fc} \cdot \rho_{H_2O}(T_{fc})}{M_{H_2O}}\right)$	$\left(\left[10^0, 10^4\right], \left[10^0, 10^1\right], \left[10^3, 10^5\right]\right)$
$\boldsymbol{\theta_{19}}$	$\left(\theta_{19,1}, \theta_{19,2}\right) = \frac{\rho_{mem} \cdot M_{H_2O} \cdot e^{2416\left[\frac{1}{303} - \frac{1}{T_{fc}}\right]} \cdot 10^{-5}}{\rho_{H_2O}(T_{fc}) \cdot M_{eq} \cdot H_{cl} \cdot \varepsilon_{cl}} \left(1.14, 4.59\right), \theta_{19,3} = \frac{M_{eq}}{\rho_{mem}}, \theta_{19,4} = \frac{M_{H_2O}}{\rho_{H_2O}(T_{fc})}$	$\left(\left[10^{-2}, 10^0\right], \left[10^{-2}, 10^0\right], 10^{-4}, 10^{-5}\right)$
$\boldsymbol{\theta_{20}}$	$\left(0.3, \frac{10.8 \cdot RT_{fc}}{P_{sat}(T_{fc})}, -\frac{16.0 \cdot R^2 {T_{fc}}^2}{{P_{sat}(T_{fc})}^2}, \frac{14.1 \cdot R^3 {T_{fc}}^3}{{P_{sat}(T_{fc})}^3}\right)$	$\left(10^{-1}, \left[10^{-1}, 10^0\right], \left[10^{-2}, 10^{-1}\right], \left[10^{-4}, 10^{-1}\right]\right)$
θ_{21}	$\frac{1}{y_{O_2,ext}} \frac{A_{act}}{4 \cdot F \cdot H_{gc} \cdot W_{gc} \cdot L_{gc}}$	$\left[10^{-2}, 10^{-1}\right]$
$\boldsymbol{\theta_{22}}$	$\left(\theta_{22,1}, \theta_{22,2}, \theta_{22,3}\right) = \frac{2 \cdot \sigma(T_{fc}) \cdot K_0 \cdot \lvert cos\left(\frac{\theta_{c,gdl} + \theta_{c,cl}}{2}\right) \rvert \cdot \sqrt{\frac{\varepsilon_{gdl} + \varepsilon_{cl}}{2K_0}}}{\mu_l(T_{fc}) \cdot \varepsilon_{gdl} \cdot H_{gdl} \cdot \left[H_{gdl} + H_{cl}\right]} \left(1.417, -4.24, 3.789\right), \theta_{22,4} = e$	$\left[10^0, 10^4\right]^3, [\![3,5]\!]$
$\boldsymbol{\theta_{23}}$	$\left(\frac{\gamma_{cond} M_{H_2O}}{\rho_{H_2O}(T_{fc})}, \frac{P_{sat}(T_{fc})}{RT_{fc}}, \gamma_{evap} \cdot RT_{fc}\right)$	$\left(\left[10^{-5}, 10^{-1}\right], \left[10^0, 10^1\right], \left[10^{-2}, 10^0\right]\right)$
$\boldsymbol{\theta_{24}}$	$\left(\theta_{24,1}, \theta_{24,2}, \theta_{24,3}\right) = \frac{\sigma(T_{fc}) \cdot K_0 \cdot \lvert cos(\theta_{c,gdl}) \rvert \cdot \sqrt{\frac{\varepsilon_{gdl}}{K_0}}}{\mu_l(T_{fc}) \cdot \varepsilon_{gdl} \cdot {H_{gdl}}^2} \left(1.417, -4.24, 3.789\right), \theta_{24,4} = e$	$\left[10^1, 10^5\right]^3, [\![3,5]\!]$
$\boldsymbol{\theta_{25}}$	$\left(\theta_{25,1}, \theta_{25,2}, \theta_{25,3}\right) = \frac{2 \cdot \sigma(T_{fc}) \cdot K_0 \cdot \lvert cos\left(\frac{\theta_{c,gdl} + \theta_{c,cl}}{2}\right) \rvert \cdot \sqrt{\frac{\varepsilon_{gdl} + \varepsilon_{cl}}{2K_0}}}{\mu_l(T_{fc}) \cdot \varepsilon_{cl} \cdot H_{cl} \cdot \left[H_{gdl} + H_{cl}\right]} \left(1.417, -4.24, 3.789\right), \theta_{25,4} = e$	$\left[10^2, 10^6\right]^3, [\![3,5]\!]$
$\boldsymbol{\theta_{26}}$	$\left(\frac{5.1 \cdot 10^{-10}}{\varepsilon_{mc} \cdot H_{cl}[H_{mem} + H_{cl}]}, 1.0, -1.8, 0.71\right)$	$\left(\left[10^{-2}, 10^2\right], 10^0, 10^0, 10^{-1}\right)$
$\boldsymbol{\theta_{27}}$	$\left(\theta_{27,1}, \theta_{27,2}\right) = \frac{M_{H_2O} \cdot e^{2416\left[\frac{1}{303} - \frac{1}{T_{fc}}\right]} \cdot 10^{-5}}{\rho_{H_2O}(T_{fc}) \cdot H_{cl} \cdot \varepsilon_{mc}} \left(1.14, 4.59\right), \theta_{27,3} = \frac{M_{eq}}{\rho_{mem}}, \theta_{27,4} = \frac{M_{H_2O}}{\rho_{H_2O}(T_{fc})}$	$\left(\left[10^{-6}, 10^{-3}\right], \left[10^{-2}, 10^0\right], 10^{-4}, 10^{-5}\right)$
$\boldsymbol{\theta_{28}}$	$\frac{5.7 \cdot 10^{-2} \cdot M_{eq}}{\rho_{mem} \cdot H_{cl} \cdot F \cdot \varepsilon_{mc}}$	$\left[10^{-6}, 10^{-5}\right]$
$\boldsymbol{\theta_{29}}$	$\frac{M_{eq}}{\rho_{mem} \cdot H_{cl} \cdot 2F \cdot \varepsilon_{mc}}$	$\left[10^{-5}, 10^{-3}\right]$
$\boldsymbol{\theta_{30}}$	$\left(\frac{5.1 \cdot 10^{-10}}{H_{mem}[H_{mem} + H_{cl}]}, 1.0, -1.8, 0.71\right)$	$\left(\left[10^{-3}, 10^0\right], 10^0, 10^0, 10^{-1}\right)$
$\boldsymbol{\theta_{31}}$	$\frac{5.7 \cdot 10^{-2} \cdot M_{eq}}{\rho_{mem} \cdot H_{mem} \cdot F}$	$\left[10^{-6}, 10^{-5}\right]$

Table 4.2. – Summary table of the constants used in the system of differential equations with their orders of magnitude (2/2).

4.3.3. Functions used in the system of differential equations

4.3.3.1. Empirical functions

These functions are based on experimental data, and there are generally several similar functions available to describe the same phenomenon (see section 1.2). Therefore, it is possible to consider new mathematical functions with more favorable properties for system stability, while still adequately describing the physical phenomena.

— Π_θ corresponds to the **effective diffusion coefficient of two chemical species i and j:** $D_{i/j}^{eff}(C, \mathrm{s})$.

— The division by 2 of the variables is a result of numerical resolution, intended to average the values between two discrete numerical points, and does not stem from the original continuous physics.

— Similarly, in figure 4.11, the intervals of z_1 and z_2 are twice as large as that typically assigned to the physical quantities these mathematical variables represent, because it systematically involves the sum of two physical quantities (e.g., $z_2 = \mathrm{s}_{ccl} + \mathrm{s}_{cgdl}$).

$$\Pi_\theta(\boldsymbol{z}) = \pi_\theta\left(\frac{z_1}{2}\right) \cdot \left[1 - \frac{z_2}{2}\right]^2 \tag{4.26}$$

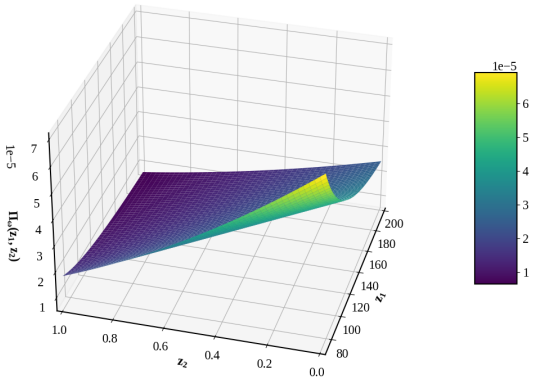

Figure 4.11. – Evolution of Π_θ

— $\beta_{\boldsymbol{\theta}}$ corresponds to the **diffusion coefficient of liquid water, a function of liquid water saturation** $D_{cap}(\mathrm{s})$. θ_4 represents the capillary exponent and is a fixed integer parameter taking values in $\{3, 4, 5\}$.

— The division by 2 of the variables is a result of numerical resolution, intended to average the values between two discrete numerical points, and does not originate from the initial continuous physics.

— Similarly, in figure 4.12, the interval of z is twice as large as typically given for the physical quantities these mathematical variables represent, as it systematically involves the sum of two physical quantities (e.g., $z = \mathrm{s}_{ccl} + \mathrm{s}_{cgdl}$).

$$\beta_{\boldsymbol{\theta}}(z) = \theta_1 \cdot \left(\frac{z}{2}\right)^{\theta_4} + \theta_2 \cdot \left(\frac{z}{2}\right)^{\theta_4+1} + \theta_3 \cdot \left(\frac{z}{2}\right)^{\theta_4+2} \tag{4.27}$$

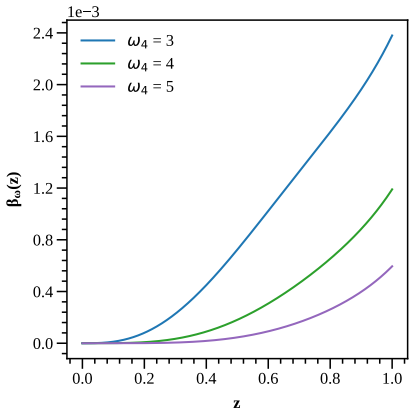

Figure 4.12. – Evolution of β_θ

— $\delta_{\boldsymbol{\theta}}$ corresponds to the **phase transfer rate of water vapor condensation, as a function of fuel concentration, water vapor concentration, and liquid water saturation:** $S_{vl}(C_{tot}, C_v, \mathrm{s})$.

$$\delta_{\boldsymbol{\theta}}(\boldsymbol{z}) = \begin{cases} \theta_1 \frac{z_2}{z_1+z_2} [z_2 - \theta_2] [1 - z_3], & \text{si } z_2 > \theta_2 \\ -\theta_3 [\theta_2 - z_2] \cdot z_3, & \text{si } z_2 \leq \theta_2 \end{cases} \tag{4.28}$$

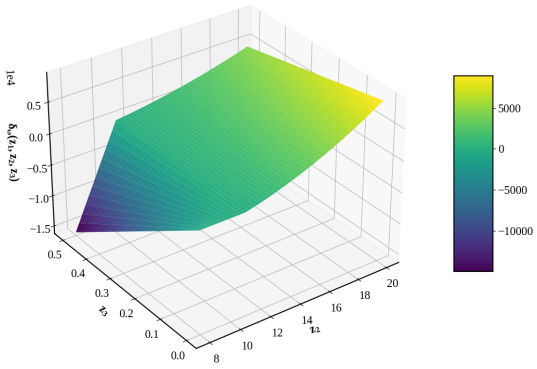

Figure 4.13. – Evolution of δ_θ, for a fixed value of $C_{H_2} + C_v = 70\ mol.m^{-3}$

— $\phi_{\boldsymbol{\theta}}$ corresponds to the **diffusion coefficient of dissolved water in the membrane, a function of dissolved water in the membrane:** $D(\lambda)$.

— The division by 2 of the variables is a result of numerical resolution, intended to average values between two discrete numerical points, and does not originate from the initial continuous physics.

— Similarly, in figure 4.14, the interval of z is twice as large as the interval typically assigned to the physical quantities that this mathematical variable represents, because it systematically involves the sum of two physical quantities (e.g., $z = \lambda_{ccl} + \lambda_{cgdl}$).

$$\phi_{\boldsymbol{\theta}}(z) = \theta_1 \cdot \left(\frac{z}{2}\right)^{0.15} \left[\theta_2 + tanh\left(\theta_3 + \theta_4 \frac{z}{2}\right)\right] \tag{4.29}$$

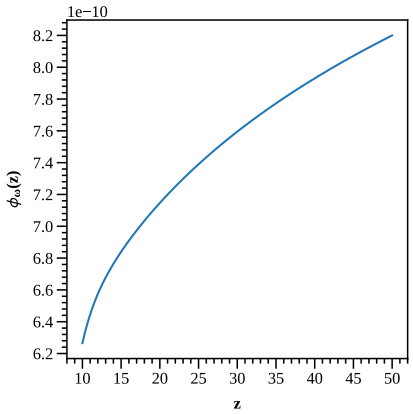

Figure 4.14. – Evolution of ϕ_θ

— $\Psi_{\boldsymbol{\theta},\boldsymbol{\mu}}$ corresponds to the **water sorption rate in the membrane, a function of water vapor concentration and water content dissolved in the membrane:** $\gamma_{sorp}(C_v, \lambda)$. This is a well-documented discontinuous function that refers to a difference in behavior between absorption and desorption (entry or exit from the membrane does not occur in the same manner).

$$\Psi_{\boldsymbol{\theta}}(\boldsymbol{z}) = \begin{cases} \theta_1 \cdot \psi_{(\theta_3,\theta_4)}(z_2), & \text{si } z_2 \leq \alpha_\theta(z_1) \\ \theta_2 \cdot \psi_{(\theta_3,\theta_4)}(z_2), & \text{si } z_2 > \alpha_\theta(z_1) \end{cases} \tag{4.30}$$

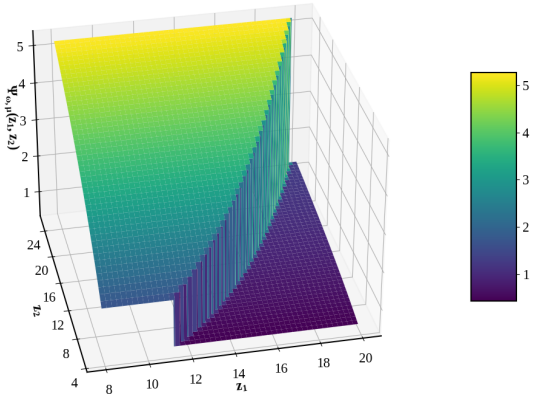

Figure 4.15. – Evolution of $\psi_{\theta,\mu}$

— $\alpha_{\boldsymbol{\theta}}$ corresponds to the **quantity of dissolved water at equilibrium as a function of the vapor concentration:** $\lambda_{eq}(C_v)$. A major simplification has been made by assuming that liquid water does not penetrate the membrane. The current theory on this subject is not yet fully developed.

$$\alpha_{\boldsymbol{\theta}}(z) = \theta_1 + \theta_2 \cdot z + \theta_3 \cdot z^2 + \theta_4 \cdot z^3 \tag{4.31}$$

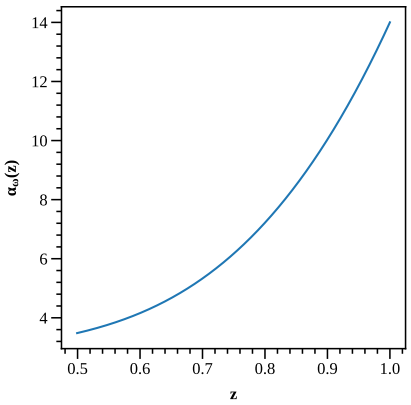

Figure 4.16. – Evolution of α_θ

— $\rho_{\boldsymbol{\theta}}$ corresponds to the **coefficient used to extract the water vapor portion from a fuel stream at a desired humidity**. There is no specific letter dedicated to this coefficient in the field of physics. It takes as input the sum of the concentrations of chemical species in the considered location.

$$\rho_{\boldsymbol{\theta},u}(z) = \frac{\theta_1 \cdot u}{\theta_2 \cdot z - \theta_3 \cdot u} \tag{4.32}$$

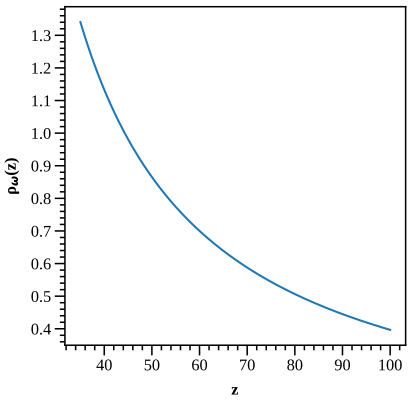

Figure 4.17. – Evolution of $\rho_{\boldsymbol{\theta}}$ for $u = 0.6$

4.3.3.2. Functions serving as intermediate calculations

These functions are involved in the expression of the empirical functions.

— π_θ is related to the **binary diffusion coefficient of gases i and j:** $D_{i/j}(C)$.

$$\pi_\theta(z) = \frac{\theta}{z} \tag{4.33}$$

— $\psi_{\boldsymbol{\theta}}$ corresponds to the **fraction of the membrane's water volume:** $f_\nu(\lambda)$.

$$\psi_{\boldsymbol{\theta}}(z) = \frac{z}{\theta_1 + \theta_2 \cdot z} \tag{4.34}$$

4.4. Summary of model improvements and reuse

In this chapter, a theoretical interpretation of the limit liquid water saturation coefficient (s_{lim}) was presented. The theoretical framework established for s_{lim} provides deeper insights into the voltage drop associated with liquid water presence, paving the way for more effective humidity control strategies using models such as AlphaPEM. The theoretical results suggest a significant potential for increasing peak power density while maintaining acceptable efficiency levels. Specifically, the proposed rule-based control strategy indicates a 66% rise in peak power density, with only a minor decrease in overall cell efficiency. However, further experimental validation is essential to confirm the theoretical findings.

Additionally, incorporating the proton charge conservation equation into the model enables a satisfactory representation of the electrochemical impedance spectroscopy (EIS) curve of a fuel cell, despite convection and thermal exchanges not yet being modeled. This modeling approach is particularly valuable as it could validate the model's dynamic behavior, facilitate a better understanding of fuel cell degradation, and serve as a tool for analyzing experimental EIS curves. For instance, it may help reveal diffusion phenomena that are often masked in such curves.

Finally, a state-space representation of a reduced version of the model was proposed. This representation aims to serve as a foundation for future research to develop a model fully compatible with predictive control frameworks.

Conclusion

The work carried out during this thesis contributed to advancing the understanding of proton exchange membrane fuel cell (PEMFC) modeling to enhance the performance of these converters in embedded applications. Indeed, multi-physics models allow for increasing the available information to better control PEM fuel cells, which is valuable given the difficulty of placing sensors inside a cell. In this study, a critical synthesis of modeling equations from the literature was conducted, a dynamic and one-dimensional PEMFC model with a good balance between execution speed and accuracy was developed, an open-source collaborative software based on this model was released under the name AlphaPEM, and initial applications based on this model were proposed to improve fuel cell performance.

Following this critical review of the literature, further researches appear necessary to develop more advanced models for each of the physical processes occurring within PEMFCs. In particular, efforts should focus on improving the understanding of water sorption at the triple points in a biphasic state, matter sorption at the GDL/GC interface, and the impact of flooding on voltage. Similarly, it is important to conduct a new, well-documented study with minimal limitations, covering a wide range of recent fuel cells, to update the parameters used in these models. Current data often dates back to the early 1990s and are therefore obsolete, given that fuel cells and experimental protocols have evolved since then [56]. Specifically, the expressions for electro-osmotic drag, equilibrium water content, capillary pressure, and protonic conductivity need to be updated.

Based on equations synthesized from the literature, a one-dimensional, dynamic, two-phase, isothermal model of the PEMFC system has been developed, and a finite-difference resolution method was proposed. This model aims to achieve an optimal balance between computational speed and result accuracy. Its static behavior has been validated against several published experimental polarization curves. The model operates two orders of magnitude faster than comparable 1D models in commercial software like COMSOL Multiphysics, and up to five orders of magnitude faster than 3D models reported in the literature. It is well-suited for embedded applications while offering significantly greater precision than lumped-parameter models.

A new coefficient has been introduced to replace the limit current density coefficient (i_{lim}). This coefficient, the limit liquid water saturation coefficient (s_{lim}), also determines the voltage drop at high current densities. s_{lim} offers the added advantage of establishing a physical connection between this voltage drop, the internal states of the cell, and the operating conditions. Moreover, this parameter has been proven to be a function of the pressure imposed by the operators P_{des}. The information provided by this coefficient allows for the implementation of a control strategy for the incoming

humidity of the fuel cell, theoretically improving its power output by up to 60%.

This work led to the publication of AlphaPEM, an open-source, user-friendly, collaborative, and modular software package in Python, designed for PEM fuel cell modeling in embedded applications. This framework is based on the model developed in this thesis. It employs a solver that uses an implicit numerical method to solve the system of differential equations. In practice, AlphaPEM provides real-time access to the internal states and voltage of fuel cell systems and can generate polarization and EIS curves. It also automatically calibrates the model's undetermined parameters to fit any real fuel cell system. This simulator, along with the state-space representation formulated on a reduced version of it, therefore, paves the way for improving the real-time control of the operating conditions of fuel cell systems, thereby enhancing their performance and longevity.

In upcoming research, experimental verification will be conducted to determine whether s_{lim} is dependent on other operating conditions, such as the temperature T_{fc}. Experimental tests will also be carried out to evaluate the proposed control of incoming humidity based on the model. Further attention will be given to enhancing the model's control design. Additionally, the model will be refined through the incorporation of heat exchange modeling, extension to a '1D+1D' model, and the addition of microporous layers (MPLs) within the cell, all while maintaining computational efficiency. Finally, degradation models will be incorporated into AlphaPEM to attempt to use this simulator to accurately predict degradation phenomena and thus take action to mitigate them. These perspectives will be developed preferentially with various research partners, ensuring that the improvement of AlphaPEM is collaborative, enabling more consensual and faster progress.

Bibliography

[1] United Nations. *The Paris Agreement*. Dec. 2015 (cit. on p. 18).

[2] IEA. *The Future of Hydrogen*. June 2019 (cit. on pp. 18–20).

[3] Yun Wang, Ken S. Chen, Jeffrey Mishler, et al. "A Review of Polymer Electrolyte Membrane Fuel Cells: Technology, Applications, and Needs on Fundamental Research". In: *Applied Energy* 88.4 (Apr. 2011), pp. 981–1007. ISSN: 03062619. DOI: 10.1016/j.apenergy.2010.09.030 (cit. on p. 18).

[4] Gouvernement français. *Présentation de la stratégie nationale pour le développement de l'hydrogène décarboné en France*. Sept. 2020 (cit. on p. 18).

[5] Andrew Dicks and D. A. J. Rand. *Fuel Cell Systems Explained*. Third edition. Hoboken, NJ: Wiley, 2018. ISBN: 978-1-118-61352-8 (cit. on pp. 18, 21–24, 27, 30, 65, 68, 72, 73, 111, 146, 190).

[6] Kui Jiao, Jin Xuan, Qing Du, et al. "Designing the next Generation of Proton-Exchange Membrane Fuel Cells". In: *Nature* 595.7867 (July 2021), pp. 361–369. ISSN: 0028-0836, 1476-4687. DOI: 10.1038/s41586-021-03482-7 (cit. on pp. 18–22, 24).

[7] Ademe. *Le véhicule électrique dans la Transition écologique en France* (cit. on p. 18).

[8] Ademe. *Analyse de cycle de vie relative à l'hydrogène* (cit. on p. 18).

[9] Jianping Wen, Dan Zhao, and Chuanwei Zhang. "An Overview of Electricity Powered Vehicles: Lithium-ion Battery Energy Storage Density and Energy Conversion Efficiency". In: *Renewable Energy* 162 (Dec. 2020), pp. 1629–1648. ISSN: 09601481. DOI: 10.1016/j.renene.2020.09.055 (cit. on p. 18).

[10] IFPEN. *Les véhicules essence et Diesel* (cit. on p. 18).

[11] Tesla. *The Longest-Range Electric Vehicle Now Goes Even Farther* (cit. on p. 18).

[12] Anna Tomaszewska. "Lithium-Ion Battery Fast Charging: A Review". In: (2019) (cit. on p. 19).

[13] Bibaswan Bose, A. Garg, B.K. Panigrahi, et al. "Study on Li-ion Battery Fast Charging Strategies: Review, Challenges and Proposed Charging Framework". In: *Journal of Energy Storage* 55 (Nov. 2022), p. 105507. ISSN: 2352152X. DOI: 10.1016/j.est.2022.105507 (cit. on p. 19).

[14] Martin Schulz and SAE International. *Solving the Challenges of Megawatt Chargers*. 2022 (cit. on p. 19).

[15] European Union. *Clean Hydrogen Joint Undertaking. Strategic Research and Innovation Agenda 2021 – 2027*. 2022 (cit. on pp. 19, 21).

[16] France Bleu. *Les bus électriques sont-ils écologiques ? - France Bleu*. Oct. 2019 (cit. on p. 19).

[17] European Union. *Critical Raw Materials Resilience: Charting a Path towards Greater Security and Sustainability*. 2020 (cit. on p. 19).

[18] CNRS Le journal. *L'hydrogène tiendra-t-il ses promesses ?* (Cit. on pp. 19, 20).

[19] Jinyong Kim, Gang Luo, and Chao-Yang Wang. "Modeling Two-Phase Flow in Three-Dimensional Complex Flow-Fields of Proton Exchange Membrane Fuel Cells". In: *Journal of Power Sources* 365 (Oct. 2017), pp. 419–429. ISSN: 03787753. DOI: 10.1016/j.jpowsour.2017.09.003 (cit. on pp. 19, 47, 51, 57).

[20] Renault Group. *Tout savoir sur l'entretien d'une voiture électrique* (cit. on p. 19).

[21] H2mobile. *Carlos Tavares : La technologie hydrogène ne sera gagnante que si nous réussissons à la rendre abordable* (cit. on p. 21).

[22] S. Mekhilef, R. Saidur, and A. Safari. "Comparative Study of Different Fuel Cell Technologies". In: *Renewable and Sustainable Energy Reviews* 16.1 (Jan. 2012), pp. 981–989. ISSN: 13640321. DOI: 10.1016/j.rser.2011.09.020 (cit. on p. 21).

[23] Ryan P. O'Hayre, Suk-Won Cha, Whitney G. Colella, et al. *Fuel Cell Fundamentals*. Third edition. Hoboken, New Jersey: Wiley, 2016. ISBN: 978-1-119-11380-5 (cit. on pp. 21–24, 27, 53–58, 65, 66, 68, 72, 73, 111).

[24] Marine Jouin, Rafael Gouriveau, Daniel Hissel, et al. "Degradations Analysis and Aging Modeling for Health Assessment and Prognostics of PEMFC". In: *Reliability Engineering & System Safety* 148 (Apr. 2016), pp. 78–95. ISSN: 0951-8320. DOI: 10.1016/j.ress.2015.12.003 (cit. on p. 22).

[25] H. Tawfik, Y. Hung, and D. Mahajan. "Metal Bipolar Plates for PEM Fuel Cell—A Review". In: *Journal of Power Sources*. Selected Papers Presented at the FUEL PROCESSING FOR HYDROGEN PRODUCTION SYMPOSIUM at the 230th American Chemical SocietyNational Meeting Washington, DC, USA, 28 August – 1 September 2005 163.2 (Jan. 2007), pp. 755–767. ISSN: 0378-7753. DOI: 10.1016/j.jpowsour.2006.09.088 (cit. on p. 22).

[26] Shahram Karimi, Norman Fraser, Bronwyn Roberts, et al. "A Review of Metallic Bipolar Plates for Proton Exchange Membrane Fuel Cells: Materials and Fabrication Methods". In: *Advances in Materials Science and Engineering* 2012.1 (2012), p. 828070. ISSN: 1687-8442. DOI: 10.1155/2012/828070 (cit. on p. 22).

[27] Yuxi Song, Caizhi Zhang, Chun-Yu Ling, et al. "Review on Current Research of Materials, Fabrication and Application for Bipolar Plate in Proton Exchange Membrane Fuel Cell". In: *International Journal of Hydrogen Energy*. Progress in Fuel Cells 45.54 (Nov. 2020), pp. 29832–29847. ISSN: 0360-3199. DOI: 10.1016/j.ijhydene.2019.07.231 (cit. on p. 22).

[28] Cheng Bao and Wolfgang G. Bessler. "Two-Dimensional Modeling of a Polymer Electrolyte Membrane Fuel Cell with Long Flow Channel. Part I. Model Development". In: *Journal of Power Sources* 275 (Feb. 2015), pp. 922–934. ISSN: 03787753. DOI: 10.1016/j.jpowsour.2014.11.058 (cit. on pp. 24, 38, 66, 68–70, 74, 87, 188–190, 192, 193).

[29] Manik Mayur, Stephan Strahl, Attila Husar, et al. "A Multi-Timescale Modeling Methodology for PEMFC Performance and Durability in a Virtual Fuel Cell Car". In: *International Journal of Hydrogen Energy* 40.46 (Dec. 2015), pp. 16466–16476. ISSN: 03603199. DOI: 10.1016/j.ijhydene.2015.09.152 (cit. on pp. 24, 87).

[30] *COMSOL: Multiphysics Software for Optimizing Designs* (cit. on p. 24).

[31] Biao Xie, Guobin Zhang, Yang Jiang, et al. ""3D+1D" Modeling Approach toward Large-Scale PEM Fuel Cell Simulation and Partitioned Optimization Study on Flow Field". In: *eTransportation* 6 (Nov. 2020), p. 100090. ISSN: 25901168. DOI: 10.1016/j.etran.2020.100090 (cit. on pp. 24, 86).

[32] Hao Wu. "Mathematical Modeling of Transient Transport Phenomena in PEM Fuel Cells". PhD thesis. Waterloo, Ontario, Canada: University of Waterloo, 2009 (cit. on pp. 24, 42, 50, 86).

[33] Linhao Fan, Guobin Zhang, and Kui Jiao. "Characteristics of PEMFC Operating at High Current Density with Low External Humidification". In: *Energy Conversion and Management* 150 (Oct. 2017), pp. 763–774. ISSN: 01968904. DOI: 10.1016/j.enconman.2017.08.034 (cit. on pp. 24, 34, 36, 37, 41, 42, 47–49, 52–55, 66, 68–70, 74, 86, 124, 187–190).

[34] *Ansys Fluent | Fluid Simulation Software* (cit. on p. 24).

[35] Juergen O. Schumacher, Jens Eller, Guido Sartoris, et al. "2+1D Modelling of a Polymer Electrolyte Fuel Cell with Glassy-Carbon Microstructures". In: *Mathematical and Computer Modelling of Dynamical Systems* 18.4 (Aug. 2012), pp. 355–377. ISSN: 1387-3954, 1744-5051. DOI: 10.1080/13873954.2011.642390 (cit. on pp. 24, 87).

[36] *Wolfram Mathematica: Modern Technical Computing* (cit. on p. 24).

[37] Steven B. Beale, Hae-Won Choi, Jon G. Pharoah, et al. "Open-Source Computational Model of a Solid Oxide Fuel Cell". In: *Computer Physics Communications* 200 (Mar. 2016), pp. 15–26. ISSN: 0010-4655. DOI: 10.1016/j.cpc.2015.10.007 (cit. on p. 24).

[38] Shidong Zhang, Steffen Hess, Holger Marschall, et al. "openFuelCell2: A New Computational Tool for Fuel Cells, Electrolyzers, and Other Electrochemical Devices and Processes". In: *Computer Physics Communications* 298 (May 2024), p. 109092. ISSN: 0010-4655. DOI: 10.1016/j.cpc.2024.109092 (cit. on p. 24).

[39] Shidong Zhang, Steffen Hess, and Steven Beale. *openFuelCell2*. Sept. 2023 (cit. on p. 24).

[40] *OpenFOAM*. June 2024 (cit. on p. 24).

[41] Jay T. Pukrushpan, Huei Peng, and Anna G. Stefanopoulou. "Control-Oriented Modeling and Analysis for Automotive Fuel Cell Systems". In: *Journal of Dynamic Systems, Measurement, and Control* 126.1 (Mar. 2004), pp. 14–25. ISSN: 0022-0434, 1528-9028. DOI: 10.1115/1.1648308 (cit. on pp. 24, 28, 36, 37, 51, 59, 66, 73, 87, 102, 103, 108, 111).

[42] Jay Tawee Pukrushpan, Anna G. Stefanopoulou, and Huei Peng. *University of Michigan Fuel Cell Stack Simulation Package*. 2002 (cit. on p. 24).

[43] Roman Vetter and Jürgen O. Schumacher. "Free Open Reference Implementation of a Two-Phase PEM Fuel Cell Model". In: *Computer Physics Communications* 234 (Jan. 2019), pp. 223–234. ISSN: 00104655. DOI: 10.1016/j.cpc.2018.07.023 (cit. on p. 25).

[44] Juergen Schumacher, Roman Vetter, and Robert Herrendörfer. *PEMFC-1DMMM*. 2020 (cit. on p. 25).

[45] Kui Jiao and Xianguo Li. "Water Transport in Polymer Electrolyte Membrane Fuel Cells". In: *Progress in Energy and Combustion Science* 37.3 (June 2011), pp. 221–291. ISSN: 03601285. DOI: 10.1016/j.pecs.2010.06.002 (cit. on pp. 27, 31–34, 36, 37, 41, 42, 44, 46, 47, 50, 52, 56, 58, 65, 66, 74, 134, 187, 189, 190, 192, 193, 196).

[46] Raphaël Gass, Zhongliang Li, Rachid Outbib, et al. "A Critical Review of Proton Exchange Membrane Fuel Cells Matter Transports and Voltage Polarisation for Modelling". In: *Journal of The Electrochemical Society* (2024). ISSN: 1945-7111. DOI: 10.1149/1945-7111/ad305a (cit. on pp. 28, 134).

[47] Adam Z Weber and John Newman. "Transport in Polymer-Electrolyte Membranes". In: *Journal of The Electrochemical Society* 151.2 (2004), A311. DOI: 10.1149/1.1639157 (cit. on pp. 32, 61, 111).

[48] Georg A. Futter, Pawel Gazdzicki, K. Andreas Friedrich, et al. "Physical Modeling of Polymer-Electrolyte Membrane Fuel Cells: Understanding Water Management and Impedance Spectra". In: *Journal of Power Sources* 391 (July 2018), pp. 148–161. ISSN: 03787753. DOI: 10.1016/j.jpowsour.2018.04.070 (cit. on p. 32).

[49] J. Newman and K. E. Thomas-Alyea. *Electrochemical Systems, 3rd Edition*. John Wiley & Sons, 2004 (cit. on p. 32).

[50] T. E. Springer, T. A. Zawodzinski, and S. Gottesfeld. "Polymer Electrolyte Fuel Cell Model". In: *Journal of The Electrochemical Society* 138.8 (Aug. 1991), pp. 2334–2342. ISSN: 0013-4651, 1945-7111. DOI: 10.1149/1.2085971 (cit. on pp. 32, 34, 36, 37, 40, 42, 67, 74, 75, 192).

[51] A. A. Kulikovsky. "Quasi-3D Modeling of Water Transport in Polymer Electrolyte Fuel Cells". In: *Journal of The Electrochemical Society* 150.11 (2003), A1432. ISSN: 00134651. DOI: 10.1149/1.1611489 (cit. on pp. 32–35, 189, 191).

[52] Ling Xu, Zunyan Hu, Chuan Fang, et al. "A Reduced-dimension Dynamic Model of a Proton-exchange Membrane Fuel Cell". In: *International Journal of Energy Research* 45.12 (Oct. 2021), pp. 18002–18017. ISSN: 0363-907X, 1099-114X. DOI: 10.1002/er.6945 (cit. on pp. 32, 34, 41, 45, 53, 65, 66, 68–70, 74, 77, 87, 102, 103, 128, 189, 190, 192).

[53] Junming Hu, Jianqiu Li, Liangfei Xu, et al. "Analytical Calculation and Evaluation of Water Transport through a Proton Exchange Membrane Fuel Cell Based on a One-Dimensional Model". In: *Energy* 111 (Sept. 2016), pp. 869–883. ISSN: 03605442. DOI: 10.1016/j.energy.2016.06.020 (cit. on pp. 32, 42, 49, 56, 188–190).

[54] Lei Xing, Prodip K. Das, Xueguan Song, et al. "Numerical Analysis of the Optimum Membrane/Ionomer Water Content of PEMFCs: The Interaction of Nafion® Ionomer Content and Cathode Relative Humidity". In: *Applied Energy* 138 (Jan. 2015), pp. 242–257. ISSN: 03062619. DOI: 10.1016/j.apenergy.2014.10.011 (cit. on pp. 32, 36, 37, 41, 42, 46, 47, 49, 52, 53, 74, 190, 196).

[55] Xiao-Guang Yang, Qiang Ye, and Ping Cheng. "Matching of Water and Temperature Fields in Proton Exchange Membrane Fuel Cells with Non-Uniform Distributions". In: *International Journal of Hydrogen Energy* 36.19 (Sept. 2011), pp. 12524–12537. ISSN: 03603199. DOI: 10.1016/j.ijhydene.2011.07.014 (cit. on pp. 32, 34, 36, 37, 41, 42, 49, 51–53, 55, 56, 74, 187–190).

[56] Mohammad Bagher Karimi, Fereidoon Mohammadi, and Khadijeh Hooshyari. "Recent Approaches to Improve Nafion Performance for Fuel Cell Applications: A Review". In: *International Journal of Hydrogen Energy* 44.54 (Nov. 2019), pp. 28919–28938. ISSN: 0360-3199. DOI: 10.1016/j.ijhydene.2019.09.096 (cit. on pp. 33, 34, 36, 75, 78, 167).

[57] Edmund J. F. Dickinson and Graham Smith. "Modelling the Proton-Conductive Membrane in Practical Polymer Electrolyte Membrane Fuel Cell (PEMFC) Simulation: A Review". In: *Membranes* 10.11 (Oct. 2020), p. 310. ISSN: 2077-0375. DOI: 10.3390/membranes10110310 (cit. on pp. 33, 36, 75).

[58] Thomas A. Zawodzinski, Michal Neeman, Laurel O. Sillerud, et al. "Determination of Water Diffusion Coefficients in Perfluorosulfonate Ionomeric Membranes". In: *The Journal of Physical Chemistry* 95.15 (July 1991), pp. 6040–6044. ISSN: 0022-3654, 1541-5740. DOI: 10.1021/j100168a060 (cit. on pp. 33, 36, 37).

[59] Sathya Motupally, Aaron J. Becker, and John W. Weidner. "Diffusion of Water in Nafion 115 Membranes". In: *Journal of The Electrochemical Society* 147.9 (2000), p. 3171. ISSN: 00134651. DOI: 10.1149/1.1393879 (cit. on pp. 34, 36, 191).

[60] Xuhai Wang and Trung Van Nguyen. "Modeling the Effects of Capillary Property of Porous Media on the Performance of the Cathode of a PEMFC". In: *Journal of The Electrochemical Society* 155.11 (2008), B1085. ISSN: 00134651. DOI: 10.1149/1.2965512 (cit. on pp. 34, 36, 37, 46, 47, 49, 52, 187, 189, 191, 196).

[61] Hubertus P. L. H. van Bussel, Frans G. H. Koene, and Ronald K. A. M. Mallant. "Dynamic Model of Solid Polymer Fuel Cell Water Management". In: *Journal of Power Sources* 71.1 (Mar. 1998), pp. 218–222. ISSN: 0378-7753. DOI: 10.1016/S0378-7753(97)02744-4 (cit. on p. 34).

[62] Ugur Pasaogullari and Chao-Yang Wang. "Two-Phase Modeling and Flooding Prediction of Polymer Electrolyte Fuel Cells". In: *Journal of The Electrochemical Society* 152.2 (2005), A380. ISSN: 00134651. DOI: 10.1149/1.1850339 (cit. on pp. 36, 37, 41, 46, 49, 56, 74, 189, 191, 196).

[63] James T. Hinatsu, Minoru Mizuhata, and Hiroyasu Takenaka. "Water Uptake of Perfluorosulfonic Acid Membranes from Liquid Water and Water Vapor". In: *Journal of The Electrochemical Society* 141.6 (June 1994), pp. 1493–1498. ISSN: 0013-4651, 1945-7111. DOI: 10.1149/1.2054951 (cit. on pp. 36, 187, 192).

[64] Shanhai Ge, Xuguang Li, Baolian Yi, et al. "Absorption, Desorption, and Transport of Water in Polymer Electrolyte Membranes for Fuel Cells". In: *Journal of The Electrochemical Society* 152.6 (2005), A1149. ISSN: 00134651. DOI: 10.1149/1.1899263 (cit. on pp. 36, 40, 42–44, 192).

[65] T Zawodzinskijr, T Springer, F Uribe, et al. "Characterization of Polymer Electrolytes for Fuel Cell Applications". In: *Solid State Ionics* 60.1-3 (Mar. 1993), pp. 199–211. ISSN: 01672738. DOI: 10.1016/0167-2738(93)90295-E (cit. on p. 36).

[66] Qiang Ye and Trung Van Nguyen. "Three-Dimensional Simulation of Liquid Water Distribution in a PEMFC with Experimentally Measured Capillary Functions". In: *Journal of The Electrochemical Society* 154.12 (2007), B1242. ISSN: 00134651. DOI: 10.1149/1.2783775 (cit. on pp. 36, 46, 47, 49, 52, 74, 75, 189, 191, 196).

[67] Hao Wu, Peter Berg, and Xianguo Li. "Modeling of PEMFC Transients with Finite-Rate Phase-Transfer Processes". In: *Journal of The Electrochemical Society* 157.1 (2010), B1. ISSN: 00134651. DOI: 10.1149/1.3248005 (cit. on p. 42).

[68] Hua Meng. "A Two-Phase Non-Isothermal Mixed-Domain PEM Fuel Cell Model and Its Application to Two-Dimensional Simulations". In: *Journal of Power Sources* 168.1 (May 2007), pp. 218–228. ISSN: 03787753. DOI: 10.1016/j.jpowsour.2007.03.012 (cit. on pp. 42, 47, 49, 52, 134, 189, 191).

[69] Jinmoo Nam, Purushothama Chippar, Whangi Kim, et al. "Numerical Analysis of Gas Crossover Effects in Polymer Electrolyte Fuel Cells (PEFCs)". In: *Applied Energy* 87.12 (Dec. 2010), pp. 3699–3709. ISSN: 03062619. DOI: 10.1016/j.apenergy.2010.05.023 (cit. on pp. 45, 61, 62).

[70] Stephen Whitaker. *The Method of Volume Averaging*. Vol. 13. Theory and Applications of Transport in Porous Media. Dordrecht: Springer Netherlands, 1999. ISBN: 978-94-017-3389-2. DOI: 10.1007/978-94-017-3389-2 (cit. on pp. 46, 193).

[71] Manolis M. Tomadakis and Teri J. Robertson. "Viscous Permeability of Random Fiber Structures: Comparison of Electrical and Diffusional Estimates with Experimental and Analytical Results". In: *Journal of Composite Materials* 39.2 (Jan. 2005), pp. 163–188. ISSN: 0021-9983, 1530-793X. DOI: 10.1177/0021998305046438 (cit. on pp. 47, 48, 54).

[72] Z. Fishman and A. Bazylak. "Heterogeneous Through-Plane Distributions of Tortuosity, Effective Diffusivity, and Permeability for PEMFC GDLs". In: *Journal of The Electrochemical Society* 158.2 (2011), B247. ISSN: 00134651. DOI: 10.1149/1.3524284 (cit. on pp. 47, 48, 53–55, 140).

[73] Zhiming Bao, Yanan Li, Xia Zhou, et al. "Transport Properties of Gas Diffusion Layer of Proton Exchange Membrane Fuel Cells: Effects of Compression". In: *International Journal of Heat and Mass Transfer* 178 (Oct. 2021), p. 121608. ISSN: 00179310. DOI: 10.1016/j.ijheatmasstransfer.2021.121608 (cit. on pp. 48, 54).

[74] Nada Zamel and Xianguo Li. "Effective Transport Properties for Polymer Electrolyte Membrane Fuel Cells – With a Focus on the Gas Diffusion Layer". In: *Progress in Energy and Combustion Science* 39.1 (Feb. 2013), pp. 111–146. ISSN: 03601285. DOI: 10.1016/j.pecs.2012.07.002 (cit. on p. 48).

[75] Sung-Dae Yim, Byung-Ju Kim, Young-Jun Sohn, et al. "The Influence of Stack Clamping Pressure on the Performance of PEM Fuel Cell Stack". In: *Current Applied Physics* 10.2 (Mar. 2010), S59–S61. ISSN: 15671739. DOI: 10.1016/j.cap.2009.11.042 (cit. on p. 48).

[76] Yulin Wang, Tao Liu, Huan Sun, et al. "Investigation of Dry Ionomer Volume Fraction in Cathode Catalyst Layer under Different Relative Humilities and Nonuniform Ionomer-Gradient Distributions for PEM Fuel Cells". In: *Electrochimica Acta* 353 (Sept. 2020), p. 136491. ISSN: 00134686. DOI: 10.1016/j.electacta.2020.136491 (cit. on pp. 49, 52, 53, 55, 66, 74, 187, 189, 190).

[77] N. B. Vargaftik, B. N. Volkov, and L. D. Voljak. "International Tables of the Surface Tension of Water". In: *Journal of Physical and Chemical Reference Data* 12.3 (July 1983), pp. 817–820. ISSN: 0047-2689, 1529-7845. DOI: 10.1063/1.555688 (cit. on p. 49).

[78] Ugur Pasaogullari and Chao-Yang Wang. "Two-Phase Transport and the Role of Micro-Porous Layer in Polymer Electrolyte Fuel Cells". In: *Electrochimica Acta* 49.25 (Oct. 2004), pp. 4359–4369. ISSN: 0013-4686. DOI: 10.1016/j.electacta.2004.04.027 (cit. on pp. 49, 50).

[79] C Y Wang and P Cheng. "A Multiphase Mixture Model for Multiphase, Multicomponent Transport in Capillary Porous Media I. Model Development". In: *International Journal of Heat and Mass Transfer* 39 (Nov. 1996), p. 3607. DOI: 10.1016/0017-9310(96)00036-1 (cit. on pp. 49–51).

[80] Toshikazu Kotaka, Yuichiro Tabuchi, Ugur Pasaogullari, et al. "Impact of Interfacial Water Transport in PEMFCs on Cell Performance". In: *Electrochimica Acta* 146 (Nov. 2014), pp. 618–629. ISSN: 00134686. DOI: 10.1016/j.electacta.2014.08.148 (cit. on p. 51).

[81] Liang Hao, Koji Moriyama, Wenbin Gu, et al. "Modeling and Experimental Validation of Pt Loading and Electrode Composition Effects in PEM Fuel Cells". In: *Journal of The Electrochemical Society* 162.8 (2015), F854–F867. ISSN: 0013-4651, 1945-7111. DOI: 10.1149/2.0221508jes (cit. on p. 51).

[82] Yun Wang, Suman Basu, and Chao-Yang Wang. "Modeling Two-Phase Flow in PEM Fuel Cell Channels". In: *Journal of Power Sources* 179.2 (May 2008), pp. 603–617. ISSN: 03787753. DOI: 10.1016/j.jpowsour.2008.01.047 (cit. on p. 51).

[83] Fangming Jiang and Chao-Yang Wang. "Numerical Modeling of Liquid Water Motion in a Polymer Electrolyte Fuel Cell". In: *International Journal of Hydrogen Energy* 39.2 (Jan. 2014), pp. 942–950. ISSN: 03603199. DOI: 10.1016/j.ijhydene.2013.10.113 (cit. on p. 51).

[84] Yubai Li and Shi-Chune Yao. "Porous Media Modeling of Microchannel Cooled Electronic Chips with Nonuniform Heating". In: *Journal of Thermophysics and Heat Transfer* 29.4 (Oct. 2015), pp. 695–704. ISSN: 0887-8722, 1533-6808. DOI: 10.2514/1.T4509 (cit. on p. 51).

[85] Jun Jie Liu, Hua Zhang, S. C. Yao, et al. "Porous Media Modeling of Two-Phase Microchannel Cooling of Electronic Chips With Nonuniform Power Distribution". In: *Journal of Electronic Packaging* 136.2 (June 2014), p. 021008. ISSN: 1043-7398, 1528-9044. DOI: 10.1115/1.4027420 (cit. on p. 51).

[86] U Imke. "Porous Media Simplified Simulation of Single- and Two-Phase Flow Heat Transfer in Micro-Channel Heat Exchangers". In: *Chemical Engineering Journal* 101.1-3 (Aug. 2004), pp. 295–302. ISSN: 13858947. DOI: 10.1016/j.cej.2003.10.012 (cit. on p. 51).

[87] Chao-Yang Wang, Manfred Groll, Stefan Rösler, et al. "Porous Medium Model for Two-Phase Flow in Mini Channels with Applications to Micro Heat Pipes". In: *Heat Recovery Systems and CHP* 14.4 (July 1994), pp. 377–389. ISSN: 08904332. DOI: 10.1016/0890-4332(94)90041-8 (cit. on p. 51).

[88] D. Sugumar and Kek-Kiong Tio. "Thermal Analysis of Inclined Micro Heat Pipes". In: *Journal of Heat Transfer* 128.2 (Feb. 2006), pp. 198–202. ISSN: 0022-1481, 1528-8943. DOI: 10.1115/1.2137763 (cit. on p. 51).

[89] Kek-Kiong Tio, Chang Yu Liu, and Kok Chuan Toh. "Thermal Analysis of Micro Heat Pipes Using a Porous-Medium Model". In: *Heat and Mass Transfer* 36.1 (Mar. 2000), pp. 21–28. ISSN: 0947-7411, 1432-1181. DOI: 10.1007/s002310050359 (cit. on p. 51).

[90] Suman Basu, Jun Li, and Chao-Yang Wang. "Two-Phase Flow and Maldistribution in Gas Channels of a Polymer Electrolyte Fuel Cell". In: *Journal of Power Sources* 187.2 (Feb. 2009), pp. 431–443. ISSN: 03787753. DOI: 10.1016/j.jpowsour.2008.11.039 (cit. on p. 51).

[91] Yun Wang and Chao-Yang Wang. "Modeling Polymer Electrolyte Fuel Cells with Large Density and Velocity Changes". In: *Journal of The Electrochemical Society* 152.2 (2005), A445. ISSN: 00134651. DOI: 10.1149/1.1851059 (cit. on p. 51).

[92] S. Strahl, A. Husar, P. Puleston, et al. "Performance Improvement by Temperature Control of an Open-Cathode PEM Fuel Cell System". In: *Fuel Cells* 14.3 (June 2014), pp. 466–478. ISSN: 1615-6846, 1615-6854. DOI: 10.1002/fuce.201300211 (cit. on p. 52).

[93] Jin Hyun Nam, Kyu-Jin Lee, Gi-Suk Hwang, et al. "Microporous Layer for Water Morphology Control in PEMFC". In: *International Journal of Heat and Mass Transfer* 52.11-12 (May 2009), pp. 2779–2791. ISSN: 00179310. DOI: 10.1016/j.ijheatmasstransfer.2009.01.002 (cit. on pp. 53, 56, 189, 191).

[94] Biao Xie, Meng Ni, Guobin Zhang, et al. "Validation Methodology for PEM Fuel Cell Three-Dimensional Simulation". In: *International Journal of Heat and Mass Transfer* 189 (June 2022), p. 122705. ISSN: 00179310. DOI: 10.1016/j.ijheatmasstransfer.2022.122705 (cit. on pp. 53, 68, 116, 124, 128).

[95] Nada Zamel, Xianguo Li, and Jun Shen. "Correlation for the Effective Gas Diffusion Coefficient in Carbon Paper Diffusion Media". In: *Energy & Fuels* 23.12 (Dec. 2009), pp. 6070–6078. ISSN: 0887-0624, 1520-5029. DOI: 10.1021/ef900653x (cit. on p. 53).

[96] Y. Bultel, K. Wiezell, F. Jaouen, et al. "Investigation of Mass Transport in Gas Diffusion Layer at the Air Cathode of a PEMFC". In: *Electrochimica Acta* 51.3 (Oct. 2005), pp. 474–488. ISSN: 00134686. DOI: 10.1016/j.electacta.2005.05.007 (cit. on pp. 56, 191).

[97] Jean Taine, Franck Enguehard, and Estelle Iacona. *Transferts Thermiques - Introduction Aux Transferts d'énergie*. Dunod, 2014. ISBN: 978-2-10-082750-3 (cit. on p. 56).

[98] Liangfei Xu, Junming Hu, Siliang Cheng, et al. "Robust Control of Internal States in a Polymer Electrolyte Membrane Fuel Cell Air-Feed System by Considering Actuator Properties". In: *International Journal of Hydrogen Energy* 42.18 (May 2017), pp. 13171–13191. ISSN: 03603199. DOI: 10.1016/j.ijhydene.2017.03.191 (cit. on pp. 59, 87, 102, 103, 105).

[99] Yangbin Shao, Liangfei Xu, Xingwang Zhao, et al. "Comparison of Self-Humidification Effect on Polymer Electrolyte Membrane Fuel Cell with Anodic and Cathodic Exhaust Gas Recirculation". In: *International Journal of Hydrogen Energy* 45.4 (Jan. 2020), pp. 3108–3122. ISSN: 03603199. DOI: 10.1016/j.ijhydene.2019.11.150 (cit. on pp. 59, 69, 70, 87, 102, 103).

[100] J.J. Giner-Sanz, E.M. Ortega, and V. Pérez-Herranz. "Hydrogen Crossover and Internal Short-Circuit Currents Experimental Characterization and Modelling in a Proton Exchange Membrane Fuel Cell". In: *International Journal of Hydrogen Energy* 39.25 (Aug. 2014), pp. 13206–13216. ISSN: 03603199. DOI: 10.1016/j.ijhydene.2014.06.157 (cit. on pp. 61, 72).

[101] Nguyen The Truc, Shun Ito, and Kazuyoshi Fushinobu. "Numerical and Experimental Investigation on the Reactant Gas Crossover in a PEM Fuel Cell". In: *International Journal of Heat and Mass Transfer* 127 (Dec. 2018), pp. 447–456. ISSN: 00179310. DOI: 10.1016/j.ijheatmasstransfer.2018.07.092 (cit. on p. 61).

[102] R.K. Ahluwalia and X. Wang. "Buildup of Nitrogen in Direct Hydrogen Polymer-Electrolyte Fuel Cell Stacks". In: *Journal of Power Sources* 171.1 (Sept. 2007), pp. 63–71. ISSN: 03787753. DOI: 10.1016/j.jpowsour.2007.01.032 (cit. on p. 61).

[103] Shyam S. Kocha, J. Deliang Yang, and Jung S. Yi. "Characterization of Gas Crossover and Its Implications in PEM Fuel Cells". In: *AIChE Journal* 52.5 (May 2006), pp. 1916–1925. ISSN: 0001-1541, 1547-5905. DOI: 10.1002/aic.10780 (cit. on p. 61).

[104] Kyung Don Baik and Min Soo Kim. "Characterization of Nitrogen Gas Crossover through the Membrane in Proton-Exchange Membrane Fuel Cells". In: *International Journal of Hydrogen Energy* 36.1 (Jan. 2011), pp. 732–739. ISSN: 03603199. DOI: 10.1016/j.ijhydene.2010.09.046 (cit. on pp. 63, 192).

[105] Zirong Yang, Qing Du, Zhiwei Jia, et al. "Effects of Operating Conditions on Water and Heat Management by a Transient Multi-Dimensional PEMFC System Model". In: *Energy* 183 (Sept. 2019), pp. 462–476. ISSN: 03605442. DOI: 10.1016/j.energy.2019.06.148 (cit. on pp. 66, 68, 73, 111).

[106] Patrick Zihrul, Ingmar Hartung, Sebastian Kirsch, et al. "Voltage Cycling Induced Losses in Electrochemically Active Surface Area and in H \textsubscript2 /Air-Performance of PEM Fuel Cells". In: *Journal of The Electrochemical Society* 163.6 (2016), F492–F498. ISSN: 0013-4651, 1945-7111. DOI: 10.1149/2.0561606jes (cit. on pp. 66, 68–70, 74).

[107] Allen J. Bard and Larry R. Faulkner. *Electrochemical Methods: Fundamentals and Applications*. 2nd ed. New York: Wiley, 2001. ISBN: 978-0-471-04372-0 (cit. on p. 66).

[108] Edmund J. F. Dickinson and Gareth Hinds. "The Butler-Volmer Equation for Polymer Electrolyte Membrane Fuel Cell (PEMFC) Electrode Kinetics: A Critical Discussion". In: *Journal of The Electrochemical Society* 166.4 (2019), F221–F231. ISSN: 0013-4651, 1945-7111. DOI: 10.1149/2.0361904jes (cit. on pp. 66–68, 139, 140).

[109] Jintae Kim, Minjin Kim, Taegon Kang, et al. "Degradation Modeling and Operational Optimization for Improving the Lifetime of High-Temperature PEM (Proton Exchange Membrane) Fuel Cells". In: *Energy* 66 (Mar. 2014), pp. 41–49. ISSN: 03605442. DOI: 10.1016/j.energy.2013.08.053 (cit. on p. 68).

[110] Bowen Wang, Kangcheng Wu, Zirong Yang, et al. "A Quasi-2D Transient Model of Proton Exchange Membrane Fuel Cell with Anode Recirculation". In: *Energy Conversion and Management* 171 (Sept. 2018), pp. 1463–1475. ISSN: 01968904. DOI: 10.1016/j.enconman.2018.06.091 (cit. on pp. 69, 70, 87).

[111] N Khajeh-Hosseini-Dalasm, M J Kermani, D Ghadiri Moghaddam, et al. "A Parametric Study of Cathode Catalyst Layer Structural Parameters on the Performance of a PEM Fuel Cell". In: *international journal of hydrogen energy* (2010) (cit. on pp. 69, 70).

[112] A. Hamnett. *The Components of an Electrochemical Cell*. 1st ed. Wiley, Dec. 2010. ISBN: 978-0-470-74151-1. DOI: 10.1002/9780470974001.f101001 (cit. on pp. 69, 70).

[113] Jian Zhao, Xianguo Li, Chris Shum, et al. "A Review of Physics-Based and Data-Driven Models for Real-Time Control of Polymer Electrolyte Membrane Fuel Cells". In: *Energy and AI* 6 (Dec. 2021), p. 100114. ISSN: 26665468. DOI: 10.1016/j.egyai.2021.100114 (cit. on pp. 69, 70).

[114] Robert M. Darling and Jeremy P. Meyers. "Kinetic Model of Platinum Dissolution in PEMFCs". In: *Journal of The Electrochemical Society* 150.11 (2003), A1523. ISSN: 00134651. DOI: 10.1149/1.1613669 (cit. on p. 70).

[115] Steven G. Rinaldo, Wendy Lee, Jürgen Stumper, et al. "Catalyst Degradation: Nanoparticle Population Dynamics and Kinetic Processes". In: *ECS Transactions* 50.2 (Mar. 2013), pp. 1505–1513. ISSN: 1938-5862, 1938-6737. DOI: 10.1149/05002.1505ecst (cit. on p. 70).

[116] Heather A. Baroody and Erik Kjeang. "Predicting Platinum Dissolution and Performance Degradation under Drive Cycle Operation of Polymer Electrolyte Fuel Cells". In: *Journal of The Electrochemical Society* 168.4 (Apr. 2021), p. 044524. ISSN: 0013-4651, 1945-7111. DOI: 10.1149/1945-7111/abf5aa (cit. on p. 70).

[117] M.G. Santarelli, M.F. Torchio, and P. Cochis. "Parameters Estimation of a PEM Fuel Cell Polarization Curve and Analysis of Their Behavior with Temperature". In: *Journal of Power Sources* 159.2 (Sept. 2006), pp. 824–835. ISSN: 03787753. DOI: 10.1016/j.jpowsour.2005.11.099 (cit. on pp. 73, 111).

[118] Minkmas V Williams, H Russell Kunz, and James M Fenton. "Analysis of Polarization Curves to Evaluate Polarization Sources in Hydrogen/Air PEM Fuel Cells". In: *Journal of The Electrochemical Society* 152.3 (2005), A635. DOI: 10.1149/1.1860034 (cit. on pp. 73, 111).

[119] J. Ramousse, J. Deseure, O. Lottin, et al. "Modelling of Heat, Mass and Charge Transfer in a PEMFC Single Cell". In: *Journal of Power Sources* 145.2 (Aug. 2005), pp. 416–427. ISSN: 03787753. DOI: 10.1016/j.jpowsour.2005.01.067 (cit. on p. 76).

[120] K. C. Neyerlin, Wenbin Gu, Jacob Jorne, et al. "Cathode Catalyst Utilization for the ORR in a PEMFC". In: *Journal of The Electrochemical Society* 154.2 (2007), B279. ISSN: 00134651. DOI: 10.1149/1.2400626 (cit. on pp. 76, 77).

[121] Rohit Makharia, Mark F. Mathias, and Daniel R. Baker. "Measurement of Catalyst Layer Electrolyte Resistance in PEFCs Using Electrochemical Impedance Spectroscopy". In: *Journal of The Electrochemical Society* 152.5 (2005), A970. ISSN: 00134651. DOI: 10.1149/1.1888367 (cit. on pp. 77, 191).

[122] Quentin Meyer, Yachao Zeng, and Chuan Zhao. "In Situ and Operando Characterization of Proton Exchange Membrane Fuel Cells". In: *Advanced Materials* (2019) (cit. on p. 79).

[123] Adam Z. Weber, Rodney L. Borup, Robert M. Darling, et al. "A Critical Review of Modeling Transport Phenomena in Polymer-Electrolyte Fuel Cells". In: *Journal of The Electrochemical Society* 161.12 (Sept. 2014), F1254. ISSN: 1945-7111. DOI: 10.1149/2.0751412jes (cit. on p. 79).

[124] Guobin Zhang and Kui Jiao. "Multi-Phase Models for Water and Thermal Management of Proton Exchange Membrane Fuel Cell: A Review". In: *Journal of Power Sources* 391 (July 2018), pp. 120–133. ISSN: 0378-7753. DOI: 10.1016/j.jpowsour.2018.04.071 (cit. on p. 79).

[125] George Em Karniadakis, Ioannis G. Kevrekidis, Lu Lu, et al. "Physics-Informed Machine Learning". In: *Nature Reviews Physics* 3.6 (June 2021), pp. 422–440. ISSN: 2522-5820. DOI: 10.1038/s42254-021-00314-5 (cit. on pp. 79, 88).

[126] Khemraj Shukla, Patricio Clark Di Leoni, James Blackshire, et al. "Physics-Informed Neural Network for Ultrasound Nondestructive Quantification of Surface Breaking Cracks". In: *Journal of Nondestructive Evaluation* 39.3 (Aug. 2020), p. 61. ISSN: 1573-4862. DOI: 10.1007/s10921-020-00705-1 (cit. on p. 79).

[127] Wenqian Chen, Qian Wang, Jan S. Hesthaven, et al. "Physics-Informed Machine Learning for Reduced-Order Modeling of Nonlinear Problems". In: *Journal of Computational Physics* 446 (Dec. 2021), p. 110666. ISSN: 00219991. DOI: 10.1016/j.jcp.2021.110666 (cit. on p. 79).

[128] Rui Ding, Shiqiao Zhang, Yawen Chen, et al. "Application of Machine Learning in Optimizing Proton Exchange Membrane Fuel Cells: A Review". In: *Energy and AI* 9 (Aug. 2022), p. 100170. ISSN: 26665468. DOI: 10.1016/j.egyai.2022.100170 (cit. on p. 79).

[129] Manik Mayur, Mathias Gerard, Pascal Schott, et al. "Lifetime Prediction of a Polymer Electrolyte Membrane Fuel Cell under Automotive Load Cycling Using a Physically-Based Catalyst Degradation Model". In: *Energies* 11.8 (Aug. 2018), p. 2054. ISSN: 1996-1073. DOI: 10.3390/en11082054 (cit. on p. 79).

[130] T Jahnke. "Performance and Degradation of Proton Exchange Membrane Fuel Cells: State of the Art in Modeling from Atomistic to System Scale". In: *Journal of Power Sources* (2016) (cit. on p. 79).

[131] Christophe Robin, Mathias Gerard, Julien d'Arbigny, et al. "Development and Experimental Validation of a PEM Fuel Cell 2D-model to Study Heterogeneities Effects along Large-Area Cell Surface". In: *International Journal of Hydrogen Energy* 40.32 (Aug. 2015), pp. 10211–10230. ISSN: 03603199. DOI: 10.1016/j.ijhydene.2015.05.178 (cit. on p. 87).

[132] Erwan Tardy, Jean-Philippe Poirot-Crouvezier, Pascal Schott, et al. "Investigation of Liquid Water Heterogeneities in Large Area Proton Exchange Membrane Fuel Cells Using a Darcy Two-Phase Flow Model in a Multiphysics Code". In: *International Journal of Hydrogen Energy* 47.91 (Nov. 2022), pp. 38721–38735. ISSN: 03603199. DOI: 10.1016/j.ijhydene.2022.09.039 (cit. on pp. 87, 128).

[133] M. Grimm, M. Hellmann, H. Kemmer, et al. "Water Management of PEM Fuel Cell Systems Based on the Humidity Distribution in the Anode Gas Channels". In: *Fuel Cells* 20.4 (Aug. 2020), pp. 477–486. ISSN: 1615-6846, 1615-6854. DOI: 10.1002/fuce.202000070 (cit. on p. 87).

[134] O. Lottin, B. Antoine, T. Colinart, et al. "Modelling of the Operation of Polymer Exchange Membrane Fuel Cells in the Presence of Electrodes Flooding". In: *International Journal of Thermal Sciences* 48.1 (Jan. 2009), pp. 133–145. ISSN: 12900729. DOI: 10.1016/j.ijthermalsci.2008.03.013 (cit. on pp. 87, 112).

[135] O. Shamardina, A. A. Kulikovsky, A. V. Chertovich, et al. "A Model for High-Temperature PEM Fuel Cell: The Role of Transport in the Cathode Catalyst Layer". In: *Fuel Cells* 12.4 (Aug. 2012), pp. 577–582. ISSN: 1615-6846, 1615-6854. DOI: 10.1002/fuce.201100144 (cit. on p. 87).

[136] Zirong Yang, Zhanrui Liu, Lichao Fan, et al. "Modeling of Proton Exchange Membrane Fuel Cell System Considering Various Auxiliary Subsystems". In: *The Energy Mix for Sustaining Our Future*. Ed. by Ahmad Vasel and David S.-K. Ting. Cham: Springer International Publishing, 2019, pp. 18–33. ISBN: 978-3-030-00104-9 978-3-030-00105-6. DOI: 10.1007/978-3-030-00105-6_2 (cit. on p. 87).

[137] Zirong Yang, Kui Jiao, Zhi Liu, et al. "Investigation of Performance Heterogeneity of PEMFC Stack Based on 1+1D and Flow Distribution Models". In: *Energy Conversion and Management* 207 (Mar. 2020), p. 112502. ISSN: 01968904. DOI: 10.1016/j.enconman.2020.112502 (cit. on pp. 87, 128).

[138] D.S. Falcão, V.B. Oliveira, C.M. Rangel, et al. "Water Transport through a PEM Fuel Cell: A One-Dimensional Model with Heat Transfer Effects". In: *Chemical Engineering Science* 64.9 (May 2009), pp. 2216–2225. ISSN: 00092509. DOI: 10.1016/j.ces.2009.01.049 (cit. on p. 87).

[139] Fei Gao, Benjamin Blunier, Abdellatif Miraoui, et al. "A Multiphysic Dynamic 1-D Model of a Proton-Exchange-Membrane Fuel-Cell Stack for Real-Time Simulation". In: *IEEE Transactions on Industrial Electronics* 57.6 (June 2010), pp. 1853–1864. ISSN: 0278-0046, 1557-9948. DOI: 10.1109/TIE.2009.2021177 (cit. on p. 87).

[140] D.S. Falcão, C. Pinho, and A.M.F.R. Pinto. "Water Management in PEMFC: 1-D Model Simulations". In: *Ciência & Tecnologia dos Materiais* 28.2 (July 2016), pp. 81–87. ISSN: 08708312. DOI: 10.1016/j.ctmat.2016.12.001 (cit. on p. 87).

[141] F. Van Der Linden, E. Pahon, S. Morando, et al. "Proton-Exchange Membrane Fuel Cell Ionomer Hydration Model Using Finite Volume Method". In: *International Journal of Hydrogen Energy* 47.51 (June 2022), pp. 21803–21816. ISSN: 03603199. DOI: 10.1016/j.ijhydene.2022.05.012 (cit. on pp. 87, 141).

[142] Jiankang Wang, Hai Jiang, Gaojian Chen, et al. "Integration of Multi-Physics and Machine Learning-Based Surrogate Modelling Approaches for Multi-Objective Optimization of Deformed GDL of PEM Fuel Cells". In: *Energy and AI* 14 (Oct. 2023), p. 100261. ISSN: 2666-5468. DOI: 10.1016/j.egyai.2023.100261 (cit. on p. 88).

[143] Bowen Wang, Zijun Yang, Mingxi Ji, et al. "Long Short-Term Memory Deep Learning Model for Predicting the Dynamic Performance of Automotive PEMFC System". In: *Energy and AI* 14 (Oct. 2023), p. 100278. ISSN: 2666-5468. DOI: 10.1016/j.egyai.2023.100278 (cit. on p. 88).

[144] Raphaël Gass, Zhongliang Li, Rachid Outbib, et al. "An Advanced 1D Physics-Based Model for PEM Hydrogen Fuel Cells with Enhanced Overvoltage Prediction". In: *International Journal of Hydrogen Energy* 97 (Jan. 2025), pp. 1108–1125. ISSN: 0360-3199. DOI: 10.1016/j.ijhydene.2024.11.374 (cit. on p. 89).

[145] SciPy. *Scipy.Integrate.Solve_ivp*. 2024 (cit. on pp. 92, 124).

[146] Raphaël Gass, Zhongliang Li, Rachid Outbib, et al. "AlphaPEM: An Open-Source Dynamic 1D Physics-Based PEM Fuel Cell Model for Embedded Applications". In: *SoftwareX* 29 (Feb. 2025), p. 102002. ISSN: 2352-7110. DOI: 10.1016/j.softx.2024.102002 (cit. on pp. 119, 124).

[147] Meziane Ait Ziane. “Contrôle et Diagnostic sans Modèle a Priori, Application Au Système Pile à Combustible PEMFC”. PhD thesis. Université de la Réunion, Dec. 2022 (cit. on p. 119).

[148] GNU. *GNU General Public License*. June 2007 (cit. on p. 124).

[149] Numpy. *Style Guide*. 2024 (cit. on p. 124).

[150] *EH Group Clean Energy Generation* (cit. on pp. 124, 146, 147).

[151] *Baltic FuelCells* (cit. on p. 124).

[152] Demetry Pascal. *Geneticalgorithm2*. 2024 (cit. on p. 124).

[153] Ryan Solgi. *Geneticalgorithm*. 2020 (cit. on p. 124).

[154] Dietmar Gerteisen, Timothy Heilmann, and Christoph Ziegler. “Modeling the Phenomena of Dehydration and Flooding of a Polymer Electrolyte Membrane Fuel Cell”. In: *Journal of Power Sources* 187.1 (Feb. 2009), pp. 165–181. ISSN: 03787753. DOI: 10.1016/j.jpowsour.2008.10.102 (cit. on p. 138).

[155] J Wu, X Yuan, H Wang, et al. “Diagnostic Tools in PEM Fuel Cell Research: Part I Electrochemical Techniques”. In: *International Journal of Hydrogen Energy* 33.6 (Mar. 2008), pp. 1735–1746. ISSN: 03603199. DOI: 10.1016/j.ijhydene.2008.01.013 (cit. on p. 144).

[156] M. Chandesris, C. Robin, M. Gerard, et al. “Investigation of the Difference between the Low Frequency Limit of the Impedance Spectrum and the Slope of the Polarization Curve”. In: *Electrochimica Acta* 180 (Oct. 2015), pp. 581–590. ISSN: 0013-4686. DOI: 10.1016/j.electacta.2015.08.089 (cit. on pp. 144, 149).

[157] A. P. Young, J. Stumper, and E. Gyenge. “Characterizing the Structural Degradation in a PEMFC Cathode Catalyst Layer: Carbon Corrosion”. In: *J. Electrochem. Soc.* 156.8 (2009), B913. ISSN: 00134651. DOI: 10.1149/1.3139963 (cit. on p. 144).

[158] Farhana S. Saleh and E. Bradley Easton. “Diagnosing Degradation within PEM Fuel Cell Catalyst Layers Using Electrochemical Impedance Spectroscopy”. In: *J. Electrochem. Soc.* 159.5 (2012), B546–B553. ISSN: 0013-4651, 1945-7111. DOI: 10.1149/2.098205jes (cit. on p. 144).

[159] Quentin Meyer, Yachao Zeng, and Chuan Zhao. “Electrochemical Impedance Spectroscopy of Catalyst and Carbon Degradations in Proton Exchange Membrane Fuel Cells”. In: *Journal of Power Sources* 437 (Oct. 2019), p. 226922. ISSN: 0378-7753. DOI: 10.1016/j.jpowsour.2019.226922 (cit. on p. 144).

[160] Digby D. Macdonald. “Reflections on the History of Electrochemical Impedance Spectroscopy”. In: *Electrochimica Acta* 51.8-9 (Jan. 2006), pp. 1376–1388. ISSN: 00134686. DOI: 10.1016/j.electacta.2005.02.107 (cit. on p. 144).

[161] Tatyana Reshetenko and Andrei Kulikovsky. "A Quasi Three–Dimensional Model for PEM Fuel Cell Impedance: The Effect of Local Oxygen Depletion under the Flow Field Rib". In: *Mater. Res. Express* 10.11 (Nov. 2023), p. 115504. ISSN: 2053-1591. DOI: 10.1088/2053-1591/ad09a6 (cit. on p. 144).

[162] M Eikerling and A.A Kornyshev. "Electrochemical Impedance of the Cathode Catalyst Layer in Polymer Electrolyte Fuel Cells". In: *Journal of Electroanalytical Chemistry* 475.2 (Oct. 1999), pp. 107–123. ISSN: 15726657. DOI: 10.1016/S0022-0728(99)00335-6 (cit. on pp. 145, 146).

[163] A. A. Kulikovsky. "The Regimes of Catalyst Layer Operation in a Fuel Cell". In: *Electrochimica Acta* 55.22 (Sept. 2010), pp. 6391–6401. ISSN: 0013-4686. DOI: 10.1016/j.electacta.2010.06.053 (cit. on pp. 145, 146).

[164] Andrei Kulikovsky. "Analytical Impedance of Oxygen Transport in the Channel and Gas Diffusion Layer of a PEM Fuel Cell". In: *Journal of The Electrochemical Society* (2021) (cit. on pp. 145, 146, 149).

[165] S. Westerlund and L. Ekstam. "Capacitor Theory". In: *IEEE Transactions on Dielectrics and Electrical Insulation* 1.5 (Oct. 1994), pp. 826–839. ISSN: 1558-4135. DOI: 10.1109/94.326654 (cit. on p. 146).

[166] Katarina Wiezell, Peter Gode, and Göran Lindbergh. "Steady-State and EIS Investigations of Hydrogen Electrodes and Membranes in Polymer Electrolyte Fuel Cells". In: *J. Electrochem. Soc.* 153.4 (2006), A749. ISSN: 00134651. DOI: 10.1149/1.2172559 (cit. on p. 146).

[167] Damien Chanal, Nadia Yousfi Steiner, Raffaele Petrone, et al. "Online Diagnosis of PEM Fuel Cell by Fuzzy C-Means Clustering". In: *Encyclopedia of Energy Storage*. Ed. by Luisa F. Cabeza. Oxford: Elsevier, Jan. 2022, pp. 359–393. ISBN: 978-0-12-819730-1. DOI: 10.1016/B978-0-12-819723-3.00099-8 (cit. on p. 146).

[168] Haijiang Wang, Xiao-Zi Yuan, and Hui Li, eds. *PEM Fuel Cell Diagnostic Tools*. Boca Raton: CRC Press, Sept. 2011. ISBN: 978-0-429-10625-5. DOI: 10.1201/b11100 (cit. on p. 149).

[169] Niklas Hensle, Debora Brinker, Sebastian Metz, et al. "On the Role of Inductive Loops at Low Frequencies in PEM Electrolysis". In: *Electrochemistry Communications* 155 (Oct. 2023), p. 107585. ISSN: 13882481. DOI: 10.1016/j.elecom.2023.107585 (cit. on p. 149).

[170] Mark E. Orazem and Bernard Tribollet. *Electrochemical Impedance Spectroscopy*. 2nd ed. The Electrochemical Society Series. Hoboken: John Wiley & Sons, 2017. ISBN: 978-1-119-36368-2 (cit. on p. 149).

[171] George S. Kell. "Density, Thermal Expansivity, and Compressibility of Liquid Water from 0.Deg. to 150.Deg.. Correlations and Tables for Atmospheric Pressure and Saturation Reviewed and Expressed on 1968 Temperature Scale". In: *Journal of Chemical & Engineering Data* 20.1 (Jan. 1975), pp. 97–105. ISSN: 0021-9568, 1520-5134. DOI: 10.1021/je60064a005 (cit. on p. 187).

[172] Alexander H.-D. Cheng and Daisy T. Cheng. “Heritage and Early History of the Boundary Element Method”. In: *Engineering Analysis with Boundary Elements* 29.3 (Mar. 2005), pp. 268–302. ISSN: 09557997. DOI: 10.1016/j.enganabound.2004.12.001 (cit. on p. 193).

[173] S. P. Neuman. “Theoretical Derivation of Darcy’s Law”. In: *Acta Mechanica* 25.3-4 (Sept. 1977), pp. 153–170. ISSN: 0001-5970, 1619-6937. DOI: 10.1007/BF01376989 (cit. on p. 195).

ANNEXES

A. Appendix

A.1. Other physical quantities with temperature dependencies

In this section, equations that establish connections between specific fundamental physical quantities and temperature are provided.

Vapour saturated pressure: P_{sat}

The vapour saturated pressure is expressed as (A.1). This correlation demonstrates acceptable agreement with the experimental data across the temperature range of -50 to 100 °C [33, 45, 55, 60, 63, 76].

$$P_{sat}\left(T_{fc}\right) = 101325 \cdot 10^{-2.1794+0.02953\left[T_{fc}-273.15\right]-9.1837\cdot10^{-5}\left[T_{fc}-273.15\right]^2+1.4454\cdot10^{-7}\left[T_{fc}-273.15\right]^3} \tag{A.1}$$

Liquid water density: ρ_{H_2O}

Liquid water density expression is expressed as (A.2) [171]. At 70°C, this expression yields $\rho_{H_2O} = 977.77\ kg.m^{-3}$.

$$\begin{aligned}\rho_{H_2O} = & \frac{999.83952 + 16.945176\left[T_{fc}-273.15\right] - 7.9870401\cdot10^{-3}\left[T_{fc}-273.15\right]^2}{1+16.879850\cdot10^{-3}\left[T_{fc}-273.15\right]} \\ & + \frac{-46.170461\cdot10^{-6}\left[T_{fc}-273.15\right]^3 + 105.56302\cdot10^{-9}\left[T_{fc}-273.15\right]^4}{1+16.879850\cdot10^{-3}\left[T_{fc}-273.15\right]} \\ & - \frac{280.54253\cdot10^{-12}\left[T_{fc}-273.15\right]^5}{1+16.879850\cdot10^{-3}\left[T_{fc}-273.15\right]}\end{aligned} \tag{A.2}$$

Liquid water dynamic viscosity: μ_l

Liquid water dynamic viscosity is expressed as (A.3) [33].

$$\mu_l = 2.414 \cdot 10^{-5+\frac{247.8}{T_{fc}-140.0}} \tag{A.3}$$

The following table A.1 compares equation (A.3) with data from alternative sources. Equation (A.3) is evaluated there at 70°C.

	Fan [33]	Hu [53]	Yang [55]	Bao [28]
μ_l (10^{-4} Pa.s)	4.01	3.56	3.517	3.508

Table A.1. – Comparison between the values given by the mentioned expression for the liquid water dynamic viscosity and values found in other works

Liquid water kinematic viscosity: ν_l

Liquid water kinematic viscosity is expressed as (A.4). At 70°C, this expression yields $\nu_l = 4.10 \cdot 10^{-7} m^2.s^{-1}$, which is a close to $\nu_l = 3.7 \cdot 10^{-7} m^2.s^{-1}$ obtained from [53].

$$\nu_l \triangleq \frac{\mu_l}{\rho_{H_2O}} \tag{A.4}$$

A.2. Synthesis of the constant values founded in the literature

The objective of this appendix is to furnish a large set of constants utilized by previous researchers. These constants are presented in tables A.2, A.3 and A.4.

References Year	[52] 2021	[76] 2020	[33] 2017	[53] 2016	[28] 2015	[45] 2011	[55] 2011	[93] 2009	[60] 2008	[66] 2007	[68] 2007	[62] 2005	[51] 2003
Operating inputs													
$T_{fc}\ (K)$	343	353	353		353		343	343					353
$P_{in}\ (Pa)$	$[1.3-1.5]\cdot 10^5$		101325		202650			101325			202650		303975
S_a	1.4	2.0	2.0							6 [a]			1.5
S_c	1.8	3.0	1.5						3	3 [a]			1.5
$\Phi_{a,in}$									1	1			
$\Phi_{c,in}$		0.6							1	1			
Physical constants													
$F\ (C.mol^{-1})$	96485												
$R\ (J.mol^{-1}.K^{-1})$	8.314												
$M_{H2O}\ (kg.mol^{-1})$	0.018												
$\gamma_{O_2,in}\ (C.mol^{-1})$	0.2095												
K_e^0					6.2								
$\Delta H^0\ (J.mol^{-1})$					$5.23\cdot 10^4$								
$\mu_{cg}\ (Pa.s)$				$1.881\cdot 10^{-5}$		$2.075\cdot 10^{-5}$						$1.881\cdot 10^{-5}$	
Mathematical factors													
K_{shape}	5				2								

[a] at 1 $A.cm^{-2}$

Table A.2. – Comparison of constant values from different sources (1/3)

References Year	[52] 2021	[76] 2020	[5] 2018	[33] 2017	[53] 2016	[28] 2015	[54] 2015	[45] 2011	[55] 2011
Fuel cell physical parameters									
$L_{gc}\ (m)$	12	0.1		0.1	1.298	0.9282			0.2
$H_{gc}\ (m)$	$5 \cdot 10^{-4}$	10^{-3}		10^{-3}	10^{-3}	10^{-3}	$5 \cdot 10^{-4}$		$5 \cdot 10^{-4}$
$W_{gc}\ (m)$	$8 \cdot 10^{-4}$	10^{-3}		$8 \cdot 10^{-4}$			$7.5 \cdot 10^{-4}$		10^{-3}
$H_{gdl}\ (m)$	$2.3 \cdot 10^{-4}$	$3 \cdot 10^{-4}$		$4.2 \cdot 10^{-4}$	$2.1 \cdot 10^{-4}$	$3 \cdot 10^{-4}$	$3.8 \cdot 10^{-4}$	$2 \cdot 10^{-4}$	$2 \cdot 10^{-4}$
ε_{gdl}		0.7		0.6	0.6	0.4	0.4		0.7
$H_{cl}\ (m)$	10^{-5}	10^{-5}		10^{-5}	10^{-5}			10^{-5}	10^{-5}
ε_{cl}	0.2	0.3		0.3	0.6				0.2
ε_{mc}	0.2	0.25[a]		0.22/0.27					
s_{lim}	0.2735[b]								
$H_{mem}\ (m)$	$2.5 \cdot 10^{-5}$	$2.5 \cdot 10^{-5}$		$5 \cdot 10^{-5}$	$2.5 \cdot 10^{-5}$	$5 \cdot 10^{-5}$		$5 \cdot 10^{-5}$	$2.5 \cdot 10^{-5}$
$\rho_{mem}\ (kg.m^{-3})$		1980		1980	1980	2000	2000	1980	1980
$M_{eq}\ (kg.mol^{-1})$		1.1		1.1	1.1	1.1	1.1	1.1	1.1
$A_{act}\ (m^2)$	$2.91 \cdot 10^{-2}$								
Constants based on the interaction between water and the structure									
$\gamma_v\ (s^{-1})$	1.3			1.3				1.3	
$\gamma_{cond}\ (s^{-1})$		$5 \cdot 10^3$		$5 \cdot 10^3$	10^4		10^2	$[1, 10^4]$	10^2
$\gamma_{evap}\ (Pa^{-1}.s^{-1})$		10^{-4}		10^{-4}			10^{-3}		10^{-3}
θ_c^{cl} (ř)	120	95		95	110		120		95
θ_c^{gdl} (ř)	120	110		120	110		120		110
Referenced values									
$i_{0,c}\ (A.m^{-2})$			0.67			150[c]			
$i_{0,c}\ (A.m^{-3})$		120[c]		120[c]					
$i_{0,a}\ (A.m^{-3})$				10^{8}[c]					
α_c		0.5	0.5	0.5		0.18			
$E_{act}\ (J.mol^{-1})$		$6.568 \cdot 10^4$		$6.568 \cdot 10^4$		$7.32 \cdot 10^4$			
$C_{O_2}^{ref}\ (mol.m^{-3})$		3.39		3.39		40.89	3.39		
$C_{H_2}^{ref}\ (mol.m^{-3})$		56.4		56.4		40.89	56.4		
$P_{ref}\ (Pa)$				10^5		10^5		10^5	

[a] optimal value according to [76]
[b] value obtained with experimental fits from [52]
[c] at 353.15 K

Table A.3. – Comparison of constant values from different sources (2/3)

References Year	[93] 2009	[60] 2008	[66] 2007	[68] 2007	[62] 2005	[96] 2005	[121] 2005	[51] 2003	[59] 2000
Fuel cell physical parameters									
$L_{gc}\ (m)$			0.2						1.36
$H_{gc}\ (m)$	10^{-3}		$5 \cdot 10^{-4}$	10^{-3}	10^{-3}			$2 \cdot 10^{-3}$	$7.6 \cdot 10^{-4}$
$W_{gc}\ (m)$			10^{-3}					10^{-3}	$1.59 \cdot 10^{-3}$
$H_{gdl}\ (m)$	$2.5 \cdot 10^{-4}$	$2.5 \cdot 10^{-4}$	$1.8 \cdot 10^{-4}$	$3 \cdot 10^{-4}$	$3 \cdot 10^{-5}$				
ε_{gdl}		0.5	0.7	0.6	0.5				
$H_{cl}\ (m)$	10^{-5}	$1.6 \cdot 10^{-5}$	$1.5 \cdot 10^{-5}$	10^{-5}	10^{-5}			$5 \cdot 10^{-5}$	
ε_{cl}	0.2 – 0.3	0.12	0.2	0.12					
ε_{mc}		0.393		0.4	0.2		0.15		
s_{lim}									
$H_{mem}\ (m)$		$5 \cdot 10^{-5}$	$5 \cdot 10^{-5}$	$2.5 \cdot 10^{-5}$	$5 \cdot 10^{-5}$			$2 \cdot 10^{-4}$	$1.5 \cdot 10^{-4}$
$\rho_{mem}\ (kg.m^{-3})$				1980	1980		2000		2000
$M_{eq}\ (kg.mol^{-1})$				1.1	1.1				1.1
$A_{act}\ (m^2)$									$5 \cdot 10^{-3}$
Constants based on the interaction between water and the structure									
$\gamma_v\ (s^{-1})$									
$\gamma_{cond}\ (s^{-1})$		10^2	1.0	$5 \cdot 10^{3}$[a]					
$\gamma_{evap}\ (Pa^{-1}.s^{-1})$		10^{-3}	$5 \cdot 10^{-5}$	10^{-4}[a]					
θ_c^{cl} (ř)				95	110				
θ_c^{gdl} (ř)				110	110				
Referenced values									
$i_{0,c}\ (A.m^{-2})$	0.1	0.01				0.42			
$i_{0,c}\ (A.m^{-3})$			10^{4}[b]		120				
$i_{0,a}\ (A.m^{-3})$				10^9		10^8			
α_c	1	1	1	1	1			1	
$E_{act}\ (J.mol^{-1})$									
$C_{O_2}^{ref}\ (mol.m^{-3})$	40.89	5.55	5.24[b]	40					
$C_{H_2}^{ref}\ (mol.m^{-3})$				40					
$P_{ref}\ (Pa)$									

[a] optimal value according to [68]
[b] at 343 K

Table A.4. – Comparison of constant values from different sources (3/3)

A.3. Synthesis of the hypothesis made in this work

The purpose of the appendix is to succinctly summarize and categorize all hypotheses formulated in this work.

Globally

— The cells in the concerned stack are identical, in terms of parameters and operating conditions.
— The stack temperature is considered constant and uniform (the cooling system is not represented).
— All the gas species behave ideally [52].
— The effect of gravity is ignored.
— The cell is operated with pure hydrogen, thus no contamination effects are considered.
— Nitrogen is supposed to be homogenous in all the cathode and the CGC.

In the membrane

— The experimental equations were generally measured on Nafion®-117 membrane [28, 50, 63].
— Certain experiments were conducted at a fixed temperature of 30°C or 80°C. It is assumed that these data can be used at any working PEMFC temperature [28, 50, 63].
— The thickness of the membrane at different water contents is assumed to be unchanged. The membrane expansion is ignored [64].
— Water generated at the triple points is produced in dissolved form in the membrane [45].
— The flow of water through the membrane to a catalytic layer is assumed to be a flow of dissolved water which becomes vapor water [64].
— N_2 crossover is neglected. Please refer to [104] for more information.
— Since the catalytic layer is very thin compared to the other layers, it is considered that the λ value of the electrolyte present in the CL is instantly the same as at the membrane boundary [52] :

$$\lambda_{acl} = \lim_{x \to acl} \lambda_{mem} \text{ and } \lambda_{ccl} = \lim_{x \to ccl} \lambda_{mem}$$

In the CLs

— The gas flow in the CL exhibits laminar characteristics.
— The electrolyte in the CL is assumed to have the same tortuosity characteristics as the CL carbon structure.
— The CLs are modelled as an agglomerate of packed spherical particles.
— The redox reactions of oxygen and hydrogen are considered to be infinitely fast.

In the GDLs

— The GDLs are modelled as a fibrous porous media composed of randomly oriented cylindrical fibers.
— To characterize water transport in GDLs, the Leverett function is employed. This function is derived from experimental data obtained from structures distinct from those found in PEMFCs. Nevertheless, it continues to be extensively utilized [45].
— The gas flow in the GDL exhibits laminar characteristics.
— The deformation of the porous medium is considered negligible, and the water flow is sufficiently slow to result in a small Reynolds number under stationary conditions [70].
— Gas motions transport liquid water, which generate a convective flow denoted as $J_{l,conv}$. Nevertheless, it is neglected compared to the capillary flow $J_{l,cap}$.

In the GCs

— The gas flow in the channel is predominantly convective.
— Liquid water is considered nonexistent in the GC, and a Dirichlet boundary condition [172] is imposed at the GDL/GC interface, setting the liquid water saturation variable s to zero.
— All gases have the same velocity in the gas mixture.
— All concentrations are uniform in the GC.
— Water phase change is ignored in the GC.
— The 'dividing line', or boundary between convective-dominated flow inside the core of the GC and diffusive-dominated flow inside the core of the electrodes, is assumed to occur at the interface between the GC and the GDL.
— Without better knowledge, it is considered that both concentrations at the two side of the GDL/GC interface are instantaneously equal. This is available for all gases : $C_{gc}^{\text{inter}} = C_{gdl}^{\text{inter}}$.

For the voltage

— It is assumed that the stack can follow the imposed current density.
— Anode overpotential is neglected.
— Anode potential is set to zero.
— Among the four elementary steps of the oxidation reduction reaction on the $Pt_{(111)}$ surface, OH formation reaction is the rate-limiting step [28].
— The membrane is considered to be perfectly impermeable to electrons, neglecting the internal short circuit.

In the auxiliary system

— Each of the auxiliary system components is modeled in 0D, meaning the internal parameters in each component are homogeneous.

— The temperature T_{fc} is assumed constant throughout the fuel cell system. Thus, the heat exchanger is disregarded here. This assumption is significant, but is expected to be eliminated in future works.
— Pressure losses along fuel cell gas channels are not modeled.
— The liquid water separator is not modeled. It is assumed that water droplets evacuate so rapidly and efficiently that they do not exist in the auxiliaries. Similarly, any condensation within the auxiliary components is presumed to be promptly removed.
— The H_2 tank and its pressure relief valve are not directly modeled. It is assumed that this reservoir is infinite, and its valve is perfectly regulated to continuously produce a flow at a constant controled pressure $P_{a,des}$ at the inlet of the supply anode manifold.
— The electronic purge valve is inactive in this study and so $k_{purge} = 0$ in (2.37).
— The dynamic behavior of the compressor and humidifier is simplified at first order considering the desired steady-state flows $W_{cp,des}$ and $W_{c,inj,des}$, along with the time constants τ_{cp} and τ_{hum}.
— It is assumed that the pressure at the compressor outlet equals the pressure in the supply manifold of the cathode: $P_{cp} = P_{csm}$.
— It is considered that the recirculation pump reaches its steady state instantly, being much faster than other devices.

A.4. Demonstrations

A.4.1. Additional information concerning the capillary flow $J_{l,cap}$ and the convective flow $J_{l,conv}$

To enhance the understanding of $J_{l,cap}$ and $J_{l,conv}$, supplementary information is provided herein. First, an adaptation of Darcy's law incorporating the variables of this study is expressed as A.5 [173].

$$\boldsymbol{J_l} = -\frac{K_l}{\nu_l}\boldsymbol{\nabla P_l} \tag{A.5}$$

where $\boldsymbol{J_l}$ is the liquid water flow, K_l (m^2) is the liquid phase permeability, and P_l (Pa) is the liquid-phase pressure.

Then, the standard approach for calculating P_l involves the utilization of capillary pressure P_c as defined in (A.6). This is because P_c is exclusively influenced by pore geometry, fluid characteristics, and phase saturation. Consequently, it is a measurable quantity.

$$P_c \triangleq P_g - P_l \tag{A.6}$$

where P_g (Pa) is the gas-phase pressure. For information, within a liquid, the intermolecular cohesive forces (e.g., hydrogen bonding for water) compensate each other. Each molecule generates interaction forces in all directions in a isotropic manner with neighbouring molecules, the resultant of these forces is therefore zero. However, at the surface, this is not the case (interactions with gas molecules are negligible) and the resultant of the forces for the molecules at the surface is directed towards the interior of the liquid. Therefore, there is an additional force, which counterbalances the pressure of the liquid at its surface; this is the capillary pressure Pc. In fact, wherever we are in the liquid, the pressure is globally the same (if we set aside gravity) and is mainly owing to the concentration of the species and their temperature. However, the surface molecules are slowed down, which reduces the pressure at the surface. As this surface pressure is at equilibrium equal to the gas pressure, it follows that liquid water is at a higher pressure, which is logical as it is a much more condensed phase.

Subsequently, by reapplying Darcy's law to establish the relationship between the gas phase pressure P_g and its velocity u_g, (A.7) is derived. Two distinct flows are identified: the capillary flow, as discussed in 1.2.2.2, and the convective flow, as discussed in 1.2.2.5.

$$\boldsymbol{J_l} = \frac{K_l}{\nu_l}\boldsymbol{\nabla P_c} + \frac{\mu_g}{\nu_l}\frac{K_l}{K_g}\boldsymbol{u_g} = \boldsymbol{J_{l,cap}} + \boldsymbol{J_{l,conv}} \tag{A.7}$$

where μ_g $(Pa.s)$ is the gas mixture dynamic viscosity, $K_l = K_0 s^e$ (m^2) is the liquid water phase permeability, $K_g = K_0 (1-s)^e$ (m^2) is the gas mixture phase permeability, and $\boldsymbol{u_g}$ $(m.s^{-1})$ is the gas mixture velocity.

Capillary flow requires further refinement to become practical. Consequently, (A.8)

is extracted from (A.7).

$$\boldsymbol{J_{l,cap}} = \frac{K_l}{\nu_l}\boldsymbol{\nabla P_c} \tag{A.8}$$

The subsequent step involves emphasizing s, representing the liquid water saturation. To achieve this, the gradient $\boldsymbol{\nabla}$ is transitioned from P_c to s, reinterpreting (A.8) as a Fick-like equation in (A.9), where D_{cap} $(kg.m^{-1}.s^{-1})$ represents the capillary diffusion coefficient.

$$\begin{cases} \boldsymbol{J_{l,cap}} = -D_{cap}\boldsymbol{\nabla}\mathrm{s} \\ D_{cap} = -\frac{K_l}{\nu_l}\frac{\partial P_c}{\partial \mathrm{s}} \end{cases} \tag{A.9}$$

Next, the permeability of the liquid phase can be determined through (A.10), while the capillary pressure is correlated with the properties of porous materials as indicated in (A.11) [45, 54, 60, 62, 66].

$$K_l = K_0 \mathrm{s}^{\mathrm{e}} \tag{A.10}$$

$$P_c = -\sigma\,|\cos(\theta_c)|\sqrt{\frac{\varepsilon}{K_0}}J(\mathrm{s}) \tag{A.11}$$

where K_0 (m^2) is the intrinsic permeability and $J(s)$ is the Leverett function.

For information, k_{rl} can also be sourced from existing literature. It represents the relative permeability of the liquid phase and is solely a function of phase saturation, as expressed in (A.12).

$$k_{rl} = \frac{K_l}{K_0} = \mathrm{s}^{\mathrm{e}} \tag{A.12}$$

Then, the Leverett function J, depicted in A.13, relies on experimental data obtained from homogeneous soil or a sand bend with uniform wettability, which differs from the structures of GDL and CL in PEMFC. Additional experimental measurements have been undertaken in an effort to evaluate the actual conditions in PEMFC. Nonetheless, the obtained results exhibit discrepancies. As a consequence, the aforementioned equation continues to be extensively employed in PEMFC studies [45].

$$J(\mathrm{s}) = 1.417\mathrm{s} - 2.12\mathrm{s}^2 + 1.263\mathrm{s}^3 \tag{A.13}$$

Finally, given all of these considerations, it is possible to derive the mainly used expression of $\boldsymbol{J_{l,cap}}$ as shown in 1.25.

A.4.2. Additional information concerning the convective-diffusive flow at the GDL/GC interface $J_{v,codi}$

The expression of $J_{v,codi}$ in (1.39) needs further explanations. This flow is primary based on the diffusive theory, which rules that a diffusive flow is proportional to the

gradient of its characteristic variable, which is here the vapour concentration, as shown in (A.14).

$$J_{v,dif} = D_v \nabla \mathbf{C} \tag{A.14}$$

However, this theory is applicable only in case of a very thin volume at the GDL/GC interface at the GC side, where diffusion is the dominant flow. The thickness of this thin volume is written as ε_{gc}. Elsewhere in the GC, convection is dominant and leads, for simple modelling, to an homogeneous value of the concentration in the x direction (see figure 1.1). This homogeneity is only valid along the thickness. Thus, in the GC outside the mentioned thin volume, $C_{v,gc}$ is not function of x anymore. Considering that ε_{gc} is very small, the diffusive flow can then be rewritten as in (A.15).

$$J_{v,dif} = \pm D_v \frac{C_{v,gc} - C_{v,gc}^{\text{inter}}}{\varepsilon_{gc}} \imath \tag{A.15}$$

ε_{gc} is a variable influenced by both the GC geometry and the characteristics of the flows. The challenge in measuring ε_{gc} is circumvented by introducing a dimensionless number, the Sherwood number S_h, which is defined as follows:

$$S_h = \frac{H_{gc}}{\varepsilon_{gc}} \tag{A.16}$$

with H_{gc} the characteristic thickness of the GC. Then, equation (A.15) becomes (A.17).

$$J_{v,dif} = \pm S_h \frac{D_v}{H_{gc}} \left[C_{v,gc} - C_{v,gc}^{\text{inter}} \right] \imath \tag{A.17}$$

As $C_{v,gc}$ is unaffected by the x direction due to convection, determining its value becomes straightforward. Finally, these coefficients are encompassed within h_v, as elaborated in 1.2.3.5, resulting in (1.40).

A.4.3. Simplified flows at the inlet of the AGC

The consumed molar rate of hydrogen is given by equation (A.18). It is important to extract the active area from the fuel flow, considering that MEA and GC have different flow areas.

$$\dot{n}_{H_2,\text{cons}} = A_{\text{act}} \cdot J_{H_2,c} = A_{\text{act}} \frac{i_{fc}}{2F} \tag{A.18}$$

where $\dot{n}$ $(mol.s^{-1})$ is the temporal derivative of the number of moles n.

In the simplified model, the inlet flow of hydrogen at the anode is selected to be a certain amount of time $\dot{n}_{H_2,\text{cons}}$. This coefficient is the anode stoichiometric ratio of hydrogen : S_a.

$$\dot{n}_{H_2,\text{in}} = A_{\text{act}} \frac{S_a i_{fc}}{2F} \tag{A.19}$$

Using the ideal gas law and the definition of the relative humidity, a link between n_{H_2} and n_{H_2O} is obtained as (A.20)

$$\frac{n_{H_2O}}{n_{H_2}} = \frac{P_{H_2O}}{P_{H_2}} = \frac{\Phi_a P_{sat}}{P - \Phi_a P_{sat}} \tag{A.20}$$

Thus, assuming the humidity of the incoming gases is automatically adjusted to the desired humidity Φ_{des} and approximating the pressure of the incoming gases as the pressure of the gases in the GC inlet $P_{agc,in}$, while neglecting pressure losses, equation (A.21) is derived.

$$\dot{n}_{H_2O,in} = \frac{\Phi_{a,des} P_{sat}}{P_{agc,in} - \Phi_{a,des} P_{sat}} A_{act} \frac{S_a \left[i_{fc} + i_n \right]}{2F} \tag{A.21}$$

Finally, the simplified flow of water at the inlet of the AGC is given in (A.22).

$$\begin{aligned} J_{v,in}^{agc} &= \frac{\dot{n}_{H20,in}}{H_{gc} W_{gc}} \\ &= \frac{\Phi_{a,des} P_{sat}}{P_{agc,in} - \Phi_{a,des} P_{sat}} \frac{A_{act}}{H_{gc} W_{gc}} \frac{S_a \left[i_{fc} + i_n \right]}{2F} \end{aligned} \tag{A.22}$$

A.4.4. Simplified flows at the inlet of the CGC

The consumed molar rate of oxygen is given by equation (A.23).

$$\dot{n}_{O_2,\text{cons}} = \frac{i_{fc}}{4F} A_{\text{act}} \tag{A.23}$$

In this model, the cathode inlet oxygen flow is chosen to be proportional to $\dot{n}02,\text{cons}$. The proportionality coefficient is denoted as the cathode stoichiometric ratio of oxygen, represented by S_c. Thus, equation (A.24) is derived.

$$\dot{n}_{O_2,\text{in}} = \frac{S_c i_{fc}}{4F} A_{\text{act}} \tag{A.24}$$

Using the ideal gas law and the definition of the relative humidity, a link between the dry air n_a, composed of $y_{O_2,in} = 20.95\%$ of O_2 and 79.05% of N_2, and n_{H_2O} is obtained as (A.25).

$$\frac{n_{H_2O}}{n_a} = \frac{P_{H_2O}}{P_a} = \frac{\Phi_c P_{sat}}{P - \Phi_c P_{sat}} \tag{A.25}$$

Moreover, by definition of the molar fraction of oxygen in dry air, is given in (A.26).

$$y_{O_2} = \frac{n_{O_2}}{n_a} \tag{A.26}$$

Thus, assuming the humidity of the incoming gases is automatically adjusted to the desired humidity Φ_{des} and approximating the pressure of the incoming gases as the

pressure of the gases in the GC inlet $P_{cgc,in}$, while neglecting pressure losses, equation (A.27) is derived.

$$\dot{n}_{H_2O,in} = \frac{\Phi_{c,des} P_{sat}}{P_{cgc,in} - \Phi_{c,des} P_{sat}} \frac{1}{y_{O_2,ext}} A_{act} \frac{S_c \left[i_{fc} + i_n \right]}{4F} \tag{A.27}$$

Finally, the simplified flow of water at the inlet of the CGC is given in (A.28).

$$\begin{aligned} J_{v,in}^{cgc} &= \frac{\dot{n}_{H_20,in}}{H_{gc} W_{gc}} \\ &= \frac{\Phi_{c,des} P_{sat}}{P_{cgc,in} - \Phi_{c,des} P_{sat}} \frac{1}{y_{O_2,ext}} \frac{A_{act}}{H_{gc} W_{gc}} \frac{S_c \left[i_{fc} + i_n \right]}{4F} \end{aligned} \tag{A.28}$$